

ALMA MATER STUDIORUM · UNIVERSITÀ DI BOLOGNA

DOTTORATO DI RICERCA IN
Matematica
Ciclo XXXVI

Settore Concorsuale: 01/A5
Settore Scientifico Disciplinare: MAT/08

**INSIDE STANDARD AND HYPERSPECTRAL
LOW-DOSE CT VARIATIONAL IMAGING:
PARAMETER IDENTIFICATION AND
MATERIAL DECOMPOSITION**

Presentata da: **FRANCESCA BEVILACQUA**

Coordinatore Dottorato
VALERIA SIMONCINI

Supervisore
FIGURELLA SGALLARI
Co-supervisori
ALESSANDRO LANZA
MONICA PRAGLIOLA

Esame Finale Anno 2024

Abstract

The main contribution of this thesis is the proposal of novel strategies for the selection of parameters arising in variational models employed for the solution of inverse problems with data corrupted by Poisson noise. In light of the importance of using a significantly small dose of X-rays in Computed Tomography (CT), and its need of using advanced techniques to reconstruct the objects due to the high level of noise in the data, we will focus on parameter selection principles especially for low photon-counts, i.e. low dose Computed Tomography. For completeness, since such strategies can be adopted for various scenarios where the noise in the data typically follows a Poisson distribution, we will show their performance for other applications such as photography, astronomical and microscopy imaging.

More specifically, in the first part of the thesis we will focus on low dose CT data corrupted only by Poisson noise by extending automatic selection strategies designed for Gaussian noise and improving the few existing ones for Poisson. The new approaches will show to outperform the state-of-the-art competitors especially in the low-counting regime. Moreover, we will propose to extend the best performing strategy to the hard task of multi-parameter selection showing promising results.

Finally, in the last part of the thesis, we will introduce the problem of material decomposition for hyperspectral CT, which data encodes information of how different materials in the target attenuate X-rays in different ways according to the specific energy. We will conduct a preliminary comparative study to obtain accurate material decomposition starting from few noisy projection data.

Contents

I	Introduction	1
1	Preamble	3
1.1	Motivation	3
1.2	Contribution	5
1.3	Organization	6
1.4	Publications	7
2	The CT Inverse Problem	9
2.1	Inverse Problems in Imaging	9
2.2	The CT inverse problem	13
2.2.1	The discretized CT model	15
2.3	Noise modelling in CT	21
2.3.1	Noise Approximations	25
3	Behind the mathematical model: the Physics of X-ray Tomography	29
3.1	The nature and generation of X-rays	30
3.2	Photon-matter interaction	33
3.2.1	Lambert-Beer Law of attenuation	33
3.2.2	The evolution of the Lambert-Beer Law	34
3.3	X-ray detection	35
3.4	Statistical properties of CT	36
3.4.1	Statistical properties of the X-ray source	37
3.4.2	Statistical properties of the detector	37

3.5	The evolution of Computed Tomography	39
4	On and beyond standard reconstruction methods	41
4.1	The Standard Back-Projection (BP) Method	42
4.2	The Fourier-Based methods	44
4.3	The algebraic methods	45
4.4	Comparative evaluation of the standard methods	49
4.5	Variational Methods	51
4.5.1	Bayesian Formulation	54
4.5.2	Priors	55
4.5.3	Likelihoods	57
4.5.4	The Maximum A Posteriori (MAP) approach	58
4.6	The \mathcal{R} -KL model	59
4.6.1	The TV-KL model	61
4.6.2	Other regularization and fidelity terms	61
4.7	The importance of the choice of the parameter	63
II	Automatic selection of the parameters	67
5	State of The Art strategies	69
5.1	The discrepancy Principle	70
5.2	The Quadratic Discrepancy Principle	73
5.3	Masked Principles	74
6	The Nearly Exact Discrepancy Principle	77
6.1	Limits of the Approximate Discrepancy Principle	77
6.2	The New nearly exact discrepancy principle	84
6.3	Numerical Results	88
6.3.1	CT Reconstruction	89
6.3.2	Image Restoration	93
6.3.3	Discussion	109

7	Poisson Whiteness Principle (PWP)	111
7.1	The Whiteness Principles for Additive Noise	112
7.2	The Poisson Whiteness Principle	115
7.3	Numerical Results	119
7.3.1	CT image reconstruction	120
7.3.2	Image restoration	128
7.3.3	Discussion	134
8	Masked Unbiased Principles	137
8.1	The “unmasked” principles	138
8.2	The “masked biased” principles	139
8.3	The “masked unbiased” principles	141
8.3.1	The new random variable: the Positive Poisson	141
8.3.2	Masked unbiased approximate discrepancy principle (ADP- M)	145
8.3.3	Masked unbiased quadratic discrepancy principle (QDP- MU)	145
8.3.4	Masked unbiased nearly exact discrepancy principle (NEDP-MU)	146
8.3.5	Masked unbiased whiteness principle (WP-MU)	146
8.3.6	Analysis of bias	147
8.4	Numerical Results	150
8.4.1	CT Reconstruction	154
8.4.2	Image Restoration	160
8.4.3	Discussion	171
9	The Multi-parameter Whiteness Principle	177
9.1	A more complex CT model	178
9.2	The Multi-parameter Whiteness Principle	179
9.2.1	The MWP for Mixed Poisson-Gaussian noise in CT reconstruction	180

9.3	Numerical Results	182
9.3.1	Derivative free minimization of the Whiteness function	186
10	Numerical Solution of Variational Models by ADMM	191
10.1	Numerical solution for the \mathcal{R} -KL model	191
10.1.1	The \mathbf{t} -subproblem	195
10.1.2	The \mathbf{u} -subproblem	197
10.2	Numerical solution for the mixed noise model	201
III	Spectral CT	205
11	Material Decomposition in Spectral Tomography	207
11.1	The attenuation coefficients and the energies	208
11.2	Spectral Tomography and its model	211
11.3	Reconstruction and Material Decomposition Methods	213
11.3.1	Two-stage	214
11.3.2	One-stage	216
11.4	Numerical results	218
11.4.1	Experimental setup	219
11.4.2	One-stage vs two-stage method	222
11.4.3	L_2 vs WL_2	224
11.4.4	Regularization	225
11.4.5	Test on Real Data	227
	Conclusions	233
	Bibliography	237

List of Symbols

\mathbb{R}	The set of real numbers
\mathbb{R}_+	The set of non negative real numbers
\mathbb{R}_{++}	The set of positive real numbers
\mathbb{N}	The set of natural numbers
\mathbb{N}_+	The set of positive natural numbers
χ_C	Characteristic function on the set C
ι_C	Indicator function on the set C
x	Deterministic scalar
\mathbf{x}	Deterministic vector
\mathbf{X}	Deterministic matrix
$B \sim \mathcal{N}$	Random scalar variable B distributed as \mathcal{N}
$\mathcal{B} \sim \mathcal{N}$	Random field \mathcal{B} distributed as \mathcal{N}
$p_B(b)$	Probability density function of a random variable B
$P_B(b)$	Probability mass function of a random variable B
$E[B]$	Expected value of a random variable B
$\text{Var}[B]$	Variance of a random variable B
r.v.	Random variable
r.f.	Random field
$\mathbf{I}_{m \times m}$	Identity matrix of dimension $m \times m$
$\mathbf{1}_m$	Column vector with m components all equal to 1
$\mathbf{0}_m$	Column vector with m components all equal to 0
$\mathbf{0}_{m \times n}$	$m \times n$ matrix with components all equal to 0
$ \mathbf{A} $	Determinant of a matrix \mathbf{A}
$\nabla(\cdot)$	Discrete gradient operator acting on vectors
$\nabla^2(\cdot)$	Discrete hessian operator acting on vectors
$\ \cdot\ _2$	Euclidean norm
$\ \cdot\ _1$	L1 norm
$\ \cdot\ _F$	Frobenius norm
$\ \cdot\ _W$	Weighted norm

Part I

Introduction

Chapter 1

Preamble

1.1 Motivation

The invention of Computed Tomography (in short, CT) in the early 1970s, by Allan Cormack and Godfrey Hounsfield, has led to a radical change in clinical investigation techniques as well as in industrial applications and safety routines. Its ability to visualize the internal structure of an object without invasive procedures is the reason for its effectiveness. This is achieved by irradiating the target with X-rays: once running through the object, they are attenuated in a way that changes according to the encountered materials and are then collected by a detector. Since a single direction is not enough to determine the inside structure of the target (due to the superposition of the structures along the irradiation lines), the procedure must be repeated from different directions. Despite all the benefits that come from visualizing the internal structure of the human body, and therefore to diagnose the disease, Computed Tomography also has disadvantages to take into account. One of the main problems is the high dose of X-rays to which the patient is exposed; in fact, the probability of occurrence of malignant pathologies increases with the dose. This is especially reflected in the case of young patients, who are more sensitive to ionizing radiation, or when the therapy requires more examinations over time. Moreover, standard tomography requires cumbersome

machinery and long acquisition-time to achieve high-quality data, both being conditions that are not applicable in emergency scenarios. Finally, in some medical application, e.g. mammography, the irradiation can be performed only within a particular range of angles, thus producing data with different degrees of informativeness depending on the area of the image.

The research work presented in this thesis, that is related to the project of developing innovative numerical models and methods for CT reconstruction for the realization of small CT equipments, founded by the Carisbo Foundation, will focus on investigating the low dose CT scenarios and improving the quality of the reconstructions. As introduced before, such conditions arise in important clinical situations, such as emergency scanning where powerful CT machines can not be employed due to their big dimensions and the long acquisition times. This is especially the case where small and transportable CT machines can make a difference; however, they can not have the same characteristics (power, resolution, dimension, etc.) as the standard ones, resulting with fewer and noisier data to work on. At the same time, low dose CT is crucial especially for the care of young children or when dealing with specific parts of the body which are more vulnerable to X-rays (e.g. ovaries, thyroid or lymphoid tissues). In fact, the main danger of CT is the exposition to ionizing radiation that can cause an increase in a person's lifetime risk of developing cancer and it is of particular concern in pediatric patients because the cancer risk per unit dose of ionizing radiation is higher for younger patients than adults, and younger patients have a longer lifetime for the effects of radiation exposure to manifest as cancer. With this in mind, since the X-ray dose is directly proportional to the exposure time of each projection and the number of used directions, a low dose CT scan can be performed by decreasing the exposure time and/or the number of projections and/or the intensity of the X-ray.

Besides the motivations regarding the medical field, low dose X-ray Tomography is also used for industrial applications due to the limited scan time available (e.g. security procedures) or to the specific characteristics of the

machinery. Compared to standard CT, the data acquired with a low dose of X-rays is typically characterized by a larger noise level. Due to the electromagnetic nature of X-rays, every photon-counting applications, as the case of CT, is affected by Poisson noise which becomes more and more degrading as the number of incoming photons decreases. Nonetheless standard CT reconstruction algorithms tend to amplify noise in images and this behavior is particularly emphasized in the case of low dose CT where such algorithms are no longer capable of achieving good quality results. In this scenario, variational methods are typically employed to mitigate the effects of noise propagation: such strategies combine *a priori* information on the object with the noise statistics that connects the target to the data. Although variational methods can preserve the significant details in the target while removing noise and artifacts, their performance strongly depends on the choice of one or more parameters that, in most of the cases, are hand-tuned. In this perspective, the main contribution of this work concerns the proposal of novel parameter selection strategies in variational methods working for low dose CT problems where data are corrupted by Poisson noise. Moreover, thanks to the collaboration with the Technical University of Denmark, where I have been twice as a visiting PhD student, the low-dose regime has been extended to the case of hyperspectral CT data, that encodes information of how different materials in the target attenuate X-ray beams with different energies.

1.2 Contribution

The main contribution of this thesis is the proposal of novel parameter selection strategies for the solution of inverse problems with data corrupted by Poisson noise. In light of the importance of using a significantly small dose of X-rays in Computed Tomography, and its need of using advanced techniques to reconstruct the objects due to the high level of noise in the data, we will focus on parameter selection principles especially for low photon-counts, i.e. Low Dose Computed Tomography. Although the CT reconstruction in

low-dose, e.g. particularly noisy, scenarios is the real world problem that motivates the derivation of the strategies proposed in this thesis, we are going to prove the validity of the designed approaches for different imaging problems that are typically affected by Poisson noise: photography, astronomical and microscopy imaging.

1.3 Organization

In Chapter 2 we introduce the CT inverse problem by describing the mathematical formulation of the process and the noise that characterizes it. Chapter 3 explains the physics behind the mathematical model of Computed Tomography from the generation of X-rays to the statistical properties underneath the CT model defined in 2. Moreover, in Chapter 4 the standard CT reconstruction techniques are explained, along with their results in different CT condition (i.e. different doses and angles of projections). In order to overcome the poor-quality results of the above strategies for low dose CT, we introduce variational methods and how to derive them. Finally we highlight the importance of the choice of the parameters, which is crucial for a good reconstruction and that will be the topic of the following chapters.

In Chapter 6 and 7 the state of the art strategy proposed by Bertero and co-authors [25, 26, 27] are explained, together with its strengths and weaknesses. Starting from the latter, we highlight the theoretical limits of the approach and then propose a nearly exact version of it based on Monte Carlo simulations and weighted least-square fitting. In addition, we extend the so-called residual whiteness principle originally designed for additive white noise to Poisson data and perform an extensive comparison between the three strategies.

In Chapter 8 we first review the *unmasked* selection criteria (including the two very recent ones proposed in 6 and 7) which consider all pixels in the selection procedure. Then, based on an idea proposed by Carlván and Blanc-Feraud in [31] to effectively deal with dark backgrounds and/or low

photon-counting regimes, we introduce and discuss the *masked* versions of the considered unmasked selection principles formulated by simply discarding the pixels measuring zero photons. However, we prove that discarding the zero pixels yields a bias in the resulting principles that can be overcome by introducing a novel positive Poisson distribution correctly modeling the statistical properties of the undiscarded noisy data. Such distribution is at the core of newly proposed *masked unbiased* counterparts of the discussed strategies. We extensively and reliably test the three categories of principles on different problems and noise levels. In Chapter 9 we extend the Whiteness principle to the case of multi-parameter selection and test the method on CT reconstruction problems with two free parameters. Then, Chapter 10 describes the algorithm to solve the different variational models used until then.

Finally, in the last part of the thesis we will focus on material decomposition for Hyperspectral Computed Tomography. In Chapter 11 this new developing technique, that exploits the property of materials to attenuate X-rays in different ways depending on the specific energy, is introduced, together with the concept of material decomposition and standard reconstruction methods. We will show results both on real and synthetic data and discuss the advantages and disadvantages of the different strategies.

1.4 Publications

The main part of the discussion in this thesis refers to published and upcoming works. In particular, the first part of the thesis, from Chapter 6 to Chapter 10, is based on the following works:

- Bevilacqua, F.; Lanza, A.; Pragliola, M.; Sgallari, F.: *Nearly Exact Discrepancy Principle for Low-Count Poisson Image Restoration*. *J. Imaging* 2022, 8, 1.
- Bevilacqua, F.; Lanza, A.; Pragliola, M.; Sgallari, F.: *Whiteness-based*

parameter selection for Poisson data in variational image processing. Applied Mathematical Modelling, vol. 117, pp. 197-218, 2023

- Bevilacqua, F.; Lanza, A.; Pragliola, M.; Sgallari, F.: *Masked unbiased principles for parameter selection in variational image restoration under Poisson noise.* Inverse Problems, vol. 39(3), 034002, 2023.

On the other hand, in the second part of the thesis, Chapter 11 refers to the work:

- Bevilacqua, F.; Dong, Y.; Jørgensen, J.S.: *Regularized Material Decomposition for K-edge Separation in Hyperspectral Computed Tomography.* Scale Space and Variational Methods in Computer Vision. SSVM 2023. Lecture Notes in Computer Science, vol 14009. Springer, Cham. (2023).

Chapter 2

The CT Inverse Problem

In this thesis we focus on image reconstruction for Computed Tomography (CT), which, from a mathematical point of view, is the task of computing the spatial structure of an object using its projections. These problems are known as *inverse problems* where one aims to determine an unknown quantitative cause that produces the observed data through a given measurement model. Before describing the CT inverse problem we introduce the class of inverse problems in imaging, of which the CT is part, and the challenges that characterize them. Then, the continuous and discrete formulation of the CT acquisition process are explained, together with the degradation effects (i.e. noise) that affects the data. In this work we consider reconstruction of 2D objects with a particular, but commonly used geometry: the Fan Beam CT (which will be explained later in the chapter). However, we highlight that the descriptions and the new contributions outlined can be extended in a straightforward manner to other geometries.

2.1 Inverse Problems in Imaging

Over the last few decades, the communication has developed more and more through images. This is due to the advancement of new technologies and to the way images can be used in different fields of application to display

data that would be difficult to interpret in another way or that can not be seen by the human eye. Typical examples are microscopic and astronomical images, focused on collecting information about cellular and celestial structure, respectively. Furthermore, images obtained from radiation sources such as those acquired in CT and Positron Emission Tomography (PET) applications, are indispensable for patient care in the medical field, but are also used for security reasons in airports or to study the structure of archaeological finds.

Image processing it is a discipline that allows us to develop strategies to interpret, manipulate, transmit and improve the quality of the data. Depending on the applications at hand, the space of the measurement data may not coincide with the space to which the target images belong. In general, one wants to determine an unknown quantitative cause that produces the observed data through a given measurement model. Problems like these are called *inverse problems*.

In mathematics, inverse problems arise when investigating an unknown cause that produces the observed data (or effect) with a given cause-to-effect forward model. Reconstructing the unknown source is not an easy task; it involves decisions and risks mainly related to the loss of the well-posedness of the problem. The mathematician Jacques Hadamard defined, in the early 20th century, a problem to be *well-posed* if:

- admits a solution;
- the solution is unique;
- the solution depends continuously on the data.

If a problem does not satisfy at least one of these properties is it said to be *ill-posed*. Most of the challenging inverse problems fall in this category and require ad hoc strategies to compensate the ill-posedness. Typically, if the existence is not guaranteed one can extend the set of feasible of solutions, while the non-uniqueness can be overcome by imposing additional constraints

to be fulfilled. Finally, when a small perturbation of the data produces a very large change in the solution, advanced strategies need to be implemented to control the error in the solution.

Before exploring the approaches to solve ill-posed inverse problems, topic that will be discussed in the following chapters, we are giving a brief overview of the most studied problems in image processing.

- Denoising: is the problem of removing the noise from images without losing information about local features. It is caused by the quantum nature of electromagnetic radiation or the atmospheric distortion.
- Deblurring: is the problem of restoring images corrupted by blur. This can be caused by the features of the tool used to capture the data, as for microscopy, or by the relative motion between the object and the camera.
- Inpainting: is the task of filling parts of the image missing because of occlusions or other damages.
- Reconstruction: is the problem of retrieving an image from data that does not belong to the image space. This is the case of PET (positron emission tomography), MRI (magnetic resonance imaging) and CT (computed tomography) where the data collects information of how the object responds to some kind of input.
- Super-Resolution: is the task of enhancing the resolution of an image from low-resolution to high.
- Image Decomposition: is the separation of semantic different component of an image.

Mathematically, a continuous signal \bar{x} can be modeled as a function in the function space \mathcal{X} from \mathbb{R}^r to \mathbb{R}^n

$$\bar{x} \in \mathcal{X}, \quad \bar{x}(z) : \Omega \subset \mathbb{R}^r \rightarrow \mathbb{R}^n,$$

where Ω is a compact set of \mathbb{R}^r and $r, n \geq 1$. When both $r = 1$ and $n = 1$ \bar{x} represents a one-dimensional signal, while for $r = 2, 3$ we have a 2D signal (image) or a 3D signal (volume). For $n \geq 2$, \bar{x} represents a signal with multiple channels; for example, if $n = 3$, \bar{x} is a color image with red-green-blue (RGB) color channels. It is important to recall that this continuous formalization of the signals provides a modelling of the inherently “analogic” human acquisition process, and will be helpful to describe the forward model of our inverse problems. However, the measured data, which are typically digital, along with the necessity of solving the problem with a machine, will require a discretization both of the forward model and the solution.

The *degradation model* can be expressed in the form:

$$b = \mathcal{T}(\bar{x}) = \text{Noise}(\bar{\lambda}), \quad \bar{\lambda} = g(\mathcal{A}(\bar{x})) \quad (2.1)$$

where $b \in \mathcal{B}$, with \mathcal{B} the function space from \mathbb{R}^h to \mathbb{R}^m , is the observed data, $\mathcal{T} : \mathcal{X} \rightarrow \mathcal{B}$ is a model of the measurement process which here is defined as a combination of a deterministic linear mapping \mathcal{A} acting on \bar{x} , a generic function g (which is non linear or the identity function) and a random noise operator Noise. As already recalled, \mathcal{X} may differ from \mathcal{B} , as it happens in some applications.

For example, in the denoising problem, both \mathcal{A} and g are the identity operator $g(\mathcal{A}(\bar{x})) = \bar{x}$; while, for image deblurring, g is the identity function and \mathcal{A} takes the form of the space variant blur operator

$$\mathcal{A}(\bar{x}) = \int_{\Omega} k(y, z) \bar{x}(z) dz$$

where $k(y, z)$ is the blur kernel. In case of inpainting g is the identity function and $\mathcal{A}(\bar{x}) = \chi_C(\bar{x})$, with χ_C the characteristic function of the subset C of the image domain Ω . For the image reconstruction problems both g and \mathcal{A} take different forms depending on the specific case. This latter case will be described extensively in the next sessions as it will be the main focus of this thesis. Moreover, this is a typical case where \mathcal{X} differs from \mathcal{B} .

2.2 The CT inverse problem

Computed Tomography has evolved into an indispensable imaging method both in clinical routines and industrial applications. It was the first non-invasive method to acquire images of the inside the human body that were not biased by superposition of distinct anatomical structures. This is done by analyzing the projection of the internal information of the object from different angles. The fundamental difference between various medical imaging modalities is the property of the material (i.e. tissue) that they image and the source of energy used to extract this information. Magnetic Resonance Imaging (MRI) excites and detects the change of direction of the rotational axis of the protons present in the aqueous component of the tissues, while Positron Emission Tomography (PET) tracks the positrons emitted by radioactive tracer injected in the patient that will collect into areas with higher levels of metabolic or biochemical activity, which are often the area of the disease.

On the other hand, X-ray Computed Tomography is based on the capability of the tissues to attenuate X-rays. In CT the X-rays are attenuated at varying extents when running through the object and the local absorption is measured by a detector. Naturally, the “shadow” that is cast in only one direction does not represent a sufficient information for the determination of the spatial distribution of distinct structures inside the target. To this purpose, it is necessary to irradiate the object from multiple directions. When the different attenuation or absorption profiles are plotted over the angles of rotation a sinusoidal arrangement is obtained, called the *sinogram*.

The X-ray is known to have a very high, material-dependent capability of matter penetration. However, the number of photons, i.e., the radiation intensity, decreases exponentially while crossing an object along the incident direction. The reason for an exponential reduction in photon number is that each photon is removed individually from the incident beam by an interaction with the matter. The attenuation of the X-ray, with an initial radiation intensity $I_0 > 0$, that passes through the object along the segment L , Figure

2.1, can be formalized by the **Lambert-Beer's law** in the following form [2]

$$I = I_0 \exp \left(- \int_L \bar{x}(z_1(\ell), z_2(\ell)) d\ell \right). \quad (2.2)$$

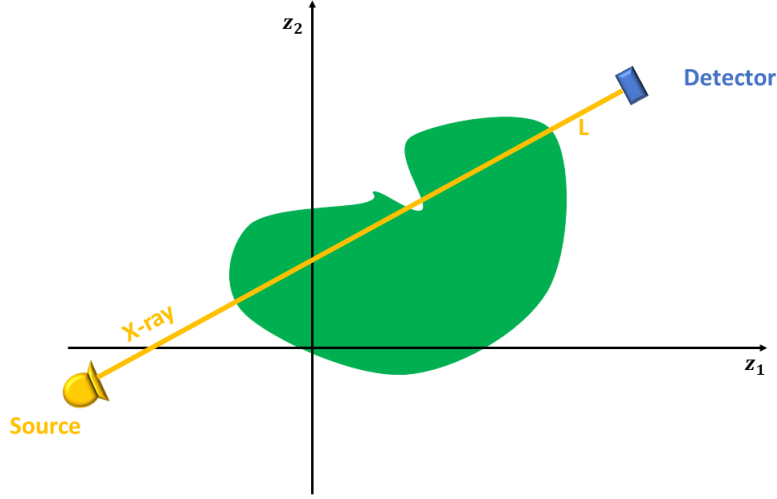


Figure 2.1: An X-ray passing through the object along the segment L .

In the Fan Beam CT, the unknown target object is a 2D object, the source emits a 2D conical X-rays beam, and the 1D (linear) detector measures the X-ray intensities at different locations after the attenuation process has occurred. Then, the source and the detector rotate together around a center of rotation (as near as possible to the center of the object), and the procedure is repeated - see Figure 2.2(left).

In particular, for a given acquisition angle $\theta \in [0, 2\pi)$, the detector measures at its location $\xi \in \mathbb{R}$ the intensity of the X-ray after its passing through the object along the line between the source and the detector location ξ ; see Figure 2.2(right).

In the continuous setting, denoting by $\bar{x}(z_1(\ell), z_2(\ell)) : \mathbb{R}^2 \rightarrow \mathbb{R}_+$ the X-ray attenuation coefficients of the target object as a function of the space coordinates, according to the Lambert-Beer's law in (2.2), the measure obtained by the Fan Beam CT acquisition process is as follows

$$I(\theta, \xi) = I_0 \exp(-\mathcal{A}(\bar{x})(\theta, \xi)), \quad \theta \in [0, 2\pi), \quad \xi \in \mathbb{R}, \quad (2.3)$$

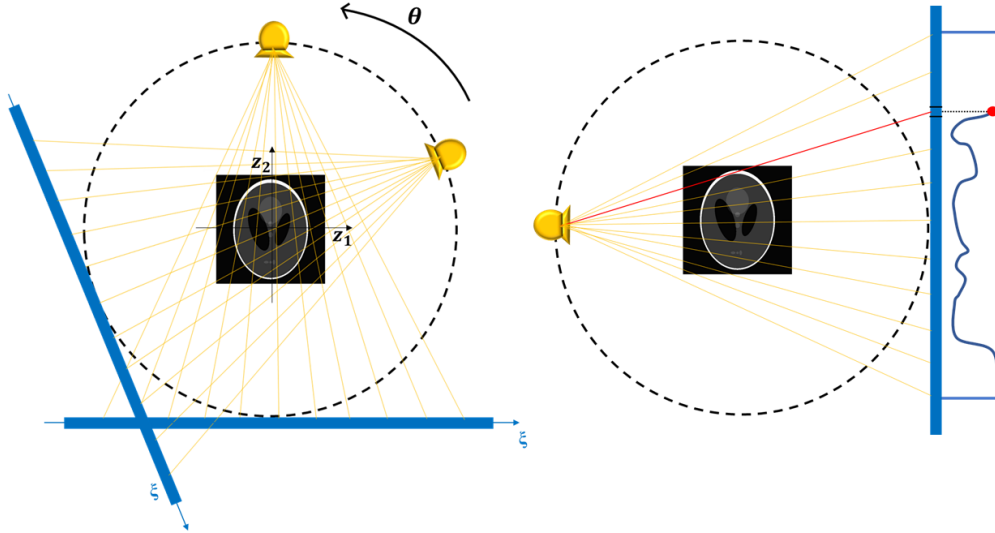


Figure 2.2: Fan Beam CT procedure. *Left*: the source emits a conical X-rays beam, the 1D linear detector measures the intensities after the attenuation process, and the procedure is repeated after rotating the source and the detector. *Right*: for each acquisition angle, the measure captured by the detector at a pixel is the intensity of the X-ray after passing through the object along the line between the source and the detector pixel.

where $\mathcal{A}(\bar{x}) = \mathcal{R}(\bar{x})$, with $\mathcal{R}(\bar{x})$ indicating the 2D Radon transform of the target function \bar{x} , namely

$$\mathcal{R}(\bar{x})(\theta, \xi) = \int_{L(\theta, \xi)} \bar{x}(z_1(\ell), z_2(\ell)) d\ell. \quad (2.4)$$

The $\mathcal{R}(\bar{x})$ function defined above is commonly referred as the *sinogram*.

2.2.1 The discretized CT model

Although the above physical processes have been described in continuous settings, a discretization stage has to be performed in order to make the objects of interest computer-readable. The continuous 2D object x is converted into a discrete image which is a matrix whose elements are referred to as pixels. The quality of the discretization, also known as sampling, depends

on how well the discrete grid of the matrix approximates the continuous object \bar{x} . In what follows, we introduce the notations used for the discretized detector location $\boldsymbol{\xi}$, the target image $\bar{\mathbf{x}}$ and the acquisition angle $\boldsymbol{\theta}$:

$$\begin{aligned}\bar{\mathbf{x}} &= (\bar{x}_1; \dots; \bar{x}_j; \dots; \bar{x}_n) \text{ is the vectorized (by rows) target image,} \\ \boldsymbol{\xi} &= (\xi_1; \dots; \xi_i; \dots; \xi_d) \text{ is the set of detector pixel locations,} \\ \boldsymbol{\theta} &= (\theta_1; \dots; \theta_l; \dots; \theta_s) \text{ is the set of considered acquisition angles.}\end{aligned}$$

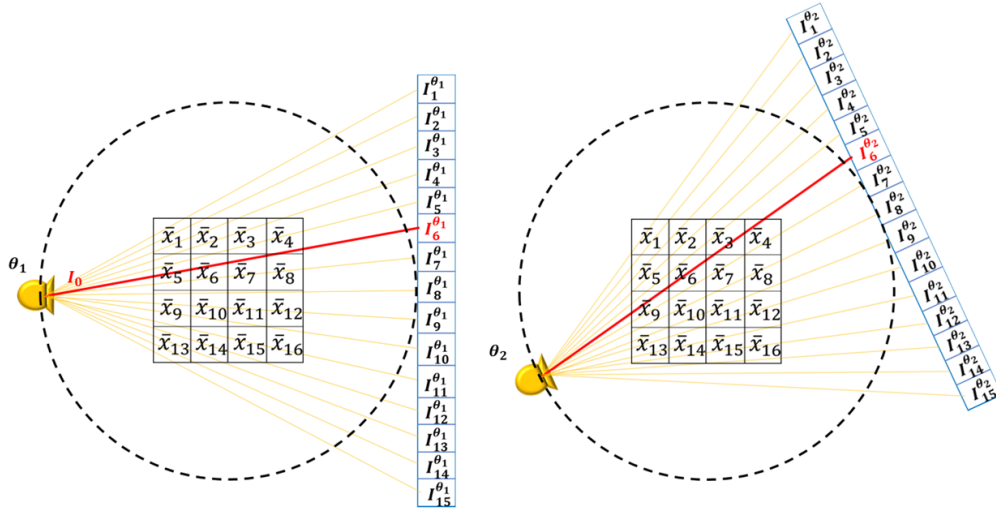
We notice that, in this discrete setting, a single line integral as the one in (2.3) is replaced by a scalar product. Hence, the discrete, finite set of all considered line integrals (for the s projection angles and the d detector pixels) is replaced by a matrix $\mathbf{A} \in \mathbb{R}^{m \times n}$, with $m = sd$, which represents the discrete Radon transform matrix, i.e. a discrete version of the Radon transform operator $\mathcal{R}[x]$ in (2.3). Hence, according to the Lambert-Beer's law, the discrete projection data $\mathbf{I} \in \mathbb{R}^m$ can be written as

$$\mathbf{I} = \begin{bmatrix} \mathbf{I}^{\theta_1} \\ \mathbf{I}^{\theta_2} \\ \vdots \\ \mathbf{I}^{\theta_s} \end{bmatrix} = I_0 \exp \left(- \begin{bmatrix} \mathbf{A}^{\theta_1} \\ \mathbf{A}^{\theta_2} \\ \vdots \\ \mathbf{A}^{\theta_s} \end{bmatrix} \bar{\mathbf{x}} \right) \quad (2.5)$$

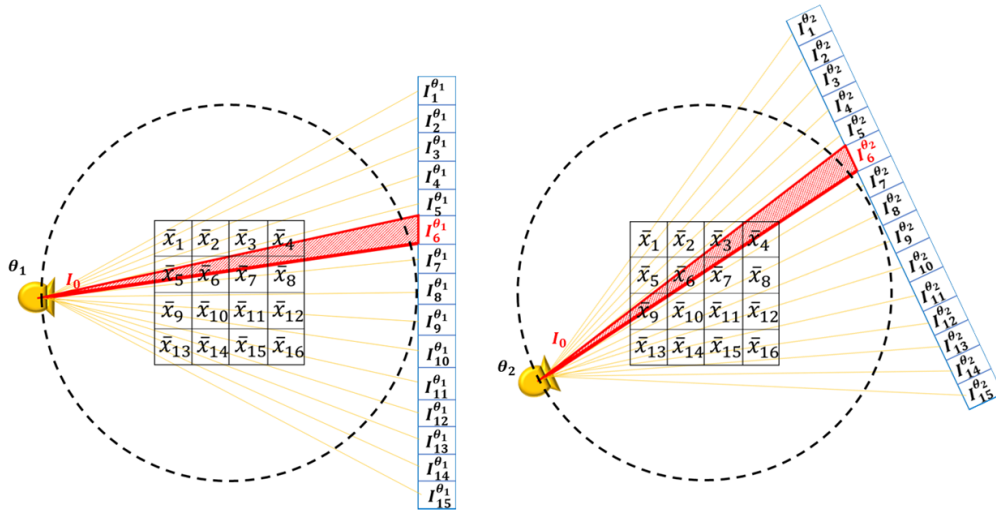
where $\mathbf{A}^{\theta_l} \in \mathbb{R}^{d \times n}$ is the projection matrix for acquisition angle θ_l and I_0 is the X-ray emission intensity.

The product between the projection matrix \mathbf{A} and the object $\bar{\mathbf{x}}$, which theoretically represents the set of all X-ray line integrals, can be modeled in different ways in the discretization. The elements of the matrix $\mathbf{A}^{\theta_l} = (a_{i,j}^{\theta_l})$ can be interpreted as:

- $(a_{i,j}^{\theta_l}) = \begin{cases} 1 & \text{if } \bar{x}_j \text{ is crossed by the } i\text{-th X-ray at the proj. } \theta_l \\ 0 & \text{if } \bar{x}_j \text{ is NOT crossed by the } i\text{-th X-ray at the proj. } \theta_l \end{cases}$
- $(a_{i,j}^{\theta_l}) = \text{length of the segment of intersection between the pixel } \bar{x}_j \text{ and the } i\text{-th X-ray at the projection } \theta_l, \text{ Figure 2.3a.}$
- $(a_{i,j}^{\theta_l}) = \text{area of intersection between pixel } \bar{x}_j \text{ and the triangle with base on the } i\text{-th pixel at the projection } \theta_l, \text{ Figure 2.3b.}$



(a) Line intersections



(b) Strip intersections

Figure 2.3: Discretization of the process at two projection angles θ_1 and θ_2 . (a) is done considering the line integrals between the source and the center of the 6-th detector pixel. (b) considers the triangle with base on the 6-th detector pixel and the vertex on the source.

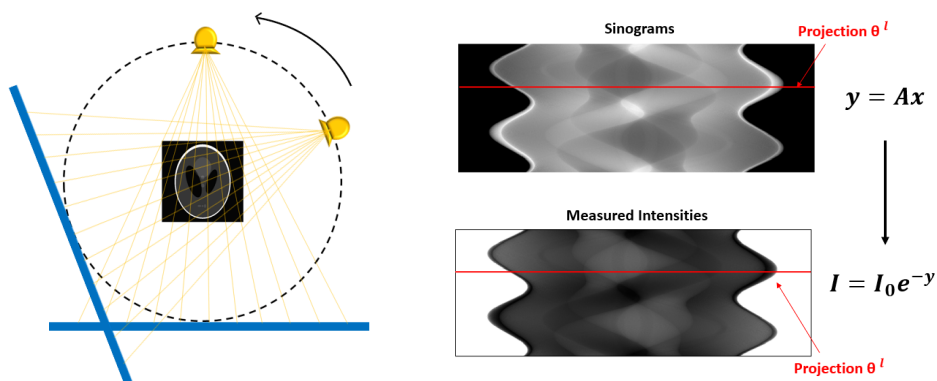


Figure 2.4: Computed Tomography.

(Left) The acquisition process: the source emits x-rays, which are attenuated passing through the object, and the detector measures the amount of rays that arrives. Then the source and the detector rotate together around the rotation axis, so all the projections can be taken.

(Top Right) The sinograms (or projections) $\bar{\mathbf{y}} := \mathbf{A}\bar{\mathbf{x}} = -\ln \frac{\mathbf{I}}{I_0}$: where \mathbf{A} is the Radon transform matrix, which describe the effect of the line integrals. Every row corresponds to an angle of projection.

(Bottom Right) The detected intensities \mathbf{I} (number of photons that arrive to the detector). Every row corresponds to an angle of projection.

The acquired intensities $\mathbf{I}^{\theta_1}, \dots, \mathbf{I}^{\theta_s}$ can be rearranged so as to form a matrix where every row refers to a projection angle, see Figure 2.4. One refers to the sinusoidal data obtained after the re-arranging the original \mathbf{I} as a *sinogram*, in formulas

$$\bar{\mathbf{y}} := \mathbf{A}\bar{\mathbf{x}} = -\ln \frac{\mathbf{I}}{I_0}.$$

We now give a closer look to the projection matrix \mathbf{A} by considering a mock object $\bar{\mathbf{x}} \in \mathbb{R}^{16}$ (4×4 image), and a detector with 15 pixels.

Figure 2.3a shows the supports of the line integrals (red lines) for the 6-th pixel of the detector, and for two angles θ_1 and θ_2 . In this way, the measured intensity at the 6-th pixel of the detector, at angle θ_1 can be written as:

$$I_6^{\theta_1} = I_0 \exp \left(- \left(a_{6,1}^{\theta_1} \bar{x}_1 + a_{6,2}^{\theta_1} \bar{x}_2 + \dots + a_{6,16}^{\theta_1} \bar{x}_{16} \right) \right) = I_0 \exp \left(- \langle \mathbf{A}_6^{\theta_1}, \bar{\mathbf{x}} \rangle \right)$$

with $A_6^{\theta_1}$ denoting the 6-th row of matrix \mathbf{A}^{θ_1} and $\langle \cdot, \cdot \rangle$ the scalar product.

We can note that, considering the line intersection (Figure 2.3a) at the angle θ_1 , the 6-th X-ray intersects only the pixels $\bar{x}_3, \bar{x}_4, \bar{x}_5, \bar{x}_6$ and \bar{x}_7 , so $a_{6,j}^{\theta_1} \neq 0$ for $j = 3, 4, 5, 6, 7$ and $a_{6,j}^{\theta_1} = 0$ for the others. While, at the angles θ_2 the 6-th X-ray intersects only the pixels $\bar{x}_3, \bar{x}_4, \bar{x}_5, \bar{x}_6, \bar{x}_7$ and \bar{x}_9 , so $a_{6,j}^{\theta_2} \neq 0$ for $j = 3, 4, 5, 6, 7, 9$ and $a_{6,j}^{\theta_2} = 0$ for the others.

Summarizing, the first projection can be expressed as

$$\mathbf{I}^{\theta_1} = \begin{bmatrix} I_1^{\theta_1} \\ I_2^{\theta_1} \\ I_3^{\theta_1} \\ I_4^{\theta_1} \\ \vdots \\ I_{15}^{\theta_1} \end{bmatrix} = I_0 \exp \left(- \begin{bmatrix} A_1^{\theta_1} \\ A_2^{\theta_1} \\ A_3^{\theta_1} \\ A_4^{\theta_1} \\ \dots \\ \vdots \\ \dots \\ A_{15}^{\theta_1} \end{bmatrix} \times \begin{bmatrix} \bar{x}_1 \\ \bar{x}_2 \\ \bar{x}_3 \\ \bar{x}_4 \\ \vdots \\ \bar{x}_{16} \end{bmatrix} \right).$$

Considering also the second projection angle, we have:

$$\begin{bmatrix} \mathbf{I}^{\theta_1} \\ \mathbf{I}^{\theta_2} \end{bmatrix} = \begin{bmatrix} I_1^{\theta_1} \\ \vdots \\ I_{15}^{\theta_1} \\ I_1^{\theta_2} \\ \vdots \\ I_{15}^{\theta_2} \end{bmatrix} = I_0 \exp \left(- \begin{bmatrix} A_1^{\theta_1} \\ \vdots \\ A_{15}^{\theta_1} \\ A_1^{\theta_2} \\ \vdots \\ A_{15}^{\theta_2} \end{bmatrix} \times \begin{bmatrix} \bar{x}_1 \\ \bar{x}_2 \\ \bar{x}_3 \\ \bar{x}_4 \\ \vdots \\ \bar{x}_{16} \end{bmatrix} \right)$$

Considering all the s projection angles:

$$\begin{bmatrix} \mathbf{I}^{\theta_1} \\ \mathbf{I}^{\theta_2} \\ \vdots \\ \mathbf{I}^{\theta_s} \end{bmatrix} = \begin{bmatrix} I_1^{\theta_1} \\ \vdots \\ I_{15}^{\theta_1} \\ I_1^{\theta_2} \\ \vdots \\ I_{15}^{\theta_2} \\ \vdots \\ I_1^{\theta_s} \\ \vdots \\ I_{15}^{\theta_s} \end{bmatrix} = I_0 \exp \left(- \begin{bmatrix} A_1^{\theta_1} \\ \vdots \\ A_{15}^{\theta_1} \\ A_1^{\theta_2} \\ \vdots \\ A_{15}^{\theta_2} \\ \vdots \\ A_1^{\theta_s} \\ \vdots \\ A_{15}^{\theta_s} \end{bmatrix} \times \begin{bmatrix} \bar{x}_1 \\ \bar{x}_2 \\ \bar{x}_3 \\ \bar{x}_4 \\ \vdots \\ \bar{x}_{16} \end{bmatrix} \right)$$

This small example suggests that the projection matrix is in general very sparse in the normal setup, because the X-rays (that arrives at a detector pixel) intersect only a few pixel of the object.

Based on the above discussion, after denoting by $\mathbf{A} \in \mathbb{R}^{m \times n}$ with $m = s d$ and by \mathbf{g} the function $\mathbf{g} : \mathbb{R}^{m \times m}$ where $\mathbf{g}(\cdot) = I_0 \exp(-\cdot)$, the general degradation model for the CT problem reads:

$$\mathbf{b} = \mathbf{Noise}(\bar{\boldsymbol{\lambda}}) \quad \text{where } \bar{\boldsymbol{\lambda}} := \mathbf{g}(\mathbf{A}\bar{\mathbf{x}}), \quad \mathbf{g}(\mathbf{t}) = I_0 e^{-\mathbf{t}}. \quad (2.6)$$

More details on the random operator \mathbf{Noise} will be given in Section 2.3.

Remark 2.2.1. Before going into the details of the noise degradation, it is worth mentioning the discrete version of a general denoising and deblurring problem that can be used to describe problems in the application fields of astronomy and microscopy, where the blurring effect often derives from the features of the tool used to capture the data, i.e telescope and microscope. It takes the following form:

$$\mathbf{b} = \mathbf{Noise}(\bar{\boldsymbol{\lambda}}), \quad \bar{\boldsymbol{\lambda}} = \mathbf{A}\bar{\mathbf{x}},$$

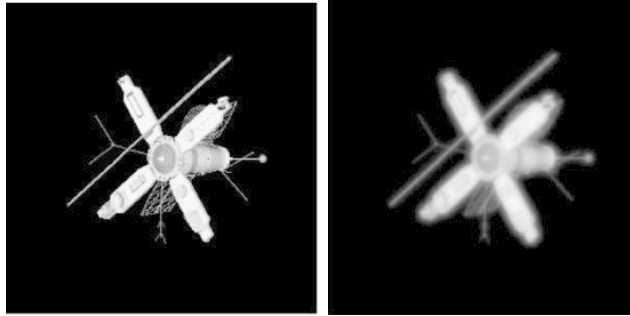


Figure 2.5: *Left*: Original image. *Right*: Image corrupted by blur.

where $\mathbf{A} \in \mathbb{R}^{m \times n}$ models the action of the blur on the unknown image and \mathbf{g} becomes the identity function. An example of the effect of the blurring operator can be seen in Figure 2.5.

2.3 Noise modelling in CT

In this section we describe the noise that characterizes the data in Computed Tomography, namely Poisson noise, Gaussian noise and the mixed Poisson-Gaussian noise, [5]. First we introduce the related probability distributions; then, we will discuss the applicative scenarios in which they arise and explain the reasons behind their presence/action. In this thesis we will indicate with capital letters B and \mathcal{B} the random variables and random fields, while their realization will be denoted by lowercase letters b and \mathbf{b} , respectively. Moreover the letter p will stand for the probability density functions (pdf) and P for the probability mass functions (pmf).

Definition 2.3.1 (Poisson random variable and independent random field). A univariate discrete random variable B is said to be Poisson distributed with parameter $\lambda \in \mathbb{R}_{++}$, where \mathbb{R}_{++} indicates the set of positive real numbers, denoted by $B \sim \mathcal{P}(\lambda)$, if its probability mass function reads

$$P_B(b | \lambda) = \frac{\lambda^b e^{-\lambda}}{b!}, \quad b \in \mathbb{N}.$$

The expected value and variance of random variable B are given by

$$\mathbb{E}[B] = \text{Var}[B] = \lambda.$$

A (vectorized) random field $\mathbf{B} = \{B_i\}$ is said to be independent Poisson distributed with parameter $\mathbf{\Lambda} = \{\lambda_i\} \in \mathbb{R}_{++}^m$, denoted by $\mathbf{B} \sim \mathcal{P}(\mathbf{\Lambda})$, if it satisfies:

$$B_i \sim \mathcal{P}(\lambda_i) \quad \forall i = 1, \dots, m, \quad p_{\mathbf{B}}(\mathbf{b} | \mathbf{\Lambda}) = \prod_{i=1}^m P_{B_i}(b_i | \lambda_i). \quad (2.7)$$

Definition 2.3.2 (Gaussian random variable and independent random field).

A univariate continuous random variable (r.v.) B is said to be Gaussian distributed with mean $\eta \in \mathbb{R}$ and standard deviation $\sigma \in \mathbb{R}_{++}$ denoted by $B \sim \mathcal{G}(\eta, \sigma^2)$, if its probability density function reads

$$p_B(b | \eta, \sigma) = \frac{1}{\sqrt{2\pi}\sigma} \exp\left(-\frac{(b - \eta)^2}{2\sigma^2}\right), \quad b \in \mathbb{R}.$$

The expected value and variance of random variable B are given by

$$\mathbb{E}[B] = \eta, \quad \text{Var}[B] = \sigma^2.$$

A vectorized random field (r.f.) $\mathbf{B} = \{B_i\}$ is said to be independent Gaussian distributed with mean $\boldsymbol{\eta} = \{\eta_i\} \in \mathbb{R}^m$ and diagonal covariance matrix $\boldsymbol{\Sigma} = \text{diag}(\sigma_i) \in \mathbb{R}^{m \times m}$, denoted by $\mathbf{B} \sim \mathcal{G}(\boldsymbol{\eta}, \boldsymbol{\Sigma})$, if it satisfies:

$$B_i \sim \mathcal{G}(\eta_i, \sigma_i^2) \quad \forall i = 1, \dots, m, \quad p_{\mathbf{B}}(\mathbf{b} | \boldsymbol{\eta}, \boldsymbol{\Sigma}) = \prod_{i=1}^m p_{B_i}(b_i | \eta_i, \sigma_i). \quad (2.8)$$

In particular, a Gaussian random field $\mathbf{B} = \{B_i\}$ is said to be independent identically distributed (i.i.d.) if the mean vector and the covariance matrix have the following form:

$$\boldsymbol{\eta} = \eta \mathbf{1}_m, \quad \boldsymbol{\Sigma} = \sigma^2 \mathbf{I}_{m \times m}$$

with $\eta \in \mathbb{R}$, $\sigma \in \mathbb{R}_+$, $\mathbf{1}_m$ denoting the unit vector of dimension m and $\mathbf{I}_{m \times m}$ the identity matrix of dimension $m \times m$. In this case, $\mathbf{B} \sim \mathcal{G}(\eta \mathbf{1}_m, \sigma^2 \mathbf{I}_{m \times m})$ and its probability density function reads

$$p_{\mathbf{B}}(\mathbf{b} | \eta \mathbf{1}_m, \sigma^2 \mathbf{I}_{m \times m}) = \prod_{i=1}^m \frac{1}{\sqrt{2\pi}\sigma} \exp\left(-\frac{(b_i - \eta)^2}{2\sigma^2}\right).$$

Definition 2.3.3 (Mixed Poisson-Gaussian random variable and independent random field). A univariate continuous random variable B is said to be Mixed Poisson-Gaussian distributed if it is the sum of two independent random variables C and D , with C a Poisson distributed r.v. with parameter $\lambda \in \mathbb{R}_{++}$ ($C \sim \mathcal{P}(\lambda)$) and D a Gaussian distributed r.v. with mean $\eta \in \mathbb{R}$ and standard deviation $\sigma \in \mathbb{R}_+$ ($D \sim \mathcal{G}(\eta, \sigma^2)$). B is denoted as

$$B \sim \mathcal{MPG}(\lambda, \eta, \sigma^2)$$

and its probability density function reads [51]

$$\begin{aligned} p_B(b \mid \lambda, \eta, \sigma) &= \sum_{b_n \in \mathbb{N}} P_C(b_n \mid \lambda) \cdot p_D((b - b_n) \mid \eta, \sigma) \\ &= \sum_{b_n \in \mathbb{N}} \left(\frac{\lambda^{b_n} e^{-\lambda}}{b_n!} \right) \cdot \left(\frac{1}{\sqrt{2\pi}\sigma} \exp \left(-\frac{((b - b_n) - \eta)^2}{2\sigma^2} \right) \right), \end{aligned}$$

with $b \in \mathbb{R}$. The expected value and variance of random variable B are given by

$$\mathbb{E}[B] = \lambda + \eta, \quad \text{Var}[B] = \lambda + \sigma^2.$$

A vectorized random field $\mathbf{B} = \{B_i\}$ is said to be independent Mixed Poisson-Gaussian distributed, denoted by $\mathbf{B} \sim \mathcal{MPG}(\mathbf{\Lambda}, \boldsymbol{\eta}, \boldsymbol{\Sigma})$, if it is the sum of an independent Poisson distributed r.f. $\mathbf{C} = \{C_i\}$ with parameter $\mathbf{\Lambda} = \{\lambda_i\} \in \mathbb{R}_{++}^m$ ($\mathbf{C} \sim \mathcal{P}(\bar{\mathbf{\Lambda}})$) and an independent Gaussian distributed r.f. \mathbf{D} with mean $\boldsymbol{\eta} = \{\eta_i\} \in \mathbb{R}^m$ and diagonal covariance matrix $\boldsymbol{\Sigma} = \text{diag}(\sigma_i) \in \mathbb{R}^{m \times m}$ ($\mathbf{D} \sim \mathcal{G}(\boldsymbol{\eta}, \boldsymbol{\Sigma})$) and satisfies

$$B_i \sim \mathcal{MPG}(\lambda_i, \eta_i, \sigma_i^2) \forall i = 1, \dots, m, \quad p_{\mathbf{B}}(\mathbf{b} \mid \mathbf{\Lambda}, \boldsymbol{\eta}, \boldsymbol{\Sigma}) = \prod_{i=1}^m p_{B_i}(b_i \mid \lambda_i, \eta_i, \sigma_i).$$

In particular, when \mathbf{D} is a i.i.d. Gaussian random field with $\boldsymbol{\eta} = \eta \mathbf{1}_m$ and $\boldsymbol{\Sigma} = \sigma^2 \mathbf{I}_{m \times m}$, the probability density functions of \mathbf{B} reads

$$\begin{aligned} p_{\mathbf{B}}(\mathbf{b} \mid \mathbf{\Lambda}, \eta \mathbf{1}_m, \sigma^2 \mathbf{I}_{m \times m}) &= \prod_{i=1}^m p_{B_i}(b_i \mid \lambda_i, \eta, \sigma) \\ &= \prod_{i=1}^m \left(\sum_{b_n \in \mathbb{N}} \left(\frac{\lambda^{b_n} e^{-\lambda}}{b_n!} \right) \cdot \left(\frac{1}{\sqrt{2\pi}\sigma} \exp \left(-\frac{((b_i - b_n) - \eta)^2}{2\sigma^2} \right) \right) \right). \end{aligned}$$

Poisson noise is related to the inherent statistical nature of electromagnetic waves and arises when data is acquired by photon counting, i.e. by counting the number of photons emitted by a source arriving on the detector, [2, 1, 10]. This quantity portrays the average value of the number of detected photons; in fact the effective measured number depends on the oscillations during the emission process and varies on the time interval when the phenomenon is observed. It is present in many medical applications, such as CT and Microscopy Imaging, but also in other application such as astronomical imaging. The Poisson noise is a signal-dependent noise, where the standard deviation depends on the underlying noiseless signal $\bar{\lambda}_i$. Therefore the level of noise will be different at each pixel of the data. When the number of photons hitting the data domain ($\bar{\lambda}_i$) increases, the noise quantified by the standard deviation $\sqrt{\bar{\lambda}_i}$ increases with the square root of the intensity, meaning that the signal increases more than the noise. Since in our applications we measure the number of photons, which arrive at different times, the relative noise in the data can be reduced by increasing the acquisition time or the dose of X-rays. Unfortunately this is not applicable in all the cases, due to external or internal causes (specific situation or equipment limits) or by the fact that exposing the patient to and higher dose of X-rays might be more dangerous without returning any significant benefits.

It is worth mentioning that given $X \sim \mathcal{P}(\bar{\lambda}_1)$ and $Y \sim \mathcal{P}(\bar{\lambda}_2)$ two univariate Poisson random variables, then the sum $X + Y$ is a Poisson random variable with mean and variance $\bar{\lambda}_1 + \bar{\lambda}_2$, in formula:

$$X + Y \sim \mathcal{P}(\bar{\lambda}_1 + \bar{\lambda}_2).$$

Gaussian noise affects digital images of various fields and arises both during the acquisition (due to the poor illumination or high temperature) and the transmission phases (inside the electronic circuit). For the CT case, electronic noise originates from the X-ray detection system, it is unrelated to the number of photons detected and does not carry any diagnostic information. In fact, the electronic noise can be observed in a CT projection even if a black image (i.e. without the X-ray source) is acquired. The main source of

electronic noise is the analog electronic of circuits in the detection system. Once the analog signal is converted to a digital signal, it becomes relatively immune to sources of electronic noise [2, 13].

According to the previously introduced formal definitions 2.3.1, 2.3.2 and 2.3.3, we can now formalize the probabilistic version of the data acquisition process considered in this work. The random field $\mathcal{B} = \{B_i\}$, of which the measured data are a realization, is the following

$$\mathcal{B} \sim \mathcal{MPG}(\bar{\Lambda}, \eta \mathbf{1}_m, \sigma^2 \mathbf{I}_{m \times m})$$

where $\bar{\Lambda} = \{\bar{\lambda}_i\}$, $\bar{\lambda}_i = I_0 e^{-(\mathbf{A}\bar{x})_i}$ for $i = 1, \dots, m$. Since the mean η of background signals can be estimated using blank measurements prior to each scan, it is common to subtract it from the measured intensity \mathbf{b} and assume $\eta = 0$ in the model:

$$\mathcal{B} \sim \mathcal{MPG}(\bar{\Lambda}, \mathbf{0}_m, \sigma^2 \mathbf{I}_{m \times m}),$$

where $\mathbf{0}_m$ denotes the zero vector with dimension m .

2.3.1 Noise Approximations

Even with the assumption $\eta = 0$, the probability density function of \mathcal{B} is complicated and harder to consider when designing a solution algorithm. For this reason, the above random field is often approximated by a shifted Poisson or a Gaussian one.

Shifted Poisson

The Shifted Poisson approximation of the mixed Poisson-Gaussian r.f.

$$\begin{aligned} \mathcal{C} + \mathcal{D} = \mathcal{B} &\sim \mathcal{MPG}(\bar{\Lambda}, \mathbf{0}_m, \sigma^2 \mathbf{I}_{m \times m}) \\ \text{where } \mathcal{C} &\sim \mathcal{P}(\bar{\Lambda}), \mathcal{D} \sim \mathcal{G}(\mathbf{0}_m, \sigma^2 \mathbf{I}_{m \times m}) \end{aligned} \quad (2.9)$$

can be defined by replacing the Gaussian r.f. \mathcal{D} with a Poisson one:

$$\mathcal{D} \sim \mathcal{G}(\eta \mathbf{1}_m, \sigma^2 \mathbf{I}_{m \times m}) \approx \mathcal{E} \sim \mathcal{P}(\sigma^2 \mathbf{1}_m).$$

With this replacement, \mathcal{B} is approximated the sum of two independent Poisson r.f.f., which is also an independent Poisson r.f.

$$\mathcal{B} = \mathcal{C} + \mathcal{D} \approx \mathcal{C} + \mathcal{E} \sim \mathcal{P}(\bar{\Lambda} + \sigma^2 \mathbf{1}_m).$$

This approximation is particularly convenient when the Poisson noise contribution takes over, as it happens for low dose CT acquisitions.

Gaussian Approximation

In (2.9), if instead of approximating the Gaussian r.f. with a Poisson one, we replace the Poisson r.f. \mathcal{C} with a Gaussian r.f. $\mathcal{H} \sim \mathcal{G}(\bar{\Lambda}, \text{diag}(\bar{\Lambda}))$; then \mathcal{B} is the sum of two independent Gaussian r.f.f., which is also a Gaussian r.f.:

$$\mathcal{B} = \mathcal{C} + \mathcal{D} \approx \mathcal{H} + \mathcal{D} \sim \mathcal{G}(\bar{\Lambda}, \text{diag}(\bar{\Lambda} + \sigma^2 \mathbf{1}_m)).$$

Since this approximation depends on the Stirling approximation of the factorial

$$n! \approx \sqrt{2\pi n} \left(\frac{n}{e}\right)^n, \quad \text{for } n \rightarrow \infty,$$

it can be applied when the number of photons $\bar{\lambda}_i$ is sufficiently large, namely when using an high dose of X-rays.

Gaussian Approximation of the noise in the sinogram If instead of the intensity \mathbf{b} , for the CT forward model, we consider the absorption $\mathbf{y} = -\log(\frac{\mathbf{b}}{I_0})$ (sinogram), it turns out that it also can be approximated by a Gaussian distribution when working with an high number of photons. As said before, for higher doses the intensity random variable B_i can be approximated as

$$B_i \approx \mathcal{G}(\bar{\lambda}_i, \bar{\lambda}_i + \sigma^2) = \bar{\lambda}_i + \sqrt{\bar{\lambda}_i + \sigma^2} \mathcal{G}(0, 1)$$

where $\bar{\lambda}_i = I_0 e^{-(\mathbf{A}\bar{\mathbf{x}})_i}$. By taking the negative logarithm we obtain:

$$\begin{aligned}
Y_i &= -\log\left(\frac{B_i}{I_0}\right) \approx -\log\left(e^{-(\mathbf{A}\bar{\mathbf{x}})_i} + \frac{\sqrt{I_0 e^{-(\mathbf{A}\bar{\mathbf{x}})_i} + \sigma^2}}{I_0} \mathcal{G}(0, 1)\right) \\
&\approx -\log\left(e^{-(\mathbf{A}\bar{\mathbf{x}})_i} \left(1 + \frac{1}{\sqrt{I_0 e^{-(\mathbf{A}\bar{\mathbf{x}})_i}}} \mathcal{G}(0, 1)\right)\right) = \\
&= (\mathbf{A}\bar{\mathbf{x}})_i - \log\left(1 + \frac{1}{\sqrt{I_0 e^{-(\mathbf{A}\bar{\mathbf{x}})_i}}} \mathcal{G}(0, 1)\right) = \\
&\approx (\mathbf{A}\bar{\mathbf{x}})_i - \frac{1}{\sqrt{I_0 e^{-(\mathbf{A}\bar{\mathbf{x}})_i}}} \mathcal{G}(0, 1).
\end{aligned} \tag{2.10}$$

where from the first to the second row we approximate $\sqrt{I_0 e^{-(\mathbf{A}\bar{\mathbf{x}})_i} + \sigma^2}$ with $\sqrt{I_0 e^{-(\mathbf{A}\bar{\mathbf{x}})_i}}$ (since the Gaussian approximation of B_i holds for high values of I_0 , σ^2 is not comparable with $I_0 e^{-(\mathbf{A}\bar{\mathbf{x}})_i}$) and the last row is obtained by the first-order Taylor approximation $\log(1 + z) \approx z$ (that can be used for small values of z , i.e. large values of $I_0 e^{-(\mathbf{A}\bar{\mathbf{x}})_i}$). From (2.10) we derive that the absorption coefficient y_i can be approximated by a Gaussian distribution with mean $(\mathbf{A}\bar{\mathbf{x}})_i$ and standard deviation $\frac{1}{\sqrt{I_0 e^{-(\mathbf{A}\bar{\mathbf{x}})_i}}}$.

Chapter 3

Behind the mathematical model: the Physics of X-ray Tomography

Wilhelm Conrad Röntgen was awarded with the first Nobel Prize for physics in 1901 for the discovery of a new radiation capable of high levels of penetration, which he names X-rays. Nevertheless, the first commercial CT scanners appeared in the early 1970s invented independently by Allan Cormack and Godfrey Hounsfield [3, 4], both of them being recipient of the Nobel Prize in Medicine in 1979. In this chapter, we will provide some details on these two Nobel-Prize-worthy discoveries. First, we will focus on the physics behind the generation of X-rays, the CT components, photon-matter interaction and X-ray detection, [1, 2]. Then, we will briefly discuss the statistical properties of CT, which somehow determine the noise model considered in the inverse problem formulation, and the different CT setups used from its invention, [2].

3.1 The nature and generation of X-rays

X-ray radiation is of electromagnetic nature; it is part of the electromagnetic spectrum, which also includes radio waves, radar and microwaves, infrared, visible and ultraviolet light and γ -rays. As every wave, an X-ray is characterized by its frequency ν , i.e. the number of vibrations for each second, ranging from $3 \cdot 10^{16}$ and $3 \cdot 10^{19}$ and it is measured in Hertz (Hz). The wavelength of a wave is the distance between successive crests and it can be computed as $f = \frac{c}{\nu}$, where $c = 2.998 \cdot 10^8$ m/s is the velocity of light in vacuum. Hence, the wavelengths of X-rays belongs to the range [10nm, 10^{-3} nm]. From a quantum-mechanic viewpoint, electromagnetic radiation can be regarded as emissions of quanta (photons), which are the smallest discrete amount of electromagnetic radiation. In this perspective, the X-ray radiation is a flow of moving photons, which, in vacuum, have the same velocity v . The energy E of each photon depends on the frequency, according to the following relation:

$$E = h \nu,$$

with $h = 6.626070 \cdot 10^{-34}$ m²· kg/s being the Plank's constant, and it is expressed in *electron Volt* (eV): 1 eV is the energy that an electron will gain if it is accelerated by an electrical potential of one Volt. So X-rays with frequencies between $3 \cdot 10^{16}$ and $3 \cdot 10^{19}$ Hz correspond to energies between 124 eV and $1.24 \cdot 10^6$ eV.

Generation of X-rays

The X-ray radiation is generated by the deceleration of fast electrons entering a solid metal anode. An X-ray source is in fact composed by a cathode and a metal anode placed inside a vacuum tube. The cathode is characterized by a filament circuit in which the current runs through when the X-ray source is turned on, Figure 3.1. Therefore, the filament is heated by the current and, by thermal excitation, emits electrons. Due to the electric field between cathode and anode, these electrons are accelerated and hit the

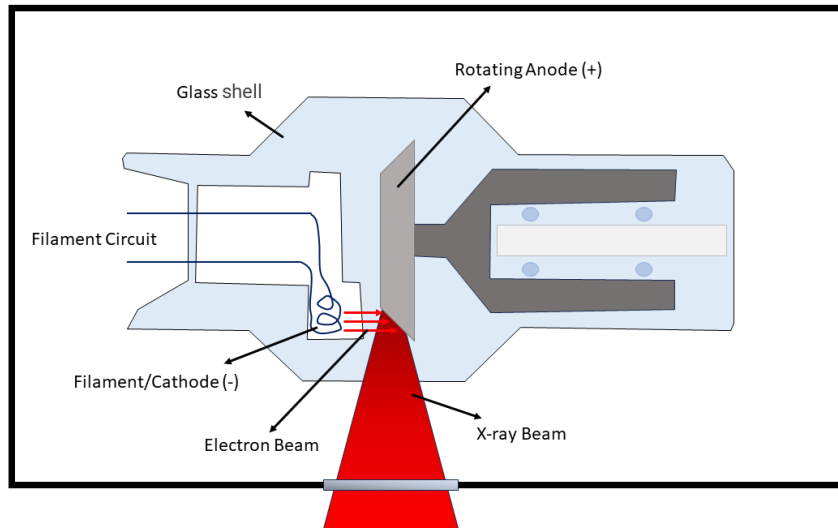


Figure 3.1: Typical X-ray Source.

anode with high speed transferring their kinetic energy to the anode. Once the electrons collide with the anode, the X-ray radiation is emitted by two types of interaction: Bremsstrahlung and characteristic radiation.

Bremsstrahlung

Bremsstrahlung is a German word that describes the fact that a high-speed electron is decelerated when passing near the nucleus of an anode atom. This happens because the positively charged nucleus deflects and slows down the electrons, causing a loss of kinetic energy that corresponds to the emission of X-ray radiation (with energy the one that is lost by the electron). The energy of the emitted photons (and thus the amount of deceleration) depends on the distance between the incoming electron and the nucleus of the atom: the larger the distance, the smaller the deflection and the deceleration of the electron; on the other hand, if it clashes with the nucleus, it decelerates completely. In the first case a low energy photon is emitted (due to the small loss of kinetic energy), while in the latter, a high-energy photon is released, Figure 3.2. As a result, the maximum energy of the photons corresponds to

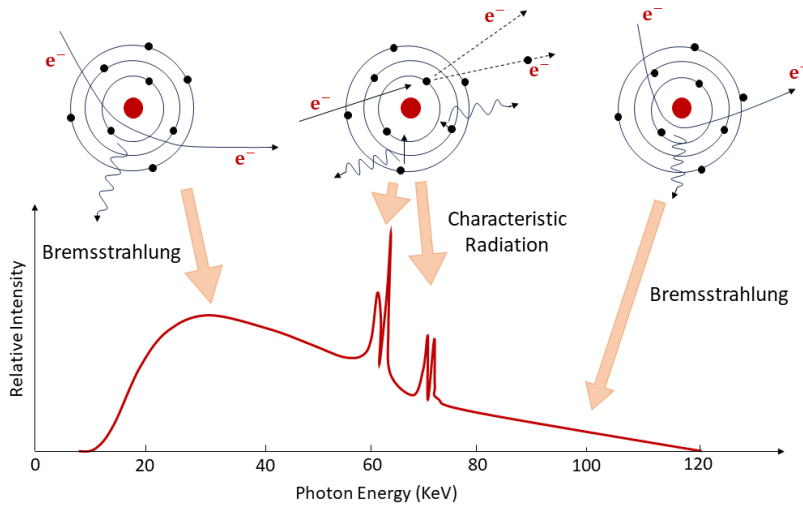


Figure 3.2: X-ray spectrum of a 120 KeV X-ray tube. The continuous part of the spectrum corresponds to the Bremsstrahlung, while the peaks to the characteristic radiation.

the maximum kinetic energy of the electrons that hit the anode.

Characteristic radiation

In addition to the generation of X-rays due to the loss of kinetic energy, X-ray photons can be emitted by characteristic radiation. This happens when a high-speed electron collides with an inner-shell electron of the atom. In this case, the electron of the atom is ejected and the empty spot in its energy level is filled by an outer-shell electron that falls down to the lowest energy position. The energy difference between the two shells leads to the release of a photon (with energy corresponding to the difference in energy levels of the shells), Figure 3.2. These photons have only specific discrete energy values that depend on the anode atom, and are thus called characteristic radiation.

3.2 Photon-matter interaction

When X-ray photons pass through a material they interact both with electrons and nuclei of the material's atoms, and can be either absorbed or scattered. The most important interactions are the following: Photoelectric effect, Compton scattering and Rayleigh scattering [12]. Here, we will not detail the three interactions; however, generally speaking, the absorption-based interactions cause the disappearance of the photon, while the scattering-based interactions yield that the photon is deviated from its original path. In all the cases, the detector element that would record the photon in absence of interaction will not detect the photon. All this yields to a reduction in the number of detected photons, which is called *attenuation* and refers to the decrease of the beam intensity. This phenomenon is described by the Lambert-Beer Law of attenuation, which we introduced in 2.2 and that will be derived in the following paragraph.

3.2.1 Lambert-Beer Law of attenuation

Consider an X-ray propagating along a line parametrized in terms of the position ℓ and passing through an object with thickness $\Delta\ell$; physics principles state that the change of radiation intensity after the beam has crossed the object is proportional to the thickness of the object; in formula

$$I(\ell + \Delta\ell) = I(\ell) - \bar{x}(\ell)I(\ell)\Delta\ell,$$

with $\bar{x}(\ell)$ being the proportionality constant referred to as *linear attenuation coefficient*. Manipulating the above equation, we get that the limit of the quotient is

$$\lim_{\Delta\ell \rightarrow 0} \frac{I(\ell + \Delta\ell) - I(\ell)}{\Delta\ell} = \frac{dI}{d\ell} = -\bar{x}(\ell)I(\ell). \quad (3.1)$$

If the material is assumed to be homogeneous, i.e. the attenuation coefficient is constant $\bar{x}(\ell) = \bar{x}$, along the entire length of penetration, the equality in (3.1) becomes an ordinary linear and homogeneous, first-order differential equation with constant coefficients, Figure 3.3.

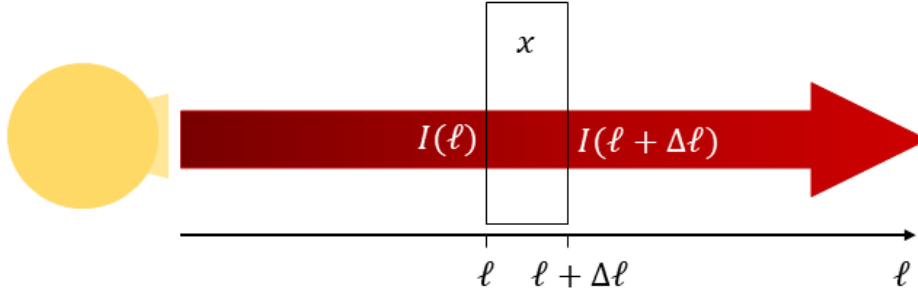


Figure 3.3: Mathematical model of monochromatic X-ray attenuation. The photons are running through an object of thickness $\Delta\ell$ with a constant attenuation coefficient, \bar{x} . Equal parts of the same absorbing medium attenuate equal fractions of the radiation.

The solution is obtained by separation of variables:

$$\frac{dI}{I(\ell)} = -\bar{x} \cdot d\ell. \quad (3.2)$$

By integrating both sides of (3.2)

$$\int \frac{dI}{I(\ell)} = -\bar{x} \int d\ell$$

$$\ln(I) = -\bar{x} \ell + C$$

Since the intensity is a positive quantity, after imposing an initial condition $I(0) = I_0$, the special solution of the differential equation (3.1) can be written as

$$I(\ell) = I_0 e^{-\bar{x} \ell}, \quad (3.3)$$

which is also known as Lambert-Beer's law of attenuation.

3.2.2 The evolution of the Lambert-Beer Law

In the case of spatially varying attenuation, $\bar{x}(\ell)$, the exponent in (3.3) is replaced by the integral of the unknown coefficients along a linear path of

length s :

$$I(s) = I_0 e^{-\int_0^s \bar{x}(\ell) d\ell}. \quad (3.4)$$

This applies when considering a monochromatic X-ray source, i.e. a single photon energy, and, as a result, the model can be rearranged as follows:

$$y(s) := -\log\left(\frac{I(s)}{I_0}\right) = \int_0^s \bar{x}(\ell) d\ell, \quad (3.5)$$

with y indicating the absorption. In the case of multiple photon energies (polychromatic source), the monochromatic model (3.4) can be modified so as to account for the dependence of the attenuation on the energy:

$$I(s) = \int_{E_{min}}^{E_{max}} I_0(E) e^{-\int_0^s \bar{x}(\ell, E) d\ell} dE. \quad (3.6)$$

In practice, conventional CT detectors measure only one intensity value, obtained by summing all the photons coming with different energy levels, as in (3.6). For the polychromatic model the rearrangement into a line-integral linear equation, as in 3.5, is no longer feasible, as it would produce a modelling approximation.

In recent years, photon counting detectors have been released on the market: they allow to distinguish the photons coming from different energies and to monitor how data changes across the energy channels. However this technology is fairly new; most of the current detectors can differentiate only between few energy channels and the collected intensities in each channel are obtained by integrating the photons over the energy channel interval. In this thesis, we will first consider a monochromatic X-ray source and then discuss the polychromatic scenario (spectral CT).

3.3 X-ray detection

X-ray quanta are measured by a detector, and the process can be divided into two steps. The first is characterized by a scintillator that absorbs the X-ray photons and converts them to visible light. Then, the visible light is

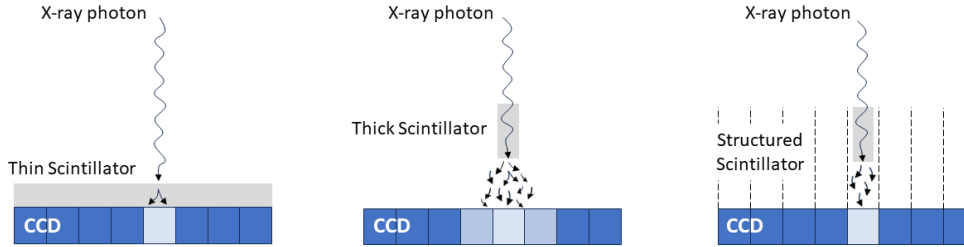


Figure 3.4: Different kind of scintillators.

coupled to a charge-coupled device (CCD) that records the lights and finally the digital signal is collected.

The scintillation layer can be made in different ways, each of them yielding to different image quality. This is because light will scatter through the scintillator when passing, with consequent diffusion on adjacent pixels of the following layer. In this perspective, a thick scintillator will give a lower resolution compared to a thin one. On the other hand, it will absorb more of the incident radiation so it will lead to an higher Signal-to-Noise Ratio (SNR). The two problems are solved using a structured scintillator: the X-ray photons are guided in the right direction, allowing a thick scintillator (high SNR) without diffusion (high resolution), Figure 3.4.

The CCD layer contains an grid of pixel sensors sensitive to light; when a photon hits one of them, it is converted to into photoelectron (electric charge). Finally the amount of the charge in each detector pixel is measured and converted into binary form.

3.4 Statistical properties of CT

To better understand the degradation process it is important to explain the statistical properties of the X-rays and the detector, [2].

3.4.1 Statistical properties of the X-ray source

To derive the statistical photon model, we need to introduce the X-ray quanta generation statistics inside the focus area on the X-ray tube anode. As mentioned at the beginning of the chapter, the lattice atoms of the anode material are bombarded with fast electrons that are accelerated during their transit from the cathode to the anode. Let L electrons arrive at the active focus volume in the time window $[0; T]$ and, let each of the L electrons have a probability, r (with $0 \leq r \leq 1$), of interacting in the same time interval with one of the target atoms in such a way that an X-ray quantum emerges. It is also assumed that each collision process between fast electrons and target atoms in the lattice is not characterized by a statistical dependence on all other collisions inside the focus volume. Then, the probability, P , that the random variable, N , i.e., the number of emerging X-ray quanta, is assigned exactly to the number n is

$$P(N = n) = \binom{L}{n} r^n (1 - r)^{L-n}.$$

In other words, the number of X-ray quanta, $N \sim \text{Bin}(r)$, is a binomially distributed random variable with n out of $\{0, \dots, L\}$. For a large number of fast electrons, the probability that the random variable N is exactly assigned to n , can be calculated via the Poisson distribution mass function defined in

$$P(N = n) = \lim_{L \rightarrow \infty} \binom{L}{n} r^n (1 - r)^{L-n} = \frac{(\lambda)^n}{n!} e^{-\lambda}.$$

The parameter λ of the Poisson distribution, i.e. the expected value $E[N] = L \cdot r$ of the number of X-ray quanta, is a measure of the radiation intensity. Thus, X-ray generation is a Poisson process.

3.4.2 Statistical properties of the detector

Reviewing the X-ray detector types explained before in terms of their statistics, it becomes clear that the X-ray photon detections via the photoelectric effect can also be seen as statistically independent processes. In

statistics, such detectors are called Bernoulli detectors. Let s , with $0 \leq s \leq 1$, be the probability that entering X-ray quanta ionizes a xenon atom of the detector. It has been derived in the previous section that X-ray quanta leaving the X-ray tube are Poisson-distributed. Therefore, the detection process must be modeled for a Bernoulli detector, which receives Poisson distributed quanta. The probability that m quanta are detected, if n quanta enter the detector, is given by the conditional probability

$$P_{\text{Det}}(m|n) = \begin{cases} \binom{n}{m} s^m (1-s)^{n-m} & \text{for } m = 0, 1, \dots, n \\ 0 & \text{for } m \geq n \end{cases} \quad (3.7)$$

Since the source is modeled by the Poisson distribution,

$$P_{\text{Source}}(N = n) = \frac{(\lambda)^n}{n!} e^{-\lambda},$$

this term must be multiplied with (3.7). In this way, the probability of a Bernoulli detection of m quanta of a Poisson source can be expressed as,

$$P_{\text{SD}}(m) = \sum_{n=m}^{\infty} P_{\text{Source}}(n) \cdot P_{\text{Det}}(m|n) = e^{-\lambda} \frac{(s\lambda)^m}{m!} \sum_{n=0}^{\infty} \frac{((1-s)\lambda)^n}{n!}. \quad (3.8)$$

The sum in the right term of (3.8) is the Taylor expansion of the exponential function $e^{(1-s)\lambda}$. Ultimately, one obtains

$$P_{\text{SD}}(m) = \frac{(s\lambda)^m}{m!} e^{-s\lambda}. \quad (3.9)$$

Equation (3.9) reveals that the number of Bernoulli-detected X-ray quanta of a Poisson source is again a Poisson-distributed random variable. The final result is merely scaled by the detection probability, s , i.e., the efficiency of the detector. Equation (3.9) is extremely important because it explains why X-ray quanta show Poisson statistics after traveling through an absorbing object. Obviously, the attenuation processes inside the object are guided by binomial statistics, since the mechanisms for absorption are the same as those inside the detector. The statistical chain from generation of the quanta inside the X-ray tube, via the attenuation inside the object of interest, to the measurement by the X-ray detector, is called a cascaded Poisson process.

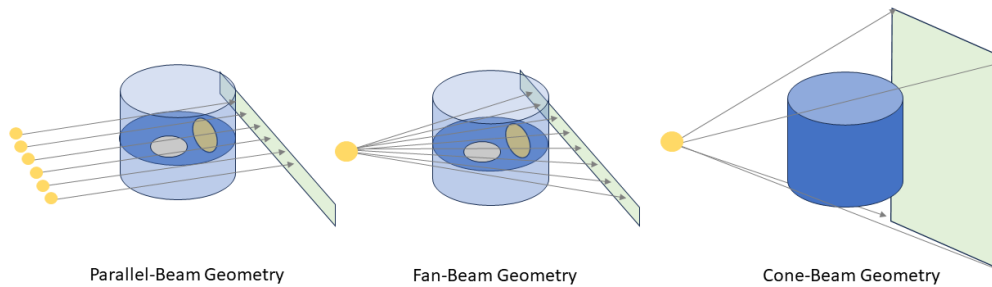


Figure 3.5: Scan geometries: Parallel Beam, Fan Beam and Cone Beam.

3.5 The evolution of Computed Tomography

Computed Tomography has evolved into different scan geometries over time. The first generation of CT involves an X-ray tube that emits a single needle-like X-ray beam, which is selected from the X-ray cone by means of an appropriate pinhole collimator. This geometry is referred to as *pencil beam*. A single detector is situated on the opposite side of the measuring field and the X-ray tube. The detector is moved synchronously along with the X-ray tube. This displacement is linear and is repeated for different projection angles; in this way a *parallel beam* set-up is obtained, Figure 3.5 left. This two configurations are time consuming, and not applicable in medical applications, so the *fan beam* computed tomography appeared soon after. Here the source emits a wide fan beam that are collected by a linear array of detectors, Figure 3.5 center. This allows to measure simultaneously the intensity values along the lines at the detector position, and to move directly to the following acquisition angle, significantly increasing the speed of the procedure. The Fan Beam CT can be generalized to the 3D case by using a divergent cone-shaped source directed through the middle of the volume of interest onto an area X-ray detector on the opposite side. This is called *Cone Beam Computed Tomography (CBCT)*, Figure 3.5 right. The X-ray source and detector rotate around a rotation fulcrum fixed within the center of the region of interest. During the rotation, multiple sequential planar projection images of the field of view are acquired. In industrial

applications, the CBCT is performed also by rotating the object between the fixed source and detector plane.

Chapter 4

On and beyond standard reconstruction methods

After detailing the CT acquisition process, both in continuous and discrete settings, and the physical principles underlying such acquisition, in this section we will focus on how to recover an image of the target object starting from the measured data. Strategies designed so as to address this task are referred to as CT image reconstruction methods. Those methods can be divided into two categories: *pre-log* and *post-log*. The *pre-log* methods directly reconstruct the CT image from the raw measurements $\mathbf{b} = \text{Noise}(\bar{\boldsymbol{\lambda}})$ with $\bar{\boldsymbol{\lambda}} = I_0 e^{-\mathbf{A}\bar{\mathbf{x}}}$. On the other hand, in the *post-log* approaches, a log transformation is first taken on the ratio between the raw measurements \mathbf{b} and the initial radiation intensity I_0 to generate post-log sinogram data that represents the line integrals of the Radon transform (see equations (2.3), (2.4)):

$$-\log\left(\frac{\mathbf{b}}{I_0}\right) := \mathbf{y} \approx \mathbf{A}\bar{\mathbf{x}}.$$

Due to the linearity of the reformulated problem $\mathbf{y} = \mathbf{A}\bar{\mathbf{x}}$, such strategies are easier and more efficient to solve and were the first to be developed. However, in most cases, the Poisson noise in the data \mathbf{b} , and that affect the noisy sinogram \mathbf{y} , is either not considered or approximated, as explained in 2.3.1, resulting in poor results for low-dose CT problems. *Pre-log* strategies

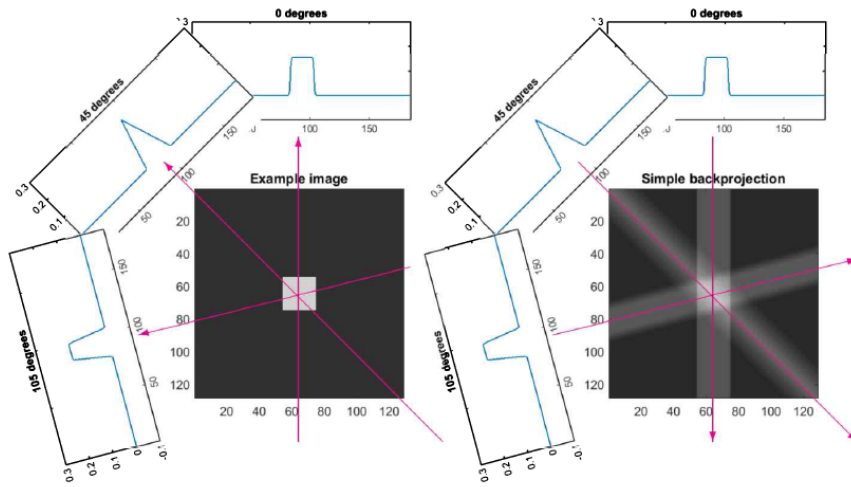


Figure 4.1: *Left*: three projections of a test image. *Right*: back-projection of the three projections, [1].

take into account the original degradation model in (2.6), which is non linear, but require advanced algorithmic techniques to solve the problem. In this chapter we will describe the existing techniques starting with the classical and standard strategies to end with the most recent ones.

4.1 The Standard Back-Projection (BP) Method

As recalled in Section 2.2, the sinogram y , i.e. the output measurement of a CT scanner after the log transformation, is obtained by applying the Radon transform to the target object \bar{x} . As a result, historically the first attempt for solving the CT reconstruction problem has focused on inverting the process, namely obtaining the image from its shadows/projections: *Back-Projection* (BP). In what follows, we are detailing the BP strategy for the simple case of parallel beam tomography: the back-projection is obtained by spreading each projection $y(\theta, \xi) = \mathcal{R}(\bar{x})(\theta, \xi)$ back onto the line of integration and then summing over all the projection angles, Fig. 4.1. The process is formalized

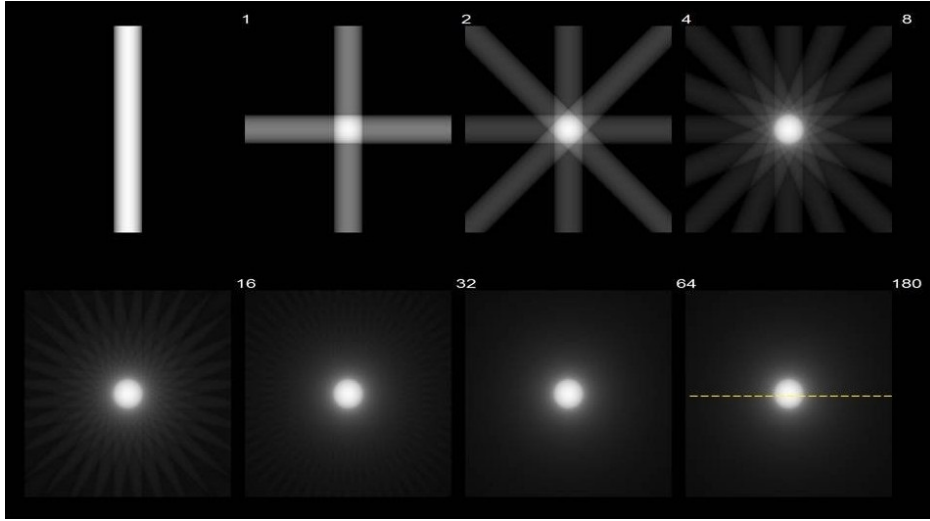


Figure 4.2: Back-projection using different number of projections angles (from 1 to 180), [1].

as follows:

$$\mathcal{R}^*[y](z_1, z_2) = \int_0^{2\pi} y(\theta, z_1 \cos \theta + z_2 \sin(\theta)) d\theta. \quad (4.1)$$

From formula (4.1) and Figure 4.1, one can note that the back-projection does not truly represent the inverse of the Radon Transform, as by smearing the projection $y(\theta, \xi)$ onto the line of integration its positive values are assigned to all the pixels of the image that belong to the projection line, even the zero valued. In this way it is not possible to retrieve all the zero valued pixels of the target image, since a lot of them are “in the shadow” of positive values. Moreover the process of spreading along the line and then summing leads to a blurring effect in the reconstruction, as shown in Fig. 4.2 where we consider BP reconstructions corresponding to different and increasing numbers of projections. Finally, it is important to note that, when using a small number of projections, the shape of the circle is not defined and the band coming from the smearing process are visible. On the other hand, a larger number of projections results into a more clear shape but with a blurring effect.

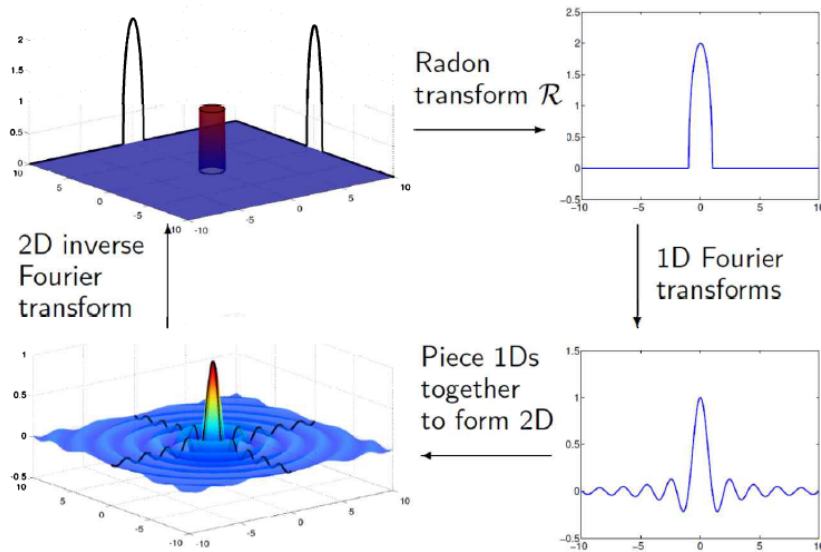


Figure 4.3: The Fourier reconstruction method, [1].

4.2 The Fourier-Based methods

The analytical formula for the inverse of the Radon transform can be obtained by the Fourier Slice Theorem. The Fourier Slice Theorem states that 1D Fourier transform of the data $y(\theta, \xi) = \mathcal{R}(\bar{x})(\theta, \xi)$ with respect to the variable ξ at a fixed projection angles θ is equal to $\sqrt{2\pi}$ times the 2D Fourier transform of the original image restricted to the corresponding line with direction vector $(\cos(\theta), \sin(\theta))$:

$$\widehat{\mathcal{R}(\bar{x})}(\theta, \xi) = \sqrt{2\pi} \widehat{\bar{x}}(\xi \cos(\theta), \xi \sin(\theta))$$

This result also yields a simple strategy for the CT reconstruction problem: given the projections $y(\theta, \xi) = \mathcal{R}(\bar{x})(\theta, \xi)$, one can apply the 1D Fourier transform for each angle of projections, the computed 1D transforms can be re-arranged as a 2D signal by aligning them radially at angle θ . Finally, the 2D inverse Fourier transform is performed on the re-arranged signal, Fig. 4.3. Despite the theoretical guarantees of the Fourier reconstruction method, it is not used for conventional CT scanning since the application of the 2D Fourier transform requires change of coordinates, from polar to

Cartesian, that is difficult to obtain. Moreover, small errors at this stage can significantly damage the output reconstructions.

The Filtered Back-projection (FBP) method

The Filtered Back-Projection (FBP) Method is the most used for reconstruction since, for simple CT problems, can achieve good results in a short amount of time. FBP is also derived by the Fourier Slice Theorem, but it circumvent the above problem of calculating the 2D Fourier Transform, [1, 2]. As the name suggests, the FBP is performed by back-projecting the data after the application of a filter: after applying the 1D Fourier transform to each projection, a ramp filter is applied and the filtered projections are obtained by means of the inverse 1D Fourier transform. Finally the result is achieved by back-projecting the filtered projections, Fig. 4.4.

The Feldkamp Davis and Kress (FDK) Method

The extension of this method to the 3D case of Cone Beam CT is known as Feldkamp Davis and Kress (FDK) method. It is articulated into three steps: weighting the projections, filtering and back-projecting them. All these procedures can be easily parallelized, thus making the FDK an ideal candidate to use in practice. A schematic representation of FDK is shown in Fig 4.5. However, these algorithms are used only for CT setups with many projections (over all directions) and high X-ray doses. In the other cases, as noisy data, limited angle or less projections, the results contain artifacts and are not reliable to use for the application field.

4.3 The algebraic methods

As an alternative to FBP or FDK, iterative algebraic reconstruction algorithms minimize the residual of the image, by iteratively comparing the reconstruction with the measured data iteratively. These algorithms have

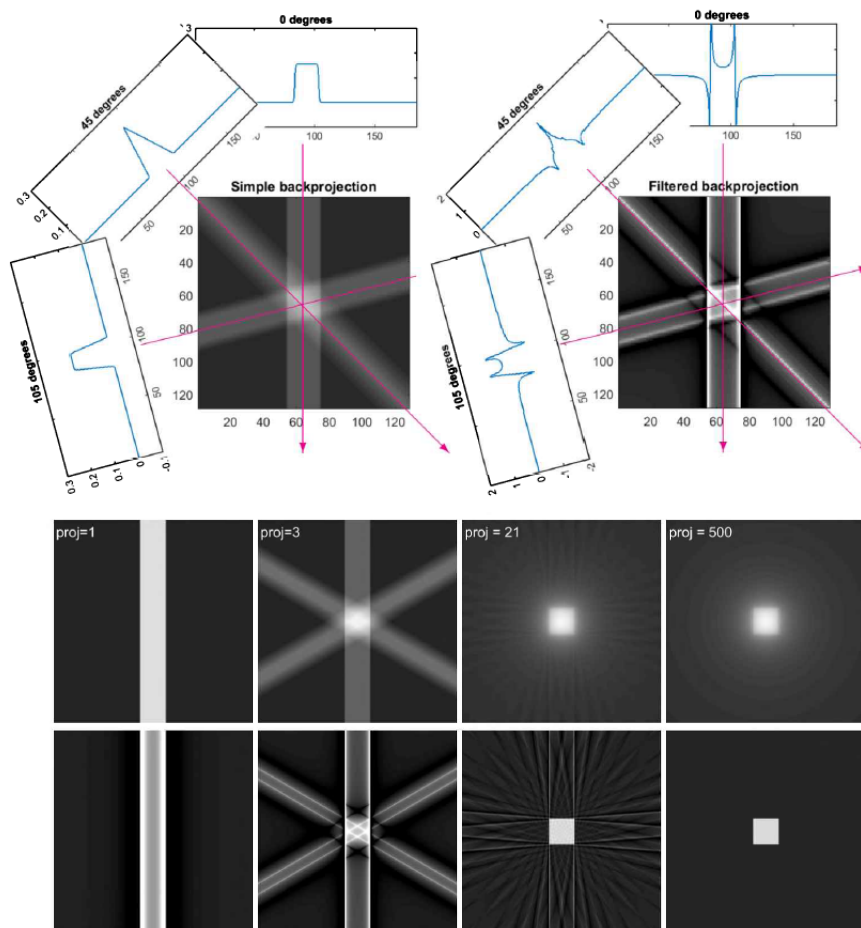


Figure 4.4: *Top Left:* Back-projection. *Top Right:* Filtered Back-projection. *Bottom part:* Reconstruction with increasing number of projection (1,3,21 and 500) with Back-projection (*Center*) and Filtered Back-projection (*Bottom*), [1].

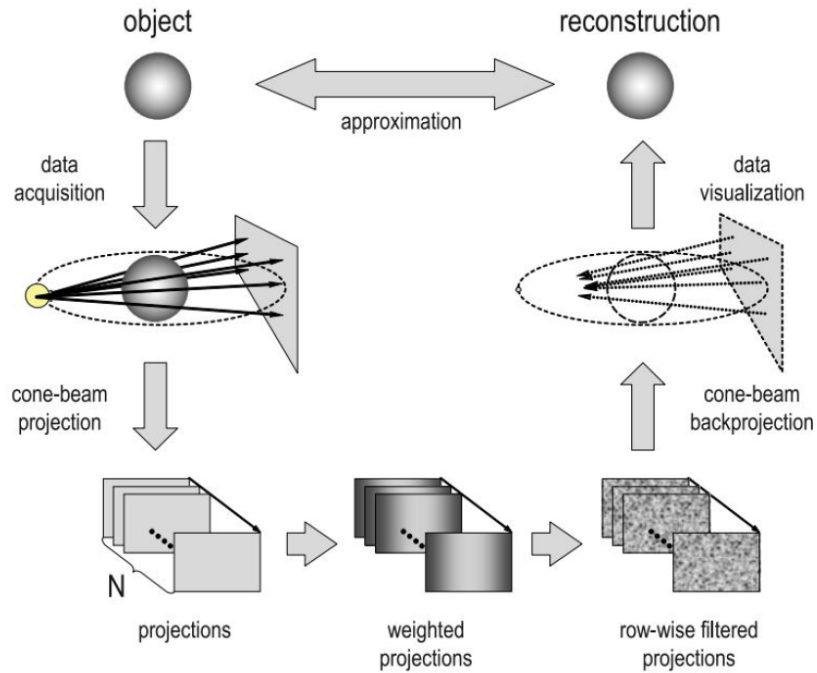


Figure 4.5: Schematic representation of the FDK method, [2].

been shown to improve the quality of the output reconstructions, specially when the data is noisy, acquired with a limited number of projections or with a limited view. While the previous reconstruction methods were defined in the continuous, for the algebraic methods we have to take into account the discrete nature of the practical realization of CT from the very beginning, i.e. by looking at the model in section 2.2.1.

The ART Method

Arguably the most well known iterative algorithm for the CT image reconstruction problem is the algebraic reconstruction technique (ART), also named as Kaczmarz method after its inventor Stefan Kaczmarz, [6]. The ART method is an iterative method that solves the linear system $\mathbf{y} = \mathbf{A}\mathbf{x}$ in a direct way by means of a sequence of orthogonal projections [6, 1, 2]. Given an initial image $x^{(0)}$, ART computes a sequence of iterative solutions

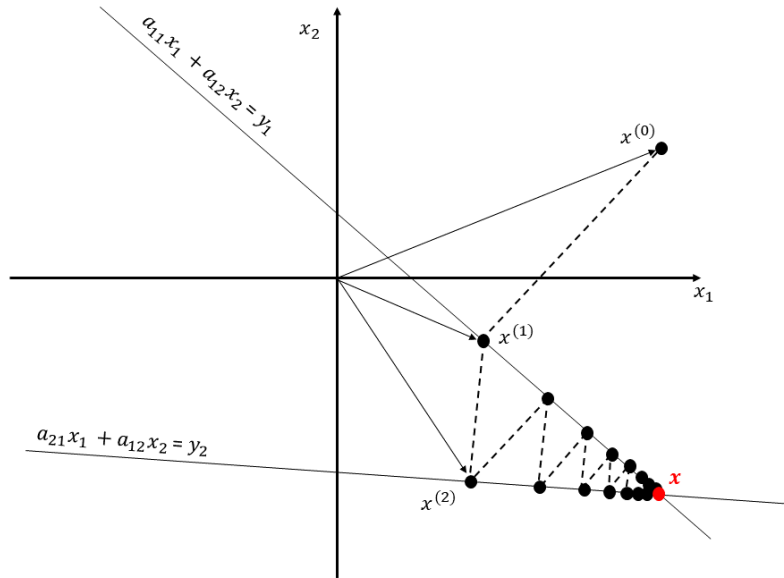


Figure 4.6: Schematic representation of the ART method.

$\{x^{(1)}, x^{(2)}, \dots\}$ that converges to the desired tomographic reconstruction. More in details, let us consider a 2×2 linear system of the form

$$\begin{cases} a_{11}x_1 + a_{12}x_2 = y_1 \\ a_{21}x_1 + a_{22}x_2 = y_2 \end{cases}.$$

In this case, the candidate solution is a point in a 2-dimensional space; the initial guess $x^{(0)}$ is projected onto the straight line defined by the first equation of the linear system, so as to get $x^{(1)}$, which is then projected onto the second line represented by the second equation, so as to give $x^{(2)}$. The described procedure is replicated many times by first projecting on the first and then on the second equation. The general update step reads:

$$x^{(k+1)} = x^{(k)} - \frac{a_i x^{(k)} - y_i}{a_i a_i^T} a_i^T,$$

where $a_i = (a_{i1}, a_{i2})$ the i -th row of the coefficient matrix. Fig 4.6 gives a visual representation of the method.

The SIRT Method

The Simultaneous Iterative Reconstruction Technique (SIRT) approach also aims to solve directly the linear system $\mathbf{y} = \mathbf{A}\mathbf{x}$. However, unlike ART, it updates the current candidate solution by simultaneously using all the system equations (instead of using one equation after the other). SIRT still does the projections like in ART, but the update of \mathbf{x} is the average of all \mathbf{x} vectors obtained when projecting onto each hyperplane:

$$\mathbf{x}^{(k+1)} = \mathbf{x}^{(k)} - \mathbf{D}_1 \mathbf{A}^T \mathbf{M}_1 (\mathbf{A}\mathbf{x}^{(k)} - \mathbf{y}),$$

where $\mathbf{D}_1 = \text{diag}\left(\frac{1}{\|c_j\|_1}\right) \in \mathbb{R}^{n \times n}$, $\mathbf{M}_1 = \text{diag}\left(\frac{1}{\|r_i\|_1}\right) \in \mathbb{R}^{m \times m}$ are diagonal matrices and the 1-norms $\|c_j\|_1$ and $\|r_i\|_1$ are the sum of the columns and rows of \mathbf{A} respectively. Both the algorithms have a convergence history that initially improves the solution for better approximation of the target image $\bar{\mathbf{x}}$, but in later iterations diverge from this letting the reconstruction to be more influenced by the noise. Different techniques can be adopted as stopping rule; most of them are based on the behavior of the residual vector $\boldsymbol{\rho}^{(k)} = \mathbf{y} - \mathbf{A}\mathbf{x}^{(k)}$, [1, 11].

4.4 Comparative evaluation of the standard methods

After describing the standard *post-log* CT reconstruction methods, here we compare them in different scenarios by changing the number of projections, their range and the level of noise in the data (the X-ray dose). For this experiment we consider the Shepp Logan phantom (500×500 pixels) inside a Fan Beam acquisition process with 500 detector pixels; Figure 7.3 shows the phantom, the intensity data \mathbf{b} and the post-log sinogram data \mathbf{y} for $I_0 = 2500$. Before going into the details, it is important to mention that all the reconstructed images are in the same range as the original phantom except the one obtained with BP, which are scaled between their minimum

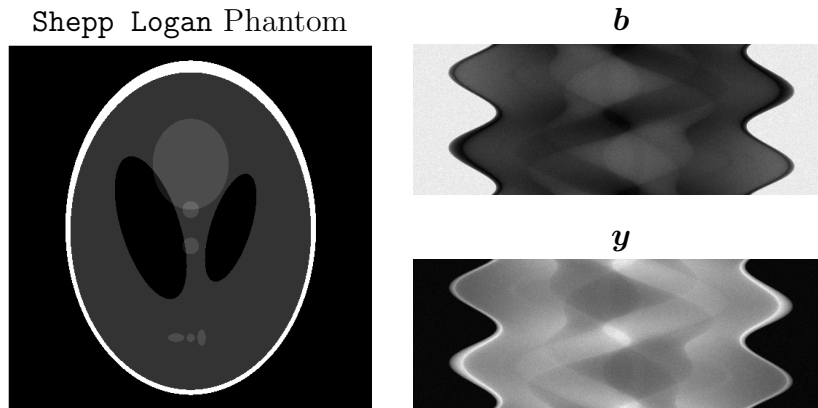


Figure 4.7: Shepp Logan phantom, the intensity data \mathbf{b} and the post-log sinogram data \mathbf{y} for $I_0 = 2500$ and 180 angles in the range $[0, 2\pi]$.

and maximum. In fact, as we previously discussed, the BP reconstructions have higher values in the pixels than the target due to the smearing process (so if we visualize them in the same range of the phantom, we will look at a white image).

In the first experiment, the algorithms BP, FBP, ART and SIRT are applied to the noisy sinogram \mathbf{y} by considering both different number of projection and angle ranges, see Figure 4.8. We can note that, for a fixed range, the quality of the reconstructions decreases with the number of projections as the inside structure become less clear and the stripe artifacts coming from the few projections arise. Moreover, by restricting the angle range, the reconstructions are less accurate, especially in the portion of the image that are less “irradiated”. In the second experiment, Figure 4.9, we compare the four algorithms by changing the level of noise in the data, namely by reducing the X-ray dose I_0 , and considering 180 projection angles in the range $[0, 2\pi]$. As one can note, the reconstructions become noisier as I_0 decreases, with SIRT returning the best results for all the considered cases. In fact, for $I_0 = 2500$ the internal structures are visible both with FBP, ART and SIRT, but the SIRT image contain less noise and sharper details. When the noise increases, the FBP results are almost only noise, while in the SIRT

reconstruction we can distinguish the main features. Nevertheless, even the SIRT outputs present some noise artifact and its results need to be improved, [7, 8, 9].

As we mentioned before, the low-dose scenario that we want to investigate arises when lowering the number of projections angles, when narrowing the range or decreasing the X-ray dose. However, since the first two cases two cases are often related to limitations of the equipment or the type of exam (such as the mammography) and lead to specific artifacts, in this thesis we will focus on the task of reducing the dose and work with more noisy data.

4.5 Variational Methods

In Chapter 2 inverse problems are introduced, together with the definition of *well-posedness* and the formulation of classical degradation models 2.1. For the case of Computed Tomography, the associated inverse problem is typically *ill-posed*. In fact, in standard CT acquisition setups many projections are acquired making the problem over-determined (non existence of the solution). In other cases, like limited angles or low dose CT where the number of measurements is less than the number of the unknowns, the problem is under-determined (non-uniqueness of the solution). Finally, even in case of as many measurements as the unknowns, noise in the observed data can propagate to very large perturbations in the solution. In the previous section we analyzed the behaviour of the standard reconstruction strategies when working with noisy data and/or with limited number of projection angles. Clearly, the simple Filtered Back-projection or the algebraic methods that solve the linear system $\mathbf{y} = \mathbf{A}\mathbf{x}$ are not enough for these problems and more advanced strategies need to be considered.

Before going any further, we recall the inverse problems we aim to solve:

$$\begin{aligned} \text{find } \mathbf{x} \in \mathbb{R}^n \text{ such that } \mathbf{b} \text{ is a realization of the random} \\ \text{noise } \mathcal{B} \sim \mathcal{N}(\boldsymbol{\lambda}) \text{ with } \boldsymbol{\lambda} = \mathbf{g}(\mathbf{A}\mathbf{x}) + \mathbf{q} \end{aligned} \quad (4.2)$$

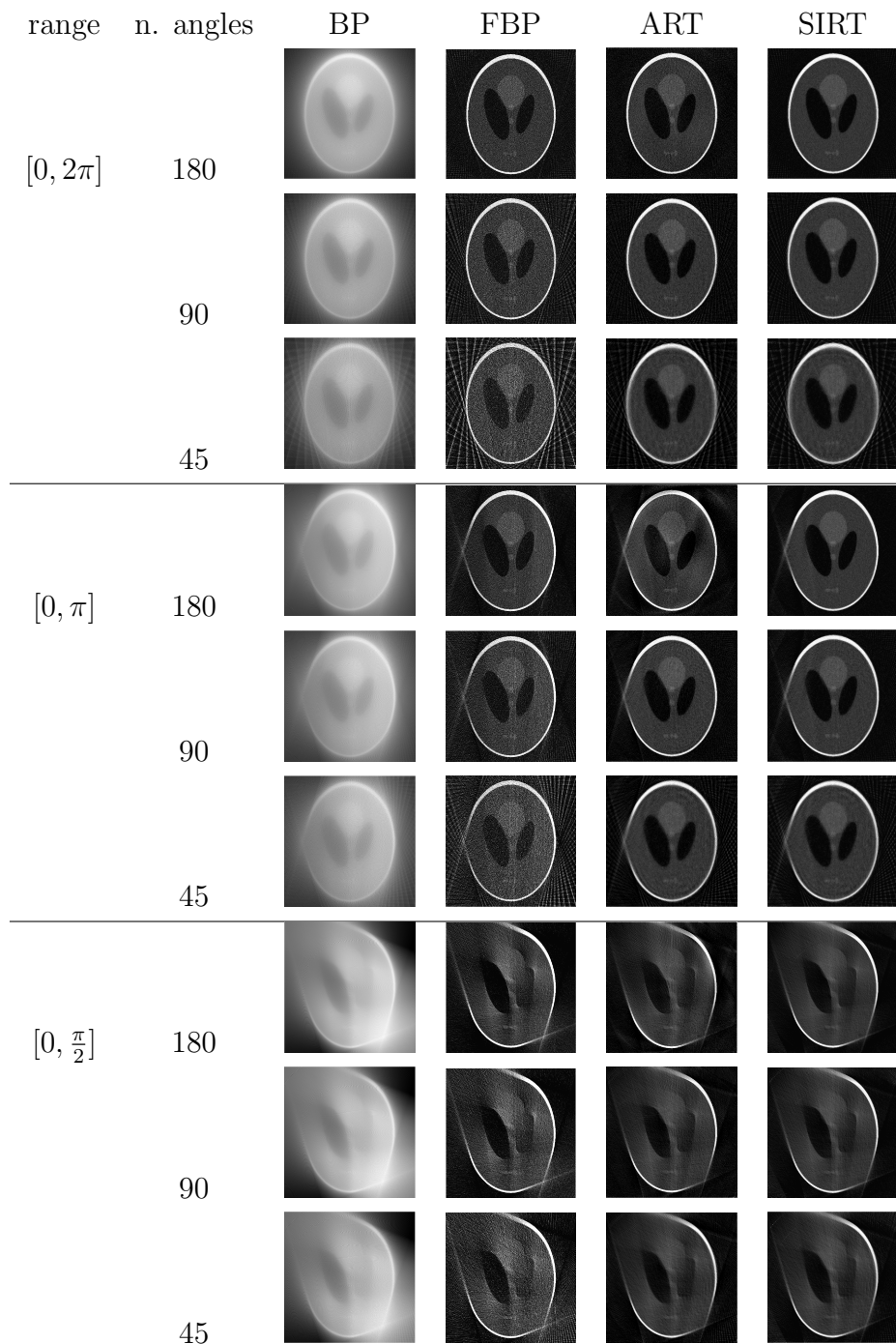


Figure 4.8: Comparison of the standard CT reconstruction methods BP, FBP, ART and SIRT applied on a Fan Beam geometry with different range of angles and number of projections.

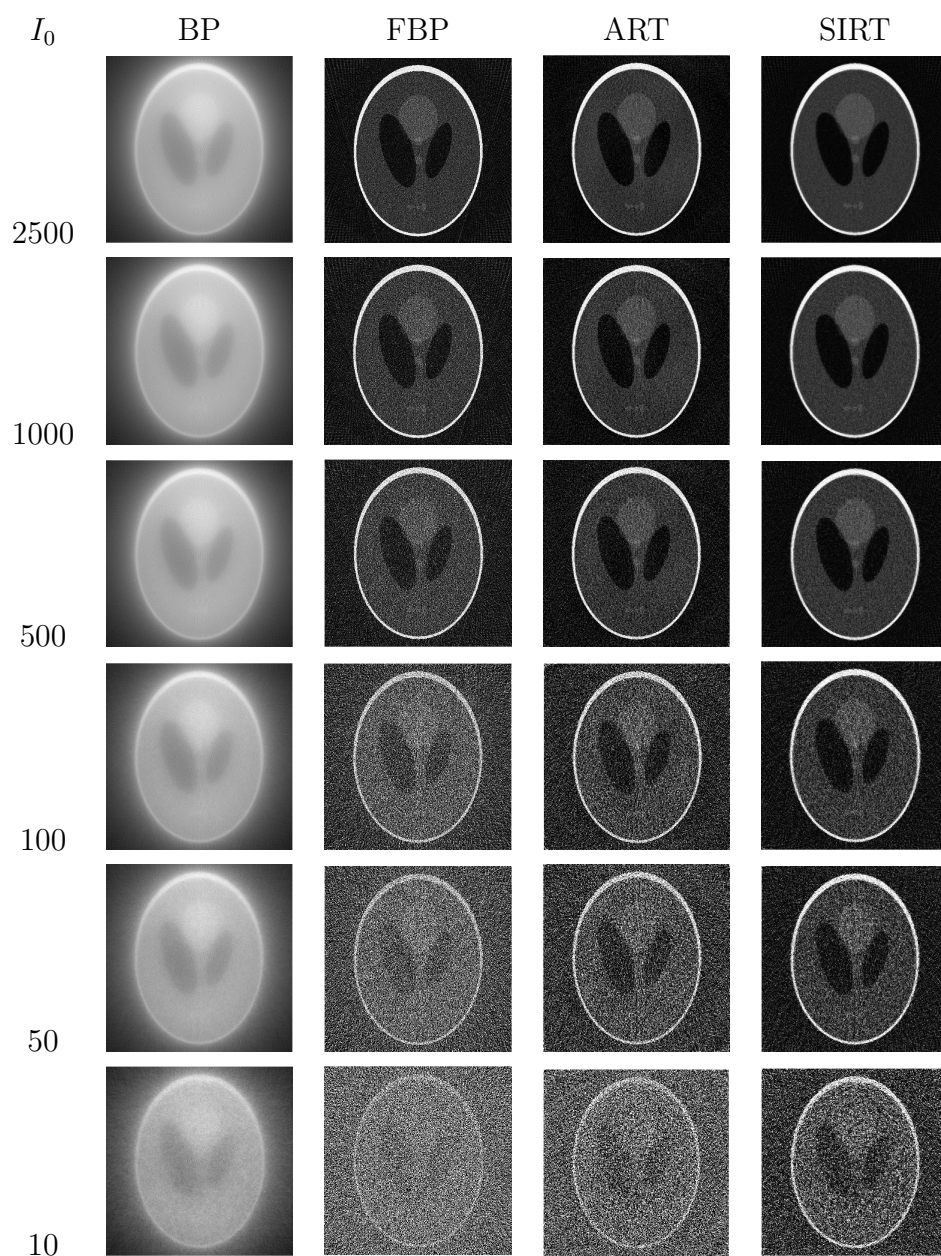


Figure 4.9: Comparison of the standard CT reconstruction methods BP, FBP, ART and SIRT applied on a Fan Beam geometry with different doses of X-rays, namely different values of I_0 . The acquisition setup considers 180 angles in the range $[0, 2\pi]$.

with $\mathbf{b}, \mathbf{q} \in \mathbb{R}^m$ and $\mathbf{A} \in \mathbb{R}^{m \times n}$.

To overcome the intrinsic ill-posedness of the above problem, one can rather solve a well-posed problem that is as close as possible to the original one. In this context, one of the most popular class of strategies is the one of Variational Methods, where the well-posed problem to solve is minimizing a cost function $\mathcal{J} : \mathbb{R}^n \rightarrow \mathbb{R}_+$. In formula:

$$\widehat{\mathbf{x}}(\mu) \in \arg \min_{\mathbf{x} \in \mathbb{R}^n} \{ \mathcal{J}(\mathbf{x}, \mu) := \mathcal{R}(\mathbf{x}) + \mu \mathcal{F}(\mathbf{x}; \mathbf{g}, \mathbf{A}, \mathbf{b}) \}, \quad (4.3)$$

where $\widehat{\mathbf{x}}$ is an approximation of the solution of the original problem. The functional \mathcal{F} is typically called *data fidelity* term, as it measures the distance between the noise-free degraded image $\mathbf{g}(\mathbf{A}\mathbf{x}) + \mathbf{q}$ and the noisy observation \mathbf{b} in a way that accounts for the noise statistics. On the other hand, we refer to \mathcal{R} as the *regularization* term, that encodes prior information or beliefs on the target uncorrupted image $\bar{\mathbf{x}}$; for instance, it can penalize heavy oscillations, force smoothness or incorporate the known sparsity patterns of the target. The regularization parameter $\mu > 0$ balances the contribution of the two terms in the overall cost function and its choice is very important as, even with the appropriate fidelity and regularization terms, an improper value μ can lead to worthless reconstructions. For this reason, in (4.3) we made explicit the dependence of the solution $\widehat{\mathbf{x}}$ on the parameter μ .

4.5.1 Bayesian Formulation

A well-established way of defining variational models suitable for the scenario at hand is to recast the problem into Bayesian probabilistic terms: it portrays the data fidelity and regularization terms based on probability density/mass functions and it helps us to understand which functional \mathcal{R} and \mathcal{F} to choose according to the noise model and the a priori information we have on the solution, [14].

In the Bayesian perspective the unknown quantity \mathbf{x} of the problem is modeled as a random field; the discrete model takes the following probabilistic

form:

$$\mathbf{B} \sim \mathcal{N}(\Lambda) \quad \Lambda = \mathbf{g}(\mathbf{A}\mathbf{X}) + \mathbf{q},$$

where \mathcal{N} denotes a generic noise distribution that, for our purposes, will be a Poisson, Gaussian and Mixed Poisson-Gaussian, and \mathbf{B} and \mathbf{X} are m - and n - random fields whose realizations are the ones denoted in the deterministic models \mathbf{b} and \mathbf{x} , respectively. In this framework we indicate with $P(\mathbf{b}|\mathbf{x})$ the *likelihood* probability mass function that encodes the information on the degradation process, while the prior assumptions on the random field \mathbf{X} are expressed into the *prior* pdf $p(\mathbf{x})$. In this context one aims to find the analytical expression of the *posterior* pdf conditional distribution $p(\mathbf{x}|\mathbf{b})$ that is related to the likelihood and the prior via the Bayes' formula, [15]:

$$p(\mathbf{x}|\mathbf{b}) = \frac{P(\mathbf{b}|\mathbf{x})p(\mathbf{x})}{P(\mathbf{b})} \propto P(\mathbf{b}|\mathbf{x})p(\mathbf{x}).$$

4.5.2 Priors

The design of the prior involves the process of mathematically formalizing the properties of the target image $\bar{\mathbf{x}}$ that one aims to recover. For example, if the target image $\bar{\mathbf{x}}$ is piece-wise constant, we expect it to have few jumps only between its flat parts with different grey levels. This leads to the assumption that the vector with the entries

$$\|(\mathbf{D}\mathbf{x})_j\|_2 = \sqrt{(\mathbf{D}_h\mathbf{x})_j^2 + (\mathbf{D}_v\mathbf{x})_j^2},$$

will be sparse, where $\mathbf{D}_h, \mathbf{D}_v \in \mathbb{R}^{n \times n}$ are two linear operators representing the finite difference discretizations of the first-order partial derivatives of the image \mathbf{x} in the horizontal and vertical direction.

Generally speaking, priors encode information about the distribution of the grey levels inside the image (for the image restoration problem) or the attenuation levels of the object (for the CT reconstruction) and their transition between different areas of the target. In this context, the unknown image is modeled as a Markov Random Field (MRF), that is the extension of a Markov Random process to more dimensions, [17]. With this framework,

one requires that a characteristic of pixel x_j of the image \mathbf{x} depends only on the behaviour of a set of its neighboring pixels x_k , $k \in \mathcal{C}_j$, where \mathcal{C}_j is the index set of the neighbors of x_j . This property is expressed as:

$$P(X_j = x_j | X_k = x_k, k \neq j) = P(X_j = x_j | X_k = x_k, k \in \mathcal{C}_j).$$

The prior distribution of a MRF is the so-called *Gibbs prior*

$$p(\mathbf{x} | \theta_{\text{pr}}) = \frac{1}{Z} \exp\left(-\sum_{j=1}^n V_{\mathcal{C}_j}(\mathbf{x}; \theta_{\text{pr}})\right)$$

where $Z > 0$ is a normalization constant, $V_{\mathcal{C}_j}$ is the *Gibbs potential function* defined on the circle of pixels centered at x_j , and θ_{pr} denotes the parameters used in the prior. Different choices of the function $V_{\mathcal{C}_j}$ lead to priors that enhance various properties of the image \mathbf{x} . A typical choice that consider the discrete gradient magnitude of the image is given by the Total Variation Gibbs prior, [17]:

$$p_{\text{TV}}(\mathbf{x}) = \frac{1}{Z} \exp\left(-\alpha \sum_{j=1}^n \|(\mathbf{D}\mathbf{x})_j\|_2\right)$$

where α is the prior parameter. Moreover, one can look at the second order derivatives and define the TV^2 prior that promotes piecewise-affine structure inside the image:

$$p_{\text{TV}^2}(\mathbf{x}) = \frac{1}{Z} \exp\left(-\alpha \sum_{j=1}^n \|(\nabla^2 \mathbf{x})_j\|_F\right)$$

where $(\nabla^2 \mathbf{x})_j \in \mathbb{R}^{2 \times 2}$ indicates the discrete Hessian of image \mathbf{x} at pixel j and $\|\cdot\|_F$ denotes the Frobenius norm. As regards images with a dark background and just a few of non zero pixels, such as astronomical images, the prior that can be applied in this case is the L_1 prior:

$$p_{L_1}(\mathbf{x}) = \frac{1}{Z} \exp\left(-\alpha \|\mathbf{x}\|_1\right).$$

In cases where a constraint on the image is known, the prior can be expressed as product of a constraint $x \in \Omega$ and an “informative” prior (as one above).

The constraint prior takes the following form:

$$p_{\Omega}(\mathbf{x}) = \begin{cases} 1 & \text{if } \mathbf{x} \in \Omega \\ 0 & \text{otherwise.} \end{cases}$$

4.5.3 Likelihoods

The selection of the prior is a hard task since it is supposed information on the pixels behavior; hence, the choice of the likelihood model is crucial to mitigate the approximation introduced by the prior. It is important to consider the physics that guides the acquisition process and the statistical assumptions connected to it.

In what follows, we give the expression of the likelihood distributions for the noise statistics typically modelling the degradation observed in CT data, namely Gaussian, Poisson and Mixed Poisson-Gaussian, as explained in 2.3. For the case of i.i.d Gaussian noise:

$$\mathbf{b} = \mathbf{g}(\mathbf{Ax}) + \mathbf{e},$$

where $\mathbf{e} \in \mathbb{R}^m$ is the realization of a multivariate Gaussian random variable with mean vector $\eta \mathbf{1}_m$ and covariance matrix $\Sigma = \sigma^2 \mathbf{I}_{m \times m}$, the likelihood pdf reads.

$$\begin{aligned} p(\mathbf{b}|\mathbf{x}) &= p(\mathbf{b} - \mathbf{g}(\mathbf{Ax})) = p(\mathbf{e}) = \prod_{i=1}^n p(e_i) \\ &= \prod_{i=1}^m \frac{1}{\sqrt{2\pi}\sigma} \exp\left(-\frac{((\mathbf{b} - \mathbf{g}(\mathbf{Ax}))_i - \eta)^2}{2\sigma^2}\right) \\ &= \frac{1}{\sqrt{2\pi}^m \sigma^m} \prod_{i=1}^n \exp\left(-\frac{((\mathbf{b} - \mathbf{g}(\mathbf{Ax}))_i - \eta)^2}{2\sigma^2}\right). \end{aligned}$$

Recalling that the Poisson forward model can be written in component-wise form as follows:

$$b_i = \text{Poiss}(\lambda_i), \quad \lambda_i = g(\mathbf{Ax})_i + q_i, \quad i = 1, \dots, m,$$

and that the noise realizations at different pixels are independent, the Likelihood for the Poisson noise reads:

$$P(\mathbf{b}|\mathbf{x}) = P(\mathbf{b}|\boldsymbol{\lambda}) = \prod_{i=1}^m P(b_i|\lambda_i) = \prod_{i=1}^m \lambda_i^{b_i} \frac{e^{-\lambda_i}}{b_i!}.$$

Considering a Mixed Poisson-Gaussian model, the acquired data can be written as:

$$b_i = \text{Poiss}(\lambda_i) + \text{Gauss}(\eta, \sigma^2), \quad \lambda_i = g(Ax)_i + q_i \quad i = 1, \dots, m,$$

and after recalling that the realization are independent and for the Gaussian contribution even i.i.d, the Likelihood for the Mixed Poisson-Gaussian model reads:

$$\begin{aligned} p(\mathbf{b} | \mathbf{x}) &= p(\mathbf{b} | \boldsymbol{\lambda}, \eta, \sigma) = \prod_{i=1}^m p(b_i | \lambda_i, \eta, \sigma) \\ &= \prod_{i=1}^m \left(\sum_{b_n \in \mathbb{N}} \left(\frac{\lambda^{b_n} e^{-\lambda}}{b_n!} \right) \cdot \left(\frac{1}{\sqrt{2\pi}\sigma} \exp \left(-\frac{((b_i - b_n) - \eta)^2}{2\sigma^2} \right) \right) \right). \end{aligned}$$

4.5.4 The Maximum A Posteriori (MAP) approach

Since investigating a distribution is particularly expensive from the computational point of view, one tends to select a single representative of the distribution summarizing its information. There is therefore the need to find a way to derive the single-point information $\hat{\mathbf{x}}$ from the posteriori distribution. One popular strategy is to use the mode of $p(\mathbf{x}|\mathbf{b})$ as a single-point representative of the posterior distribution, meaning that we want to find the image $\hat{\mathbf{x}}$ maximizing the posterior: Maximum A Posteriori (MAP),

$$\hat{\mathbf{x}} \in \arg \max_{\mathbf{x} \in \mathbb{R}^n} \{p(\mathbf{x}|\mathbf{b}) \propto P(\mathbf{b}|\mathbf{x}) p(\mathbf{x})\}. \quad (4.4)$$

We quickly recall that, the conditional mean approach selects the mean of the distributions as its representative. However the mean is calculated approximating an integral in large-dimensional spaces.

After applying the negative logarithm to (4.4) we have:

$$\hat{\mathbf{x}} \in \arg \min_{\mathbf{x} \in \mathbb{R}^n} \{-\log(P(\mathbf{b}|\mathbf{x})) - \log(p(\mathbf{x}))\}. \quad (4.5)$$

We remark that the main idea of Variational Methods, whose general form is expressed in (4.3), is to obtain a good approximation $\widehat{\mathbf{x}}$ of the solution $\bar{\mathbf{x}}$ of the original problem. This can be obtained using the MAP approach, whose form in (4.5) resembles the one in (4.3) where the cost function in (4.3) is a sum of two terms, one encoding prior information on the image ($p(\mathbf{x})$), the other modelling the noise statistics ($P(\mathbf{b}|\mathbf{x})$).

4.6 The \mathcal{R} -KL model

In this section we introduce one of the most commonly used variational models for the CT, consisting of a regularizer \mathcal{R} and a Poisson fidelity (that we will refer to as KL): the \mathcal{R} -KL model. Before deriving the \mathcal{R} -KL variational model we recall the general Poisson forward model

$$\mathbf{b} = \mathbf{Poiss}(\bar{\boldsymbol{\lambda}}), \quad \boldsymbol{\lambda} = \mathbf{g}(\mathbf{A}\bar{\mathbf{x}}) + \mathbf{q} \quad (4.6)$$

where $\mathbf{b} \in \mathbb{R}^m$, $\mathbf{x} \in \mathbb{R}^n$ and $\mathbf{q} \in \mathbb{R}^m$ are vectorized forms of the observed degraded image, the unknown uncorrupted image and the so-called (usually known) background emission image. $\mathbf{A} \in \mathbb{R}^{m \times n}$ models a linear degradation operator, whereas the vectorial function $\mathbf{g} : \mathbb{R}^m \rightarrow \mathbb{R}^m$ is the identity function or a nonlinear function modelling the possible presence of (deterministic) nonlinearities in the degradation process. \mathbf{A} and \mathbf{g} are dictated by the specific application and are assumed to be known. For the specific subject of this thesis, i.e. computed tomography, the function \mathbf{g} can be restricted to the simplified form $\mathbf{g}(\mathbf{a}) = (g(a_1), g(a_2), \dots, g(a_m))^T$ with $g : \mathbb{R}_+ \rightarrow \mathbb{R}_+$ and $\mathbf{Poiss}(\bar{\boldsymbol{\lambda}}) = (\mathbf{Poiss}(\bar{\lambda}_1), \mathbf{Poiss}(\bar{\lambda}_2), \dots, \mathbf{Poiss}(\bar{\lambda}_m))^T$, with $\mathbf{Poiss}(\bar{\lambda}_i)$ indicating the realization of a Poisson-distributed random variable with parameter (mean) $\bar{\lambda}_i$.

Starting from the above forward model (4.6) and considering a generic Gibbs prior $p_{Gibbs}(\mathbf{x} | \theta_{pr})$ together with the constraint $\mathbf{x} \in \Omega := \{\mathbf{x} \in \mathbb{R}^n, \mathbf{x} \geq 0\}$,

the posterior density takes the form

$$\begin{aligned} p(\mathbf{x}|\mathbf{b}) &\propto P(\mathbf{b}|\mathbf{x}) p(\mathbf{x}) = P(\mathbf{b}|\mathbf{x}) p_{Gibbs}(\mathbf{x} | \theta_{\text{pr}}) p_{\Omega}(\mathbf{x}) \\ &= \left(\prod_{i=1}^m \lambda_i^{b_i} \frac{e^{-\lambda_i}}{b_i!} \right) \frac{1}{Z} \exp\left(- \sum_{j=1}^n V_{\mathcal{C}_j}(\mathbf{x}; \theta_{\text{pr}}) \right) p_{\Omega}(\mathbf{x}). \end{aligned} \quad (4.7)$$

By taking the negative logarithm of the likelihood and prior we have:

$$\begin{aligned} -\log P(\mathbf{b}|\mathbf{x}) &= -\log P(\mathbf{b}|\boldsymbol{\lambda}) = -\log \prod_{i=1}^m P(b_i|\lambda_i) = -\sum_{i=1}^m \log P(b_i|\lambda_i) \\ &= \sum_{i=1}^m -\log \left(\lambda_i^{b_i} \frac{e^{-\lambda_i}}{b_i!} \right) = \sum_{i=1}^m \left(\lambda_i - b_i \log(\lambda_i) + \log(b_i!) \right) \\ -\log p(\mathbf{x}) &= -\log (p_{Gibbs}(\mathbf{x} | \theta_{\text{pr}}) + p_{\Omega}(\mathbf{x})) \\ &= \sum_{j=1}^n V_{\mathcal{C}_j}(\mathbf{x}; \theta_{\text{pr}}) + \iota_{\Omega}(\mathbf{x}) + \log(Z) \end{aligned} \quad (4.8)$$

where $\iota_{\Omega}(\mathbf{x})$ denotes the indicator function of set Ω , which is equal to 0 if $\mathbf{x} \in \Omega$ and $+\infty$ otherwise.

Finally, plugging (4.8) into (4.5), dropping out the constant term $\log Z$ and expressing the parameters in terms of μ , we obtain the \mathcal{R} -KL variational model

$$\widehat{\mathbf{x}}(\mu) \in \arg \min_{\mathbf{x} \in \Omega} \{ \mathcal{J}(\mathbf{x}, \mu) := \mathcal{R}(\mathbf{x}) + \mu \text{KL}(\boldsymbol{\lambda}, \mathbf{b}) \}, \quad \boldsymbol{\lambda} = \mathbf{g}(\mathbf{A}\mathbf{x}) + \mathbf{q} \quad (\mathcal{R}\text{-KL})$$

where $\mu \in \mathbb{R}_{++}$, $\mathcal{R}(\mathbf{x})$ is the regularizer that comes from the choice of the prior and the term $\text{KL}(\boldsymbol{\lambda}, \mathbf{b})$ indicates the generalized Kullback-Leibler (KL) divergence between $\boldsymbol{\lambda} = \mathbf{g}(\mathbf{A}\mathbf{x}) + \mathbf{q}$ and the observation \mathbf{b} , which reads

$$\text{KL}(\boldsymbol{\lambda}, \mathbf{b}) = \sum_{i \in \mathcal{J}} F(\lambda_i, b_i) \quad (4.9)$$

where

$$F(\lambda_i, b_i) = \begin{cases} \lambda_i - b_i \log(\lambda_i) + \log(b_i!) & \text{if } i \in \mathcal{J}_+ \\ \lambda_i & \text{if } i \in \mathcal{J}_0 := \mathcal{J} \setminus \mathcal{J}_+ \end{cases} \quad (4.10)$$

with \mathcal{J} , \mathcal{J}_+ , \mathcal{J}_0 the sets of pixel indices defined by

$$\mathcal{J} := \{1, \dots, m\}, \quad \mathcal{J}_+ := \{i \in \mathcal{J} \mid b_i > 0\}, \quad \mathcal{J}_0 := \mathcal{J} \setminus \mathcal{J}_+ = \{i \in \mathcal{J} \mid b_i = 0\}. \quad (4.11)$$

4.6.1 The TV-KL model

After deriving the general \mathcal{R} -KL model, here we define the TV-KL model by first plugging the Total Variation Gibbs prior into (4.7) and (4.8)

$$\begin{aligned} -\log p(\mathbf{x}) &= -\log \left(\frac{1}{Z} \exp \left(-\alpha \sum_{j=1}^n \|(\mathbf{D}\mathbf{x})_j\|_2 \right) + p_\Omega(\mathbf{x}) \right) \\ &= \alpha \sum_{j=1}^n \|(\mathbf{D}\mathbf{x})_j\|_2 + \iota_\Omega(\mathbf{x}) + \log(Z). \end{aligned}$$

Then, by placing the results into (4.5), not considering the constant term $\log Z$ and dividing the cost function by the positive scalar α , we obtain the TV-KL variational model

$$\hat{\mathbf{x}}(\mu) \in \arg \min_{\mathbf{x} \in \Omega} \{ \mathcal{J}(\mathbf{x}, \mu) := \text{TV}(\mathbf{x}) + \mu \text{KL}(\boldsymbol{\lambda}, \mathbf{b}) \}, \quad \boldsymbol{\lambda} = \mathbf{g}(\mathbf{A}\mathbf{x}) + \mathbf{q} \quad (\text{TV-KL})$$

where $\mu = 1/\alpha$, the TV semi-norm [18] is defined by

$$\text{TV}(\mathbf{x}) = \sum_{j=1}^n \|(\mathbf{D}\mathbf{x})_j\|_2. \quad (\text{TV})$$

4.6.2 Other regularization and fidelity terms

The TV-KL variational model will be extensively employed for the CT reconstruction problem in the following sections. As previously discussed, the TV term is particularly suitable when the target is a piecewise constant object but it can fail in reconstructing more articulated objects due to its downsides, such as *loss of contrast*, *staircasing effects* and its space-invariant definition. For this reason, we now recall some of the regularization terms $\mathcal{R}(\mathbf{x})$ that in the experimentations carried out in the rest of the thesis will

be also coupled with the KL data fidelity term so as to form more flexible variational models. The discussed regularizers can be all regarded as stemming from the image priors introduced in 4.5.2.

The global effect of TV works well for images with the same level of details inside, since it applies the same amount of regularization is each pixel regardless its local properties or structure, but returns poor results in cases with different textures across the image. Although the TV term is known to be particularly effective for the restoration of piece-wise constant images; it tends to promote edges producing the so-called staircasing effect on the smooth parts of the image. As a way to overcome the classical drawbacks of TV, one can employ the TV² regularizer [19] defined by

$$\mathcal{R}(\mathbf{x}) = \text{TV}^2(\mathbf{x}) := \sum_{j=1}^n \|(\nabla^2 \mathbf{x})_j\|_F, \quad (\text{TV}^2)$$

with $(\nabla^2 \mathbf{x})_j \in \mathbb{R}^{2 \times 2}$ indicating the discrete Hessian of image \mathbf{x} at pixel j and $\|\cdot\|_F$ denoting the Frobenius norm. The TV² regularizer promotes piecewise-affine structures in the image, however its ability to recover sharp edges is less than TV.

A way to incorporate the benefits of the TV and of the TV² regularizers while mitigating their shortcomings is the popular Total Generalized Variation (TGV) [21], in particular its second-order version which reads

$$\mathcal{R}(\mathbf{x}) = \text{TGV}^2(\mathbf{x}) := \min_{w \in \mathbb{R}^{2n}} \left\{ \alpha_0 \sum_{j=1}^n \|(\nabla \mathbf{x})_j - w_j\|_2 + \alpha_1 \sum_{j=1}^m \|(\mathcal{E}w)_j\|_F \right\}, \quad (\text{TGV}^2)$$

where $w = (w_1; w_2)$ with $w_1, w_2 \in \mathbb{R}^n$, $w_j := (w_{1,j}; w_{2,j}) \in \mathbb{R}^2$ and $(\mathcal{E}w)_i \in \mathbb{R}^{2 \times 2}$ denotes the discrete symmetric Jacobian of vector field w at pixel j , with α_0, α_1 being positive parameters.

Before going ahead with the discussion, here we define the TV²-KL and the TGV-KL variational models that will be employed in the following chapters.

$$\hat{\mathbf{x}}(\mu) \in \arg \min_{\mathbf{x} \in \Omega} \{ \mathcal{J}(\mathbf{x}, \mu) := \text{TV}^2(\mathbf{x}) + \mu \text{KL}(\boldsymbol{\lambda}, \mathbf{b}) \}, \quad (\text{TV}^2\text{-KL})$$

$$\hat{\mathbf{x}}(\mu) \in \arg \min_{\mathbf{x} \in \Omega} \{ \mathcal{J}(\mathbf{x}, \mu) := \text{TGV}^2(\mathbf{x}) + \mu \text{KL}(\boldsymbol{\lambda}, \mathbf{b}) \}, \quad (\text{TGV}^2\text{-KL})$$

where $\boldsymbol{\lambda} = \mathbf{g}(\mathbf{Ax}) + \mathbf{q}$.

Regarding the fidelity term, a common choice when the noise follows a Gaussian distribution or when it can be approximated by it, is to consider a Gaussian Likelihood or its space variant version:

$$\mathcal{F}(\mathbf{x}; \mathbf{g}, \mathbf{A}, \mathbf{b}) = L_2(\mathbf{x}; \mathbf{g}, \mathbf{A}, \mathbf{b}) := \frac{1}{2} \|\mathbf{g}(\mathbf{Ax}) + \mathbf{q} - \mathbf{b}\|_2^2 \quad (L_2)$$

$$\mathcal{F}(\mathbf{x}; \mathbf{g}, \mathbf{A}, \mathbf{b}) = WL_2(\mathbf{x}; \mathbf{g}, \mathbf{A}, \mathbf{b}) := \frac{1}{2} \|\mathbf{g}(\mathbf{Ax}) + \mathbf{q} - \mathbf{b}\|_W^2 \quad (WL_2)$$

where $\|\cdot\|_W^2 = \sum_i w_i \cdot_i^2$ denotes the weighted norm. Due to their simple form and easy solution, both are commonly used even for data corrupted by Poisson noise. In fact, as discussed in 2.3.1, for sufficiently large values of its mean, the Poisson distribution can be approximated by a Gaussian. Moreover, for the CT problem, we derived a way to approximate the noise in the sinogram \mathbf{y} (post-log approach) with a Gaussian distribution.

4.7 The importance of the choice of the parameter

Despite the choice of suitable fidelity and regularization terms, the solution of (4.3) strongly depends on the regularization parameter μ , whose incorrect value selection can lead to meaningless reconstruction. As we can see in (4.3) a small value of μ corresponds to a functional $\mathcal{J}(\mathbf{x}, \mu)$ where the regularization term is more strongly penalized, so the solution $\hat{\mathbf{x}}(\mu)$ will be more regularized according to the specific choice of $\mathcal{R}(\mathbf{x})$. On the other hand, larger values of μ result in noisier reconstructions but with more details. In other words, the parameter regulates the confidence that I have in the data. If the observation is very good, the data can be trusted, so the parameter μ is bigger. Otherwise, if the data is degraded, we need to balance the fidelity in the data with the a priori information that I have on the data. This behavior can be observed in Figure 4.10 where the solution $\hat{\mathbf{x}}(\mu)$ of the

TV-KL model (TV-KL) for the image restoration problem $\mathbf{b} = \mathbf{Poiss}(\bar{\boldsymbol{\lambda}})$, with $\bar{\boldsymbol{\lambda}} = I_0 \exp(-\mathbf{A}\bar{\mathbf{x}}) + \mathbf{q}$ is shown for increasing values of the regularization parameter μ (from left to right, top to boom). The synthetic data are generated considering an initial intensity $I_0 = 100$ and 180 angles in the range $[0, 2\pi]$. As one can note by comparing the reconstruction in Figure 4.10 with the one in Figure 4.9 for the same I_0 , the result obtained with the TV-KL model are characterized by more details and less noise than the best of the standard methods (the one with SIRT). However, the quality of the TV-KL reconstruction strongly depends on the choice of the parameter μ , whose incorrect choice leads to worse results than those obtained with standard methods.

Therefore, the selection of a suitable value for the regularization parameter μ is of crucial importance for obtaining high-quality results. Very often, μ is chosen empirically by brute-force optimization with respect to some visual quality metrics. Such strategy implies an high computational cost and the compromise of selecting the parameter only between the computed reconstructions and from a visual perspective.

As a results, the following part of the thesis focuses on automatic selection strategies for the choice of the regularization parameter in Variational Methods with Poisson noise data.

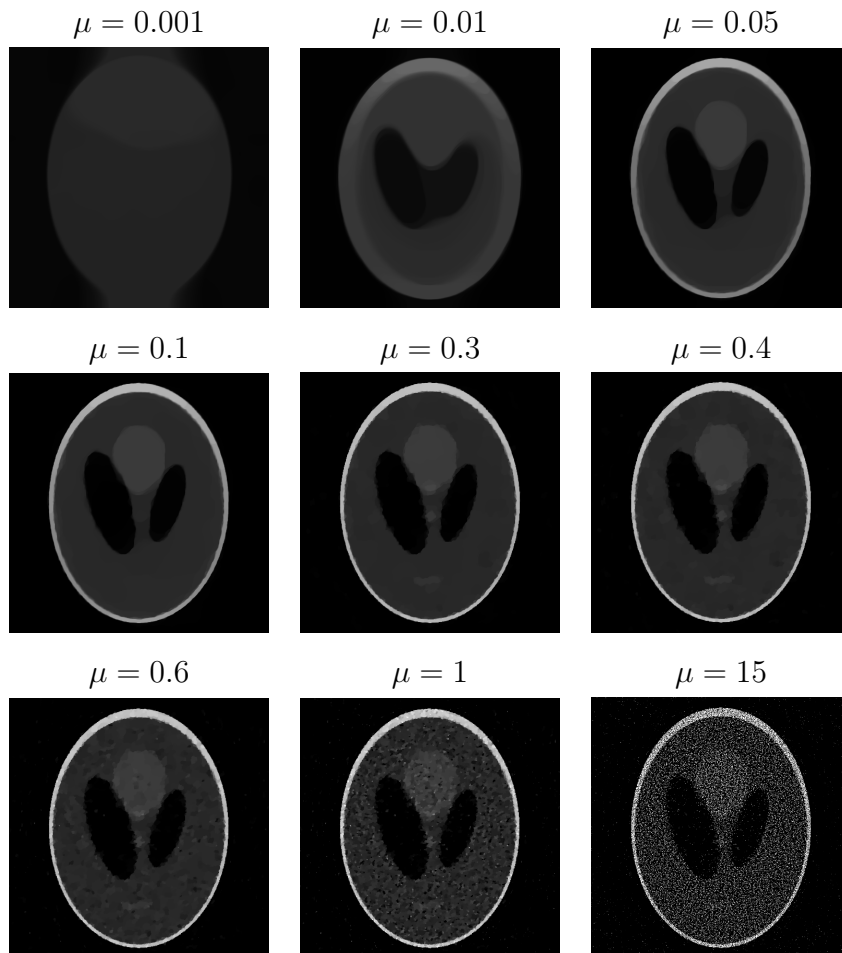


Figure 4.10: Results of the TV-KL model (TV-KL) for the CT reconstruction problem for increasing values of the regularization parameter μ (left to right, top to bottom). The synthetic data are generated considering the forward process $\mathbf{b} = \mathbf{Pois}(\bar{\boldsymbol{\lambda}})$, with $\bar{\boldsymbol{\lambda}} = I_0 \exp(-\mathbf{A}\bar{\mathbf{x}}) + \mathbf{q}$, $I_0 = 100$ and 180 angles in the range $[0, 2\pi]$.

Part II

Automatic selection of the parameters

Chapter 5

State of The Art strategies

In this part of the thesis we focus on data corrupted only by Poisson noise:

$$\mathbf{b} = \text{Poiss}(\bar{\lambda}), \quad \bar{\lambda} = \mathbf{g}(\mathbf{A}\bar{\mathbf{x}}) + \mathbf{q}.$$

In these cases, a criterion for the selection of μ in variational models of the form (\mathcal{R} -KL) reported here

$$\hat{\mathbf{x}}(\mu) \in \arg \min_{\mathbf{x} \in \Omega} \{ \mathcal{J}(\mathbf{x}, \mu) := \mathcal{R}(\mathbf{x}) + \mu \text{KL}(\boldsymbol{\lambda}, \mathbf{b}) \}, \quad \boldsymbol{\lambda} = \mathbf{g}(\mathbf{A}\mathbf{x}) + \mathbf{q},$$

can be formulated as follows

$$\text{Select } \mu = \mu^* \text{ such that } \mathcal{C}(\hat{\mathbf{x}}(\mu^*)) \text{ is satisfied,}$$

where $\hat{\mathbf{x}}(\mu) : \mathbb{R}_{++} \rightarrow \mathbb{R}^n$, is the image restoration function introduced in (4.3) and $\mathcal{C}(\cdot)$ is some selection criterion or principle.

Traditionally, the criteria proposed for the μ -selection under Poisson noise corruption are extensions of strategies for the parameter selection in presence of additive white Gaussian noise. With this idea, some attempts modify the generalized cross validation function, originally proposed in [22], in order to be applied to the case of Poisson noise [23, 24]. Bertero and co-authors proposed an effective strategy that extends the Morozov Discrepancy Principle to the case of Poisson noise, [25, 26, 27], while different methods rely on transforming the noise statistics, as it happens in [32], where the authors

consider a Gaussian approximation of the noise and then employ the popular Morozov discrepancy principle. The criteria can be thus divided into two main classes according to their original derivation set-up:

1. Principles derived from imposing the value of some μ -dependent quantity;
2. Principles derived from optimizing some μ -dependent quantity.

In this chapter we will review principles belonging to the first class, while a new proposal will be discussed in Chapter 6. Then, Chapter 7 will introduce a principle of the second class and in Chapter 8 we will explore an extension of both.

5.1 The discrepancy Principle

As typical examples of first class strategies, we mention the *discrepancy principles* (DP) whose general form reads

$$\mathcal{C}(\hat{\mathbf{x}}(\mu^*)) : \quad \mathcal{D}(\mu^*; \mathbf{b}) = \Delta \in \mathbb{R}_{++}, \quad (5.1)$$

with the so-called *discrepancy function* $\mathcal{D}(\cdot; \mathbf{b}) : \mathbb{R}_+ \rightarrow \mathbb{R}_+$ defined by

$$\mathcal{D}(\mu; \mathbf{b}) := \text{KL}(\hat{\boldsymbol{\lambda}}(\mu); \mathbf{b}) = \sum_{i=1}^m \left(\mathcal{D}_i(\mu; b_i) := F(\hat{\lambda}_i(\mu); b_i) \right), \quad (5.2)$$

with function F defined in (4.10) and

$$\hat{\boldsymbol{\lambda}}(\mu) = \mathbf{g}(\mathbf{A} \hat{\mathbf{x}}(\mu)) + \mathbf{q}. \quad (5.3)$$

The equality in (5.1) is commonly referred to as the *discrepancy equation* while Δ is the so-called *discrepancy value* which changes when considering different DP versions. The DP in (5.1)-(5.3) formalizes a quite simple idea: choose the value μ^* of the regularization parameter μ in the \mathcal{R} -KL model (\mathcal{R} -KL) such that the value of the KL data fidelity term associated with the

solution $\widehat{\mathbf{x}}(\mu^*)$ is equal to a prescribed discrepancy value Δ . However, applying the DP in an effective manner in practice is not straightforward as several issues concerning the computational efficiency and, more importantly, the quality of the output solutions arise.

Regarding the computational efficiency, the solution function $\widehat{\mathbf{x}}(\mu^*)$ of model (R-KL) does not admit a closed-form expression (for the non smooth regularizers introduced in the previous chapter) and iterative solvers must be used to compute the restored image $\widehat{\mathbf{x}}$ associated with any μ . Hence, selecting μ^* by solving the scalar discrepancy equation defined in (5.1)-(5.3) as an efficient preliminary step and then computing the sought restored image $\widehat{\mathbf{x}}(\mu^*)$ by iteratively solving model (R-KL) only once is not feasible. This issue has been successfully addressed in [31], where the authors propose to automatically update μ along the iterations of the minimization algorithm used for solving the TV-KL model so as to satisfy (at convergence) a specific version of the general DP defined in (5.1)-(5.3).

As for the quality of the solution, even if an efficient algorithm is used for the computation, the obtained restored image $\widehat{\mathbf{x}}(\mu^*)$ may be of such low quality that it is of no practical use if the discrepancy value Δ in (5.1) is not suitably chosen. So the main question that needs to be answered is the following:

how can we identify the best choice for the discrepancy value Δ ?

In the theoretical hypothesis that the target image $\bar{\mathbf{x}}$ is known, so that $\bar{\boldsymbol{\lambda}} = \mathbf{g}(\mathbf{A}\bar{\mathbf{x}}) + \mathbf{q}$ is also known, one would select μ^* such that the value of the KL fidelity term associated with the solution $\widehat{\mathbf{x}}(\mu^*)$ is equal to the value of the KL fidelity term associated with $\bar{\mathbf{x}}$. This clearly does not guarantee that the obtained solution $\widehat{\mathbf{x}}(\mu^*)$ coincides with the target image $\bar{\mathbf{x}}$. However, by constraining $\widehat{\mathbf{x}}(\mu)$ to belong to the level set of the KL fidelity term containing $\bar{\mathbf{x}}$, this abstract strategy, which we refer to as the Theoretical DP (TDP), represents an oracle for the general DP in (5.1)-(5.3). The TDP is thus formulated as follows:

$$\begin{aligned} & \text{Select } \mu = \mu^* \in \mathbb{R}_+ \text{ such that } \mathcal{D}(\mu^*; \mathbf{b}) = \Delta^{(T)}, \\ & \text{with } \Delta^{(T)} := \sum_{i=1}^m (\delta^{(T)}(\bar{\lambda}_i) := F(\bar{\lambda}_i; b_i)), \quad \bar{\boldsymbol{\lambda}} = \mathbf{g}(\mathbf{A}\bar{\mathbf{x}}) + \mathbf{q}, \end{aligned} \quad (\text{TDP})$$

with function F defined in (4.10). Clearly, the value $\Delta^{(T)}$ can not be computed in practice as the original image $\bar{\mathbf{x}}$ is not available. Like in the case of the Morozov discrepancy principle for Gaussian noise, one could replace the scalar $\Delta^{(T)}$ with the expected value of the KL-fidelity term in (4.9) regarded as a function of the m -variate random variable \mathcal{B} . We will refer to this version of the DP as Exact (or Expected value) DP (EDP). In formula:

$$\begin{aligned} & \text{Select } \mu = \mu^* \in \mathbb{R}_+ \text{ such that } \mathcal{D}(\mu^*; \mathbf{b}) = \Delta^{(E)}(\mu^*), \\ & \text{with } \Delta^{(E)}(\mu) := \sum_{i=1}^m (\delta^{(E)}(\hat{\lambda}_i(\mu)) := E_{Y_i} [F(\hat{\lambda}_i(\mu); B_i)]), \\ & \text{and } \hat{\boldsymbol{\lambda}}(\mu) = \mathbf{g}(\mathbf{A}\hat{\mathbf{x}}(\mu)) + \mathbf{q}, \end{aligned} \quad (\text{EDP})$$

where $E_{Y_i} [F(\hat{\lambda}_i(\mu); B_i)]$ denotes the expected value of $F(\hat{\lambda}_i(\mu); B_i)$ regarded as a function of the Poisson-distributed random variable Y_i . Nonetheless, unlike the Gaussian noise case, the discrepancy value is not a constant but is a function $\Delta^{(E)}(\mu)$ of the regularization parameter μ , and deriving its analytic expression is a very hard task. A popular and widespread strategy, originally proposed in [25] for denoising purposes and extended in [26] to the image restoration task, replaces the exact expected value function $\Delta^{(E)}(\mu)$ with a constant approximation coming from truncating its Taylor series expansion. We will refer to this version of the DP as Approximate DP (ADP). It reads:

$$\begin{aligned} & \text{Select } \mu = \mu^* \in \mathbb{R}_+ \text{ such that } \mathcal{D}(\mu^*; \mathbf{b}) = \Delta^{(A)}, \\ & \text{with } \Delta^{(A)} := \sum_{i=1}^m (\delta^{(A)} := \frac{1}{2}) = \frac{m}{2}. \end{aligned} \quad (\text{ADP})$$

This strategy is widely used for its simplicity in terms of applicability, and for its good theoretical properties that guarantee the existence and uniqueness, under specific conditions, of the value μ^* satisfying the ADP discrepancy equation. Despite its extensive use due to the good performance achieved in the mid- and high-count regimes, the (ADP) is known to return poor quality results in the low-count Poisson regimes [33], i.e. when the number of photons hitting the image domain is small. In the next Chapter we will address in details its weaknesses and why they arise. In fact, already in [26] where the ADP was first extended to the image deblurring task, the authors state (in Remark 3) that the choice of the constant value $\delta^{(A)} = 1/2$ in (ADP) may not be “optimal” and suggest to replace it with $1/2 + \epsilon$, where ϵ is a small positive or negative real number. Since its proposal in [25], the ADP has been (and still is) widely used for variational image restoration (see, e.g., [34], [35]) and it can be regarded as the standard extension of the Morozov DP for Gaussian noise to the Poisson noise case. Then, some literature exists working on the ADP, e.g. by proposing, analyzing and testing its usage in KL-constrained variational models [30] or by analyzing it theoretically [28]. However, to the best of the authors’ knowledge, the only attempt to improve the ADP by giving a face to the ϵ adjustment to the approximate, constant discrepancy value $\delta^{(A)} = 1/2$ is the one in [33]. The authors in [33] correctly state that ϵ must not be a constant, but a function $\epsilon(\lambda)$ of the photon count level. However, they propose to take $\epsilon(\lambda)$ as the sum of the second to tenth terms of the same Taylor expansion used in [25]. As we will highlight later in the thesis, such expansion converges only for λ approaching $+\infty$, hence the choice in [33] cannot aspire to improve the performance of ADP in low-count regimes.

5.2 The Quadratic Discrepancy Principle

In the volume where the ADP has been originally proposed, a different selection criterion also inspired by the Morozov DP has been published. In-

stead of approximating the expected value of the KL fidelity term, in [32] the authors propose to directly approximate (quadratically) the KL term in such a way that the expected value of the approximate term admits a simple closed-form expression. The approximation reads

$$\text{KL}(\boldsymbol{\lambda}; \mathbf{b}) := \sum_{i \in \mathcal{J}} F(\lambda_i; b_i) \approx \text{KL}^{(Q)}(\boldsymbol{\lambda}; \mathbf{b}) := \sum_{i \in \mathcal{J}} F^{(Q)}(\lambda_i; b_i),$$

with the introduced function $F^{(Q)}$ (approximating the function F in (4.10)) defined by

$$F^{(Q)}(\lambda_i; b_i) = \left(\frac{b_i - \lambda_i}{\sqrt{\lambda_i}} \right)^2. \quad (5.4)$$

The quadratically approximated version $\mathcal{D}^{(Q)}$ of the exact discrepancy function \mathcal{D} defined in (5.2) and used in the (ADP) thus reads

$$\mathcal{D}^{(Q)}(\mu; \mathbf{b}) := \text{KL}^{(Q)}(\widehat{\boldsymbol{\lambda}}(\mu); \mathbf{b}) = \sum_{i \in \mathcal{J}} \left(\mathcal{D}_i^{(Q)}(\mu; y_i) := F^{(Q)}(\widehat{\lambda}_i(\mu); b_i) \right). \quad (5.5)$$

By regarding $F^{(Q)}$ in (5.4) as a function of the Poisson-distributed random variable Y_i with mean λ_i , it is immediate to prove that [38]

$$\delta^{(Q)} := \text{E} [F^{(Q)}(\lambda_i; B_i)] = 1.$$

Hence, the DP version proposed in [32], referred to as Quadratic DP (QDP), reads

$$\begin{aligned} &\text{Select } \mu = \mu^* \in \mathbb{R}_{++} \text{ such that } \mathcal{D}^{(Q)}(\mu^*; \mathbf{b}) = \Delta^{(Q)}, \\ &\text{with } \Delta^{(Q)} := \sum_{i \in \mathcal{J}} (\delta^{(Q)} = 1) = m. \end{aligned} \quad (\text{QDP})$$

5.3 Masked Principles

After noting that the (ADP) and (QDP) principles can yield sub-optimal results in case of many zero-photon pixels, in [31] the authors proposed masked versions of those principles based on simply discarding all pixels measuring zero photons - i.e., pixels for which $b_i = 0$. The masked versions

of the exact discrepancy function \mathcal{D} in (5.2) used in the (ADP) and of the quadratically approximated discrepancy function $\mathcal{D}^{(Q)}$ in (5.5) used in the (QDP) - indicated by \mathcal{D}_+ and $\mathcal{D}_+^{(Q)}$, respectively - take clearly the following forms

$$\mathcal{D}_+(\mu; \mathbf{b}) := \sum_{i \in \mathcal{J}_+} F(\widehat{\lambda}_i(\mu); b_i), \quad \mathcal{D}_+^{(Q)}(\mu; \mathbf{b}) := \sum_{i \in \mathcal{J}_+} F^{(Q)}(\widehat{\lambda}_i(\mu); b_i),$$

where \mathcal{J}_+ is defined in (4.11) as $\mathcal{J}_+ := \{i = 1, \dots, m \mid b_i > 0\}$ and the functions F and $F^{(Q)}$ are defined in (4.10) and (5.4), respectively. Hence, based on their unmasked versions in (ADP) and (QDP), the ADP and QDP masked biased principles proposed in [31] - that we shortly refer to as ADP-M and QDP-M, respectively - can be formulated as follows:

$$\begin{aligned} &\text{Select } \mu = \mu^* \in \mathbb{R}_{++} \text{ such that } \mathcal{D}_+(\mu^*; \mathbf{b}) = \Delta_+^{(A)}, \\ &\text{with } \Delta_+^{(A)} := \sum_{i \in \mathcal{J}_+} \left(\delta^{(A)} = \frac{1}{2} \right) = \frac{m_+}{2}, \end{aligned} \quad (\text{ADP-M})$$

$$\begin{aligned} &\text{Select } \mu = \mu^* \in \mathbb{R}_{++} \text{ such that } \mathcal{D}_+^{(Q)}(\mu^*; \mathbf{b}) = \Delta_+^{(Q)}, \\ &\text{with } \Delta_+^{(Q)} := \sum_{i \in \mathcal{J}_+} (\delta^{(Q)} = 1) = m_+, \end{aligned} \quad (\text{QDP-M})$$

where m_+ indicates the cardinality of set \mathcal{J}_+ , namely the number of non-zero pixels. The above principles will be further discussed in Chapter 8.

Chapter 6

The Nearly Exact Discrepancy Principle

In the previous chapter we introduced the general form of the discrepancy principle for Poisson noise (5.1) and discussed the choice of the discrepancy value Δ . In this chapter we will focus on the Approximate DP by extensively analyzing its properties and limits. Then we will propose a new version of the discrepancy principle and compare its performance with ADP, [39].

6.1 Limits of the Approximate Discrepancy Principle

The discrepancy principle proposed by Zanella et al. in [25] for Poisson image denoising and then extended to image restoration by Bertero et al. in [26] relies on Lemma 1 in [25] (whose proof has been completed in [27]), which we report below for completeness.

Lemma 6.1.1. Let B_λ be a Poisson random variable with expected value $\lambda \in \mathbb{R}_{++}$ and consider the function of B_λ defined by

$$F(B_\lambda) = \lambda - B_\lambda \ln \lambda + B_\lambda \ln B_\lambda - B_\lambda = B_\lambda \ln \left(1 + \frac{B_\lambda - \lambda}{\lambda} \right) + \lambda - B_\lambda. \quad (6.1)$$

Then, the following estimate of the expected value of $F(B_\lambda)$ holds true for large λ :

$$\delta^{(E)}(\lambda) = \mathbb{E}[F(B_\lambda)] = \delta^{(A)} + O\left(\frac{1}{\lambda}\right), \quad \delta^{(A)} = \frac{1}{2}. \quad (6.2)$$

Based on the estimate above, and implicitly assuming a sufficiently large λ (i.e., a sufficiently high-count Poisson regime) such that the $O(1/\lambda)$ term can be neglected, the exact DP outlined in (EDP) is replaced in [25, 26] by the approximation given in (ADP) and recalled below:

$$\Delta = \Delta^{(A)} = \sum_{i=1}^m \delta^{(A)} = \frac{m}{2}. \quad (6.3)$$

However, the ADP performs badly for low-count Poisson images. Our goal here is to highlight that the reason for that lies precisely in the constant approximation $\delta^{(E)}(\lambda) \approx \delta^{(A)}$ used in (ADP) and then propose a nearly exact DP based on a much less approximate estimate $\delta^{(NE)}(\lambda)$ of the expected value function $\delta^{(E)}(\lambda)$.

To this purpose, first we carry out a preliminary Montecarlo simulation aimed at highlighting the error associated with the approximation in (ADP). In particular, we consider a discrete set of λ values $\lambda_i \in [0, 8]$ and, for each λ_i , we generate pseudo-randomly a large number (10^6) of realizations of the Poisson random variable B_{λ_i} . Then, we compute the associated values of the function $F(B_{\lambda_i})$ defined in (6.1) and, finally, for each λ_i , we obtain an estimate $\widehat{\delta}^{(E)}(\lambda_i)$ of $\delta^{(E)}(\lambda_i)$ by calculating the sample mean of these function values. The results of this simulation are shown in Figure 6.1. In particular, in the left figure we report the computed estimates $\widehat{\delta}^{(E)}(\lambda_i)$ whereas in the right figure we report the percentage errors (with respect to the estimates) associated with using the constant value $\delta^{(A)} = 1/2$ as in the (ADP). The percentage error approaches $+\infty$ for λ tending to zero, is in the order of -10% for $\lambda \in [1, 4]$ then, as expected, decreases (quite slowly) to zero for λ tending to $+\infty$. The error is thus quite large for small λ and this can explain the bad performance of the (ADP) in the low-count Poisson regime.

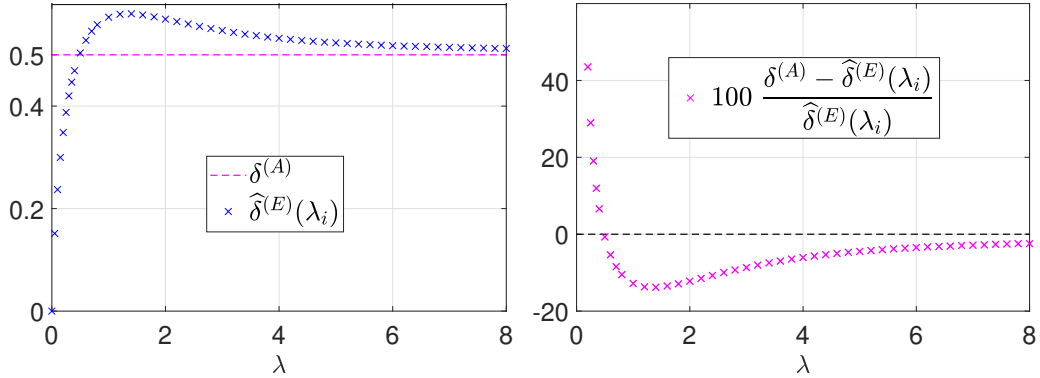


Figure 6.1: Comparison between the approximation $\delta^{(A)} = 1/2$ of $\delta^{(E)}(\lambda) = \mathbb{E}[F(B_\lambda)]$ used in the (ADP) proposed in [25, 26] and the Monte Carlo estimates $\widehat{\delta}^{(E)}(\lambda_i)$ for some $\lambda_i \in [0, 8]$.

In order to obtain a more accurate approximation or even an exact analytical expression for the expected value function $\delta^{(E)}(\lambda)$, we now retrace in detail the proof of Lemma 6.1.1 given in [25] (and completed in [27]) and check if the rough truncation carried out in [25, 27] can be avoided.

After noting that function $\ln(1 + \varphi)$ is C^∞ on its domain $(-1, +\infty)$ and considering its Taylor expansion around 0, the Taylor's theorem with remainder in integral form allows one to write:

$$\begin{aligned} \ln(1 + \varphi) &= \sum_{i=1}^N \frac{(-1)^{i+1}}{i} \varphi^i + r_N(\varphi) = \\ &= \varphi - \frac{1}{2}\varphi^2 + \frac{1}{3}\varphi^3 - \dots + \frac{(-1)^{N+1}}{N}\varphi^N + r_N(\varphi), \\ r_N(\varphi) &= (-1)^N \int_0^\varphi \frac{(\varphi - t)^N}{(1+t)^{N+1}} dt, \quad \forall \varphi \in (-1, +\infty). \end{aligned} \quad (6.4)$$

Replacing the expansion above with $\varphi = (B_\lambda - \lambda)/\lambda$ into the expression of

function F defined in (6.1), we get

$$\begin{aligned}
F(B_\lambda) &= B_\lambda \left(\sum_{i=1}^N \frac{(-1)^{i+1}}{i} \left(\frac{B_\lambda - \lambda}{\lambda} \right)^i + r_N(\varphi) \right) + \lambda - B_\lambda \\
&= B_\lambda r_N(\varphi) + (B_\lambda - \lambda + \lambda) \left(\sum_{i=1}^N \frac{(-1)^{i+1}}{i} \left(\frac{B_\lambda - \lambda}{\lambda} \right)^i \right) + \lambda - B_\lambda \\
&= B_\lambda r_N(\varphi) + (B_\lambda - \lambda) \left(\sum_{i=1}^N \frac{(-1)^{i+1}}{i} \left(\frac{B_\lambda - \lambda}{\lambda} \right)^i \right) \\
&\quad + \lambda \left(\sum_{i=1}^N \frac{(-1)^{i+1}}{i} \left(\frac{B_\lambda - \lambda}{\lambda} \right)^i \right) + \lambda - B_\lambda \\
&= B_\lambda r_N(\varphi) + \sum_{i=1}^N \frac{(-1)^{i+1}}{i} \frac{(B_\lambda - \lambda)^{i+1}}{\lambda^i} + \sum_{i=2}^N \frac{(-1)^{i+1}}{i} \frac{(B_\lambda - \lambda)^i}{\lambda^{i-1}} \\
&= B_\lambda r_N(\varphi) + \sum_{i=1}^N \frac{(-1)^{i+1}}{i} \frac{(B_\lambda - \lambda)^{i+1}}{\lambda^i} + \sum_{i=1}^{N-1} \frac{(-1)^i}{(i+1)} \frac{(B_\lambda - \lambda)^{i+1}}{\lambda^i} \\
&= B_\lambda r_N(\varphi) + \sum_{i=1}^{N-1} \left(\frac{(-1)^{i+1}}{i} + \frac{(-1)^i}{(i+1)} \right) \frac{(B_\lambda - \lambda)^{i+1}}{\lambda^i} + \frac{(-1)^{N+1}}{N} \frac{(B_\lambda - \lambda)^{N+1}}{\lambda^N} \\
&= B_\lambda r_N(\varphi) + \sum_{i=1}^{N-1} \frac{(-1)^{i+1}}{i(i+1)} \frac{(B_\lambda - \lambda)^{i+1}}{\lambda^i} + \frac{(-1)^{N+1}}{N} \frac{(B_\lambda - \lambda)^{N+1}}{\lambda^N}. \tag{6.5}
\end{aligned}$$

After noting that the only random quantity in (6.5) is B_λ , the expected value reads

$$\delta^{(E)}(\lambda) = \mathbb{E}[F(B_\lambda)] = \sum_{i=0}^{N-1} \omega_i^{(N)} \frac{\eta_{i+2}[B_\lambda]}{\lambda^{i+1}} + R_N(\lambda), \tag{6.6}$$

with coefficients $\omega_i^{(N)} \in \mathbb{Q}$, $i = 0, \dots, N-1$, and remainder function $R_N : \mathbb{R}_{++} \rightarrow \mathbb{R}$ given by

$$\omega_i^{(N)} = \begin{cases} \frac{(-1)^i}{(i+1)(i+2)} & \text{for } i = 0, \dots, N-2 \\ \frac{(-1)^i}{i+1} & \text{for } i = N-1 \end{cases}, \quad R_N(\lambda) = \mathbb{E} \left[B_\lambda r_N \left(\frac{Y_\lambda - \lambda}{\lambda} \right) \right], \tag{6.7}$$

and where

$$\eta_{i+2}[B_\lambda] = \mathbb{E} \left[(B_\lambda - \lambda)^{i+2} \right], \quad i = 0, 1, \dots$$

denote the central moments of order $i + 2$ of the Poisson random variable B_λ . It is well known (see [37], p.162) that these moments can be obtained by the recursive formula

$$\eta_1[B_\lambda] = 0, \quad \eta_2[B_\lambda] = \lambda, \quad \eta_{i+2}[B_\lambda] = \lambda \left(\frac{d\eta_{i+1}[B_\lambda]}{d\lambda} + (i+1)\eta_i[B_\lambda] \right). \quad (6.8)$$

After noting that in (6.6) only moments $\eta_{i+2}[B_\lambda]$ with $i \geq 0$ are present and that they are all divided by λ , it is easy to verify that by applying (6.8) one gets the following general algebraic polynomial expression

$$\mathcal{P}_i(\lambda) := \frac{\eta_{i+2}[B_\lambda]}{\lambda} = \sum_{j=0}^{d_i} \vartheta_i^{(j)} \lambda^j, \quad i = 0, 1, \dots, \quad (6.9)$$

where $\vartheta_i^{(j)}$ are all integer coefficients with $\vartheta_i^{(0)} = 1$ for any $i = 0, 1, \dots$, and where the degrees d_i of polynomials $\mathcal{P}_i(\lambda)$ are given by

$$d_i = \left\lfloor \frac{i}{2} \right\rfloor = 0, 0, 1, 1, 2, 2, \dots \text{ for } i = 0, 1, 2, 3, 4, 5, \dots, \quad (6.10)$$

where $\lfloor \cdot \rfloor$ denotes the floor function. The first 8 polynomials $\mathcal{P}_i(\lambda)$, $i = 0, \dots, 7$, read

$$\begin{aligned} \mathcal{P}_0(\lambda) &= 1, & \mathcal{P}_1(\lambda) &= 1, \\ \mathcal{P}_2(\lambda) &= 1 + 3\lambda, & \mathcal{P}_3(\lambda) &= 1 + 10\lambda, \\ \mathcal{P}_4(\lambda) &= 1 + 25\lambda + 15\lambda^2, & \mathcal{P}_5(\lambda) &= 1 + 56\lambda + 105\lambda^2, \\ \mathcal{P}_6(\lambda) &= 1 + 119\lambda + 490\lambda^2 + 105\lambda^3, & \mathcal{P}_7(\lambda) &= 1 + 246\lambda + 1918\lambda^2 + 1260\lambda^3. \end{aligned}$$

By replacing the expressions of $\mathcal{P}_i(\lambda)$ given in (6.9) into (6.6), one gets the following general formula

$$\delta^{(E)}(\lambda) = \mathbb{E}[F(B_\lambda)] = \sum_{i=0}^{N-1} \left(Q_i^{(N)}(\lambda) := \sum_{j=0}^{d_i} \frac{\psi_i^{(N,j)}}{\lambda^{i-j}} \right) + R_N(\lambda) \quad (6.11)$$

where the coefficients $\psi_i^{(N,j)} \in \mathbb{Q}$ of the rational polynomials $Q_i^{(N)}(\lambda)$ in (6.11) read

$$\psi_i^{(N,j)} = \omega_i^{(N)} \vartheta_i^{(j)}, \quad i = 0, 1, \dots, N-1, \quad j = 0, 1, \dots, d_i,$$

with $\omega_i^{(N)}$ given in (6.7) and $\vartheta_i^{(j)}$ defined in (6.9).

After noting that from (6.10) it follows that $d_i \leq i$ for any $i = 0, 1, \dots$, it is a matter of simple algebra to verify that (6.11) can be equivalently and more compactly rewritten as

$$\delta^{(E)}(\lambda) = \mathbb{E}[F(B_\lambda)] = \sum_{i=0}^{N-1} \frac{\gamma_i^{(N)}}{\lambda^i} + R_N(\lambda), \quad (6.12)$$

with $\gamma_i^{(N)} \in \mathbb{Q}$ computable coefficients. In particular, for $N = 1, \dots, 9$, we have

$$\begin{aligned} \delta^{(E)}(\lambda) &= 1 + R_1(\lambda) \\ &= \frac{1}{2} - \frac{1}{2\lambda} + R_2(\lambda) \\ &= \frac{1}{2} + \frac{5}{6\lambda} + \frac{1}{3\lambda^2} + R_3(\lambda) \\ &= \frac{1}{2} + \frac{1}{12\lambda} - \frac{29}{12\lambda^2} - \frac{1}{4\lambda^3} + R_4(\lambda) \\ &= \frac{1}{2} + \frac{1}{12\lambda} + \frac{31}{12\lambda^2} + \frac{99}{20\lambda^3} + \frac{1}{5\lambda^4} + R_5(\lambda) \\ &= \frac{1}{2} + \frac{1}{12\lambda} + \frac{3}{12\lambda^2} - \frac{1003}{60\lambda^3} - \frac{93}{10\lambda^4} - \frac{1}{6\lambda^5} + R_6(\lambda) \\ &= \frac{1}{2} + \frac{1}{12\lambda} + \frac{1}{12\lambda^2} + \frac{797}{60\lambda^3} + \frac{687}{10\lambda^4} + \frac{713}{42\lambda^5} + \frac{1}{7\lambda^6} + R_7(\lambda) \\ &= \frac{1}{2} + \frac{1}{12\lambda} + \frac{1}{12\lambda^2} + \frac{19}{120\lambda^3} - \frac{3001}{20\lambda^4} - \frac{39925}{168\lambda^5} - \frac{1721}{56\lambda^6} - \frac{1}{8\lambda^7} + R_8(\lambda) \\ &= \frac{1}{2} + \frac{1}{12\lambda} + \frac{1}{12\lambda^2} + \frac{19}{120\lambda^3} + \frac{1899}{20\lambda^4} + \frac{516833}{504\lambda^5} + \frac{126829}{168\lambda^6} + \frac{4007}{72\lambda^7} \\ &\quad + \frac{1}{9\lambda^8} + R_9(\lambda) \end{aligned} \quad (6.13)$$

from which we note how, as the truncation order N increases, the coefficients $\gamma_i^{(N)}$ stabilize at some values, that we denote by $\gamma_i^{(\infty)}$. Unfortunately, we are not able to obtain an explicit analytical expression for the sequence of coefficients $\gamma_i^{(\infty)}$ (as we are not able to get explicit analytic expressions for the coefficients $\vartheta_i^{(j)}$ defining the central moments of a Poisson random variable). By means of the Matlab symbolic toolbox, we were able to compute the first 34 coefficients $\gamma_i^{(\infty)}$, $i = 0, \dots, 33$, shown (in logarithmic scale) in

Figure 6.2(left). Determining the subsequent coefficients becomes unfeasible due to the huge computation time required. Hence, the following short discussion must be regarded as conjectural as it relies on the assumption that the behaviour of coefficients $\gamma_i^{(\infty)}$, $i = 34, 35, \dots$, can be smoothly extrapolated from the first 34 coefficients shown in Figure 6.2(left). These first 34 coefficients indicate that the coefficient sequence is positive and strictly increasing for $i \geq 2$. This implies that making the truncation order N tend to $+\infty$, the (infinite) weighted geometric series in (6.12) is divergent for $\lambda \leq 1$. Even without analyzing the case $\lambda > 1$, we can state that an analytical form for function $\delta^{(E)}(\lambda)$ in the low-count Poisson regime is very unlikely to be obtainable as the sum of the series in (6.12). In fact, there will be very likely at least one pixel such that $\lambda_i \leq 1$.

We believe it is worth concluding this section by pointing out the theoretical reason for non-convergence of the series in (6.12). Function $\ln(1 + \varphi)$ is analytical at $\varphi = 0$, but its Maclaurin series converges (pointwise to the function) only for $\varphi \in (-1, 1]$. Hence, as N tends to $+\infty$, the Taylor series expansion in (6.5) converges to the function $F(B_\lambda)$ only for $\varphi = (B_\lambda - \lambda)/\lambda \in (-1, 1] \iff B_\lambda \in (0, 2\lambda]$. But B_λ in (6.6) represents a Poisson random variable with parameter λ . Hence, for N tending to $+\infty$, the series in (6.6) converges to the function $\delta^{(E)}(\lambda) = E[F(B_\lambda)]$ only if the random variable B_λ satisfies

$$P(0 < B_\lambda \leq 2\lambda) = 1 \iff \sum_{i=1}^{\lfloor 2\lambda \rfloor} P_{B_\lambda}(i) = 1. \quad (6.14)$$

From Figure 6.2(right), where we plot the probability in (6.14) as a function of λ , one can notice that condition (6.14) for convergence of the series in (6.6) is fulfilled asymptotically for λ approaching $+\infty$ but it is not satisfied at all for small λ values.

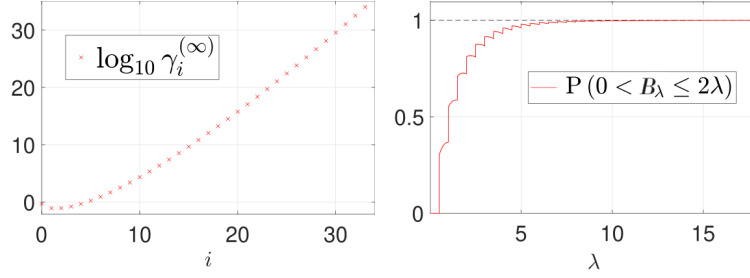


Figure 6.2: Visual representation of the first 34 terms of the sequence of coefficients $\gamma_i^{(\infty)}$, $i = 0, 1, \dots$, in (6.12) (left) and the behaviour of the probability measure defined in (6.14) as a function of λ (right).

6.2 The New nearly exact discrepancy principle

Since it is not possible to derive analytically the expression of function $\delta^{(E)}(\lambda)$ in (6.2), the goal in this section is to compute a nearly exact estimate $\delta^{(NE)}(\lambda)$ of function $\delta^{(E)}(\lambda)$ based on a simple Montecarlo simulation approach analogous to that used in the previous section. Based on the expected shape of function $\delta^{(E)}(\lambda)$ - see Figure 6.1(left) - here we consider a set of 1385 unevenly distributed λ values $\lambda_i \in [0, 250]$, namely

$$\lambda_i \in \{0, 0.01, 0.02, \dots, 5.99, 6, 6.1, 6.2, \dots, 65.9, 66, 67, 68, \dots, 249, 250\} .$$

This set comes from the union of three subsets of equally-spaced λ values, namely from 0 to 6 with step 0.01, from 6 to 66 with step 0.1 and from 66 to 250 with step 1. For each λ_i , we generate pseudo-randomly a very large number $S = 5 \times 10^7$ of samples $b_i^{(j)}$, $j = 1, \dots, S$, of the Poisson random variable B_{λ_i} , then we compute the associated values $f_i^{(j)}$, $j = 1, \dots, S$, of the function $F(B_{\lambda_i})$ defined in (6.1) and, finally, we calculate the sample mean $\widehat{\delta}^{(E)}(\lambda_i)$ and variance v_i of these function values. In formula,

$$\begin{aligned} b_i^{(j)} = \text{Pois}(B_{\lambda_i}), \quad j = 1, \dots, S &\implies f_i^{(j)} = F(b_i^{(j)}), \quad j = 1, \dots, S \\ \implies \widehat{\delta}^{(E)}(\lambda_i) = \frac{1}{S} \sum_{j=1}^S f_i^{(j)}, \quad v_i = \frac{1}{S-1} \sum_{j=1}^S (f_i^{(j)} - \widehat{\delta}^{(E)}(\lambda_i))^2 &(6.15) \end{aligned}$$

Notation for the sample means come from them representing estimates of the sought theoretical means $\delta^{(E)}(\lambda_i) = \mathbb{E}[F(B_{\lambda_i})]$, $i = 1, \dots, 1385$. The obtained values $(\lambda_i, \widehat{\delta}^{(E)}(\lambda_i))$ and (λ_i, v_i) are shown (blue crosses) in the first and second row of Figure 6.3, respectively. It is well known that $\widehat{\delta}^{(E)}(\lambda_i)$ and v_i represent unbiased estimators of the mean and standard deviation of the random variable $F(B_{\lambda_i})$ and that, according to the central limit theorem, for a very large number S of samples (which is definitely our case) the sample mean $\widehat{\delta}^{(E)}(\lambda_i)$ can be regarded as a realization of a Gaussian random variable with mean the theoretical mean $\delta^{(E)}(\lambda_i)$ of the random variable $F(B_{\lambda_i})$ and variance the sample variance v_i divided by the number of samples S . In formulas,

$$\widehat{\delta}^{(E)}(\lambda_i) = \text{Gauss}\left(\delta^{(E)}(\lambda_i), \frac{v_i}{S}\right). \quad (6.16)$$

We now want to fit a parametric model $f(\lambda; \mathbf{c})$, with \mathbf{c} the parameter vector, to the obtained Montecarlo-simulated data points $(\lambda_i, \widehat{\delta}^{(E)}(\lambda_i))$, $i = 1, \dots, 1385$. First, in accordance with the trend of these data - see the blue crosses in the first row of Fig. 6.3 - and recalling the expected asymptotic behaviour of function $\delta^{(E)}(\lambda)$ for λ approaching $+\infty$ - see the discussion in Section 6.1, in particular the first two terms of the expansion in (6.13) - we choose a model of the form

$$f(\lambda; \mathbf{c}) = \frac{1}{2} + \epsilon(\lambda; \mathbf{c}), \quad (6.17)$$

with function h exhibiting the following properties:

$$\epsilon \in C^0(\mathbb{R}_+), \quad \epsilon(0; \mathbf{c}) = -\frac{1}{2}, \quad \epsilon(\lambda; \mathbf{c}) \sim \frac{1}{12\lambda} \text{ for } \lambda \rightarrow +\infty.$$

Then, with the aim of achieving a good trade off between the model's ability to accurately fit data and the computational efficiency of its evaluation, we choose the following rational form for function ϵ :

$$\epsilon(\lambda; \mathbf{c}) = \frac{\lambda^2 + c_1\lambda + c_2}{12\lambda^3 + c_3\lambda^2 + c_4\lambda - 2c_2}. \quad (6.18)$$

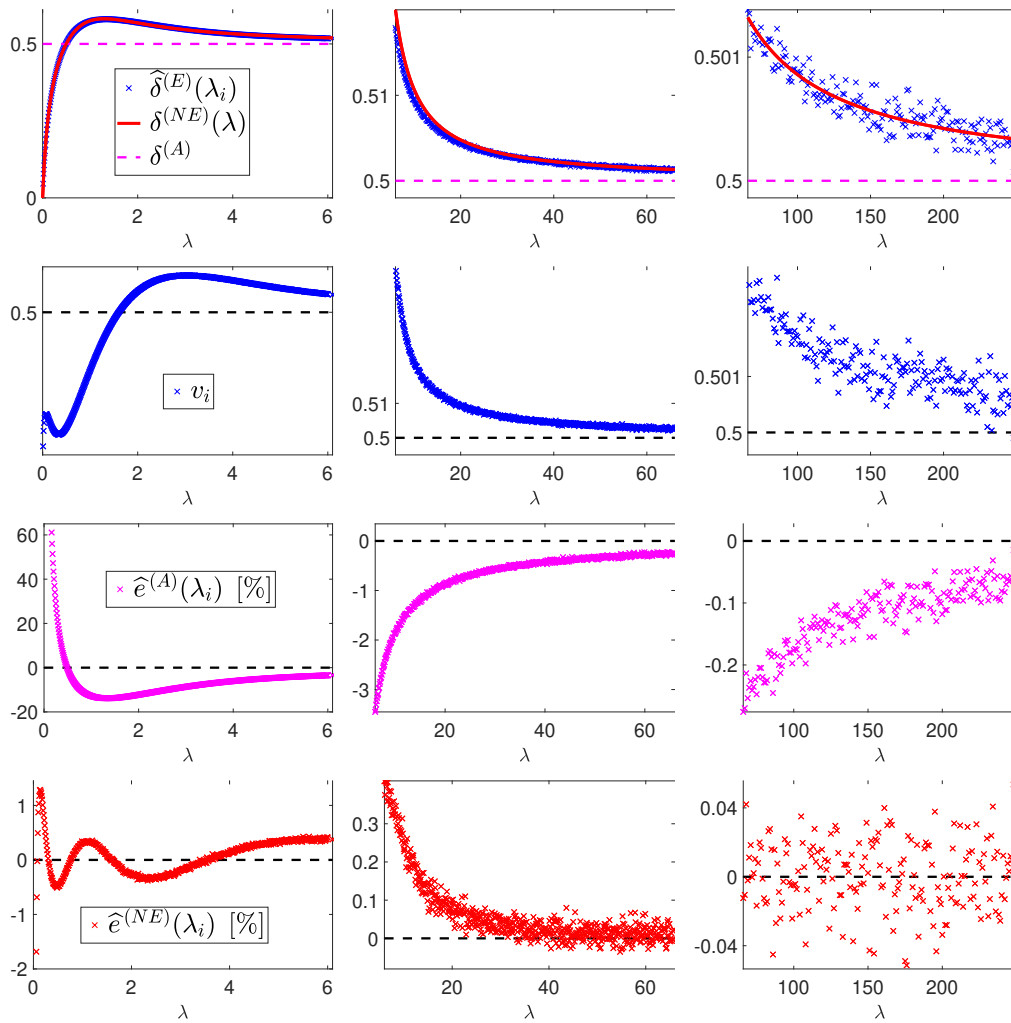


Figure 6.3: Results of Monte Carlo simulation and weighted least squares fitting for $\lambda \in [0, 6]$ (first column), $\lambda \in [6, 66]$ (second column) and $\lambda \in [66, 250]$ (third column).

Thanks to (6.16), fitting model f in (6.17) with ϵ as in (6.18) can be obtained via a Maximum Likelihood (ML) estimation of the parameter vector $\mathbf{c} = (c_1, c_2, c_3, c_4) \in \mathbb{R}^4$. In fact, according to (6.16), the likelihood reads

$$\begin{aligned} \mathcal{L}(\mathbf{c}) &= \prod_{i=1}^S p(\widehat{\delta}^{(E)}(\lambda_i) | c) = \prod_{i=1}^S \frac{1}{\sqrt{2\pi v_i/S}} \exp\left(-\frac{1}{2} \frac{(\widehat{\delta}^{(E)}(\lambda_i) - f(\lambda_i; \mathbf{c}))^2}{v_i/S}\right) \\ &= \frac{1}{(2\pi/S)^{\frac{S}{2}} \prod_{i=1}^S \sqrt{v_i}} \exp\left(-\frac{S}{2} \sum_{i=1}^S \frac{(\widehat{\delta}^{(E)}(\lambda_i) - f(\lambda_i; \mathbf{c}))^2}{v_i}\right), \end{aligned} \quad (6.19)$$

and the ML estimate $\mathbf{c}^{(ML)}$ of \mathbf{c} can be computed as follows

$$\mathbf{c}^{(ML)} \in \arg \max_{\mathbf{c} \in \mathbb{R}^4} \mathcal{L}(\mathbf{c}) = \arg \min_{\mathbf{c} \in \mathbb{R}^4} \{-\ln \mathcal{L}(\mathbf{c})\} = \arg \min_{\mathbf{c} \in \mathbb{R}^4} \sum_{i=1}^S w_i (d_i - h(\lambda_i; \mathbf{c}))^2, \quad (6.20)$$

where we dropped constants (with respect to the optimization variable \mathbf{c}) and defined

$$w_i := \frac{1}{v_i}, \quad d_i := \widehat{\delta}^{(E)}(\lambda_i) - \frac{1}{2}, \quad i = 1, \dots, S.$$

Problem (6.20) is a nonlinear (in particular, rational) weighted least-squares problem. The cost function is non-convex and local minimizers exist. We compute an estimate $\widehat{\mathbf{c}}$ of $\mathbf{c}^{(ML)}$ by solving (6.20) via the iterative trust-region algorithm 1000 times starting from 1000 different initial guesses $\mathbf{c}^{(0)}$ randomly sampled from a uniform distribution with support $[-20, 20]^4$ and then picking up the solution $\widehat{\mathbf{c}}$ yielding the minimum cost function value. The obtained parameter estimate is as follows

$$\widehat{\mathbf{c}} = (\widehat{c}_1, \widehat{c}_2, \widehat{c}_3, \widehat{c}_4) = (+2.5792, -1.5205, -5.6244, +17.9347). \quad (6.21)$$

We thus define the nearly-exact estimate $\delta^{(NE)}(\lambda)$ of the theoretical expected value function $\delta^{(E)}(\lambda) = \mathbb{E}[F(B_\lambda)]$ as the parametric function f defined in (6.17), (6.18) with parameter vector \mathbf{c} equal to $\widehat{\mathbf{c}}$ given in (6.21). In formula,

$$\delta^{(NE)}(\lambda) := f(\lambda; \widehat{\mathbf{c}}) = \frac{1}{2} + \epsilon(\lambda; \widehat{\mathbf{c}}) = \frac{1}{2} + \frac{\lambda^2 + 2.5792\lambda - 1.5205}{12\lambda^3 - 5.6244\lambda^2 + 17.9347\lambda + 3.0410}. \quad (6.22)$$

In the first row of Figure 6.3 we plot the constant approximate function $\delta^{(A)}$ and the obtained nearly-exact function $\delta^{(NE)}(\lambda)$, whereas in the third and fourth row of Figure 6.3 we report the errors $\widehat{e}^{(A)}(\lambda_i)$ and $\widehat{e}^{(NE)}(\lambda_i)$, respectively. They are defined by

$$\widehat{e}^{(X)}(\lambda_i) = 100 \times \frac{\delta^{(X)}(\lambda_i) - \widehat{\delta}^{(E)}(\lambda_i)}{\widehat{\delta}^{(E)}(\lambda_i)} \quad i = 1, 2, \dots, 1385, \quad X \in \{A, NE\},$$

and represent the percentage errors associated with using the approximations $\delta^{(A)}$ and $\delta^{(NE)}(\lambda)$ with respect to the very accurate Montecarlo estimates $\widehat{\delta}^{(E)}(\lambda_i)$ of the true underlying expected values $\delta^{(E)}(\lambda_i) = \mathbb{E}[F(B_{\lambda_i})]$. One can notice that $|\widehat{e}^{(NE)}(\lambda_i)|$ is about 20 times smaller than $|\widehat{e}^{(A)}(\lambda_i)|$ for $\lambda \in [0, 6]$ (first column of Figure 6.3) and about 10 times less for $\lambda \in [6, 250]$ (second and third column Figure 6.3). In particular, in the low-count Poisson regime (which we can roughly associate with $\lambda \in [0, 6]$) the proposed nearly-exact estimate of the theoretical expected value function $\delta^{(E)}(\lambda)$ yields a percentage error in the order of 0.5%, whereas the constant approximation used in [25, 26] leads to a percentage error in the order of 10%. Such a large error is the reason for the bad performance of the (ADP) in the low-count regime. We thus propose the following nearly exact DP (NEDP):

$$\begin{aligned} &\text{Select } \mu = \mu^* \in \mathbb{R}_+ \text{ such that } \mathcal{D}(\mu^*; \mathbf{y}) = \Delta^{(NE)}(\mu^*), \\ &\text{with } \Delta^{(NE)}(\mu) = \sum_{i=1}^m \left(\delta^{(NE)}(\widehat{\lambda}_i(\mu)) \right) = \frac{m}{2} + \sum_{i=1}^m \epsilon(\widehat{\lambda}_i(\mu); \widehat{\mathbf{c}}), \quad (\text{NEDP}) \\ &\quad \widehat{\boldsymbol{\lambda}}(\mu) = \mathbf{g}(\mathbf{A}\widehat{\mathbf{x}}(\mu)) + \mathbf{q}, \end{aligned}$$

with function ϵ and parameter vector $\widehat{\mathbf{c}}$ given in (6.18) and (6.21), respectively.

6.3 Numerical Results

In this section, we evaluate the performance of the proposed NEDP in (NEDP) for the automatic selection of the regularization parameter μ

in CT reconstruction and image restoration variational models of the TV-KL form in (TV-KL). Our approach is compared with the TDP and the ADP in (TDP) and (ADP), respectively. For each criterion, we are solving the TV-KL model for a fine grid of regularization parameters μ using the ADMM-based scheme described in section 10.1. The μ -values selected by the TDP, the ADP and the NEDP applied *a posteriori* will be denoted by $\mu^{(T)}, \mu^{(A)}, \mu^{(NE)}$, respectively. For a quantitative evaluation, the accuracy of the reconstructed images $\hat{\mathbf{x}}(\mu)$ with respect to the original image $\bar{\mathbf{x}}$ is measured by means of two scalar metrics, the Structural Similarity Index (SSIM) [36] and the Signal-to-Noise-Ratio (SNR) defined by

$$\text{SNR}(\hat{\mathbf{x}}, \bar{\mathbf{x}}) = 10 \log_{10} \frac{\|\bar{\mathbf{x}} - \mathbb{E}[\bar{\mathbf{x}}]\|_2^2}{\|\bar{\mathbf{x}} - \hat{\mathbf{x}}\|_2^2}, \quad (6.23)$$

where $\mathbb{E}[\bar{\mathbf{x}}]$ denotes the mean intensity of the original image $\bar{\mathbf{x}}$. For the image restoration case we will consider the Improved-Signal-to-Noise Ratio (ISNR), defined by

$$\text{ISNR}(\hat{\mathbf{x}}, \bar{\mathbf{x}}) = 10 \log_{10} \frac{\|\bar{\mathbf{x}} - \mathbf{b}\|_2^2}{\|\bar{\mathbf{x}} - \hat{\mathbf{x}}\|_2^2}. \quad (6.24)$$

For all tests, the iterations of the ADMM-based scheme in 10.1 are stopped as soon as

$$\delta_{\mathbf{x}}^{(k)} = \frac{\|\mathbf{x}^{(k)} - \mathbf{x}^{(k-1)}\|_2}{\|\mathbf{x}^{(k-1)}\|_2} < 10^{-5}, \quad k \in \mathbb{N} \setminus \{0\}, \quad (6.25)$$

and the ADMM penalty parameter $\gamma \in \mathbb{R}_{++}$ is manually set to achieve fast convergence.

6.3.1 CT Reconstruction

For the CT reconstruction problem we consider the test images **Shepp Logan** (500×500 , pixel size = 0.2mm) and **brain** (238×253 , pixel size=0.4mm), with pixel values between 0 and 1, shown Figures 6.4. The acquisition process of the fan beam CT setup, i.e. the projection operator \mathbf{A} , is built using the ASTRA Toolbox [40] with the following parameters: 180 equally spaced angles of projections (from 0 to 2π), a detector with 500 pixels (detector

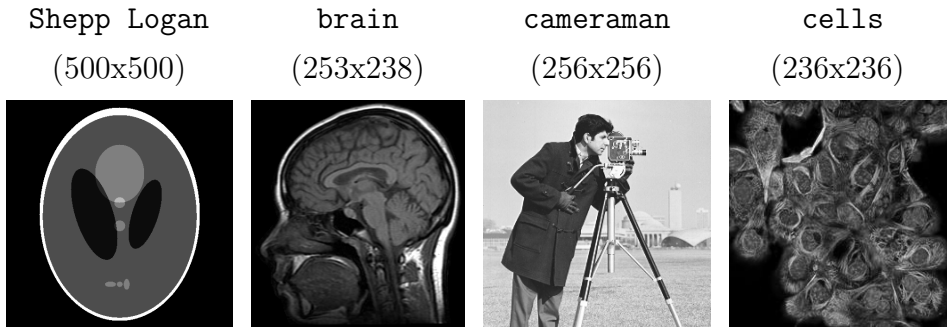


Figure 6.4: Gray scale test images considered for the numerical experiments.

pixel size = $1/3\text{mm}$), distance between the source and the center of rotation equal to 300mm, distance between the center of rotation and the detector array set equal to 200mm. Then we compute $I_0 e^{-\mathbf{A}\bar{\mathbf{x}}}$ with I_0 being a scalar factor representing the maximum emitted photon counts, i.e., the maximum number of photons that can reach each detector pixel if the X-rays are not attenuated. In particular, we consider seven different values of I_0

$$I_0 \in \{3, 5, 10, 20, 50, 100, 1000\},$$

each of which refers to a different level of noise. In the CT tests, we consider the background emission $\mathbf{q} = \mathbf{0}$ so that the solution of (10.20) can be expressed in closed-form in terms of the Lambert function. We thus obtain the observation $\mathbf{b} = \mathbf{Pois}(\bar{\boldsymbol{\lambda}})$ by sampling from a m -variate independent Poisson random process with mean vector $\bar{\boldsymbol{\lambda}}$.

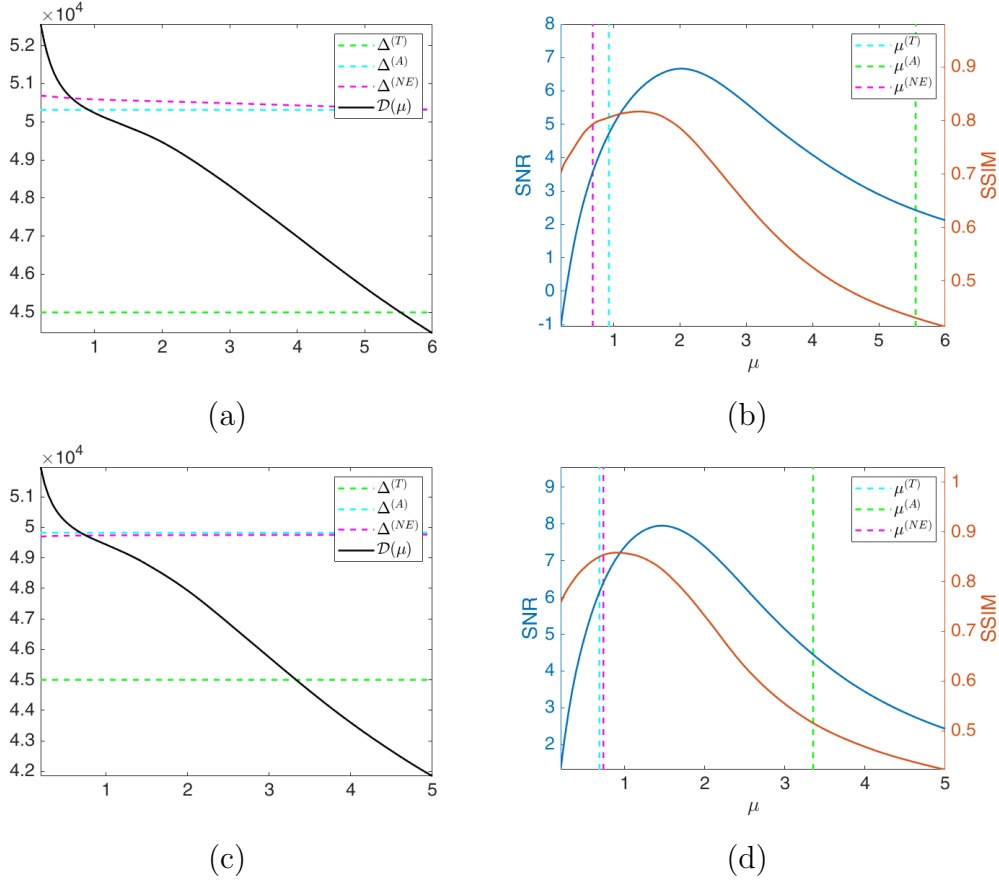
The black solid curves plotted in Figures 6.5(a), 6.5(c) represent the function $\mathcal{D}(\mu; \mathbf{b})$ as defined in (5.2) for the image Shepp Logan with $I_0 = 5$ (first row) and $I_0 = 10$ (second row). They have been computed by solving the TV-KL model in (TV-KL) for a fine grid of different μ -values, and then calculating $\mathcal{D}(\mu; \mathbf{b})$ for each μ . The horizontal dashed cyan and green lines represent the constant discrepancy values $\Delta^{(T)}$ and $\Delta^{(A)}$ used in (TDP) and (ADP), respectively, while the dashed magenta curve represents the discrepancy value function $\Delta^{(NE)}(\mu)$ defined in (NEDP). We remark that $\Delta^{(NE)}(\mu)$ has been obtained in the same way as $\mathcal{D}(\mu; \mathbf{b})$, i.e. by computing the expression in

(NEDP) for each μ of the selected fine grid. One can clearly observe that the intersection points between the curve $\Delta^{(NE)}(\mu)$ and the function $\mathcal{D}(\mu; \mathbf{b})$ and between the line representing $\Delta^{(T)}$ and $\mathcal{D}(\mu; \mathbf{b})$ are very close, and both at a significant distance from the intersection point detected by $\Delta^{(A)}$.

In Figures 6.5(b), 6.5(d), we show the SNR and SSIM values achieved for different μ -values with $I_0 = 5$ and $I_0 = 10$. The vertical cyan, green and magenta lines correspond to the μ -values detected by the intersection of $\mathcal{D}(\mu; \mathbf{b})$ and $\Delta^{(T)}$, $\Delta^{(A)}$, $\Delta^{(NE)}(\mu)$, respectively. As a reflection of the behaviour of the discrepancy function and of the three curves, the SNR/SSIM corresponding to $\mu^{(T)}$ and $\mu^{(NE)}$ are very close between each other. We also highlight that, when considering the more severe blur case, the ADP selects a larger μ -value which returns lower SNR and SSIM values.

As a further analysis, in the bottom of Figure 6.5 we report the output μ -values, the SNR and the SSIM values for the 7 I_0 -values considered obtained by the ADP (first column) and the NEDP (second column). To facilitate the comparison, we also report in blue/red the increments/decrements of the SNR and SSIM achieved by our method with respect to the approximate criterion. Notice that the NEDP outperforms the ADP both in terms of SNR and SSIM for the low-count acquisitions. However, when I_0 increases, the two methods behave very similarly, with the SNR and SSIM values obtained by the ADP being slightly larger than those obtained by the NEDP. In accordance with this analysis, the output $\mu^{(A)}$ and $\mu^{(NE)}$ are significantly different in low-count regimes, similar in mid-count regimes and particularly close in high-count regimes. Notice that this behaviour can be easily explained in light of the analysis carried out in Section 6.1, where we have shown that the approximation provided by $\Delta^{(A)}$ gets more and more accurate as the number of pixels with large values increases.

For a visual comparison, in Figure 6.6 we show the collected data (left column), the restorations via ADP (middle column) and via NEDP (right column) for different photon count regimes, ranging from very low to very high. As already observed from the SNR and SSIM values reported at the



I_0	ADP			NEDP			Difference	
	$\mu^{(A)}$	SNR	SSIM	$\mu^{(NE)}$	SNR	SSIM	SNR	SSIM
3	5.028	3.285	0.510	0.727	1.835	0.756	-1.450	+0.246
5	5.555	2.899	0.455	0.684	3.569	0.793	+0.670	+0.338
10	3.351	4.449	0.515	0.773	6.403	0.853	+1.954	+0.338
20	1.522	8.976	0.755	0.530	8.550	0.889	-0.426	+0.134
50	0.564	11.626	0.974	0.352	10.717	0.992	-0.909	+0.018
100	0.322	13.141	0.994	0.261	12.698	0.945	-0.443	-0.049
1000	0.091	17.837	0.997	0.091	17.837	0.997	0.000	0.000

Figure 6.5: Test image Shepp Logan. *Top*: discrepancy curve (left) and SNR/SSIM values achieved for different μ -values with $I_0 = 5$ and $I_0 = 10$ (first and second column respectively). *Bottom*: output μ -values and SNR/SSIM values obtained by the ADP and the NEDP for the different photon counts I_0 .

bottom of Figure 6.5, we notice that for low-count acquisitions the μ -value selected by the ADP does not allow for a proper regularization, so that NEDP clearly outperforms the competitor. However, starting from $I_0 = 20$ the two approaches return similar output images.

For the second test image **brain**, we report in Figure 6.7 the behaviour of the discrepancy function $\mathcal{D}(\mu; \mathbf{b})$ and of the SNR/SSIM curves obtained by applying the TDP, the ADP and the NEDP, for $I_0 = 5$ and $I_0 = 10$. Also in this case the NEDP and the TDP behave similarly and they almost achieve the maximum of the SSIM curves, while being more distant to the maximum of SNR. In contrast, $\mu^{(A)}$ appears to be overestimated with respect to the optimal μ - that can be intended as the one maximizing either the SNR or the SSIM, but is closer to the SNR maximum.

From the table reported at the bottom of Figure 6.7, we observe that the proposed μ -selection criterion does not outperforms ADP in terms of SNR, while its SSIM values are higher than ADP up to $I_0 = 20$. The restored images in Figures 6.8 reflect the values recorded in the table as for $I_0 \leq 20$ ADP returns noisier reconstructions (higher values of the selected $\mu^{(A)}$) than NEDP, while their behavior is similar in the high count regime.

6.3.2 Image Restoration

For the Image restoration problem we consider the two test images **cameraman** and **cells**, each with pixel values between 0 and 1, shown in Figure 6.4. The acquisition process has been simulated as follows. First, the original image is multiplied by a factor $\kappa \in \mathbb{R}_{++}$ representing the maximum emitted photon count, i.e. the maximum expected value of number of photons emitted by the scene and hitting the image domain. Clearly, the lower κ , the lower the SNR of the observed noisy image and the more difficult the image restoration problem. For each image, several values κ ranging from 3 to 1000 have been considered. Then, the resulting images have been corrupted by space-invariant Gaussian blur, with blur kernel generated by the Matlab routine `fspecial`, which is characterized by two parameters, namely the

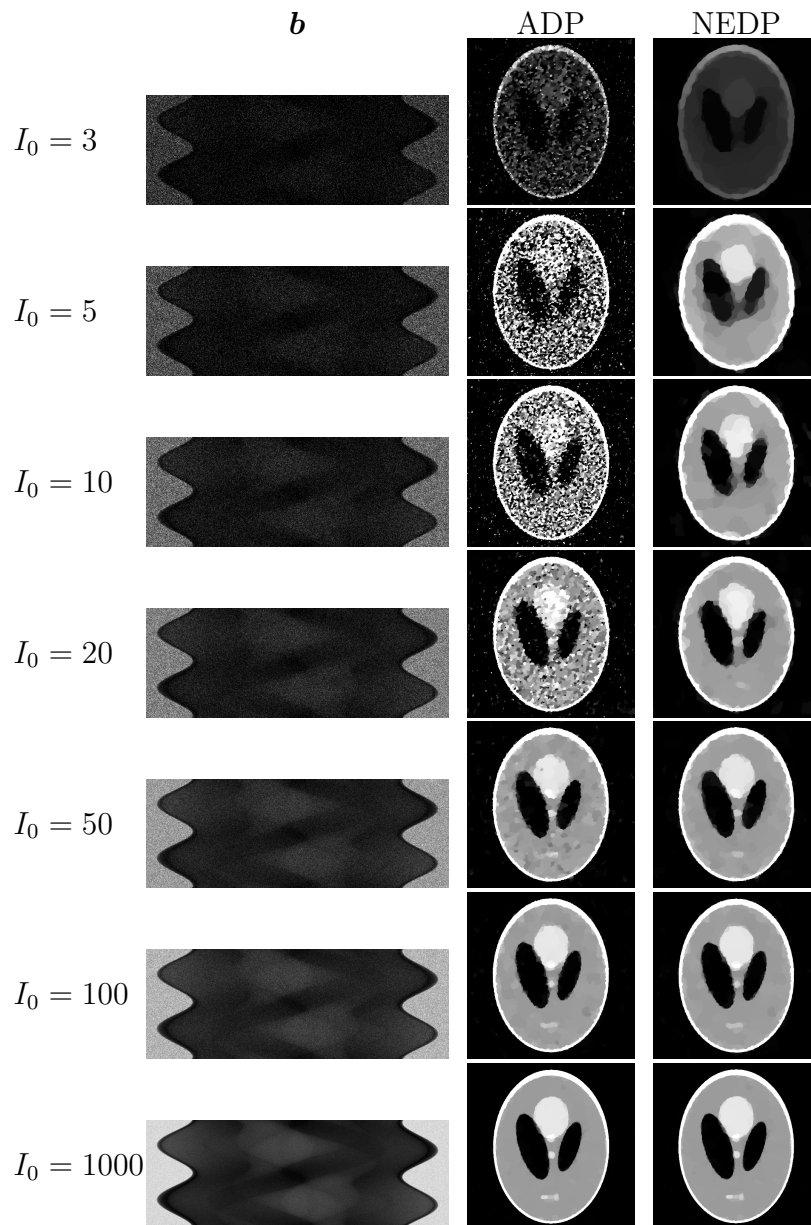
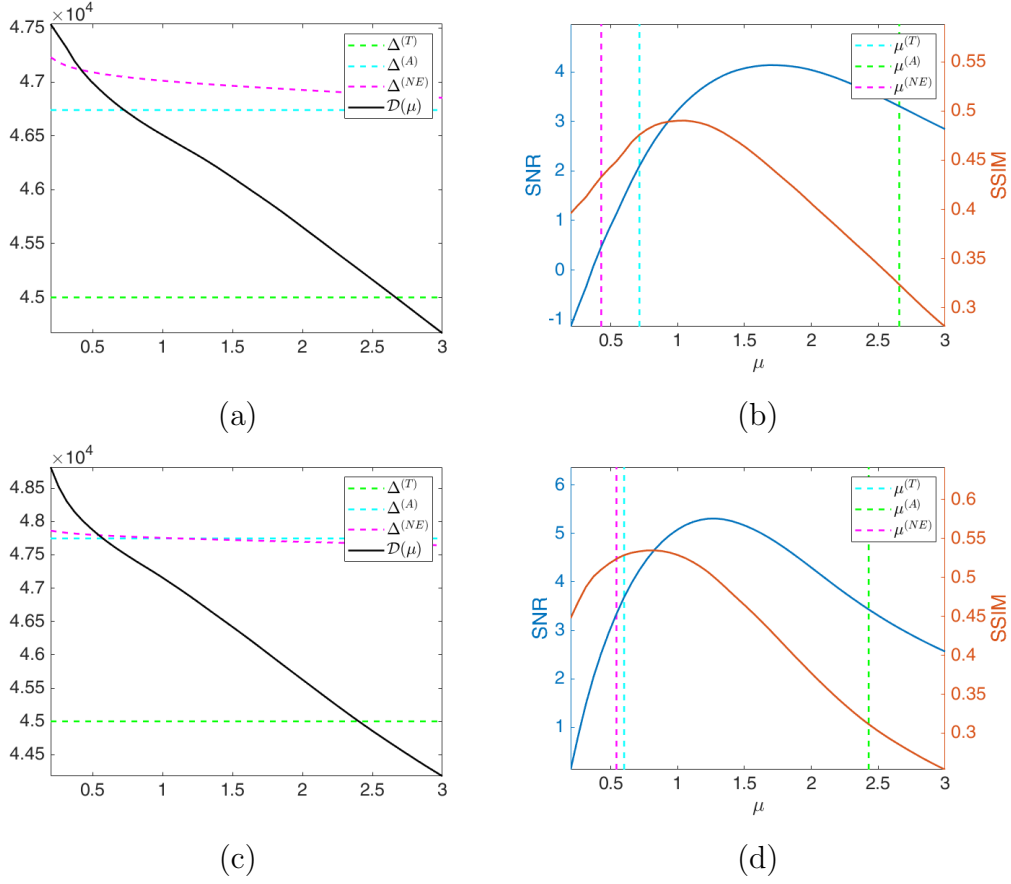


Figure 6.6: Test image Shepp Logan. *Left column*: observed data \mathbf{b} with different I_0 -values ranging from 3 to 1000. *Middle column*: CT reconstruction by ADP. *Right column*: CT reconstruction by NEDP.



I_0	ADP			NEDP			Difference	
	$\mu^{(A)}$	SNR	SSIM	$\mu^{(NE)}$	SNR	SSIM	SNR	SSIM
3	1.563	2.663	0.449	0.787	0.644	0.449	-2.019	0.000
5	2.657	3.308	0.323	0.428	0.468	0.432	-2.840	+0.109
10	2.428	3.432	0.311	0.542	3.340	0.523	-0.092	+0.212
20	1.302	6.154	0.466	0.383	4.714	0.556	-1.440	+0.090
50	0.516	8.162	0.622	0.320	7.636	0.612	-0.526	-0.010
100	0.300	8.970	0.672	0.257	8.580	0.666	-0.390	-0.006
1000	0.098	12.901	0.790	0.098	12.901	0.790	0.000	0.000

Figure 6.7: Test image **brain**. *Top*: discrepancy curve (left) and SNR/SSIM values achieved for different μ -values with $I_0 = 5$ and $I_0 = 10$ (first and second column respectively). *Bottom*: output μ -values and SNR/SSIM values obtained by the ADP and the NEDP for the different photon counts I_0 .

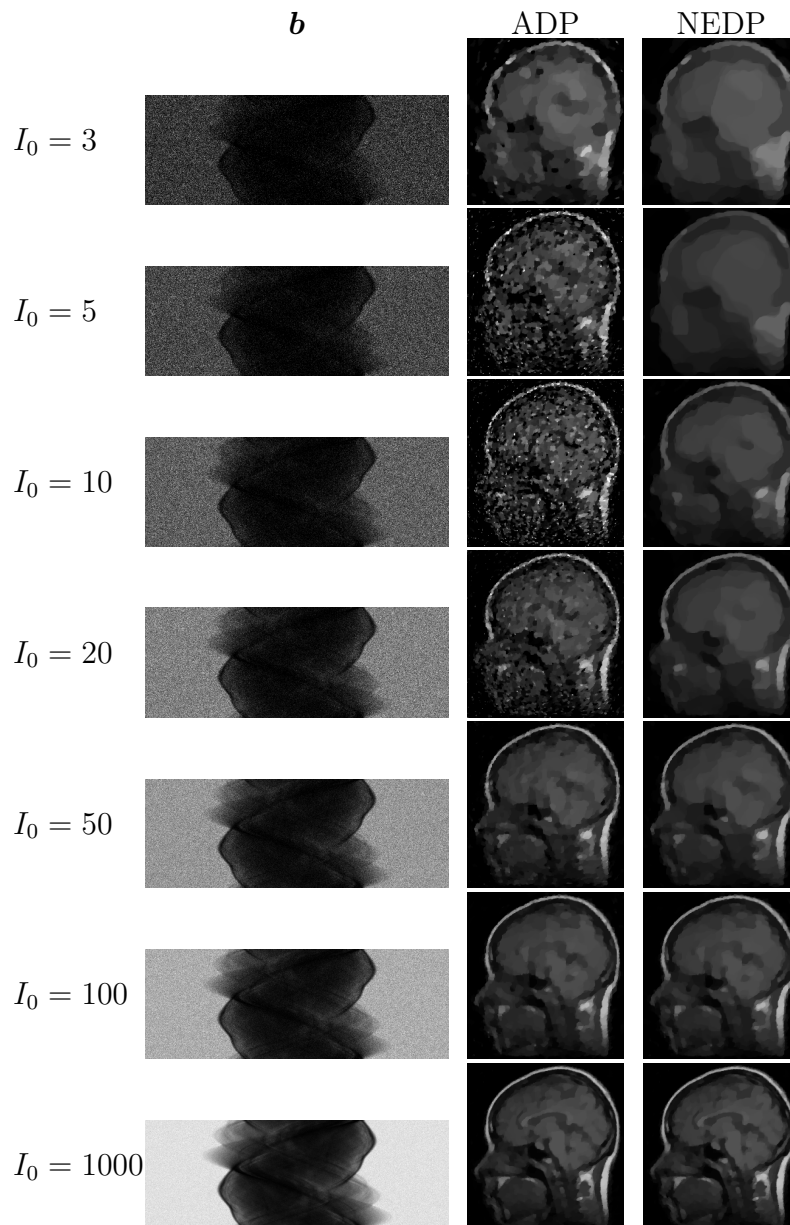
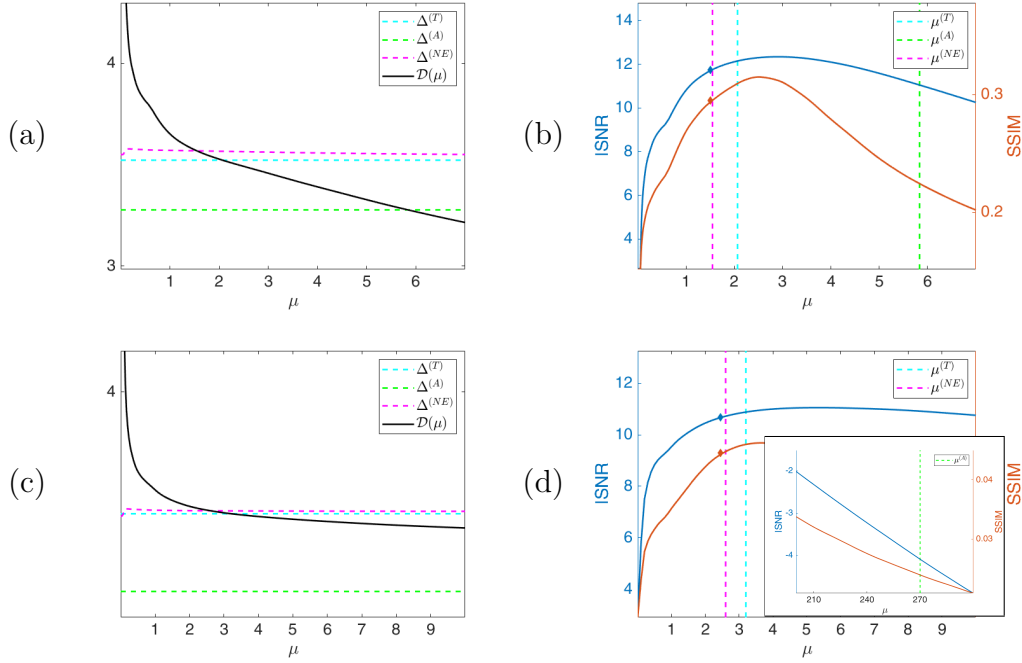


Figure 6.8: Test image brain. *Left column*: observed data \mathbf{b} with different I_0 -values ranging from 3 to 1000. *Middle column*: CT reconstruction by ADP. *Right column*: CT reconstruction by NEDP.

band parameter, representing the side length (in pixels) of the square support of the kernel, and **sigma**, that is the standard deviation (in pixels) of the isotropic bivariate Gaussian distribution defining the kernel in the continuous setting. We considered two different blur levels characterized by the parameters **band**=5, **sigma**=1 and **band**=13, **sigma**=3. The blurred noiseless image $\bar{\lambda} = \mathbf{A}\bar{x} + \mathbf{q}$ is then generated by adding to the blurred image a constant emission background \mathbf{q} of value 2×10^{-3} . The observed image $\mathbf{b} = \mathbf{Poiss}(\bar{\lambda})$ is finally obtained by pseudo-randomly generating an m -variate independent Poisson realization with mean vector $\bar{\lambda}$. In Figure 6.9, for the test image **camerman**, we report the curve of the discrepancy function $\mathcal{D}(\mu; \mathbf{b})$ obtained a posteriori as well as the curves of the ISNR and of the SSIM for $\kappa = 5$ both with the less severe (first row) and more severe (second row) blur level. As for the CT reconstruction case, also in this case the ADP selects a μ -value which is far from the optimal one, either if measured in terms of ISNR or SSIM. On the other hand, $\mu^{(T)}$ and $\mu^{(NE)}$ are very close and almost reach the maximum of the two curves. We also highlight that, when considering the more severe blur case, the ADP selects a very large μ -value which returns very low ISNR and SSIM values - see the thumbnail image in the right corner of Figure 6.9(d).

Notice that the NEDP outperforms the ADP both in terms of ISNR and SSIM for the low-count acquisitions. However, when the κ increases, the two methods behave very similarly, with the ISNR and SSIM values obtained by the ADP being slightly larger than those obtained by the NEDP. In accordance with this analysis, the output $\mu^{(A)}$ and $\mu^{(NE)}$ are significantly different in low-count regimes, similar in mid-count regimes and particularly close in high-count regimes.

From the restorations shown in Figures 6.10 and 6.11 one can notice that for low-count acquisitions the μ -value selected by the ADP does not allow for a proper regularization, so that NEDP clearly outperforms the competitor. However, starting from $\kappa = 20$ the two approaches return similar output images.



		ADP			NEDP			Difference	
	κ	$\mu^{(A)}$	ISNR	SSIM	$\mu^{(NE)}$	ISNR	SSIM	ISNR	SSIM
band=5, sigma=1	3	6.1613	10.1928	0.1654	1.3228	13.4871	0.3720	+3.2942	+0.2065
	5	5.8076	11.0567	0.2247	1.5100	11.7258	0.2949	+0.6690	+0.0701
	10	6.5414	9.9561	0.2504	3.3778	10.0664	0.2540	+0.1103	+0.0035
	20	6.7853	8.1429	0.2634	5.0019	7.9470	0.2482	-0.1959	-0.0152
	50	10.2516	5.5940	0.2982	9.5042	5.5270	0.2932	-0.0670	-0.0050
	100	15.3829	4.0231	0.3335	14.9409	3.9963	0.3316	-0.0267	-0.0019
	1000	70.4637	2.6296	0.4509	70.3529	2.6280	0.4508	-0.0015	-0.0001
band=13, sigma=3	3	291.2252	-5.3677	0.0156	2.2867	12.5234	0.3214	+17.8914	+0.3058
	5	270.6214	-4.0339	0.0241	2.4535	10.6776	0.2393	+14.7115	+0.2152
	10	117.0970	2.8109	0.0888	4.2731	8.5199	0.1657	+5.7090	+0.0769
	20	25.0534	6.4344	0.1554	6.7164	6.4093	0.1444	-0.0250	-0.0109
	50	21.0590	4.2611	0.1686	14.4928	4.1632	0.1607	-0.0978	-0.0078
	100	29.4505	3.0947	0.1868	25.1986	3.0469	0.1835	-0.0477	-0.0033
	1000	136.0108	1.9261	0.2378	134.6466	1.9233	0.2375	-0.0028	-0.0002

Figure 6.9: Test image cameraman. *Top*: discrepancy curve divided by 10^4 (left) and ISNR/SSIM values achieved for different μ -values with $\kappa = 5$ and Gaussian blur with parameters `band=5, sigma=1` (first row) and `band=13, sigma=3` (second row). *Bottom*: output μ -values and ISNR/SSIM values obtained by the ADP-ADMM and the NEDP-ADMM for the two blur levels considered and different photon counts κ .

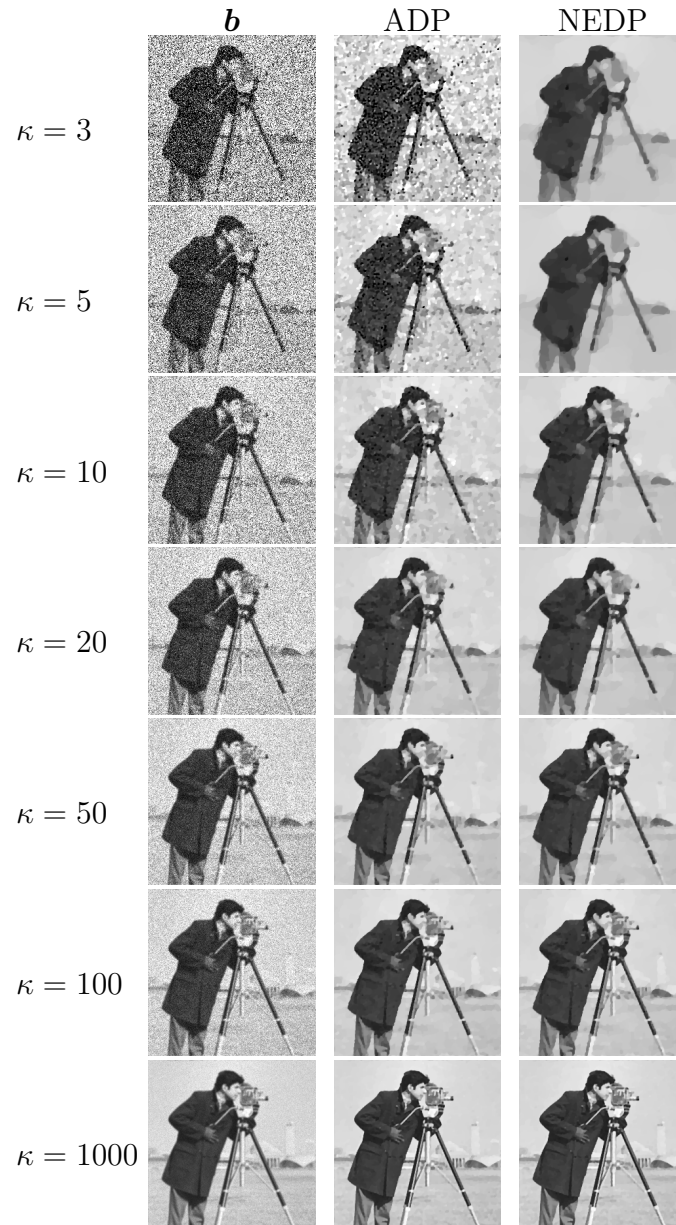


Figure 6.10: Test image cameraman. *Left column*: observed data \mathbf{b} corrupted by Gaussian blur with parameters `band=5`, `sigma=1` and Poisson noise with different κ -values ranging from 3 to 1000. *Middle column*: restorations by ADP. *Right column*: restorations by NEDP.

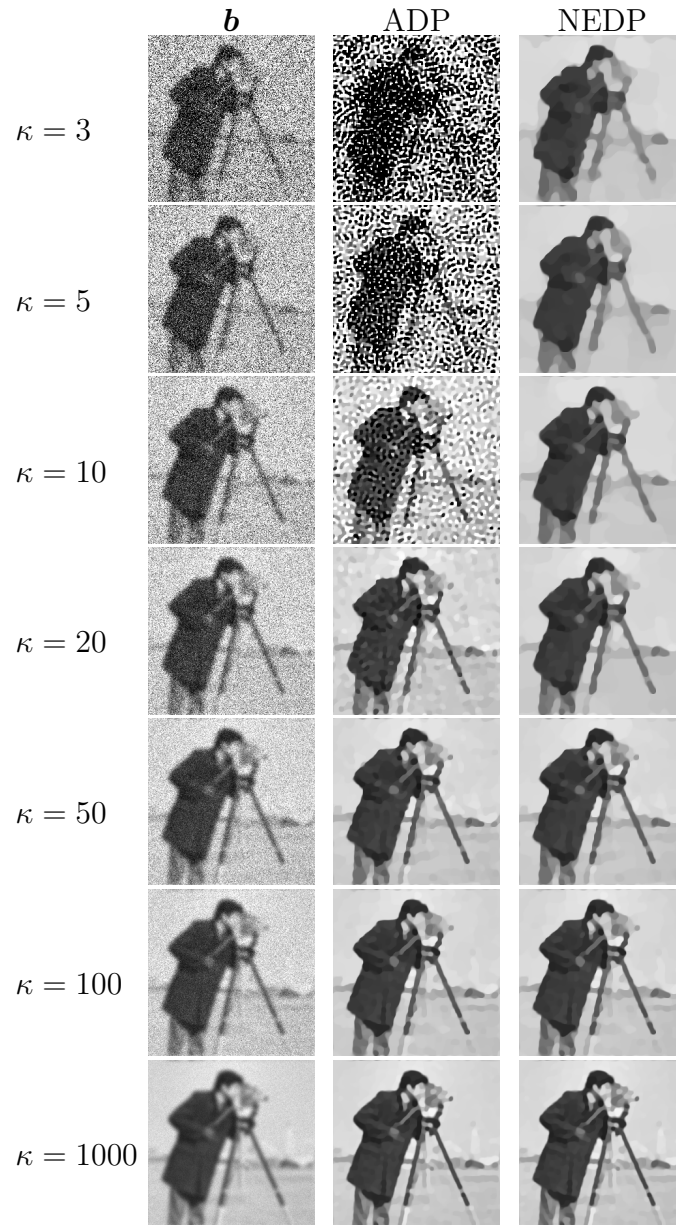


Figure 6.11: Test image `cameraman`. *Left column*: observed data \mathbf{y} corrupted by Gaussian blur with parameters `band=13`, `sigma=3` and Poisson noise with different κ -values ranging from 3 to 1000. *Middle column*: restorations by ADP. *Right column*: restorations by NEDP.

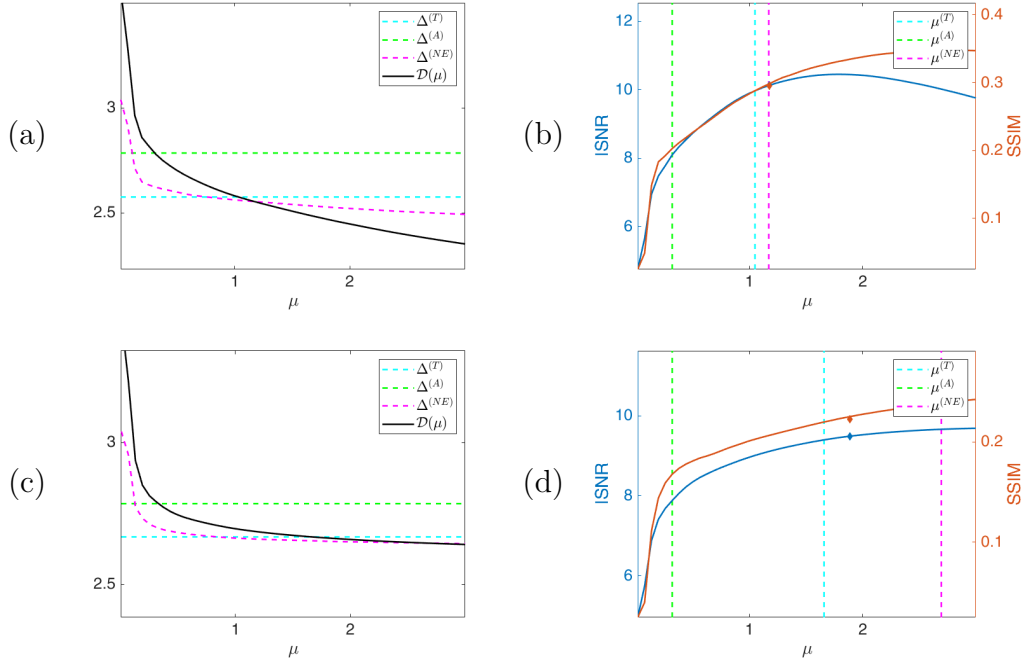
For the second test image `cells`, we show in Figures 6.12 the behaviour of the discrepancy function $\mathcal{D}(\mu; \mathbf{b})$ as well as of the ISNR and SSIM values in the *a posteriori* framework for the two blur levels and $\kappa = 3$. Note that, for both blur levels, the NEDP achieves higher ISNR and SSIM values when compared to the ADP. From the values reported in the bottom part of Figure 6.12, we notice that the NEDP outperforms the ADP in every photon-count regime. Clearly, the closer $\mu^{(A)}$ and $\mu^{(NE)}$, the smaller the difference in terms of ISNR and SSIM.

The restorations computed by the ADP and the NEDP are shown in Figure 6.13 for the smaller blur level and in Figure 6.14 for the larger one. The obtained results confirm the values reported in the bottom of Figure 6.12. Moreover, also from a visual viewpoint, the difference between the two performances increases when going from high to low-count regimes.

Updating of the regularization parameters during the iterations

In the previous experiments we set a fine grid of μ -values and computed the solution $\hat{\mathbf{x}}(\mu)$ corresponding to each μ . Then, among the recorded solutions, we selected the one such that the TDP, the ADP or the NEDP was satisfied. However, this algorithmic scheme, to which we refer as *a posteriori* optimization procedure, that - as it is well-established - can be circumvented for the TDP, ADP. In fact, in [31, 29], the authors propose to update the regularization parameter according to the ADP along the iterations of the popular Alternating Direction Method of Multipliers (ADMM). Here, we detail the steps of such algorithm and show how, and under which conditions, it can be extended for the case of NEDP. Finally, we remark that the case of the TDP is only addressed for explanatory purposes and it can not be performed in practice as $\bar{\mathbf{x}}$ is not available.

By rewriting the \mathbf{u}_2 subproblem in (10.17) and making explicit the dependence of the solution $\mathbf{u}_2^{(k+1)}$ on the parameter $\tau = \frac{\mu}{\gamma}$ for the image restoration



		ADP			NEDP			Difference	
	κ	$\mu^{(A)}$	ISNR	SSIM	$\mu^{(NE)}$	ISNR	SSIM	ISNR	SSIM
band=5, sigma=1	3	0.3042	8.0428	0.2002	1.1719	10.1281	0.2952	+2.0852	+0.0949
	5	1.1283	8.0419	0.2799	1.8656	8.7165	0.3295	+0.6745	+0.0496
	10	1.7170	5.9522	0.3167	2.6968	6.5660	0.3643	+0.6137	+0.0475
	20	2.4343	3.8227	0.3698	3.6823	4.4218	0.4155	+0.5991	+0.0457
	50	5.0053	2.0792	0.4655	7.0349	2.4818	0.4991	+0.4026	+0.0335
	100	8.4224	1.0624	0.5383	10.9451	1.3581	0.5629	+0.2957	+0.0246
	1000	45.5340	0.6410	0.7221	52.7334	0.7729	0.7310	+0.1319	+0.0089
band=13, sigma=3	3	0.3251	7.9171	0.16940	1.8841	9.4912	0.2228	+1.5740	+0.0534
	5	3.6943	8.1023	0.2420	3.9060	8.1195	0.2436	+0.0171	+0.0015
	10	3.5550	5.7064	0.2282	5.2098	5.8821	0.2425	+0.1756	+0.0143
	20	2.9412	3.5252	0.2285	5.6999	3.9632	0.2586	+0.4380	+0.0301
	50	6.1442	1.9499	0.2654	14.4495	2.3613	0.2980	+0.4114	+0.0325
	100	10.0409	1.2177	0.2862	18.6804	1.52056	0.3094	+0.3028	+0.0231
	1000	64.4743	1.0410	0.3871	98.0256	1.1868	0.4019	+0.1458	+0.0148

Figure 6.12: Test image cells. *Top*: discrepancy curve divided by 10^4 (left) and ISNR/SSIM values achieved for different μ -values with $\kappa = 3$ and Gaussian blur with parameters **band=5, sigma=1** (first row) and **band=13, sigma=3** (second row). *Bottom*: output μ -values and ISNR/SSIM values obtained by the ADP-ADMM and the NEDP-ADMM for the two blur levels considered and different photon counts κ .

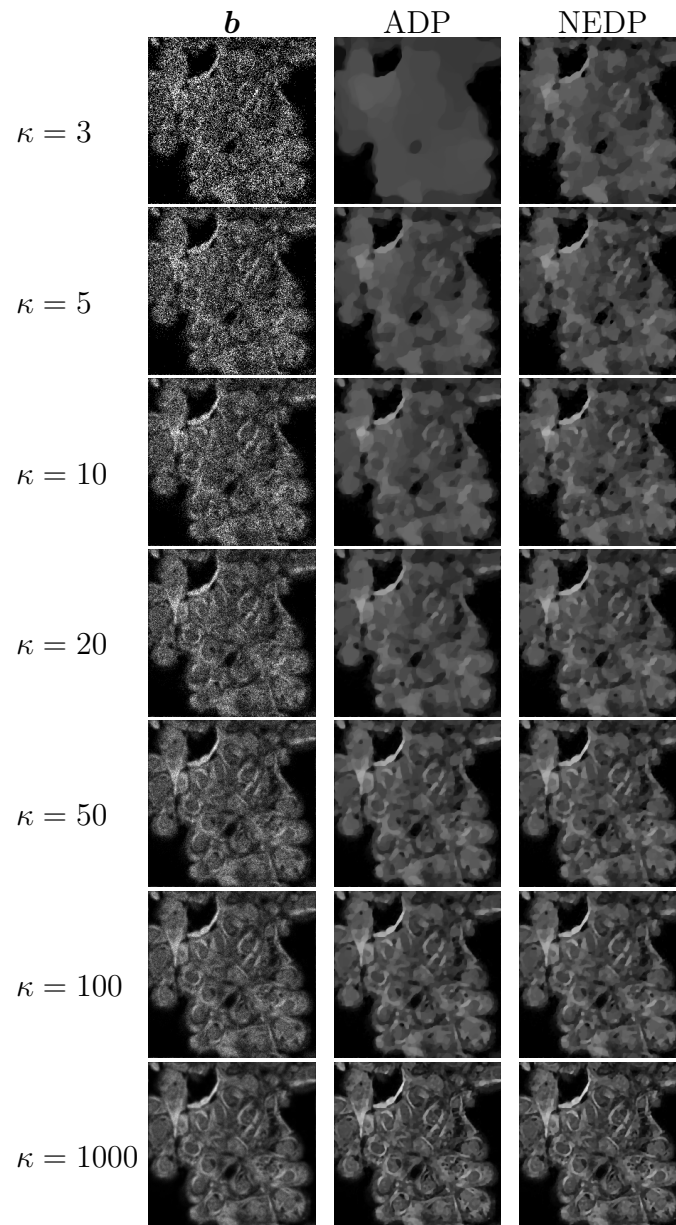


Figure 6.13: Test image `cells`. *Left column*: observed data \mathbf{y} corrupted by Gaussian blur with parameters `band=5`, `sigma=1` and Poisson noise with different κ -values ranging from 3 to 1000. *Middle column*: restorations by ADP. *Right column*: restorations by NEDP.

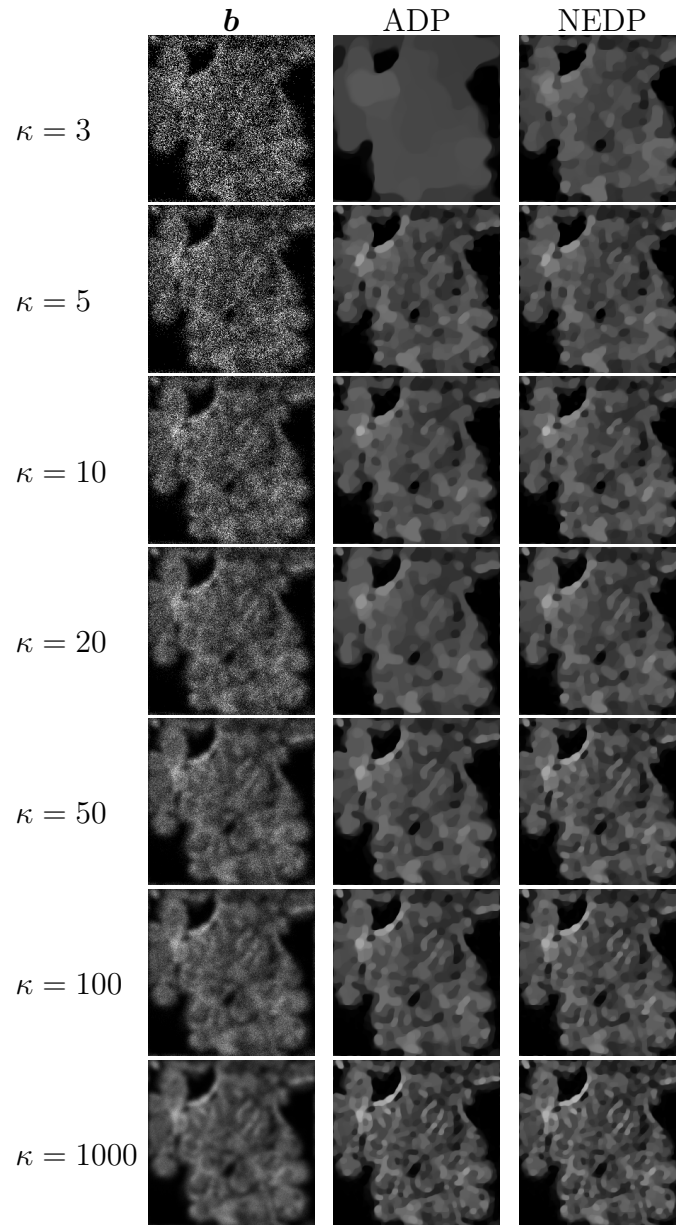


Figure 6.14: Test image cells. *Left column*: observed data \mathbf{y} corrupted by Gaussian blur with parameters `band=13`, `sigma=3` and Poisson noise with different κ -values ranging from 3 to 1000. *Middle column*: restorations by ADP. *Right column*: restorations by NEDP.

problem, we have that:

$$\mathbf{u}_2^{(k+1)}(\tau) \in \arg \min_{\mathbf{u}_2 \in \mathbb{R}^m} \left\{ \tau \text{KL}(\mathbf{A}\mathbf{u}_2 + \mathbf{q}; \mathbf{b}) + \frac{1}{2} \|\mathbf{u}_2 - \mathbf{s}_2^{(k)}\|_2^2 \right\} \quad (6.26)$$

where

$$\mathbf{s}_2^{(k)} = \mathbf{A}\mathbf{u}_2^{(k+1)} + \frac{1}{\gamma} \boldsymbol{\rho}_2^{(k)} \in \mathbb{R}^m. \quad (6.27)$$

Note that, by defining $\tau = \frac{\mu}{\gamma}$, τ plays the role of the regularization parameter μ in the DP applied to this subproblem. The problem in (6.26) can be solved component by component in the following way

$$u_i^{(k+1)}(\tau) = \frac{1}{2} \left[-(\tau + q_i - s_i) + \sqrt{(\tau + q_i - s_i)^2 + 4(s_i q_i + \tau(b_i - q_i))} \right] \quad (6.28)$$

where, for simplicity of notation, we set $u_i := u_{2,i} \in \mathbb{R}$ and $s_i = s_{2,i}^{(k)} \in \mathbb{R}$. We now want to apply one among the DP versions - namely, (TDP), (ADP) and the proposed (NEDP) for selecting a value of the free parameter τ in (6.28). In particular, we select $\tau = \tau^{(k+1)}$ such that $\tau^{(k+1)}$ satisfies the discrepancy equation which, in accordance with the general definition given in (5.2), takes here the form

$$G(\tau; \mathbf{b}) := \mathcal{D}(\tau; \mathbf{b}) - \Delta = 0 \quad (6.29)$$

where the discrepancy function reads

$$\mathcal{D}(\tau; \mathbf{b}) = \sum_{i=1}^m \mathcal{D}_i(\tau; b_i) = \sum_{i=1}^m F\left(\lambda_i^{(k+1)}(\tau); b_i\right), \quad (6.30)$$

where the function F is defined in (4.10) and the vector

$$\boldsymbol{\lambda}^{(k+1)}(\tau) = \mathbf{u}_2^{(k+1)}(\tau) + \mathbf{q} \quad (6.31)$$

with components $\lambda_i^{(k+1)}(\tau)$ refers to the mean vector of the Poisson noise. The discrepancy value Δ , according to the definitions given in (TDP), (ADP) and (NEDP), takes one of the following values/forms:

$$\Delta = \begin{cases} \Delta^{(T)} & = \sum_{i=1}^m F((\mathbf{A}\bar{\mathbf{x}} + \mathbf{q})_i; b_i) & \text{for (TDP),} \\ \Delta^{(A)} & = \frac{m}{2} & \text{for (ADP),} \\ \Delta^{(NE)}(\tau) & = \frac{m}{2} + \sum_{i=1}^m \epsilon \left(\lambda_i^{(k+1)}(\tau); \hat{\mathbf{c}} \right) & \text{for (NEDP),} \end{cases} \quad (6.32)$$

with rational polynomial function ϵ defined in (6.18) and parameter vector $\widehat{\mathbf{c}}$ given in (6.21). We notice that $\Delta^{(T)}$ and $\Delta^{(A)}$ are two positive scalars that can be computed once for all and does not change their value during the ADMM iterations, whereas $\Delta^{(NE)}(\tau)$ is a function of τ which almost certainly changes its shape along the ADMM iterations (due to function $u_i^{(k+1)}(\tau)$ in (6.28) changing its shape when vector $\mathbf{s}_2^{(k)}$ changes).

Summing up, the complete procedure for the DP-based update of the parameter τ and, then, of the variable \mathbf{u}_2 reads as follows:

$$\mathbf{s}_2^{(k)} = \mathbf{A}\mathbf{u}_2^{(k+1)} + \frac{1}{\gamma}\boldsymbol{\rho}_2^{(k)}, \quad (6.33)$$

$$\tau^{(k+1)} = \text{root of the discrepancy equation in (6.29) - (6.32)}, \quad (6.34)$$

$$u_i^{(k+1)}(\tau^{(k+1)}) \quad \text{computed by (6.28), for } i = 1, \dots, m. \quad (6.35)$$

For what concerns the ADP, in [31] the authors have proven that along the ADMM iterations, the function $\mathcal{D}(\tau; \mathbf{b})$ is convex and decreasing so that the existence and the uniqueness of the solution of the discrepancy equation in (6.29) with $\Delta = \Delta^{(A)}$ is guaranteed. The same result can be immediately extended to the case of the TDP. When considering the NEDP, the functional form of $\Delta^{(NE)}(\tau)$ is such that the above result can not be straightforwardly applied. However, the following proposition on the existence of a solution for the discrepancy equation (6.29) with $\Delta = \Delta^{(NE)}$ holds true. It is important to note that the following proposition can be applied only for the image restoration problem.

Proposition 6.3.1. Consider the discrepancy equation in (6.29)-(6.32) with $\Delta = \Delta^{(NE)}(\tau)$ and with vector $\mathbf{s}_2^{(k)}$ and function $\lambda_i^{(k+1)}(\tau)$ defined as in (6.27) and (6.31), respectively, and let

$$\mathbf{t}^{(k)} := \max \left\{ \mathbf{s}_2^{(k)}, 0 \right\}. \quad (6.36)$$

Then, the discrepancy equation admits a solution if the following condition is fulfilled:

$$\exists i : b_i \neq 0 \quad \wedge \quad \mathcal{T}(\mathbf{t}^{(k)}, \mathbf{b}) := \sum_{i=1}^m T(t_i^{(k)}, b_i) \geq \frac{m}{2}, \quad (6.37)$$

where function $T: \mathbb{R}_+ \times \mathbb{N} \rightarrow \mathbb{R}$ is defined by

$$T(t, b) = F(t; b) - \epsilon(t; \widehat{\mathbf{c}}), \quad (6.38)$$

with function F , function ϵ and parameter vector $\widehat{\mathbf{c}}$ given in (4.10), (6.18) and (6.21), respectively.

Proof. Since functions F in (4.10), ϵ in (6.18) and $\lambda_i^{(k+1)}$ in (6.31) are all continuous, then the function G defined in (6.29)-(6.32) with $\Delta = \Delta^{(NE)}(\tau)$ is continuous in the variable τ on its entire domain $\tau \in \mathbb{R}_+$, for any $\mathbf{b} \in \mathbb{N}^m$ and any $\mathbf{s}_2^{(k)} \in \mathbb{R}^m$.

Then, it is easy to prove that function $\lambda_i^{(k+1)}(\gamma)$ in (6.31) satisfies

$$\lambda_i^{(k+1)}(0) = \max \{s_i^{(k)}, 0\} = t_i^{(k)}, \quad \lim_{\tau \rightarrow +\infty} \lambda_i^{(k+1)}(\tau) = b_i, \quad (6.39)$$

with vector $\mathbf{t}^{(k)}$ defined in (6.36). It thus follows from (6.39) and from definition of functions \mathcal{D} in (6.30) and $\Delta^{(NE)}$ in (6.32) that

$$\begin{aligned} G(0; \mathbf{b}) &= \mathcal{D}(0; \mathbf{b}) - \Delta^{(NE)}(0) \\ &= \sum_{i=1}^m F(\lambda_i^{(k+1)}(0); b_i) - \frac{m}{2} - \sum_{i=1}^m \epsilon(\lambda_i^{(k+1)}(0); \widehat{\mathbf{c}}) \\ &= \sum_{i=1}^m \left(F(t_i^{(k)}; b_i) - \epsilon(t_i^{(k)}; \widehat{\mathbf{c}}) \right) - \frac{m}{2} = \mathcal{J}(\mathbf{t}^{(k)}, \mathbf{b}) - \frac{m}{2} \end{aligned} \quad (6.40)$$

and that

$$\begin{aligned} \lim_{\tau \rightarrow +\infty} G(\tau; \mathbf{b}) &= \lim_{\tau \rightarrow +\infty} (\mathcal{D}(\tau; \mathbf{b}) - \Delta^{(NE)}(\tau)) \\ &= \lim_{\tau \rightarrow +\infty} \left(\sum_{i=1}^m F(\lambda_i^{(k+1)}(\tau); b_i) - \frac{m}{2} - \sum_{i=1}^m \epsilon(\lambda_i^{(k+1)}(\tau); \widehat{\mathbf{c}}) \right) \\ &= \sum_{i=1}^m F(b_i; b_i) - \sum_{i=1}^m \left(\frac{1}{2} + \epsilon(b_i; \widehat{\mathbf{c}}) \right) \end{aligned} \quad (6.41)$$

$$= - \sum_{i=1}^m f(b_i; \widehat{\mathbf{c}}) < 0 \text{ if } \exists i: b_i \neq 0, \quad (6.42)$$

where function \mathcal{J} in (6.40) is defined in (6.37), cancelling the first summation in (6.41) comes from $F(b; b) = 0$ for any $b \in \mathbb{R}_+$ (see the definition of function

F in (4.10), where $b \ln b = 0$ for $b = 0$) and (6.42) comes from the definition of function f in (6.22).

From (6.42) and continuity of function $G(\tau; \mathbf{b})$, we can conclude that for any $\mathbf{b} \neq \mathbf{0}$ the discrepancy equation $G(\tau; \mathbf{b}) = 0$ admits a solution if $G(0; \mathbf{b}) \geq 0$. It thus follows from (6.40) that the sufficient condition in (6.36)-(6.38) holds true. \square

This proposition can not be directly extended to the CT reconstruction problem due to the different form of the function $\mathbf{u}_2(\tau)$ in (10.21). Therefore, the tests with the iterative scheme were performed only for the image restoration problem.

In the previous experiments we evaluated the performance of the proposed NEDP in (NEDP) for the automatic selection of the regularization parameter μ in image restoration variational models of the TV-KL form in (TV-KL) and compared it with the TDP and the ADP in (TDP) and (ADP), respectively. Here we discuss their application during the iterations by denoting with NEDP-ADMM, TDP-ADMM and ADP-ADMM the respective solution algorithms with the regularization parameter update along the iterations for NEDP, TDP and ADP, while the selected μ values with the iterated versions are indicated with $\hat{\mu}^{(NE)}$, $\hat{\mu}^{(A)}$ and $\hat{\mu}^{(T)}$. As stated before, the μ -selection problem along the ADMM iterations always admits a unique solution under the adoption of the ADP and TDP. For what concerns the NEDP-ADMM, at the generic iteration k of Algorithm, the regularization parameter μ is updated provided that the condition stated in Proposition 6.3.1 is satisfied. If this is not the case, the parameter update is not performed and $\mu^{(k)} = \mu^{(k-1)}$. We are interested in verifying that the proposed NEDP-ADMM scheme succeeds in automatically selecting such optimal μ in a robust and efficient way: the blue and red markers in Figures 6.9(b), 6.9(d) represent the final ISNR and SSIM values, respectively, of the image restored via NEDP-ADMM. Clearly, the markers are plotted in correspondence of $\hat{\mu}^{(NE)}$, that is - we recall - the output μ -value of the iterative scheme NEDP-ADMM; one can clearly observe that $\hat{\mu}^{(NE)}$ ends up to be very close to the optimal

$\mu^{(NE)}$ detected *a posteriori* by the NEDP. For the second test image `cells`, the blue and red markers in 6.12(b) and 6.12(d), indicating the output ISNR and SSIM, respectively, of the iterated version of our approach, are very close to the ones achieved by applying the NEDP *a posteriori*, suggesting that also $\hat{\mu}^{(NE)}$ and $\mu^{(NE)}$ are very close.

6.3.3 Discussion

In this chapter we proposed an automatic selection strategy for the regularization parameter of variational image reconstruction models under Poisson noise corruption based on a nearly-exact version of the approximate discrepancy principle originally proposed in [25]. Our approach relies on Montecarlo simulations, which have been designed with the purpose of providing meaningful insights on the limitations of the original approximate strategy, especially in the low-count Poisson regime. The proposed version of the discrepancy principle has then been derived by means of a weighted least-square fitting and embedded along the iterations of an efficient ADMM-based optimization scheme. Our approach has been extensively tested both for the CT reconstruction and image restoration problem and for different photon-count values, ranging from very low to high values. When compared to the original approximate selection criterion, the proposed strategy has been shown to improve the quality of the output restorations in low-count regimes and in mid-count/high-count regimes on images characterized by few large pixel values.

Chapter 7

Poisson Whiteness Principle (PWP)

In the previous chapters we introduced the topic of automatic selection principles and proposed the Nearly Exact DP to overcome the limitation of the Approximate DP. Despite its very good experimental performances, the NEDP is characterized by theoretical limitations which are mostly related to the lack of guarantees on the uniqueness of the solution for the discrepancy equation; such limitations are also combined with the empirical evidence of multiple solutions in very extreme scenarios where the number of zero-pixels in the acquired data is relevant.

In this chapter we will focus on the second class strategies, whose general formulation takes the following form:

$$\mathcal{C}(\widehat{\boldsymbol{x}}(\mu^*)) : \mu^* \in \arg \min_{\mu \in \mathbb{R}_{++}} \mathcal{V}(\mu),$$

where $\mathcal{V} : \mathbb{R}_{++} \rightarrow \mathbb{R}$ represents some demerit function to be minimized for selecting μ . For Poisson data, this class of strategies has not been explored as much as the former. A few decades ago, some attempts have been made in order to adapt the popular Generalized Cross Validation (GCV) approach [22] to non-Gaussian data [23, 24]; nonetheless, these strategies, which ultimately rely on a weighted approximation of the KL fidelity term and on

a slight reformulation of the classical GCV score, have not been diffusively employed for imaging problems.

Among the parameter selection strategies that have been developed in the context of additive white noise corruption, the class of minimization-based principles exploiting the noise *whiteness* property is one of the best performing [42, 43, 44, 45, 46, 47]. More specifically, one selects μ by minimizing the normalized correlation between the residual image components, that is by guaranteeing that the residual image resembles as much as possible the underlying additive noise in terms of whiteness. The whiteness-based approaches have been proven to outperform the Morozov discrepancy principle in different imaging tasks, such as, e.g., denoising/restoration [44] and super-resolution [45, 46] and, very importantly, do not need to know (or estimate) the noise standard deviation. Nonetheless, despite the encouraging results on Gaussian data, so far the whiteness principle has not been extended to Poisson noise corruption. Then we will introduce the well known whiteness approach for additive noise then move to its extension in the case of Poisson noise.

7.1 The Whiteness Principles for Additive Noise

In order to describe the Whiteness Principle for additive noise here we recall its definition considering an Additive White Gaussian Noise (AWGN) with the following forward model:

$$\mathbf{b} = \mathbf{A}\bar{\mathbf{x}} + \mathbf{e}, \quad \mathbf{e} \text{ a realization of } \mathcal{E} \sim \mathcal{N}(\mathbf{0}_m, \sigma \mathbf{I}_m) \quad (7.1)$$

where $\mathbf{x}, \mathbf{b}, \mathbf{e} \in \mathbb{R}^m$, $m = m_1 \cdot m_2$, are column major forms of the uncorrupted, corrupted and noise images, respectively, all made up of $m_1 \times m_2$ pixels, the matrix $\mathbf{A} \in \mathbb{R}^{m \times m}$ represents the discrete linear space-invariant blur operator, $\mathbf{I}_{m \times m} \in \mathbb{R}^{m \times m}$ denotes the identity matrix and \mathcal{E} is an m -variate Gaussian-distributed random vector with zero mean and scalar covariance

matrix, with σ indicating the noise standard deviation.

In the following we introduce/use notations for random fields which are different from the ones used previously in sect 2.3. In fact, there we considered vectorized random fields, while here we prefer to consider un-vectorized random fields. To shorten notations in the definitions, we preliminarily define the following two sets of integer index pairs

$$\begin{aligned} \mathbf{I} &:= \{(i, j) \in \mathbb{Z}^2: (i, j) \in [1, m_1] \times [1, m_2]\}, \\ \mathbf{L} &:= \{(l, m) \in \mathbb{Z}^2: (l, m) \in [-(m_1 - 1), (m_1 - 1)] \times [-(m_2 - 1), (m_2 - 1)]\}. \end{aligned}$$

Definition 7.1.1 (weak stationary random field). A $m_1 \times m_2$ random field $\mathfrak{Z} = \{Z_{i,j}\}$, $(i, j) \in \mathbf{I}$, is said to be weak stationary if

- $E[Z_{i,j}] = \mu_{\mathfrak{Z}} \in \mathbb{R}$, $\text{Var}[Z_{i,j}] = \sigma_{\mathfrak{Z}}^2 \in \mathbb{R}_{++}$, $\forall (i, j) \in \mathbf{I}$;
- $\text{Corr}[Z_{i_1, j_1}, Z_{i_1+l, j_1+m}] = \text{Corr}[Z_{i_2, j_2}, Z_{i_2+l, j_2+m}]$,
 $\forall (i_1, j_1) \in \mathbf{I}$, $\forall (i_2, j_2) \in \mathbf{I}$, $\forall (l, m) \in \mathbf{L}: (i_2 + l, j_2 + m) \in \mathbf{I}$.

Definition 7.1.2 (ensemble normalized auto-correlation). The ensemble normalized auto-correlation of a $m_1 \times m_2$ weak stationary random field $\mathfrak{Z} = \{Z_{i,j}\}$, $(i, j) \in \mathbf{I}$, is a $(2m_1 - 1) \times (2m_2 - 1)$ matrix $\mathbf{A}[\mathfrak{Z}] = \{a_{l,m}[\mathfrak{Z}]\}$, $(l, m) \in \mathbf{L}$, defined by

$$a_{l,m}[\mathfrak{Z}] = \frac{\text{Corr}[Z_{i,j}, Z_{i+l, j+m}]}{\sigma_{\mathfrak{Z}}^2}, \quad (l, m) \in \mathbf{L}, (i, j) \in \mathbf{I}: (i+l, j+m) \in \mathbf{I}.$$

Definition 7.1.3 (white random field). A $m_1 \times m_2$ random field $\mathfrak{Z} = \{Z_{i,j}\}$, $(i, j) \in \mathbf{I}$, is said to be white if

- it is weak stationary with $\mu_{\mathfrak{Z}} = 0$;
- it is uncorrelated, that is its ensemble normalized autocorrelation $\mathbf{A}[\mathfrak{Z}] = \{a_{l,m}[\mathfrak{Z}]\}$, $(l, m) \in \mathbf{L}$, satisfies:

$$a_{l,m}[\mathfrak{Z}] = \begin{cases} 0 & \forall (l, m) \in \mathbf{L} \setminus \{(0, 0)\}, \\ 1 & \text{if } (l, m) = (0, 0). \end{cases}$$

Definition 7.1.4 (sample normalized auto-correlation). The sample normalized auto-correlation of a $m_1 \times m_2$ non-zero matrix $\mathbf{Z} = \{z_{i,j}\}$, $(i, j) \in \mathbf{I}$, is a $(2m_1 - 1) \times (2m_2 - 1)$ matrix $\mathbf{S}(\mathbf{Z}) = \{s_{l,m}(\mathbf{Z})\}$, $(l, m) \in \mathbf{L}$, defined by

$$s_{l,m}(\mathbf{Z}) = \frac{1}{\|\mathbf{Z}\|_2^2} \sum_{(i,j) \in \mathbf{I}} z_{i,j} z_{i+l,j+m}. \quad (7.2)$$

It follows from Definition 7.1.4 that, given a non-zero matrix $\mathbf{Z} = \{z_{i,j}\}$, $(i, j) \in \mathbf{I}$, one can measure the global amount of normalized auto-correlation between the entries of \mathbf{Z} , that is how far is \mathbf{Z} from being the realization of a white random field, via the following non-negative and scale-invariant scalar measure of whiteness (or, better, of non-whiteness) ([43, 44, 46]):

$$\mathcal{W}(\mathbf{Z}) := \|\mathbf{S}(\mathbf{Z})\|_2^2 = \sum_{(l,m) \in \mathbf{L}} (s_{l,m}(\mathbf{Z}))^2, \quad (7.3)$$

with scalars $s_{l,m}(\mathbf{Z})$ defined in (7.2).

As proved in [44], when periodic boundary conditions are assumed for the $m_1 \times m_2$ matrix \mathbf{Z} , the $(2m_1 - 1) \times (2m_2 - 1)$ sample normalized auto-correlation matrix $\mathbf{S}(\mathbf{Z})$ defined in (7.2) presents some symmetries and the whiteness measure $\mathcal{W}(\mathbf{Z})$ in (7.3) can be computed very efficiently (with $O(m \log m)$ computational complexity, $m = m_1 m_2$) based on the preliminary calculation of the 2D discrete Fourier transform of \mathbf{Z} (implemented by 2D fast Fourier transform). For completeness, in Proposition 7.1.1 below we recall the result reported in [44].

Proposition 7.1.1. Let $\mathbf{Z} = \{z_{i,j}\} \in \mathbb{R}^{m_1 \times m_2}$ be a non-zero matrix and let $\tilde{\mathbf{Z}} = \{\tilde{z}_{i,j}\} \in \mathbb{C}^{m_1 \times m_2}$ be its 2D discrete Fourier transform. Then, assuming periodic boundary conditions for \mathbf{Z} , the function \mathcal{W} in (7.3) can be written as:

$$\mathcal{W}(\mathbf{Z}) = \frac{\sum_{(i,j) \in \mathbf{I}} |\tilde{z}_{i,j}|^4}{\left(\sum_{(i,j) \in \mathbf{I}} |\tilde{z}_{i,j}|^2 \right)^2}. \quad (7.4)$$

Clearly, the nearer the restored image $\hat{\mathbf{x}}(\mu)$ is to the target uncorrupted image, the closer the associated residual image $\hat{\mathbf{r}}(\mu) = \mathbf{A} \hat{\mathbf{x}}(\mu) - \mathbf{b}$ is to the white noise realization \mathbf{e} in 7.1 and, hence, the whiter is the residual image according to the scalar measure in 7.3. This motivates the residual whiteness principle (RWP) for automatically selecting the regularization parameter μ of variational models, which reads:

$$\text{Select } \mu^* \in \arg \min_{\mu \in \mathbb{R}_+} \mathcal{W}(\mu) := \mathcal{W}(\hat{\mathbf{r}}(\mu)), \quad \hat{\mathbf{r}}(\mu) = \mathbf{A} \hat{\mathbf{x}}(\mu) - \mathbf{b}. \quad (\text{RWP})$$

What we discussed here for AWGN applies to the broad class of additive white Generalized Gaussian noise, which includes AW Laplacian noise and AW Uniform noise, [47].

7.2 The Poisson Whiteness Principle

In order to introduce the theory underlying the extension of the Whiteness Principle for Poisson noise, it is useful to rewrite the vectorized image formation model (4.6) in its equivalent matrix form. Denoting by $\mathbf{B}, \bar{\mathbf{A}} \in \mathbb{R}^{m_1 \times m_2}$ and $\mathbf{Q}, \bar{\mathbf{X}} \in \mathbb{R}^{n_1 \times n_2}$ the matrix forms of vectors $\mathbf{b}, \bar{\boldsymbol{\lambda}} \in \mathbb{R}^m$ and $\mathbf{q}, \bar{\mathbf{x}} \in \mathbb{R}^n$, respectively, it reads

$$\mathbf{B} = \mathbf{POISS}(\bar{\mathbf{A}}), \quad \bar{\mathbf{A}} = \mathbf{G}(\mathbf{A}(\bar{\mathbf{X}})) + \mathbf{Q}, \quad (7.5)$$

where, with a little abuse of notation, $\mathbf{A} : \mathbb{R}^{n_1 \times n_2} \rightarrow \mathbb{R}^{m_1 \times m_2}$ indicates here the linear operator encoded by matrix $\mathbf{A} \in \mathbb{R}^{m \times n}$ in the vectorized model (4.6), and where $\mathbf{POISS}(\bar{\mathbf{A}}) = \{\text{Pois}(\bar{\lambda}_{i,j})\}$ and $\mathbf{G}(\mathbf{A}(\bar{\mathbf{X}})) = \{g((\mathbf{A}(\bar{\mathbf{X}}))_{i,j})\}$, i.e. the matrix forms of vectors $\mathbf{Poiss}(\bar{\boldsymbol{\lambda}})$ and $\mathbf{g}(\mathbf{A}\bar{\mathbf{x}})$ in (4.6).

Before going into the details, first in Definition 7.2.1 we recall the formal definition of Poisson random variable and Poisson independent random field, then in Definition 7.2.2 we introduce their standard(ized) versions, whose main properties are finally highlighted in Proposition 7.2.1.

Definition 7.2.1 (Poisson random variable and independent random field). A discrete random variable B is said to be Poisson distributed with parameter $\lambda \in \mathbb{R}_{++}$, denoted by $B \sim \mathcal{P}(\lambda)$, if its probability mass function reads

$$P_B(b | \lambda) = \frac{\lambda^b e^{-\lambda}}{b!}, \quad b \in \mathbb{N}.$$

The expected value and variance of random variable B are given by

$$E[B] = \text{Var}[B] = \lambda.$$

A random field $\mathbf{B} = \{B_{i,j}\}$ is said to be independent Poisson distributed with parameter $\mathbf{\Lambda} = \{\lambda_{i,j}\}$, denoted by $\mathbf{B} \sim \mathcal{P}(\mathbf{\Lambda})$, if it satisfies:

$$B_{i,j} \sim \mathcal{P}(\lambda_{i,j}) \quad \forall (i,j) \in \mathbf{I}, \quad P_{\mathbf{B}}(\mathbf{B} | \mathbf{\Lambda}) = \prod_{(i,j) \in \mathbf{I}} P_{B_{i,j}}(b_{i,j} | \lambda_{i,j}). \quad (7.6)$$

Definition 7.2.2 (standard Poisson random variable and independent random field). Let $B \sim \mathcal{P}(\lambda)$. We call the discrete random variable Z defined by

$$Z = S_{\lambda}(B) := \frac{B - E[B]}{\sqrt{\text{Var}[B]}} = \frac{B - \lambda}{\sqrt{\lambda}} = \frac{1}{\sqrt{\lambda}} B - \sqrt{\lambda}, \quad (7.7)$$

as standard Poisson distributed with parameter λ , denoted by $Z \sim \tilde{\mathcal{P}}(\lambda)$.

Let $\mathbf{B} \sim \mathcal{P}(\mathbf{\Lambda})$. We call the random field defined by

$$\mathbf{Z} = \{Z_{i,j}\} \quad \text{with} \quad Z_{i,j} = S_{\lambda_{i,j}}(B_{i,j}) \quad \forall (i,j) \in \mathbf{I}, \quad (7.8)$$

as independent standard Poisson distributed with parameter $\mathbf{\Lambda}$, denoted by $\mathbf{Z} \sim \tilde{\mathcal{P}}(\mathbf{\Lambda})$.

Proposition 7.2.1. Let $Z \sim \tilde{\mathcal{P}}(\lambda)$ and let S_{λ} be the standardization function defined in (9.6). Then, the probability mass function, expected value and variance of random variable Z are given by:

$$P_Z(z|\lambda) = \frac{\lambda^{S_{\lambda}^{-1}(z)} e^{-\lambda}}{(S_{\lambda}^{-1}(z))!}, \quad z \in \{S_{\lambda}(0), S_{\lambda}(1), \dots\}, \quad S_{\lambda}^{-1}(z) = \sqrt{\lambda} z + \lambda, \quad (7.9)$$

$$E[Z] = 0, \quad \text{Var}[Z] = 1. \quad (7.10)$$

Hence, any independent standard Poisson random field $\mathbf{Z} \sim \tilde{\mathcal{P}}(\mathbf{\Lambda})$ is white.

Proof. The scalar affine standardization function $S_\lambda : \mathbb{N} \rightarrow \{S_\lambda(0), S_\lambda(1), \dots\}$ in (9.6) is bijective (as $\lambda \in \mathbb{R}_{++}$), hence it admits the inverse S_λ^{-1} defined in (7.9). The expression of P_Z in (7.9) thus comes from specifying the general form of the probability mass function of a discrete random variable defined by a bijective function of another discrete random variable. The fact that Z has zero-mean and unit-variance - as stated in (7.10) - comes immediately from the definition of S_λ in (9.6).

It thus follows from the definition of a standard Poisson independent random field $\mathfrak{Z} = \{Z_{i,j}\}$ given in (9.7) and from statement (7.10) that:

$$Z_{i,j} \sim \tilde{\mathcal{P}}(\lambda_{i,j}) \implies \begin{cases} \mathbb{E}[Z_{i,j}] = \mu_{\mathfrak{Z}} = 0 \\ \text{Var}[Z_{i,j}] = \sigma_{\mathfrak{Z}}^2 = 1 \end{cases}, \forall (i,j). \quad (7.11)$$

Moreover, it clearly comes from independence of a non-standard Poisson random field \mathfrak{B} - formalized in (9.5) - and from the entry-wise definition of random field standardization in (9.7) that independence also holds true for a standard Poisson random field \mathfrak{Z} ; in formula:

$$P_{\mathfrak{Z}}(\mathbf{Z} \mid \mathbf{\Lambda}) = \prod_{(i,j)} P_{Z_{i,j}}(z_{i,j} \mid \lambda_{i,j}).$$

Since independence implies uncorrelation and based on (7.11), we have

$$\text{Corr}[Z_{i_1,j_1}, Z_{i_2,j_2}] = \begin{cases} 0 & \text{for } (i_1, j_1) \neq (i_2, j_2), \\ \text{Var}[Z_{i_1,j_1}] = \sigma_{\mathfrak{Z}}^2 = 1 & \text{for } (i_1, j_1) = (i_2, j_2). \end{cases} \quad (7.12)$$

It follows from (7.11), (7.12) and from Definition 7.1.1 that \mathfrak{Z} is a weak stationary random field. Then, it comes from (7.12) and from Definition 7.1.2 that the ensemble normalized auto-correlation $\mathbf{A}[\mathfrak{Z}] = \{a_{l,m}[\mathfrak{Z}]\}$ satisfies

$$a_{l,m}[\mathfrak{Z}] = \begin{cases} 0 & \text{for } (l, m) \neq (0, 0), \\ 1 & \text{for } (l, m) = (0, 0). \end{cases}$$

Hence, based on Definition 7.1.3, we can conclude that any standard Poisson independent random field \mathfrak{Z} is white. \square

In light of Definition 7.2.1, the image formation model (7.5) can be written in probabilistic terms as follows:

$$\mathbf{B} \text{ realization of } \mathcal{B} \sim \mathcal{P}(\bar{\Lambda}), \quad (7.13)$$

with matrix $\bar{\Lambda}$ defined in (7.5).

Then, based on Definition 7.2.2, after introducing the matrix

$$\mathbf{Z} = \{z_{i,j}\} \text{ with } z_{i,j} = S_{\bar{\lambda}_{i,j}}(b_{i,j}) = \frac{b_{i,j} - \bar{\lambda}_{i,j}}{\sqrt{\bar{\lambda}_{i,j}}}, \quad (7.14)$$

the probabilistic model (7.13) can be equivalently written in standardized form as

$$\mathbf{Z} \text{ realization of } \mathcal{Z} \sim \tilde{\mathcal{P}}(\bar{\Lambda}).$$

That is, matrix \mathbf{Z} in (7.14) with $\bar{\Lambda}$ in (7.5) is the realization of an independent standard Poisson random field \mathcal{Z} which, according to Proposition 7.2.1, is white.

We note that, unlike the observed realization \mathbf{B} in (7.13), the realization \mathbf{Z} in (7.14) is not available as it depends on $\bar{\Lambda}$ which, in its turn, depends on the unknown uncorrupted image $\bar{\mathbf{X}}$. However, the whiteness property of \mathbf{Z} can be exploited for stating a new principle for automatically selecting the value of the regularization parameter μ in the class of \mathcal{R} -KL variational models.

Denoting by $\hat{\mathbf{X}}(\mu) = \{\hat{x}_{i,j}(\mu)\}$ the matrix form of the solution of a \mathcal{R} -KL model - e.g., of the TV-KL model in (TV-KL) - we introduce the μ -dependent matrices $\hat{\Lambda}(\mu), \hat{\mathbf{Z}}(\mu) \in \mathbb{R}^{m_1 \times m_2}$ given by

$$\hat{\Lambda}(\mu) = \{\hat{\lambda}_{i,j}(\mu)\} = \mathbf{G}(\mathbf{A}(\hat{\mathbf{X}}(\mu))) + \mathbf{Q}, \quad (7.15)$$

$$\hat{\mathbf{Z}}(\mu) = \{\hat{z}_{i,j}(\mu)\} \text{ with } \hat{z}_{i,j}(\mu) = S_{\hat{\lambda}_{i,j}(\mu)}(b_{i,j}) = \frac{b_{i,j} - \hat{\lambda}_{i,j}(\mu)}{\sqrt{\hat{\lambda}_{i,j}(\mu)}}, \quad (7.16)$$

The ideal goal of any criterion for choosing μ in the class of \mathcal{R} -KL models is to select the value μ^* yielding the closest solution image $\hat{\mathbf{X}}(\mu^*)$ to the target uncorrupted image $\bar{\mathbf{X}}$, according to some distance metric. The conjecture

behind our proposal is that the closer the solution $\widehat{\mathbf{X}}(\mu)$ is to the target $\overline{\mathbf{X}}$, the closer the matrix $\widehat{\mathbf{Z}}(\mu)$ defined in (7.15)-(7.16) will be to \mathbf{Z} in (7.14), so the more $\widehat{\mathbf{Z}}(\mu)$ will resemble the realization of a white random field. Hence, the proposed criterion, that we refer to as the Poisson Whiteness Principle (PWP), consists in choosing the value of μ leading to the less auto-correlated matrix $\widehat{\mathbf{Z}}(\mu)$. Based on the scalar normalized auto-correlation measure introduced in (7.3), the PWP reads:

$$\text{Select } \mu = \mu^* \in \arg \min_{\mu \in \mathbb{R}_{++}} \left\{ W(\mu) := \mathcal{W} \left(\widehat{\mathbf{Z}}(\mu) \right) \right\},$$

with matrix $\widehat{\mathbf{Z}}(\mu)$ defined in (7.15)-(7.16) and function \mathcal{W} in (7.3).
(PWP)

7.3 Numerical Results

In this section, we evaluate the performance of the proposed (PWP) for the selection of the regularization parameter μ in the (TV-KL) model employed for the solution of the IR and CTIR imaging problems. For a quantitative evaluation, the accuracy of the reconstructed images $\widehat{\mathbf{x}}(\mu)$ with respect to the original image $\bar{\mathbf{x}}$ is measured by means of two scalar metrics, the Structural Similarity Index (SSIM) [36] and the Signal-to-Noise-Ratio (SNR) defined in (6.23). The proposed PWP approach is compared with the state-of-the-art ADP and NEDP proposed in Chapter 6. The considered parameter selection rules are all applied *a posteriori*. The (TV-KL) model is solved by the ADMM approach outlined in section 10.1 for a very fine grid of different μ -values and for each reconstructed image $\widehat{\mathbf{x}}(\mu)$ we compute both the value of the discrepancy function $\mathcal{D}(\mu; \mathbf{b})$ defined in (5.2) and involved in the (ADP) and (NEDP) and the value of the whiteness function $W(\mu)$ defined and used in (PWP). In particular, we calculate $W(\mu)$ efficiently based on the Fourier-domain formula in (7.4). Then, we select the μ -values according to the (ADP) and (NEDP), denoted by $\mu^{(A)}$ and $\mu^{(NE)}$, as the ones corresponding to the intersection of $\mathcal{D}(\mu; \mathbf{y})$ with $\Delta^{(A)}$ and $\Delta^{(NE)}(\mu)$, respectively. The μ -value selected by the (PWP) is the one minimizing the

function $W(\mu)$ and is denoted by $\mu^{(W)}$. For each μ -value in the considered grid, we also compute the SNR and SSIM of the associated reconstructed image $\hat{\mathbf{x}}(\mu)$. Moreover, to evaluate in absolute terms the performance of the three compared selection criteria, we also compute the values $\mu^{(SNR)}$ and $\mu^{(SSIM)}$ of the regularization parameter which yield the reconstructed images exhibiting the highest SNR and the highest SSIM values, respectively. The two reconstructed images $\hat{\mathbf{x}}(\mu^{(SNR)})$, $\hat{\mathbf{x}}(\mu^{(SSIM)})$ and the associated SNR and SSIM quality metrics are then regarded as the best theoretical results achievable by the compared selection strategies. In all the performed tests, the iterations of the ADMM approach outlined in section 10.1 and used for the solution of the TV-KL model are stopped (in both the standard form for IR and semi-linearized form for CTIR) as soon as

$$\delta_{\mathbf{x}}^{(k)} := \frac{\|\mathbf{x}^{(k)} - \mathbf{x}^{(k-1)}\|_2}{\|\mathbf{x}^{(k-1)}\|_2} < 10^{-6}, \quad k \in \mathbb{N} \setminus \{0\},$$

while the ADMM penalty parameter γ is set manually so as to fasten the convergence of the alternating scheme. More specifically, we made some prior numerical tests and found that a suitable value in the IR case is $\gamma = 5$, while for the CTIR we set $\gamma = 10$.

7.3.1 CT image reconstruction

For the CT reconstruction problem we consider the test images **Shepp Logan** (500×500 , pixel size = 0.2mm) and **brain** (238×253 , pixel size=0.4mm), with pixel values between 0 and 1, shown Figures 7.1a, 7.1b, respectively. The acquisition process of the fan beam CT setup, i.e. the projection operator \mathbf{A} , is built using the ASTRA Toolbox [40] with the following parameters: 180 equally spaced angles of projections (from 0 to 2π), a detector with 500 pixels (detector pixel size = 1/3mm), distance between the source and the center of rotation = 300mm, distance between the center of rotation and the detector array = 200mm. The data are generated with the same procedure explained in 6.3.1 with

$$I_0 \in \{1.5, 5, 10, 20, 50, 100, 1000\}.$$

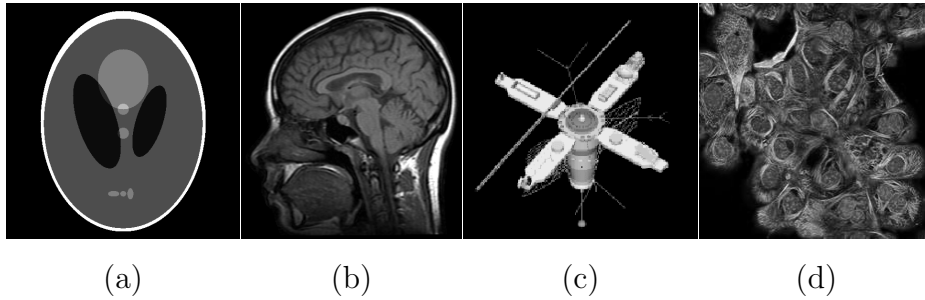


Figure 7.1: From left to right: original Shepp Logan (500×500), brain (238×253), satellite (256×256) and cells (236×236), test images considered for the numerical experiments.

In Figure 7.2c,d we show the whiteness function $W(\mu)$, as defined in PWP, for the first image Shepp Logan with $I_0 = 1.5$ (left) and $I_0 = 1000$ (right). The vertical dashed red lines correspond to the minimum of the function $W(\mu)$, i.e. to the value $\mu^{(W)}$ selected by the proposed (PWP). The black curves in Figure 7.2a,b represent the discrepancy function $\mathcal{D}(\mu; \mathbf{b})$ as defined in (5.2), while the green and magenta dashed lines represent the discrepancy values $\Delta^{(A)}$ and $\Delta^{(NE)}(\mu)$ as defined in ADP and NEDP, respectively. In Figure 7.2e,f, we show the SNR (in blue) and SSIM (in orange) values achieved for the limiting values of I_0 , i.e. $I_0 = 1.5$ (left) and $I_0 = 1000$ (right). The red, green and magenta vertical lines correspond to the μ values chosen with the newly proposed method and the two considered versions of the DP. In the case of $I_0 = 1.5$ the SNR/SSIM values achieved by ADP and NEDP are significantly far from the optimal ones. On the other hand, PWP one is very close to the maximum of both the SNR and the SSIM. For $I_0 = 1000$, the NEDP and the ADP select the same μ , which allows to achieve a larger SSIM with respect to the one obtained by PWP, while our method still outperforms the other in terms of SNR.

In Table 7.1, we report, for different counting regimes I_0 , the selected μ -values and the SNR/SSIM metrics for the three considered strategies as well as for the cases of maximum SNR and SSIM. For each I_0 , the highest values of SNR and SSIM achieved among the three compared methods, i.e.

the closest to the maximum achievable, are reported in bold.

From Table 7.1, we observe that the PWP outperforms the ADP and the NEDP in terms of SNR for each I_0 value, while the NEDP returns slightly better results in terms of SSIM for high-count acquisitions. We highlight that for mid- and high-doses, the quality metrics of the reconstructions by PWP are particularly close to the highest achievable. For a visual comparison, in Figure 7.3, we show the observed sinograms, the output reconstructions obtained by employing ADP, NEDP and PWP, and the one corresponding to the maximum SNR and SSIM for $I_0 = 1.5$ (top panels) and $I_0 = 1000$ (bottom panels). The reconstruction results shown in Figure 7.3 reflect the behavior of the plots. More specifically, for $I_0 = 1.5$ the ADP reconstruction appears to be over-regularized; NEDP allows to reconstruct only the central ellipsis, which appear to be merged; finally, in the PWP reconstruction the two ellipsis are more visible and the white edge of the phantom is sharper. In the case of $I_0 = 1000$, the three reconstructions are similar, with the PWP being more capable of separating the three fine details highlighted in the super-imposed close-up.

For the second test image, **brain**, we show in Figure 7.4 the behaviour of the discrepancy function $\mathcal{D}(\mu, \mathbf{b})$, of the whiteness function $W(\mu)$, as well as of the SNR and SSIM values for $I_0 = 1.5$ and $I_0 = 1000$. From Table 7.2, we note that the PWP achieves higher SNR and SSIM values compared to the ADP and NEDP for lower values of I_0 . However, we observe that when considering higher values of I_0 , the ADP reconstruction can outperform PWP for some of the considered doses. Moreover, notice that for some doses in the high-dose regime - e.g., $I_0 = 50, 1000$ - the PWP returns quality measures almost coinciding with the maximum SNR and SSIM achieved.

The reconstruction computed by ADP, NEDP and PWP are shown in Figure 7.5: we can see a higher level of details in the PWP reconstruction, both in the the low-dose and high-dose case. For $I_0 = 1.5$, only PWP is able to recover the upper part of the skull bone, while for $I_0 = 1000$ the difference mainly concerns the level of details present in the reconstruction, as shown

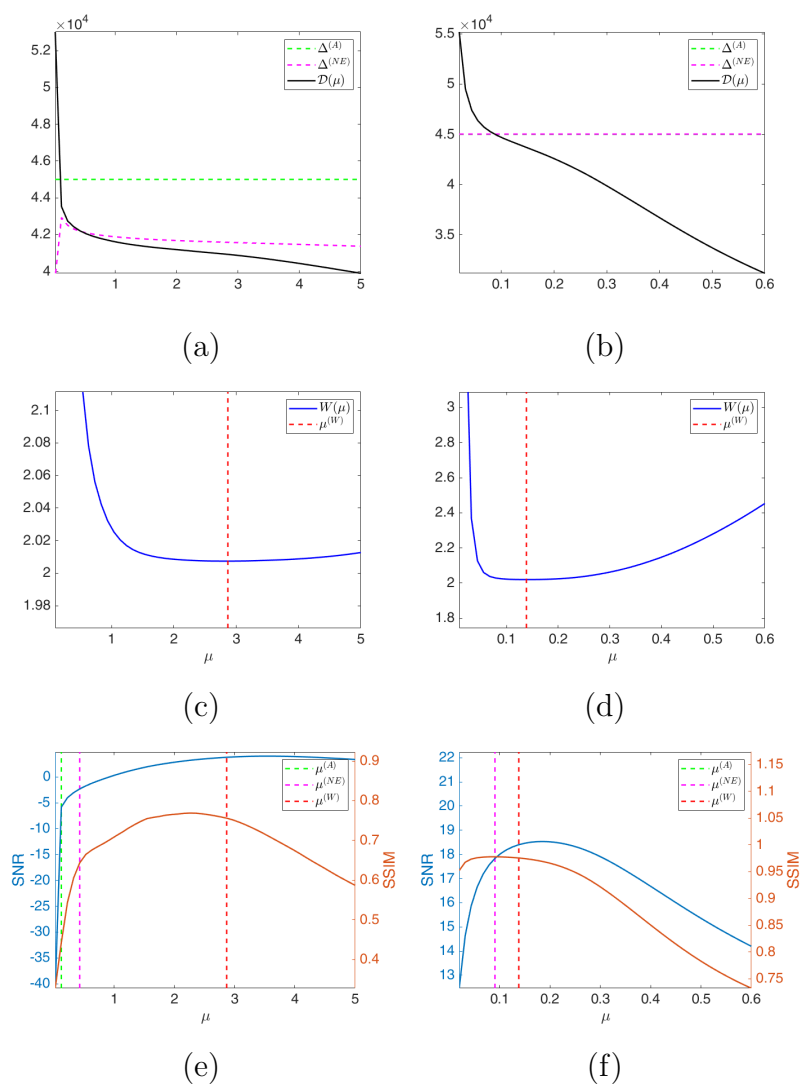


Figure 7.2: Test image Shepp Logan. From top to bottom: discrepancy curves, whiteness curves and achieved SNR/SSIM for $I_0 = 1.5$ (left) and $I_0 = 1000$ (right).

	I_0	1.5	5	10	20	50	100	1000
ADP	$\mu^{(A)}$	0.122	5.555	3.351	1.522	0.564	0.322	0.091
	SNR	-5.838	2.899	4.449	8.976	11.626	13.141	17.837
	SSIM	0.443	0.455	0.515	0.755	0.974	0.944	0.977
NEDP	$\mu^{(NE)}$	0.426	0.684	0.733	0.530	0.352	0.261	0.091
	SNR	-2.329	3.569	6.403	8.550	10.717	12.698	17.837
	SSIM	0.643	0.793	0.853	0.889	0.992	0.945	0.977
PWP	$\mu^{(W)}$	2.865	1.363	1.024	0.861	0.564	0.442	0.138
	SNR	3.785	5.997	7.441	9.786	11.626	13.436	18.401
	SSIM	0.756	0.816	0.856	0.883	0.974	0.935	0.975
SNR _{max}	$\mu^{(SNR)}$	3.470	2.042	1.461	1.001	0.654	0.443	0.186
	SNR	4.008	6.667	7.953	9.888	11.682	13.436	18.534
	SSIM	0.717	0.782	0.825	0.868	0.902	0.936	0.969
SSIM _{max}	$\mu^{(SSIM)}$	2.256	1.364	0.879	0.641	0.382	0.262	0.091
	SNR	3.202	5.997	7.009	9.165	10.945	12.698	17.838
	SSIM	0.769	0.817	0.858	0.892	0.919	0.946	0.978

Table 7.1: Test image Shepp Logan. Output μ -values and SNR/SSIM metrics for the CT reconstruction by ADP, NEDP, PWP and for the output CT reconstructions corresponding to the maximum SNR and SSIM achieved, for different I_0 .

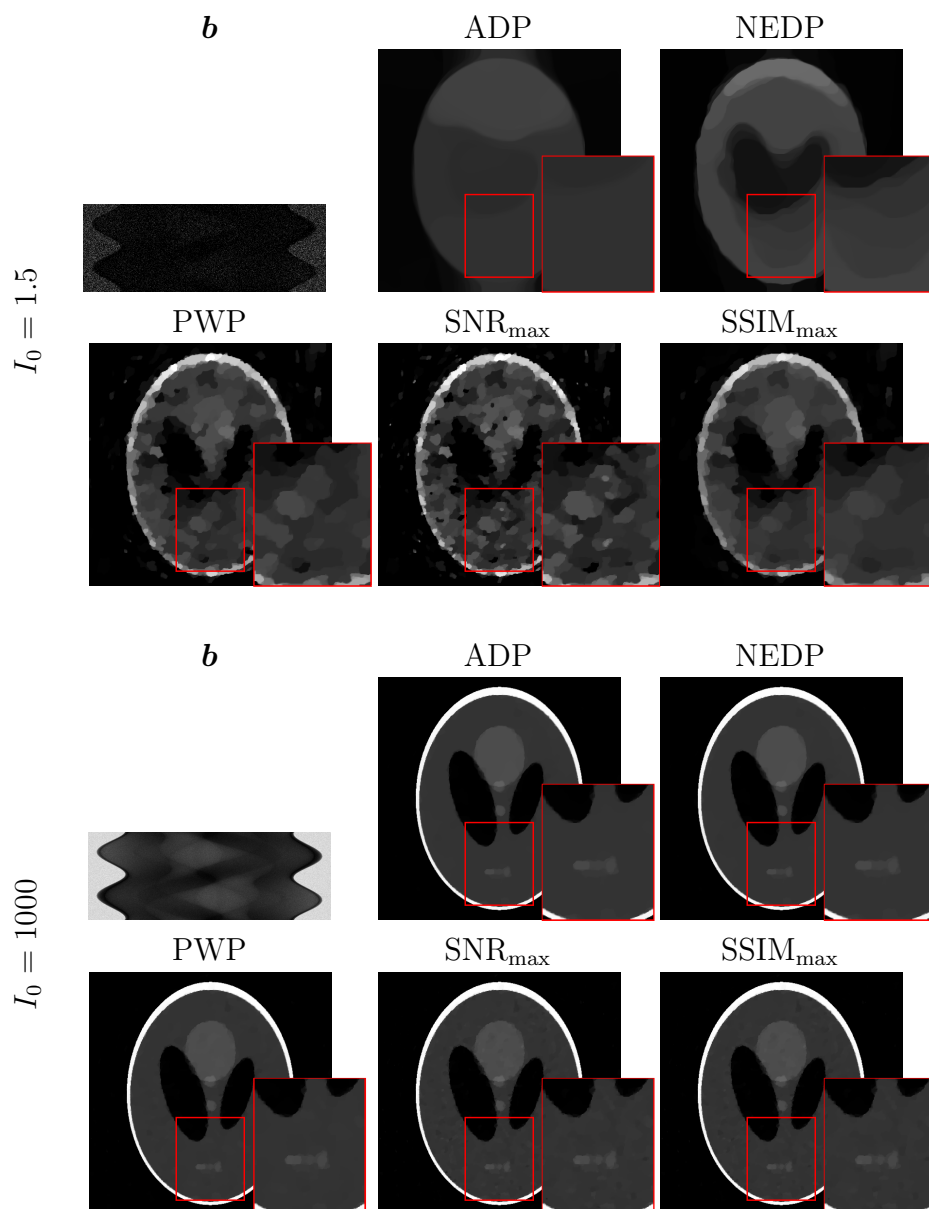


Figure 7.3: Test image Shepp Logan. Observed image b , CT reconstructions using the ADP, NEDP and PWP, and reconstructions corresponding to the maximum SNR and SSIM for $I_0 = 1.5$ (top panels) and $I_0 = 1000$ (bottom panels).

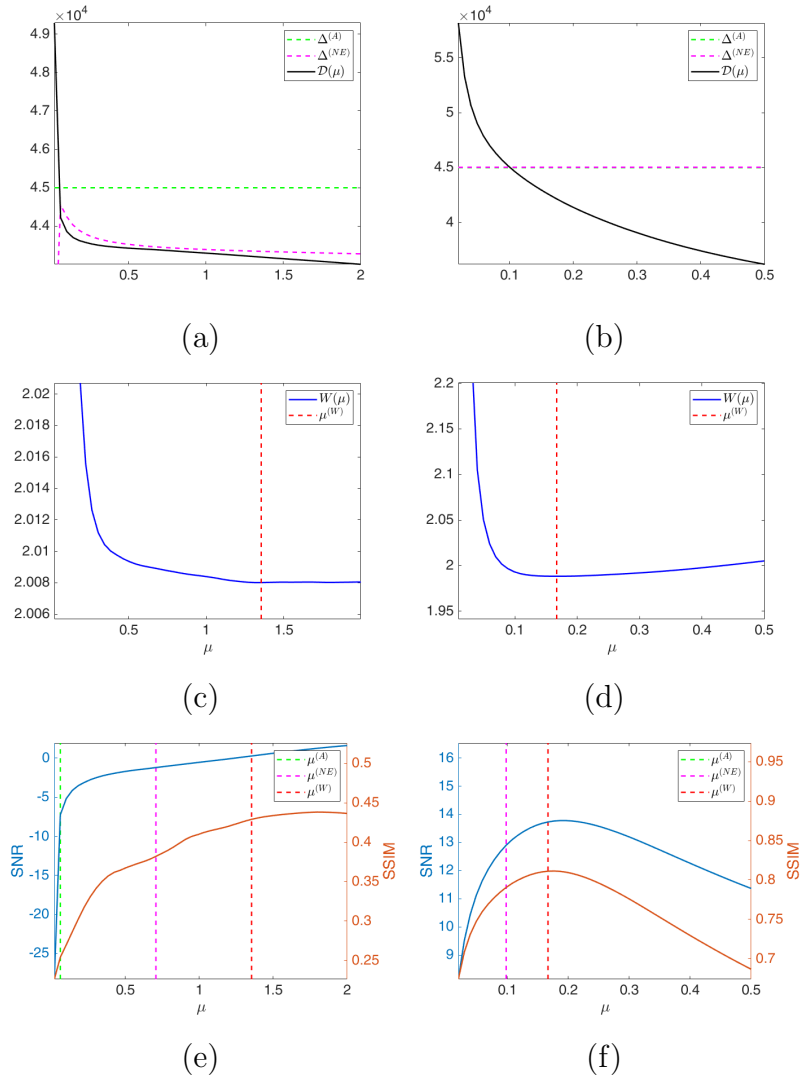


Figure 7.4: Test image **brain**. From top to bottom: discrepancy curves, whiteness curves and achieved SNR/SSIM for $I_0 = 1.5$ (left) and $I_0 = 1000$ (right).

	I_0	1.5	5	10	20	50	100	1000
ADP	$\mu^{(A)}$	0.060	2.657	2.428	1.302	0.516	0.300	0.098
	SNR	-7.251	3.308	3.432	6.154	8.162	8.970	12.901
	SSIM	0.254	0.323	0.311	0.466	0.622	0.672	0.790
NEDP	$\mu^{(NE)}$	0.706	0.428	0.542	0.383	0.320	0.257	0.098
	SNR	-1.200	0.468	3.340	4.714	7.636	8.580	12.901
	SSIM	0.382	0.432	0.523	0.556	0.612	0.666	0.790
PWP	$\mu^{(W)}$	1.853	2.200	0.771	0.420	0.589	0.286	0.166
	SNR	0.278	3.866	4.472	5.040	8.310	8.854	13.728
	SSIM	0.429	0.381	0.534	0.562	0.614	0.670	0.811
SNR _{max}	$\mu^{(SNR)}$	3.000	1.686	1.286	0.935	0.639	0.471	0.196
	SNR	2.327	4.138	5.308	6.801	8.333	9.549	13.776
	SSIM	0.374	0.444	0.499	0.547	0.606	0.663	0.810
SSIM _{max}	$\mu^{(SSIM)}$	1.798	1.057	0.829	0.641	0.467	0.343	0.177
	SNR	1.262	3.383	4.668	6.272	7.984	9.247	13.761
	SSIM	0.438	0.490	0.534	0.574	0.624	0.674	0.811

Table 7.2: Test image **brain**. Output μ -values and SNR/SSIM metrics for the CT reconstruction by ADP, NEDP, PWP and for the output reconstructions corresponding to the maximum SNR and SSIM achieved, for different I_0 .

in the close-ups.

7.3.2 Image restoration

We start testing our proposal on the image restoration task, and consider two test images, namely `satellite` (256×256 pixels) and `cells` (236×236 pixels), with pixel values between 0 and 1, shown in Figures 7.1a, 7.1b. We simulate the acquisition process in the same way as in 6.3.2 with

$$\kappa \in \{1.5, 5, 10, 20, 50, 100, 1000\}.$$

and space-invariant Gaussian blur with `band` = 5 and `sigma` = 1.

In analogy to the CT reconstruction case, in Figure 7.6 we report for the test image `satellite` the curve of the discrepancy function $\mathcal{D}(\mu, \mathbf{b})$, as well as the whiteness curve $W(\mu)$ and the curves of the SNR and SSIM for different μ values with $\kappa = 5, 10$. Note that, in the low-counting regime, the PWP achieves higher values of SNR and SSIM if compared to the ADP and NEDP.

From table 7.3 we observe that the PWP outperforms the ADP and NEDP in terms of SNR and SSIM for the low/middle counts acquisitions (up to $\kappa = 50$); in such scenarios, the obtained metrics are also particularly close to the highest SNR and SSIM achieved. For the higher counts NEDP and PWP return similar quality measures, with NEDP being slightly better. The restoration results shown in Figure 7.7 reflect the behavior of the plots. In both cases, the NEDP and the PWP return similar results, with the latter being more capable of preserving the original contrast in the image. On the other hand, the output images obtained by selecting μ according to ADP are strongly over-regularized.

For the last test image, `cells`, we report in Figure 7.8 the behavior of the discrepancy function $\mathcal{D}(\mu, \mathbf{b})$, of the whiteness function $W(\mu)$ and of the SNR/SSIM curves obtained by applying the NEDP, the ADP and the PWP, for $\kappa = 5$ (left) and $\kappa = 10$ (right). The PWP returns larger quality measures, as it is the closest to the maximum SNR/SSIM achievable.

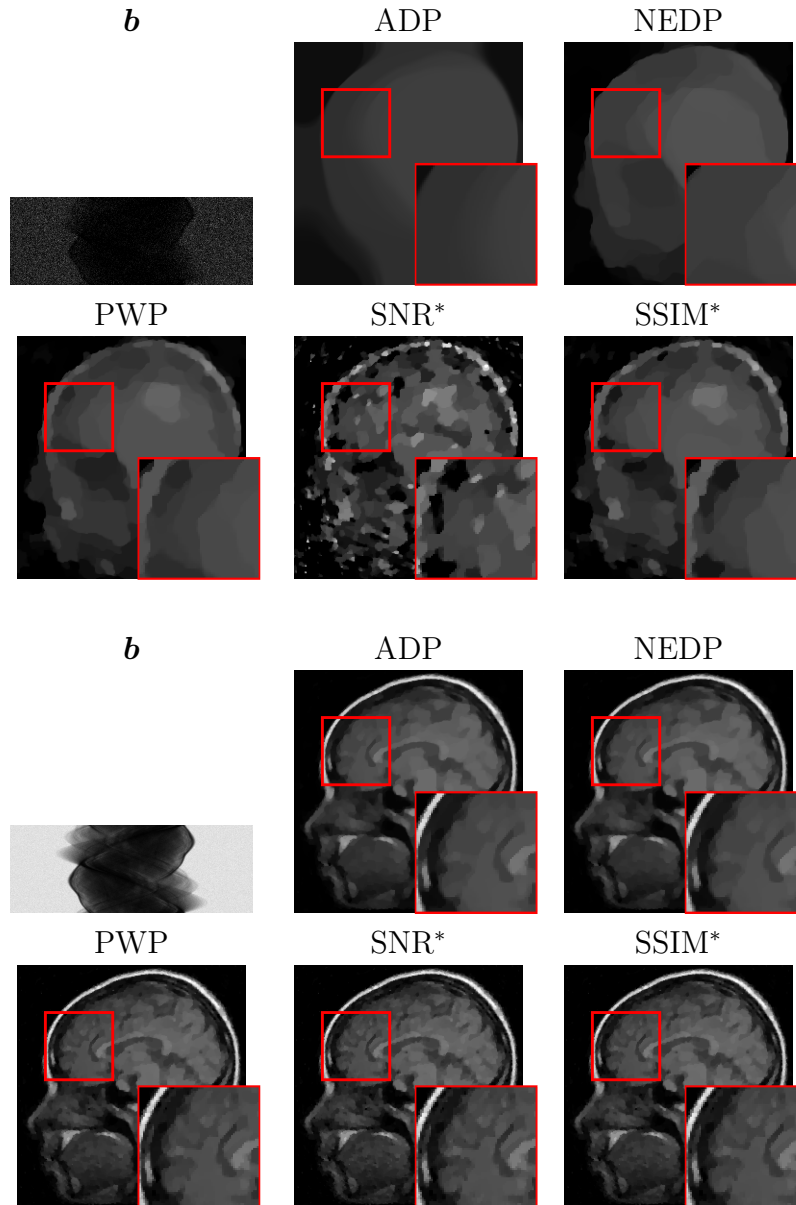


Figure 7.5: Test image brain. Observed image y , CT reconstructions using the ADP, NEDP and PWP, and reconstruction corresponding to the maximum SNR and SSIM for $I_0 = 1.5$ (top panels) and $I_0 = 1000$ (bottom panels).

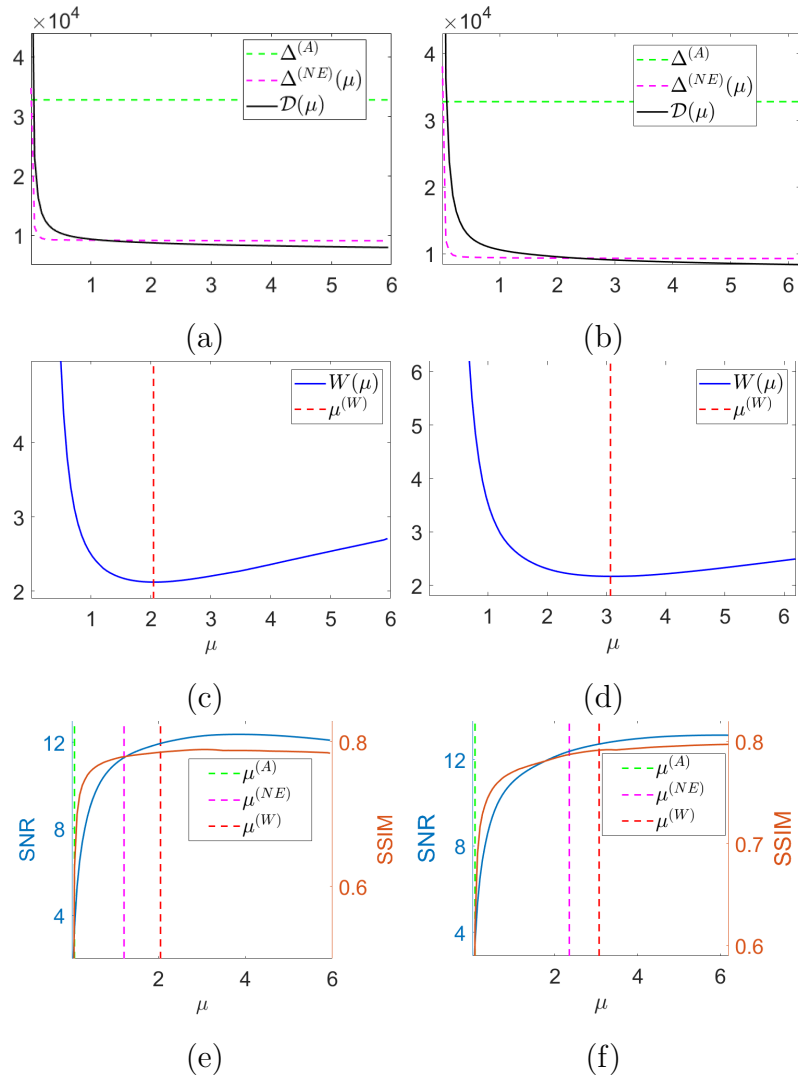


Figure 7.6: Test image satellite. From top to bottom: discrepancy curves, whiteness curves and achieved SNR/SSIM for $\kappa = 5$ (left) and $\kappa = 10$ (right).

	κ	1.5	5	10	20	50	100	1000
ADP	$\mu^{(A)}$	2×10^{-5}	0.065	0.068	0.188	0.380	0.760	8.260
	SNR	-0.001	3.408	3.508	6.580	8.688	10.574	14.747
	SSIM	0.009	0.625	0.619	0.708	0.724	0.742	0.805
NEDP	$\mu^{(NE)}$	0.841	1.205	2.348	3.848	6.800	11.380	60.760
	SNR	10.270	11.286	12.384	13.179	14.206	15.017	17.540
	SSIM	0.786	0.779	0.787	0.792	0.805	0.823	0.862
PWP	$\mu^{(W)}$	1.201	2.045	3.068	4.388	7.460	11.080	45.220
	SNR	10.618	11.944	12.719	13.328	14.313	14.983	17.225
	SSIM	0.787	0.785	0.791	0.794	0.808	0.822	0.857
SNR _{max}	$\mu^{(SNR)}$	1.561	3.845	5.948	10.841	20.563	35.562	251.685
	SNR	10.699	12.363	13.132	13.872	14.978	15.870	18.367
	SSIM	0.786	0.788	0.796	0.805	0.822	0.851	0.863
SSIM _{max}	$\mu^{(SSIM)}$	1.141	3.065	6.887	12.325	19.675	33.315	129.476
	SNR	10.589	12.302	13.105	13.851	14.977	15.860	18.130
	SSIM	0.787	0.789	0.797	0.806	0.823	0.852	0.866

Table 7.3: Test image `satellite`. Output μ -values and SNR/SSIM metrics for the restoration by ADP, NEDP, PWP and for the output restorations corresponding to the maximum SNR and SSIM achieved, for different κ .

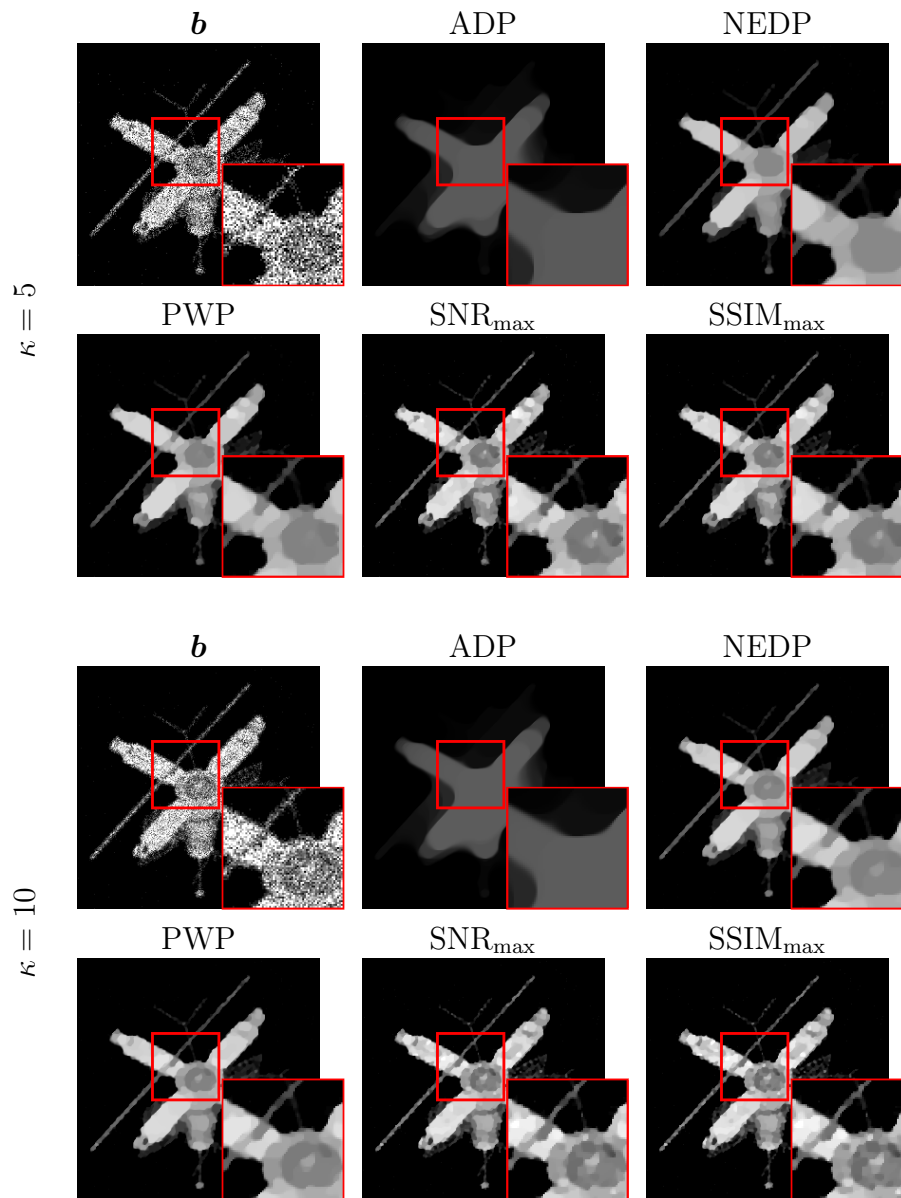


Figure 7.7: Test image *satellite*. Observed image \mathbf{b} , restorations using the ADP, NEDP and PWP, and restorations corresponding to the maximum SNR and SSIM for $\kappa = 5$ (top panels) and $\kappa = 10$ (bottom panels).

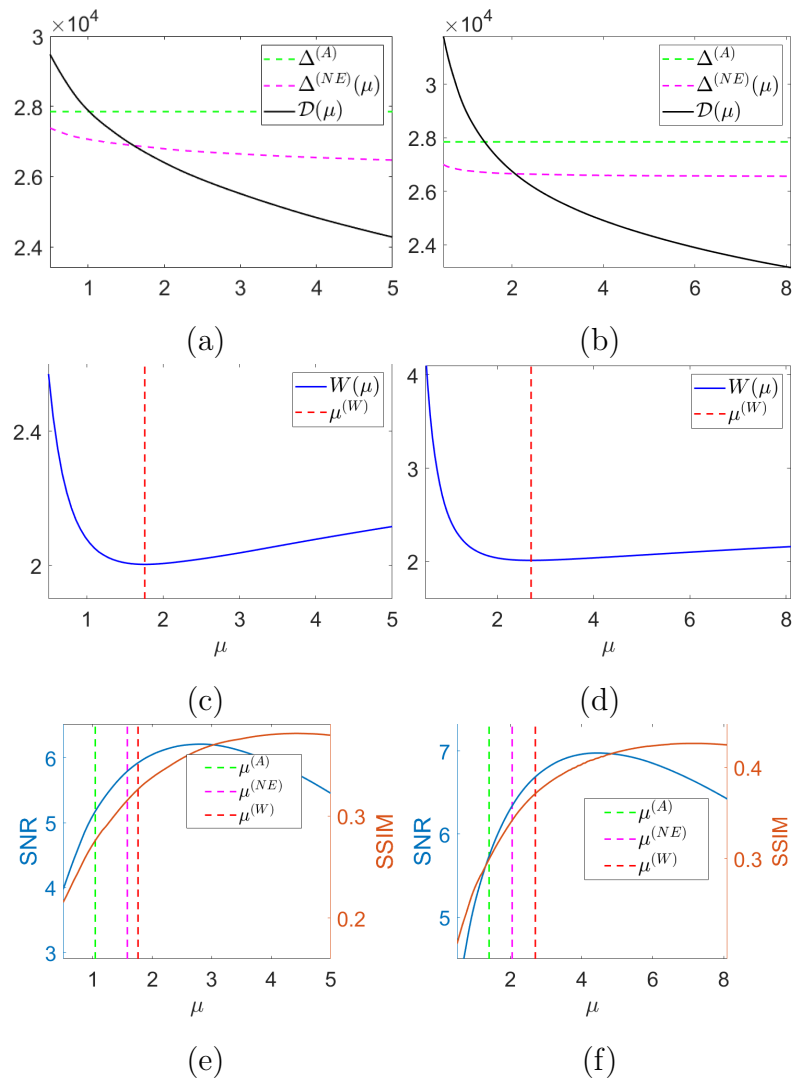


Figure 7.8: Test image cells. From top to bottom: discrepancy curves, whiteness curves and achieved SNR/SSIM for $\kappa = 5$ (left) and $\kappa = 10$ (right).

From Table 7.4, we note that the proposed μ -selection criterion returns restored images outperforming the ones obtained via the NEDP and ADP both in terms of SNR and SSIM, for every $\kappa \geq 5$. For $\kappa = 1.5$ the SNR and SSIM values of the PWP restoration are slightly lower, but very similar, to the one obtained with NEDP, while in all the other cases the difference between the PWP and the NEDP is more marked. In general, the percentage difference between the quality metrics achieved by the PWP and the ones corresponding to the maximum SNR and SSIM values appear to be very small, especially in low-counting regimes.

The restored images in Figure 7.9 reflect the values recorded in the tables: the output of the PWP preserve more details and the original contrast if compared to NEDP, while the ADP restoration seems to be less subject to over-regularization if compared to the results obtained on the test image `satellite`. This can be ascribed to the number of zeros in the image, being significantly smaller in `cells`.

7.3.3 Discussion

In this chapter we introduced a novel parameter selection strategy that relies on the extension of the whiteness principle designed for additive white noise to a suitably standardized version of the Poisson-corrupted observation. The derived Poisson whiteness principle has been extensively tested on image restoration and CT reconstruction problems. The Poisson whiteness principle has been compared experimentally with both the popular approximate discrepancy principle [25] and our nearly exact version of it illustrated in Chapter 6. The newly introduced approach has been shown to outperform the competitors especially in the low-counting regime for both the CT reconstruction and the image restoration problem.

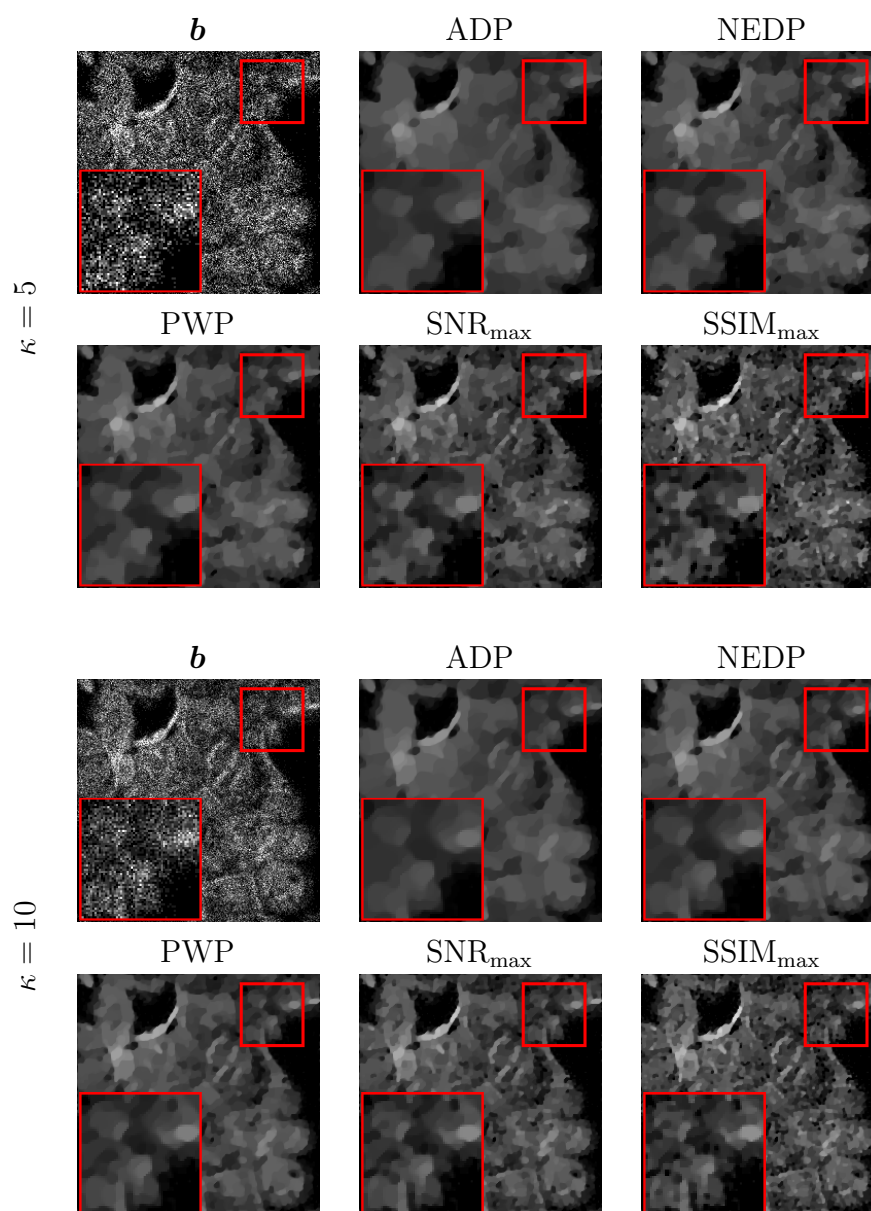


Figure 7.9: Test image `cells`. Observed image b , restorations using the ADP, NEDP and PWP, and restorations corresponding to the maximum SNR and SSIM for $\kappa = 5$ (top panels) and $\kappa = 10$ (bottom panels).

	κ	1.5	5	10	20	50	100	1000
ADP	$\mu^{(A)}$	7×10^{-5}	1.040	1.400	2.280	4.500	7.920	45.000
	SNR	0.004	5.176	5.737	6.626	7.830	8.735	11.075
	SSIM	0.077	0.276	0.299	0.363	0.452	0.532	0.717
NEDP	$\mu^{(NE)}$	0.875	1.580	2.060	3.600	6.600	10.680	52.140
	SNR	4.625	5.794	6.347	7.316	8.337	9.071	11.207
	SSIM	0.313	0.315	0.342	0.417	0.493	0.560	0.730
PWP	$\mu^{(W)}$	0.850	1.760	2.720	4.200	7.440	12.000	54.660
	SNR	4.601	5.924	6.695	7.503	8.470	9.186	11.248
	SSIM	0.311	0.326	0.372	0.433	0.505	0.571	0.733
SNR _{max}	$\mu^{(SNR)}$	1.193	2.840	4.285	7.784	15.332	24.675	179.852
	SNR	4.685	6.212	6.973	7.826	8.904	9.590	11.841
	SSIM	0.332	0.365	0.408	0.479	0.556	0.617	0.767
SSIM _{max}	$\mu^{(SSIM)}$	1.732	4.463	6.857	10.562	22.678	33.119	182.857
	SNR	4.064	5.766	6.700	7.659	8.751	9.531	11.840
	SSIM	0.340	0.380	0.426	0.487	0.563	0.623	0.768

Table 7.4: Test image cells. Output μ -values and SNR/SSIM metrics for the restoration by ADP, NEDP, PWP and for the output restorations corresponding to the maximum SNR and SSIM achieved, for different κ .

Chapter 8

Masked Unbiased Principles

In the two previous chapters we introduced and discussed the state-of-the-art discrepancy principle and two new ones (NEDP and PWP) for the automatic selection of the regularization parameter μ in the class of so-called TV-KL variational model in (TV-KL). In this chapter we will briefly review the most popular and effective existing *unmasked* principles (including the two very recent ones proposed in [39] and [41]), which fully exploit the information in the data without discarding any pixel. Then, inspired by the idea originally proposed in [31] to deal with low photon-counting scenarios, we introduce and discuss the *masked biased* versions of the previously reviewed unmasked principles, some of them already proposed in [31] and other new. These approaches come from simply discarding the zero-pixels in the acquired image when applying the principles while, at the same time, keeping the (Poisson) distribution of undiscarded data unchanged. Finally, we propose a whole new class of *masked unbiased* selection criteria based on the introduction of a novel positive Poisson distribution which suitably models the data statistics after discarding the zero-photon pixels. A theoretical analysis of the biases eliminated by using the new unbiased principles is also carried out. All this principles can be applied for the class of the so-called \mathcal{R} – KL variational models

$$\hat{\mathbf{x}}(\mu) \in \arg \min_{\mathbf{x} \in \mathbb{R}_+^n} \{ \mathcal{R}(\mathbf{x}) + \mu \text{KL}(\boldsymbol{\lambda}; \mathbf{b}) \}, \quad \boldsymbol{\lambda} = \mathbf{g}(\mathbf{A}\mathbf{x}) + \mathbf{q}, \quad (\mathcal{R}\text{-KL})$$

with \mathcal{R} being a general closed, proper and convex regularization term such as, e.g. (TV), (TV²) and (TGV²).

8.1 The “unmasked” principles

The principles introduced in the previous chapters exhibit a common property: that is they exploit all the information encoded in the observed data \mathbf{b} without discarding any pixels. For this reason, we will refer to them as *unmasked principles*. Let us briefly recall the notation and the four principles already discussed. To this aim, first we introduce the μ -dependent object

$$\widehat{\boldsymbol{\lambda}}(\mu) := \mathbf{g}(\mathbf{A} \widehat{\mathbf{x}}(\mu)) + \mathbf{q} \in \mathbb{R}^m,$$

which represents, for each selected μ value, an estimate of the unknown true noise-free target $\bar{\boldsymbol{\lambda}} = \mathbf{g}(\mathbf{A} \bar{\mathbf{x}}) + \mathbf{q}$ obtained by solving the (\mathcal{R} -KL) variational model. We also introduce the true and estimated standardized images

$$\bar{\mathbf{z}} := \frac{\mathbf{b} - \bar{\boldsymbol{\lambda}}}{\sqrt{\bar{\boldsymbol{\lambda}}}} \in \mathbb{R}^m, \quad \widehat{\mathbf{z}}(\mu) := \frac{\mathbf{b} - \widehat{\boldsymbol{\lambda}}(\mu)}{\sqrt{\widehat{\boldsymbol{\lambda}}(\mu)}} \in \mathbb{R}^m. \quad (8.1)$$

where all operations in the above definitions have to be intended component-wise. In 7.2.1 we proved that the original matrix (or image) form of vector $\bar{\mathbf{z}}$ above is the realization of a 2D white (i.e., uncorrelated) random field. In particular, each entry \bar{z}_i of $\bar{\mathbf{z}}$ is the realization of a scalar random variable with zero mean and unitary variance.

The approximate discrepancy principle (ADP)

$$\begin{aligned} &\text{Select } \mu = \mu^* \in \mathbb{R}_{++} \text{ such that } \mathcal{D}(\mu^*; \mathbf{b}) = \Delta^{(A)}, \\ &\text{with } \Delta^{(A)} := \sum_{i \in \mathcal{J}} \left(\delta^{(A)} := \frac{1}{2} \right) = \frac{m}{2}, \end{aligned} \quad (\text{ADP})$$

where $\mathcal{D}(\mu, \mathbf{b})$ is defined in (5.2).

The quadratic discrepancy principle (QDP)

$$\begin{aligned} &\text{Select } \mu = \mu^* \in \mathbb{R}_{++} \text{ such that } \mathcal{D}^{(Q)}(\mu^*; \mathbf{b}) = \Delta^{(Q)}, \\ &\text{with } \Delta^{(Q)} := \sum_{i \in \mathcal{J}} (\delta^{(Q)} = 1) = m, \end{aligned} \quad (\text{QDP})$$

where $\mathcal{D}^{(Q)}(\mu, \mathbf{b})$ is defined in (5.5).

The nearly exact discrepancy principle (NEDP)

$$\begin{aligned} &\text{Select } \mu = \mu^* \in \mathbb{R}_{++} \text{ such that } \mathcal{D}(\mu^*; \mathbf{b}) = \Delta^{(NE)}(\mu^*), \\ &\text{with } \Delta^{(NE)}(\mu) = \sum_{i \in \mathcal{J}} \left(\delta^{(NE)}(\widehat{\lambda}_i(\mu)) \right) = \frac{m}{2} + \sum_{i \in \mathcal{J}} \epsilon(\widehat{\lambda}_i(\mu)), \end{aligned} \quad (\text{NEDP})$$

where $\mathcal{D}(\mu, \mathbf{b})$ and $\Delta^{(NE)}(\mu)$ are defined in (5.2) and in (NEDP), respectively.

The whiteness principle (WP)

$$\text{Select } \mu = \mu^* \in \arg \min_{\mu \in \mathbb{R}_{++}} \{ W(\mu) := \mathcal{W}(\widehat{\mathbf{z}}(\mu)) \}, \quad (\text{PWP})$$

with matrix $\widehat{\mathbf{z}}(\mu)$ defined in (8.1) and function \mathcal{W} in (7.3).

8.2 The “masked biased” principles

After noting that the (ADP) and (QDP) principles can yield sub-optimal results in case of many zero-photon pixels, in [31] the authors proposed masked versions of those principles based on simply discarding all pixels measuring zero photons - i.e., pixels for which $b_i = 0$. We refer to these masked principles as *biased* since they do not consider that by carrying out a selection of pixels based on the value of the noise realization should require to change the statistics of the selected pixels, as it will be illustrated in the following section.

The masked versions of the exact discrepancy function \mathcal{D} in (5.2) used in the (ADP) and of the quadratically approximated discrepancy function $\mathcal{D}^{(Q)}$ in (5.5) used in the (QDP) - indicated by \mathcal{D}_+ and $\mathcal{D}_+^{(Q)}$, respectively - take clearly the following forms

$$\mathcal{D}_+(\mu; \mathbf{b}) := \sum_{i \in \mathcal{J}_+} F(\widehat{\lambda}_i(\mu); b_i), \quad \mathcal{D}_+^{(Q)}(\mu; \mathbf{b}) := \sum_{i \in \mathcal{J}_+} F^{(Q)}(\widehat{\lambda}_i(\mu); b_i),$$

with functions F and $F^{(Q)}$ defined in (4.10) and (5.4), respectively. Hence, based on their unmasked versions in (ADP) and (QDP), the ADP and QDP masked biased principles proposed in [31] - that we shortly refer to as ADP-MB and QDP-MB, respectively - can be formulated as follows:

$$\begin{aligned} &\text{Select } \mu = \mu^* \in \mathbb{R}_{++} \text{ such that } \mathcal{D}_+(\mu^*; \mathbf{b}) = \Delta_+^{(A)}, \\ &\text{with } \Delta_+^{(A)} := \sum_{i \in \mathcal{J}_+} \left(\delta^{(A)} = \frac{1}{2} \right) = \frac{m_+}{2}, \end{aligned} \quad (\text{ADP-MB})$$

$$\begin{aligned} &\text{Select } \mu = \mu^* \in \mathbb{R}_{++} \text{ such that } \mathcal{D}_+^{(Q)}(\mu^*; \mathbf{b}) = \Delta_+^{(Q)}, \\ &\text{with } \Delta_+^{(Q)} := \sum_{i \in \mathcal{J}_+} (\delta^{(Q)} = 1) = m_+, \end{aligned} \quad (\text{QDP-MB})$$

where m_+ indicates the cardinality of set \mathcal{J}_+ , namely the number of non-zero pixels.

Also the (NEDP) principle, which was proposed after [31], admits a masked biased version (NEDP-MB), which clearly reads:

$$\begin{aligned} &\text{Select } \mu = \mu^* \in \mathbb{R}_+ \text{ such that } \mathcal{D}_+(\mu^*; \mathbf{b}) = \Delta_+^{(NE)}(\mu), \\ &\text{with } \Delta_+^{(NE)}(\mu) := \sum_{i \in \mathcal{J}_+} \left(\delta^{(NE)}(\widehat{\lambda}_i(\mu)) \right) = \frac{m_+}{2} + \sum_{i \in \mathcal{J}_+} \epsilon(\widehat{\lambda}_i(\mu)). \end{aligned} \quad (\text{NEDP-MB})$$

Finally, by introducing the masked versions of standardized image in (8.1), namely

$$\widehat{\mathbf{z}}_+(\mu) = (\widehat{z}_{+,1}(\mu), \dots, \widehat{z}_{+,m}(\mu))^T \quad \text{with} \quad \widehat{z}_{+,i}(\mu) = \begin{cases} \widehat{z}_i(\mu) & \text{if } i \in \mathcal{J}_+ \\ 0 & \text{otherwise} \end{cases}, \quad (8.2)$$

the masked biased version of the WP (WP-MB) can be formulated as follows

$$\text{Select } \mu = \mu^* \in \arg \min_{\mu \in \mathbb{R}_{++}} \{ W_+(\mu) := \mathcal{W}(\widehat{\mathbf{z}}_+(\mu)) \}, \quad (\text{WP-MB})$$

with function $\mathcal{W}(\mathbf{z})$ defined as in (PWP).

8.3 The “masked unbiased” principles

As mentioned before, the *masked biased* principles are biased because they discard the zero pixels but do not change the statistics of the new data (without the zero pixels). There is therefore a bias, as we will show in the next section how the distribution changes. In the next subsection we introduce and analyze a novel scalar discrete distribution, called positive Poisson distribution, which correctly models the statistics of non-zero pixels considered in the masked selection principles. Based on such distribution, we then introduce the novel masked unbiased principles.

8.3.1 The new random variable: the Positive Poisson

In the following Definition 8.3.1 we recall the Poisson distribution and introduce the positive Poisson distribution, then in Proposition 8.3.1 we outline some important properties of positive Poisson-distributed random variables.

Definition 8.3.1 (Poisson and positive Poisson random variables). A discrete random variable B is said to be Poisson-distributed with parameter $\lambda \in \mathbb{R}_{++}$, denoted by $B \sim \mathcal{P}(\lambda)$, if its probability mass function reads

$$P_B(b) = \frac{\lambda^b \exp(-\lambda)}{b!}, \quad b \in \mathbb{N}.$$

The expected value, variance and second-order raw moment of B are given by

$$E[B] = \text{Var}[B] = \lambda, \quad E[B^2] = \lambda(\lambda + 1). \quad (8.3)$$

The discrete random variable B_+ defined by

$$B_+ := B \text{ if } B > 0 \quad (8.4)$$

is said to be positive Poisson-distributed with parameter λ and denoted by $B_+ \sim \mathcal{P}_+(\lambda)$.

Proposition 8.3.1. Let $B \sim \mathcal{P}(\lambda)$ and $B_+ \sim \mathcal{P}_+(\lambda)$, with $\lambda \in \mathbb{R}_{++}$, and let $T, V : \mathbb{R}_{++} \rightarrow \mathbb{R}$ be the functions defined by

$$T(\lambda) = \frac{1}{1 - \exp(-\lambda)}, \quad V(\lambda) = \frac{1 - (1 + \lambda) \exp(-\lambda)}{(1 - \exp(-\lambda))^2}. \quad (8.5)$$

Then, the probability mass function, expected value, second-order raw moment and variance of the positive Poisson-distributed random variable B_+ read

$$P_{B_+}(y) = T(\lambda) P_B(b) = \frac{1}{\exp(\lambda) - 1} \frac{\lambda^b}{b!}, \quad b \in \mathbb{N}_+, \quad (8.6)$$

$$E[B_+] = T(\lambda) E[B] = \frac{\lambda}{1 - \exp(-\lambda)}, \quad (8.7)$$

$$E[B_+^2] = T(\lambda) E[B^2] = \frac{\lambda(1 + \lambda)}{1 - \exp(-\lambda)}, \quad (8.8)$$

$$\text{Var}[B_+] = V(\lambda) \text{Var}[B] = \frac{\lambda}{(1 - \exp(-\lambda))^2} \left(1 - \frac{1 + \lambda}{\exp(\lambda)}\right) \quad (8.9)$$

where \mathbb{N}_+ indicates the set of positive natural numbers. For any $\lambda \in \mathbb{R}_{++}$, P_{B_+} , $E[B_+]$, $E[B_+^2]$ and $\text{Var}[B_+]$ in (8.6)-(8.9) satisfy

$$\begin{aligned} P_{B_+}(b) &> P_B(b) \quad \forall b \in \mathbb{N}_+, & E[B_+] &> E[B], \\ E[B_+^2] &> E[B^2], & \text{Var}[B_+] &< \text{Var}[B]. \end{aligned} \quad (8.10)$$

Moreover, for λ tending to 0 and λ tending to $+\infty$, we have

$$\lim_{\lambda \rightarrow 0} P_{B_+}(b) = \begin{cases} 1 & \text{for } b = 1, \\ 0 & \text{for } b > 1 \end{cases}, \quad \lim_{\lambda \rightarrow +\infty} P_{B_+}(b) = P_B(b) \quad \forall b \in \mathbb{N}_+, \quad (8.11)$$

$$\lim_{\lambda \rightarrow 0} E[B_+] = 1, \quad \lim_{\lambda \rightarrow +\infty} E[B_+] = E[B], \quad (8.12)$$

$$\lim_{\lambda \rightarrow 0} E[B_+^2] = 1, \quad \lim_{\lambda \rightarrow +\infty} E[B_+^2] = E[B^2], \quad (8.13)$$

$$\lim_{\lambda \rightarrow 0} \text{Var}[B_+] = 0, \quad \lim_{\lambda \rightarrow +\infty} \text{Var}[B_+] = \text{Var}[B]. \quad (8.14)$$

Proof. It easily follows from definition (8.4) that, for any $\lambda \in \mathbb{R}_{++}$, the probability mass function $P_{B_+}(b)$ of $B_+ \sim \mathcal{P}_+(\lambda)$ is a (positively) scaled

version of the probability mass function $P_B(b)$ of $B \sim \mathcal{P}(\lambda)$ for $b \in \mathbb{N}_+$. In formula,

$$\forall \lambda \in \mathbb{R}_{++}, \quad \exists \alpha(\lambda) \in \mathbb{R}_{++} : \quad P_{B_+}(b) = \alpha(\lambda) P_B(b) \quad \forall b \in \mathbb{N}_+. \quad (8.15)$$

By imposing that the probability mass function P_{B_+} sums to one, it is easy to prove that $\alpha(\lambda)$ in (8.15) coincides with function $T(\lambda)$ in (8.5), thus demonstrating (8.6):

$$\begin{aligned} \sum_{b=1}^{\infty} P_{B_+}(b) = 1 &\iff \alpha(\lambda) \sum_{b=1}^{\infty} P_B(b) = 1 \iff \\ &\iff \alpha(\lambda) = \frac{1}{\sum_{z=0}^{\infty} P_B(b) - P_B(0)} \iff \alpha(\lambda) = \frac{1}{1 - \exp(-\lambda)} = T(\lambda). \end{aligned}$$

Then, it easily follows from (8.6) that the m -th order raw moments of B_+ are given by

$$\begin{aligned} E[B_+^m] &= \sum_{b=1}^{\infty} b^m P_{B_+}(y) = T(\lambda) \sum_{b=1}^{\infty} b^m P_B(b) \\ &= T(\lambda) \sum_{b=0}^{\infty} b^m P_B(b) = T(\lambda) E[B^m], \end{aligned}$$

for any $m \in \mathbb{N}$. By specifying the above formula for $m = 1$ and $m = 2$, one gets (8.7) and (8.8), respectively. It follows from (8.7)-(8.8) that

$$\begin{aligned} \text{Var}[Z] &= E[(B_+ - E[B_+])^2] = E[B_+^2] - (E[B_+])^2 \\ &= T(\lambda) E[B^2] - (T(\lambda) E[B])^2 = T(\lambda) (\lambda(1 + \lambda) - T(\lambda) \lambda^2) \\ &= T(\lambda) (1 + \lambda - \lambda T(\lambda)) \lambda = V(\lambda) \text{Var}[B], \end{aligned} \quad (8.16)$$

where the last equality in (8.16) comes from the definition of functions T and V in (8.5) and from recalling that $\text{Var}[B] = \lambda$.

Then, the inequalities in (8.10) and the four asymptotic properties (for $\lambda \rightarrow +\infty$) in (8.11)-(8.14) come from (8.6)-(8.9) and the following easily

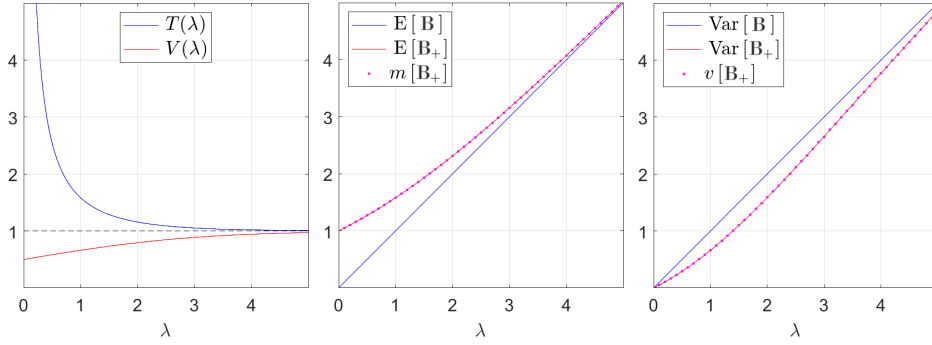


Figure 8.1: Plots of functions $T(\lambda)$, $V(\lambda)$ defined in (8.5) (left) and comparison between the expected values (centre) and the variances (right) of $B \sim \mathcal{P}(\lambda)$ and $B_+ \sim \mathcal{P}_+(\lambda)$ given in (8.3) and in (8.7),(8.9), respectively, for varying λ . The magenta dots represent the sample means $m[B_+]$ (centre) and the sample variances $v[B_+]$ (right) of very large numbers of realizations of the random variable B_+ , for 50 different values of the parameter λ , namely $\lambda \in \{0.1, 0.2, \dots, 4.9, 5\}$.

provable - see the plots in Figure 8.1 - properties of functions T and V defined in (8.5):

$$T(\lambda) > 1 \quad \forall \lambda \in \mathbb{R}_{++}, \quad V(\lambda) < 1 \quad \forall \lambda \in \mathbb{R}_{++},$$

$$\lim_{\lambda \rightarrow +\infty} T(\lambda) = \lim_{\lambda \rightarrow +\infty} V(\lambda) = 1.$$

Finally, the four asymptotic properties (for $\lambda \rightarrow 0$) in (8.11)-(8.14) comes directly from taking the limits as λ approaches 0 of the four functions defined in (8.6)-(8.9). \square

In Figure 8.1 we give a graphical representation of some of the quantities introduced in Proposition 8.3.1. In particular, the sample means $m[B_+]$ and sample variances $v[B_+]$ (indicated by magenta dots and obtained by a simple Montecarlo simulation) provide an experimental validation of the theoretically derived formulas for the expected value $E[B_+]$ in (8.7) and the variance $\text{Var}[B_+]$ in (8.9).

It is now clear that the Poisson and the positive Poisson random variables are characterized by significantly different statistical properties, especially for

small values of the parameter λ . In this perspective, Proposition 8.3.1 already warns on the approximations that the masked formulations of the principles given in Section 8.2 bring along. An analysis of the introduced biases will be carried out in Section 8.3.6.

In the next subsections, we are going to show how the newly introduced positive Poisson distribution can be adopted so as to formulate masked unbiased versions of the original principles reviewed here.

8.3.2 Masked unbiased approximate discrepancy principle (ADP-M)

As previously outlined, the approximate discrepancy value $\delta^{(A)} = 1/2$ used in the ADP relies on truncating at the first order the Taylor expansion of $E[F(\lambda; B)]$, with B a Poisson-distributed random variable with mean λ . It can be proved that, in the masked unbiased case (where B is replaced by B_+), the expected value $E[F(\lambda; B_+)]$ admits a Taylor expansion which also coincides with $1/2$ when truncated at the first order.

Hence, masked biased and masked unbiased versions of the ADP coincide; in what follows, they will be indistinctly referred to as ADP-M.

8.3.3 Masked unbiased quadratic discrepancy principle (QDP-MU)

In light of statements (8.7) and (8.9) in Proposition 8.3.1, we introduce the function

$$F^{(QU)}(\lambda_i; b_i) = \left(\frac{b_i - \lambda_i T(\lambda_i)}{\sqrt{\lambda_i V(\lambda_i)}} \right)^2, \quad b_i \in \mathbb{N} \setminus \{0\}.$$

Relying on the properties of the novel positive Poisson distribution, it is easy to observe that

$$\delta^{(QU)} := E[F^{(QU)}(\lambda_i; B_{+,i})] = 1.$$

After introducing the unbiased version of the masked quadratically approximated discrepancy function $\mathcal{D}_+^{(Q)}$ defined in (5.2) and used in the (QDP-MB), namely

$$\mathcal{D}_+^{(QU)}(\mu; \mathbf{b}) := \sum_{i \in \mathcal{J}_+} F^{(QU)}(\widehat{\lambda}_i(\mu); b_i),$$

we get the following formulation for the masked unbiased QDP, referred to as QDP-MU,

$$\begin{aligned} \text{Select } \mu = \mu^* \in \mathbb{R}_{++} \text{ such that } \mathcal{D}_+^{(QU)}(\mu^*; \mathbf{b}) = \Delta_+^{(QU)}, \\ \text{with } \Delta_+^{(QU)} := \sum_{i \in \mathcal{J}_+} (\delta^{(QU)} = 1) = m_+. \end{aligned} \quad (\text{QDP-MU})$$

8.3.4 Masked unbiased nearly exact discrepancy principle (NEDP-MU)

The masked unbiased version of NEDP (NEDP-MU) is obtained - analogously to the unmasked NEDP illustrated in [39] - by applying the weighted least squares fitting method to approximate the behavior of the sample means of large numbers of realizations of random quantity $F(\lambda_i; B_{+,i})$, with F defined in (4.10). We thus get:

$$\text{Select } \mu = \mu^* \in \mathbb{R}_{++} \text{ such that } \mathcal{D}_+(\mu^*; \mathbf{b}) = \frac{m_+}{2} + \sum_{i \in \mathcal{J}_+} \epsilon^{(U)}(\widehat{\lambda}_i(\mu)), \quad (\text{NEDP-MU})$$

with

$$\epsilon^{(U)}(\lambda) = \frac{\lambda^3 + 30.7436\lambda^2 - 2.2968\lambda + 1.0827}{12\lambda^4 + 90.1921\lambda^3 - 1.8872\lambda^2 + 6.1778\lambda}. \quad (8.17)$$

8.3.5 Masked unbiased whiteness principle (WP-MU)

We start noticing that the standardized image $\widehat{\mathbf{z}}_+(\mu)$ in (8.2), which comes from a blind masking of the original $\widehat{\mathbf{z}}(\mu)$ can not be considered a realization of a white random process. Therefore, we introduce the novel standardized

image

$$\widehat{\mathbf{z}}^{(U)}(\mu) = \frac{\mathbf{b} - \widehat{\boldsymbol{\lambda}} \mathbf{T}(\widehat{\boldsymbol{\lambda}}(\mu))}{\sqrt{\widehat{\boldsymbol{\lambda}}(\mu) \mathbf{V}(\widehat{\boldsymbol{\lambda}}(\mu))}} \in \mathbb{R}^n,$$

where $\mathbf{T}(\boldsymbol{\lambda}) := (T(\lambda_1), \dots, T(\lambda_m))^T$ and $\mathbf{V}(\boldsymbol{\lambda}) := (V(\lambda_1), \dots, V(\lambda_m))^T$, with functions T and V defined in (8.5). The masked vector $\widehat{\mathbf{z}}_+^{(U)} \in \mathbb{R}^n$ corresponding to the new standardization reads

$$\widehat{\mathbf{z}}_+^{(U)}(\mu) = \left(\widehat{z}_{+,1}^{(U)}(\mu), \dots, \widehat{z}_{+,m}^{(U)}(\mu) \right)^T \quad \text{with} \quad \widehat{z}_{+,i}^{(U)}(\mu) = \begin{cases} \widehat{z}_i^{(U)}(\mu) & \text{if } i \in \mathcal{J}_+ \\ 0 & \text{otherwise} \end{cases},$$

One can clearly observe that, in light of the results summarized in Proposition 8.3.1, $\widehat{\mathbf{z}}_+^{(U)}$ is a realization of a white random process, thus suggesting the following formulation for the masked unbiased version of the WP (WP-MU)

$$\text{Select } \mu = \mu^* \in \arg \min_{\mu \in \mathbb{R}_{++}} \left\{ W_+^{(U)}(\mu) := \mathcal{W} \left(\widehat{\mathbf{z}}_+^{(U)}(\mu) \right) \right\}, \quad (\text{WP-MU})$$

with function $\mathcal{W}(\mathbf{z})$ defined as in (PWP).

8.3.6 Analysis of bias

In light of the introduced unbiased masked principles, in this section we carry out some analysis of the pixel-wise biases of the masked biased principles illustrated in Section 8.2. To this purpose, first we give the following result.

Proposition 8.3.2. Let $B \sim \mathcal{P}(\lambda)$ and $B_+ \sim \mathcal{P}_+(\lambda)$, with $\lambda \in \mathbb{R}_{++}$, and let $Z_+^{(B)}$ and $Z_+^{(U)}$ be the biased and unbiased standardized positive Poisson random variables defined by

$$Z_+^{(B)} = \frac{B_+ - \mathbf{E}[B]}{\sqrt{\text{Var}[B]}}, \quad Z_+^{(U)} = \frac{B_+ - \mathbf{E}[B_+]}{\sqrt{\text{Var}[B_+]}}.$$

Then, it holds true that

$$\mathbf{E} \left[Z_+^{(B)} \right] = \sqrt{\lambda} (T(\lambda) - 1), \quad \mathbf{E} \left[\left(Z_+^{(B)} \right)^2 \right] = T(\lambda) - \lambda (T(\lambda) - 1), \quad (8.18)$$

$$\text{Var} \left[Z_+^{(B)} \right] = T(\lambda) (1 - \lambda (T(\lambda) - 1)), \quad (8.19)$$

$$\mathbf{E} \left[Z_+^{(U)} \right] = 0, \quad \mathbf{E} \left[\left(Z_+^{(U)} \right)^2 \right] = \text{Var} \left[Z_+^{(U)} \right] = 1. \quad (8.20)$$

Proof. First, the fact that $Z_+^{(U)}$ has zero mean and unitary second-order raw moment and variance comes in a straightforward manner from its definition.

Then, for what concern $Z_+^{(B)}$, after recalling that $E[B] = \text{Var}[B] = \lambda$, it holds true that

$$\begin{aligned} E \left[Z_+^{(B)} \right] &= E \left[\frac{B_+ - E[B]}{\sqrt{\text{Var}[B]}} \right] = E \left[\frac{B_+ - \lambda}{\sqrt{\lambda}} \right] = \frac{1}{\sqrt{\lambda}} E [B_+ - \lambda] \\ &= \frac{1}{\sqrt{\lambda}} (E [B_+] - \lambda) = \sqrt{\lambda} (T(\lambda) - 1), \end{aligned} \quad (8.21)$$

where the last equality in (8.21) comes from replacing the expression of $E[B_+]$ given in (8.7). Then, by recalling also the expression of $E [B_+^2]$ in (8.8), we have that

$$\begin{aligned} E \left[\left(Z_+^{(B)} \right)^2 \right] &= E \left[\frac{(B_+ - E[B])^2}{\text{Var}[B]} \right] = E \left[\frac{(B_+ - \lambda)^2}{\lambda} \right] \\ &= \frac{1}{\lambda} E [B_+^2 - 2\lambda B_+ + \lambda^2] = \frac{1}{\lambda} (E [B_+^2] - 2\lambda E[B_+] + \lambda^2) \\ &= \frac{1}{\lambda} (T(\lambda) (\lambda + \lambda^2) - 2\lambda^2 T(\lambda) + \lambda^2) \\ &= \frac{1}{\lambda} (\lambda T(\lambda) - \lambda^2 T(\lambda) + \lambda^2) = \lambda + T(\lambda) - \lambda T(\lambda) \\ &= T(\lambda) - \lambda (T(\lambda) - 1). \end{aligned} \quad (8.22)$$

Finally, based on (8.21) and (8.22), the variance in (8.19) can be computed as follows

$$\begin{aligned} \text{Var} \left[Z_+^{(B)} \right] &= E \left[\left(Z_+^{(B)} \right)^2 \right] - \left(E \left[Z_+^{(B)} \right] \right)^2 \\ &= T(\lambda) - \lambda (T(\lambda) - 1) - \lambda (T(\lambda) - 1)^2 \\ &= T(\lambda) - \lambda T(\lambda) + \lambda - \lambda T^2(\lambda) + 2\lambda T(\lambda) - \lambda \\ &= T(\lambda) + \lambda T(\lambda) - \lambda T^2(\lambda) = T(\lambda) (1 + \lambda - \lambda T(\lambda)) \\ &= T(\lambda) (1 - \lambda (T(\lambda) - 1)). \end{aligned} \quad (8.23)$$

□

In what follows, we compare the masked biased and masked unbiased versions of the QDP, NEDP and WP in terms of some pixel-based bias func-

tions. We recall that for the ADP the bias has to be considered constantly zero as the masked biased and the masked unbiased versions coincide.

As the definition of the QDP, in its unmasked, masked biased and masked unbiased version, is related to the behavior of the sample variance of the noise realization vector approximated by the residual image, we introduce the following bias function $\beta_{\text{QDP}} : \mathbb{R}_{++} \rightarrow \mathbb{R}$ to measure the inaccuracy introduced by the QDP-MB at each pixel

$$\beta_{\text{QDP}}(\lambda) = \mathbb{E} \left[\left(Z_+^{(B)} \right)^2 \right] - \mathbb{E} \left[\left(Z_+^{(U)} \right)^2 \right] = T(\lambda) - \lambda(T(\lambda) - 1) - 1. \quad (8.24)$$

In the case of NEDP, the bias can be measured in terms of the difference between the building functions used to approximate the behavior of the exact expected value arising in (EDP). We thus introduce the pixel-based bias function $\beta_{\text{NEDP}} : \mathbb{R}_{++} \rightarrow \mathbb{R}$ which is defined as

$$\beta_{\text{NEDP}}(\lambda) = \epsilon(\lambda) - \epsilon_U(\lambda) \quad (8.25)$$

with $\epsilon(\lambda)$, $\epsilon_U(\lambda)$ given in (6.22), (8.17), respectively.

Finally, for what concerns the WP, we point out that measuring the bias in terms of the auto-correlation of the normalized random variables $Z_+^{(B)}$, $Z_+^{(U)}$ - that would be the most natural choice in this scenario - is unfeasible; hence we rather measure how far is $Z_+^{(B)}$ from being a zero-mean random variable with constant (unitary) standard deviation. In other words, we introduce the two pixel-based bias functions $\beta_{\text{WP},\eta}, \beta_{\text{WP},\sigma} : \mathbb{R}_{++} \rightarrow \mathbb{R}$ defined as

$$\begin{aligned} \beta_{\text{WP},\eta}(\lambda) &= \mathbb{E} \left[Z_+^{(B)} \right] - \mathbb{E} \left[Z_+^{(U)} \right] = \sqrt{\lambda} (T(\lambda) - 1), \\ \beta_{\text{WP},\sigma}(\lambda) &= \sqrt{\text{Var} \left(Z_+^{(B)} \right)} - \sqrt{\text{Var} \left(Z_+^{(U)} \right)} = \sqrt{T(\lambda) (1 - \lambda(T(\lambda) - 1))} - 1. \end{aligned} \quad (8.26)$$

In Figure 8.2, we show the behavior of the pixel-based bias functions in (8.24), (8.25), (8.26) for three different ranges of λ , namely $(0, 0.1]$, $(0.1, 5]$, $(5, 200]$. Notice that the bias is particularly relevant for very small values of λ , while it tends to 0 as λ increases. Such behavior reflects the theoretical results given in Proposition 8.3.2, whence we have that the statistical properties of $Z_+^{(B)}$, $Z_+^{(U)}$ coincide as $\lambda \rightarrow +\infty$.

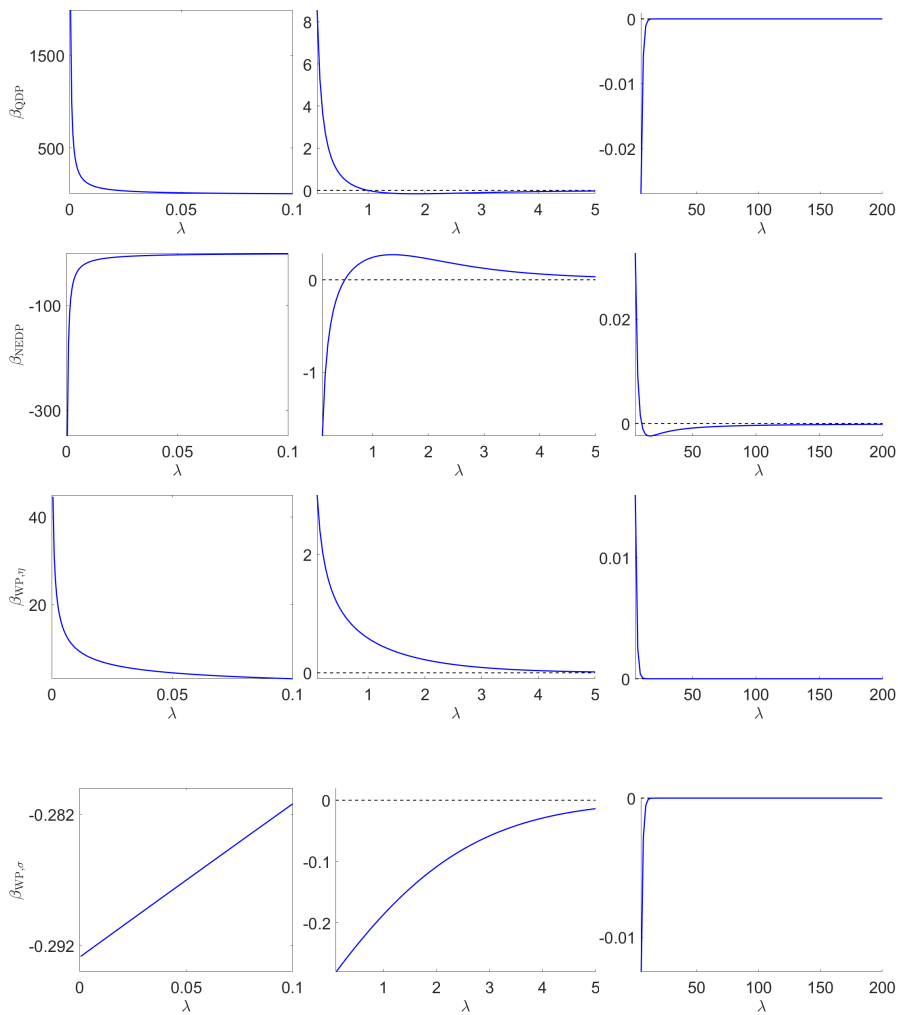


Figure 8.2: From top to bottom: plot of the pixel-based bias functions modeling the approximation introduced by the masked biased version of the QDP, NEDP and WP on different λ intervals in the range $(0, 200]$.

8.4 Numerical Results

In this section, we perform a reliable quantitative experimental comparison among the performance of the eleven different parameter selection criteria outlined in Section 8.1 (unmasked), Section 8.2 (masked biased) and Section 8.3 (masked unbiased), namely the four unmasked principles (ADP), (QDP), (NEDP), (PWP) proposed in [25], [32], [39], [41], respectively, the

two masked biased criteria (ADP-MB), (QDP-MB) presented in [31], the two newly proposed masked biased principles (NEDP-MB), (WP-MB) and the three novel masked unbiased criteria (QDP-MU), (NEDP-MU), (WP-MU).

In order to make the results of the comparison as solid as possible, we act in three directions. First, we consider the the two inverse problems of CT reconstruction and image restoration with two test images **Shepp Logan** and **brain** and three test images **satellite**, **stem** and **cells** respectively, Figures 8.3 and 8.4. Each of them is characterized by different properties so that specific regularizers should be selected for the their processing; more specifically, we test the eleven selection criteria for the TV-KL CT reconstruction and the three (TV-KL, TV²-KL and TGV²-KL image restoration models. Second, for each test image/model we simulate different photon-counting scenarios, ranging from very low- to high-counting ones. Third, for each image/model and each photon-counting level, we consider a number of different (independent) Poisson noise realizations and collect statistics (minimums, maximums and averages) of the quantitative accuracy results achieved by the principles. In particular, we measure the quality of the restored images $\hat{\mathbf{x}}(\mu)$ (with respect to the target uncorrupted image \bar{x}) obtained by applying the different criteria by means of two accuracy metrics, the SSIM and the SNR defined in (6.23) For the case of image restoration, instead of the SNR we will consider the Improved-Signal-to-Noise-Ratio ISNR defined in (6.24). All tests have been performed in Matlab R2022b, on a Windows 10 Platform. The code is available at <https://github.com/MonicaPragliola/MU-principles>.

Analysis. Unlike the previous chapters, here, to avoid heavy notations we will denote with κ both the photon-level factor of the image restoration problem and the I_0 initial intensity value of the CT case.

For each test image and each of the nine photon-level factors κ in (8.29), the ten generated degraded data images $\mathbf{b}^\kappa(j)$ (each corresponding to a different realization of the Poisson noise for the selected image and κ value) are processed as follows. For each $\mathbf{b}^\kappa(j)$, we compute the solution of the \mathcal{R} -KL

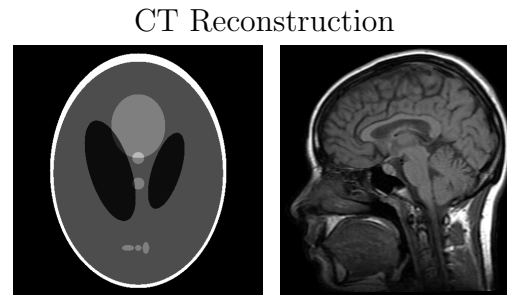


Figure 8.3: From left to right: original Shepp Logan (256×256 pixels) and brain (253×238 pixels) test images considered in the numerical experiments for the CT reconstruction.

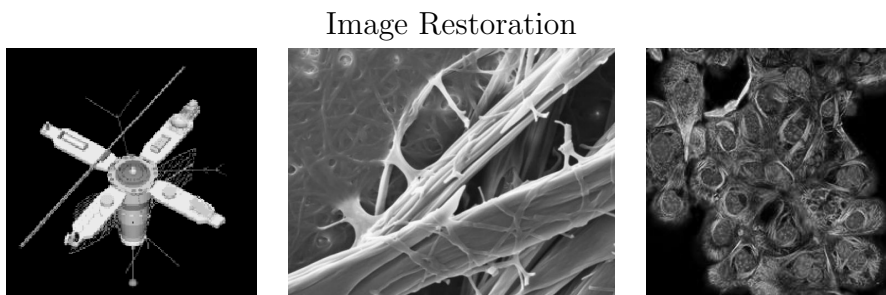


Figure 8.4: From left to right: original satellite (256×256 pixels), stem (453×592 pixels) and cells (236×236 pixels) test images considered in the numerical experiments for image restoration.

variational model for a very fine grid of different μ -values and then, based on the obtained μ -dependent restorations, we apply the eleven different criteria to get the selected regularization parameter values

$$\widehat{\mu}_C^\kappa(j), \quad C \in \mathcal{C} := \{\text{ADP, QDP, NEDP, WP, ADP-M, QDP-MB, NEDP-MB, WP-MB, QDP-MU, NEDP-MU, WP-MU}\},$$

and the corresponding restored images $\widehat{\mathbf{x}}(\widehat{\mu}_C^\kappa(j))$. We then compute and record the associated SNR and SSIM values denoted by $\iota_C^\kappa(j)$ and $\sigma_C^\kappa(j)$, respectively, as well as the optimal (i.e., maximum) SNR and SSIM values achieved on the fine grid of μ -values considered, denoted by $\iota_{\text{OPT}}^\kappa(j)$ and $\sigma_{\text{OPT}}^\kappa(j)$, respectively. We recall that, for the image restoration, we evaluate the results in terms of the ISNR instead of the SNR. However, to avoid excessive notation, we do not introduce a different symbol for the ISNR values for image restoration and instead consider $\iota_C^\kappa(j)$ both for SNR and ISNR, depending on the application.

After processing the ten degraded observations $\mathbf{b}^\kappa(j)$, we thus get the following sets of quantitative results:

$$\begin{aligned} I_C^\kappa &:= \{\iota_C^\kappa(1), \dots, \iota_C^\kappa(10)\}, & S_C^\kappa &:= \{\sigma_C^\kappa(1), \dots, \sigma_C^\kappa(10)\}, & C \in \mathcal{C}, \\ I_{\text{OPT}}^\kappa &:= \{\iota_{\text{OPT}}^\kappa(1), \dots, \iota_{\text{OPT}}^\kappa(10)\}, & S_{\text{OPT}}^\kappa &:= \{\sigma_{\text{OPT}}^\kappa(1), \dots, \sigma_{\text{OPT}}^\kappa(10)\}. \end{aligned}$$

Then, for each $\iota_C^\kappa(j) \in I_C^\kappa$ and each $\sigma_C^\kappa(j) \in S_C^\kappa$ we compute the percentage difference with respect to the corresponding optimal values $\iota_{\text{OPT}}^\kappa(j)$ and $\sigma_{\text{OPT}}^\kappa(j)$, respectively,

$$\epsilon_{I_C^\kappa}(j) := 100 \times \frac{\iota_{\text{OPT}}^\kappa(j) - \iota_C^\kappa(j)}{\iota_{\text{OPT}}^\kappa(j)}, \quad \epsilon_{S_C^\kappa}(j) := 100 \times \frac{\sigma_{\text{OPT}}^\kappa(j) - \sigma_C^\kappa(j)}{\sigma_{\text{OPT}}^\kappa(j)}.$$

The behavior of each selection criterion for a given photon-counting level is thus synthesized by the expected values (or, better, sample means) of the SNR/ISNR and SSIM percentage errors achieved for the ten different noise realizations,

$$\eta_{I_C^\kappa} := \frac{1}{10} \sum_{j=1}^{10} \epsilon_{I_C^\kappa}(j), \quad \eta_{S_C^\kappa} := \frac{1}{10} \sum_{j=1}^{10} \epsilon_{S_C^\kappa}(j). \quad (8.27)$$

Moreover, to monitor the variability of the performance of each criterion with respect to different noise realizations, we also compute

$$\bar{\epsilon}_{I_C^\kappa} = \max_j \epsilon_{I_C^\kappa}(j), \quad \bar{\epsilon}_{S_C^\kappa} = \max_j \epsilon_{S_C^\kappa}(j), \quad \underline{\epsilon}_{I_C^\kappa} = \min_j \epsilon_{I_C^\kappa}(j), \quad \underline{\epsilon}_{S_C^\kappa} = \min_j \epsilon_{S_C^\kappa}(j). \quad (8.28)$$

Numerical method. For all the experiments, CT reconstruction and image restoration are performed by means of the \mathcal{R} -KL variational model - in particular, TV-KL model for `Shepp-Logan`, `brain` and `satellite`, TV²-KL for `stem` and TGV²-KL for `cells` - solved numerically by the iterative ADMM schemes outlined in Section 10.1. In all the tests, the ADMM iterations are stopped as soon as the relative change between two subsequent \mathbf{x} -iterates satisfies

$$\delta_{\mathbf{x}}^{(k)} < 10^{-6},$$

where $\delta_{\mathbf{x}}^{(k)}$ is defined in (6.25), while the ADMM penalty parameter γ is set manually so as to fasten the convergence of the alternating scheme. More specifically, the numerical tests indicated the range $\gamma \in [1, 10]$ as a good choice.

8.4.1 CT Reconstruction

Data Generation For the CT reconstruction problem we consider the test images `Shepp Logan` (250×250 , pixel size = 0.4mm) and `brain` (238×253 , pixel size=0.4mm), with pixel values between 0 and 1, shown Figures 8.3. The acquisition process of the fan beam CT setup, i.e. the projection operator \mathbf{A} , is built using the ASTRA Toolbox [40] with the following parameters: 180 equally spaced angles of projections (from 0 to 2π), a detector with 500 pixels (detector pixel size = 1/3mm), distance between the source and the center of rotation = 300mm, distance between the center of rotation and the detector array = 200mm. The data are generated with the same procedure explained in 6.3.1. In order to analyze the strategies for many

photon-counting levels, we consider the following noise-free intensity data

$$\bar{\lambda}^k = \kappa e^{-\mathbf{A}\bar{x}}, \quad \kappa = I_0 \in \{1, 3, 5, 10, 20, 50, 100, 500, 1000\}.$$

Finally, for each noise-free image $\bar{\lambda}^k$, ten different noisy observations

$$\mathbf{b}^\kappa(j), \quad j = 1, \dots, 10,$$

are generated by sampling as many independent realizations from an m -variate Poisson random process with mean $\bar{\lambda}^k$, using the Matlab routine `poissrnd`.

Test image Shepp Logan: parameter selection in the (TV-KL) model

We start analyzing the behavior of the expected and limiting values defined in (8.27), (8.28), respectively, within the four classes of ADP-, QDP-, NEDP- and WP-based criteria. In Figure 8.5 for each class we plot the sample means $\eta_{I_C^\kappa}$ corresponding to the different counting regimes $\kappa = I_0$ expressed in \log_{10} -scale, and we show the confidence intervals determined by the limiting values $\bar{\epsilon}_{I_C^\kappa}, \underline{\epsilon}_{I_C^\kappa}$.

For what concerns the ADP-based strategies, we recall that the MB and MU versions of the principle coincide. Notice that the masked criterion achieves slightly better results as the red band has no picks in the low count regime.

In the case of QDP-based approaches, one can immediately observe that the percentage differences achieved by the masked biased principle are particularly large for $\kappa \leq 10$. In those regimes, the MB version returns better results than the unmasked one by staying below the 30% (in mean). On the other hand, we highlight that the MU principle presents a very robust behavior along the whole range of counting factors, as the corresponding percentage differences are always below the 30%.

When analyzing the NEDP-based approaches, one can notice that the MB method returns the poorer results in the low counting regimes while it mimics the unmasked and MU version in the mid- and high-counting regimes.

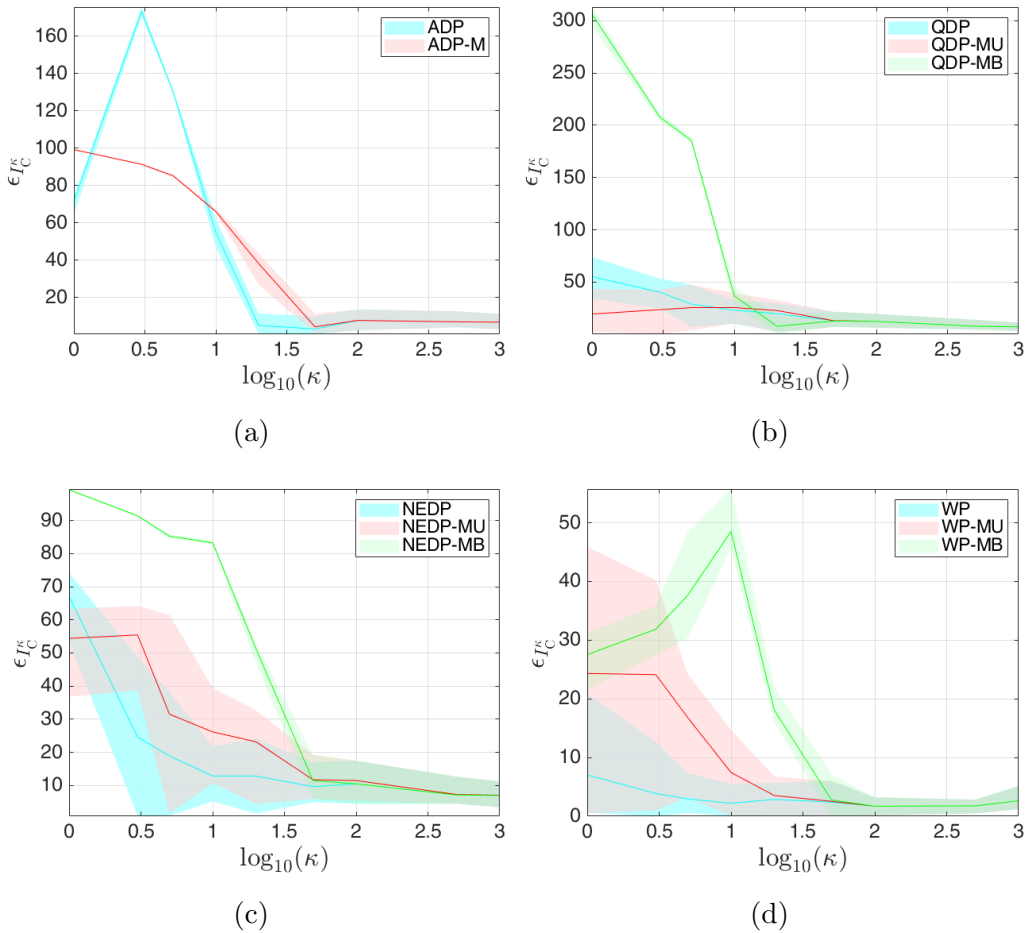


Figure 8.5: Test image **Shepp Logan**. Expected values and confidence intervals for the SNR values achieved in different counting regimes.

On the other hand, the unmasked principle achieves the larger SNR values for all the considered regimes except $\kappa = 1$.

Finally, for the WP-based principles we notice that the MB criterion performs poorly in the low- and mid- counting regimes, while the green band stays below the 10% for $\kappa \geq 50$. One can also observe that the unmasked and the masked unbiased principles present a better behavior with respect to the considered κ -values, with the unmasked staying around 10% (mean) for all the values.

Figure 8.6 shows, for each class of methods, the sample means $\eta_{S_C}^{\kappa}$ and the

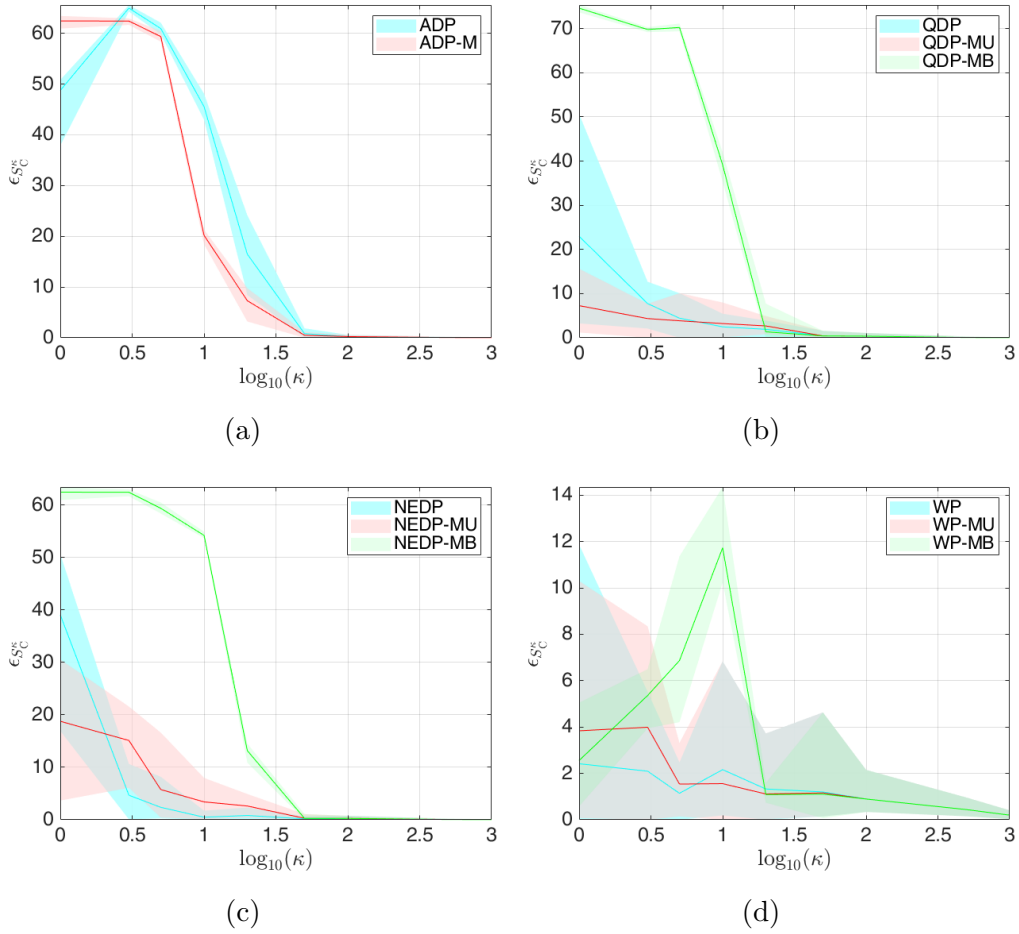


Figure 8.6: Test image Shepp Logan. Expected values and confidence intervals for the SSIM values achieved in different counting regimes.

confidence intervals related to the computed $\bar{\epsilon}_{S_C}^{\kappa}$, $\underline{\epsilon}_{S_C}^{\kappa}$, i.e. the performances of the considered principles in terms of the SSIM. One can easily notice that the SSIM bands present the same behavior of the SNR curves shown in Figure 8.5, so that similar conclusions on the performances of the unmasked, MB and MU criteria can be drawn.

To analyze the results from a different point of view, in Figures 8.7a, 8.7b, 8.7c we show the sample means $\eta_{I_C}^{\kappa}$ of the unmasked, masked biased and masked unbiased principles, respectively, in the range [0%, 25%], so as to visualize the best performances. In the unmasked category, WP is the only

principle staying below the 10% for all $\kappa = I_0$, with NEDP obtaining better results than the remaining for the low- and mid- counting regimes. Among the MB principles, all the strategies stay in the interval of interest only in correspondence of the high-counting regimes. Finally, in the MU class, the QDP-MU and WP-MU methods are in the visible range for almost every $\kappa(I_0)$, with WP-MU bringing the best results for all κ .

Figures 8.7d, 8.7e, 8.7f show the sample means $\eta_{S_C^\kappa}$ of the unmasked, MB and MU principles, respectively, in the range up to [0%, 5%]. The three plots confirm the considerations done for the SNR about the best method within each group.

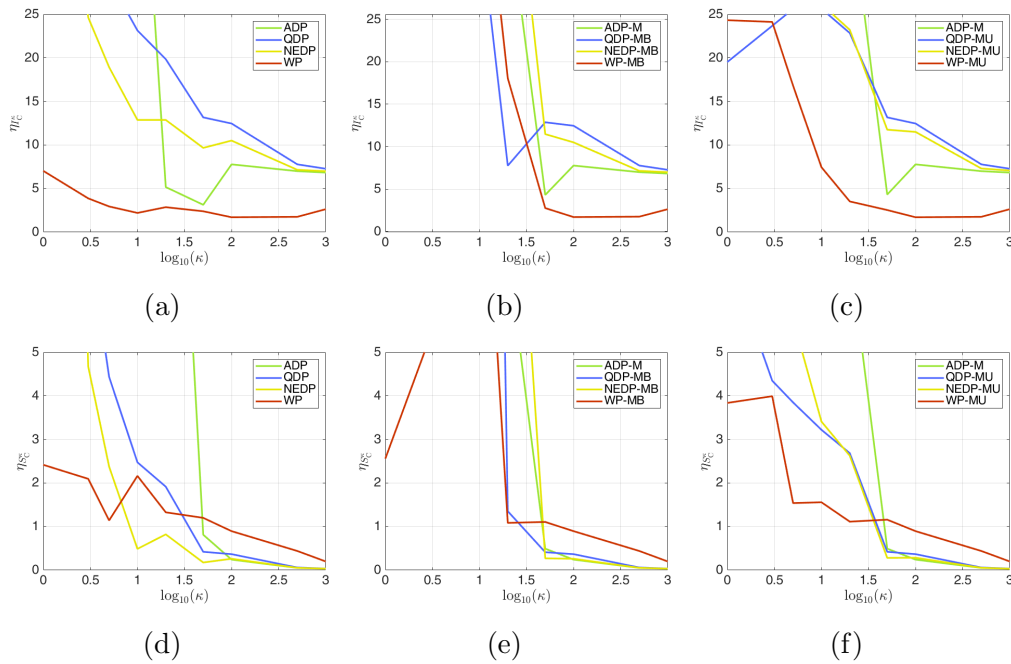


Figure 8.7: Test image Shepp Logan. Zoom of the expected values $\eta_{I_C^\kappa}$ (top row), and $\eta_{S_C^\kappa}$ (bottom row) for the SNR and SSIM values achieved in different counting regimes.

Test image brain: parameter selection in the (TV-KL) model

For the second example of CT reconstruction we consider the test image **brain** in Figure 8.3. In Figure 8.8 we plot the sample means $\eta_{I_0^\kappa}$ and the confidence intervals corresponding to the different counting regimes I_0 for the four classes of ADP-, QDP-, NEDP-, and WP-based criteria. For the ADP-based approaches, one can notice that the masked criterion reaches worse results than the unmasked one, which stays below the 60% for almost every counting regime. For what concerns the QDP-based strategies, we can immediately notice that, as for the previous image, the biased masked version returns poor results for lower counting regimes. On the other hand, both the unmasked and the unbiased masked achieve good and similar results, as they return percentage differences that are always below 50% for all the intensities I_0 . In the case of the NEDP-based approaches one can notice a similar behavior to the QDP-based strategies, where the unmasked and unbiased masked achieve analogue results staying below the 50% for all I_0 and the biased masked strategy works poorly for $\kappa \leq 50$. Finally, for the WP-based principles, the unmasked one returns the better results for all cases, staying below the 30%. On the other hand, the masked biased and unbiased achieve the same results as the unmasked for the high count regimes, with the masked unbiased following the unmasked for the mid to low photon counts but returning poor reconstructions in the lowest intensity cases.

The same observations can be done by analyzing the SSIM results plotted in Figure 8.9.

In Figure 8.10 we show the expected values $\eta_{I_0^\kappa}$ (top row) and $\eta_{S_0^\kappa}$ (bottom row), in the range [0%, 25%] and [0%, 5%] respectively, divided by the type of principle: unmasked, biased masked and unbiased masked. Looking at both the SNR and SSIM graphs we can note that, in the unmasked category, the best result is achieved by the WP in all the range of I_0 . Among the biased masked strategies, the WP-MB seems the best as it reaches higher SNR than the others for the lower and higher values of I_0 . Finally, for the unbiased masked principles, the WP-MU obtains the best result in terms of SNR for

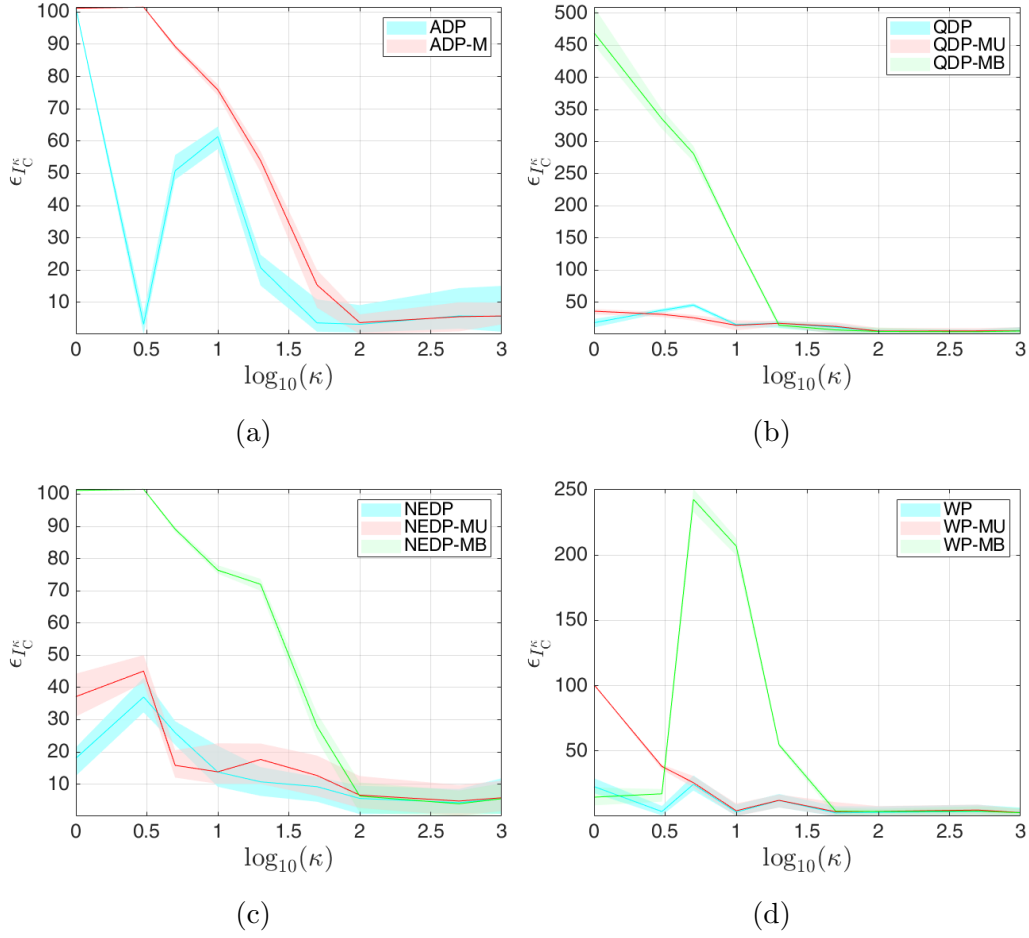


Figure 8.8: Test image brain. Expected values and confidence intervals for the SNR values achieved in different counting regimes.

all the regimes.

8.4.2 Image Restoration

Data Generation For each of the three test images, in order to simulate different photon-counting scenarios, first we (affinely) scale the image in the range $[0, 1]$ and denote by $\bar{\mathbf{x}}_{\text{norm}}$ the obtained normalized image. Then, nine uncorrupted images $\bar{\mathbf{x}}^{\kappa}$ for nine different photon-counting levels are simulated

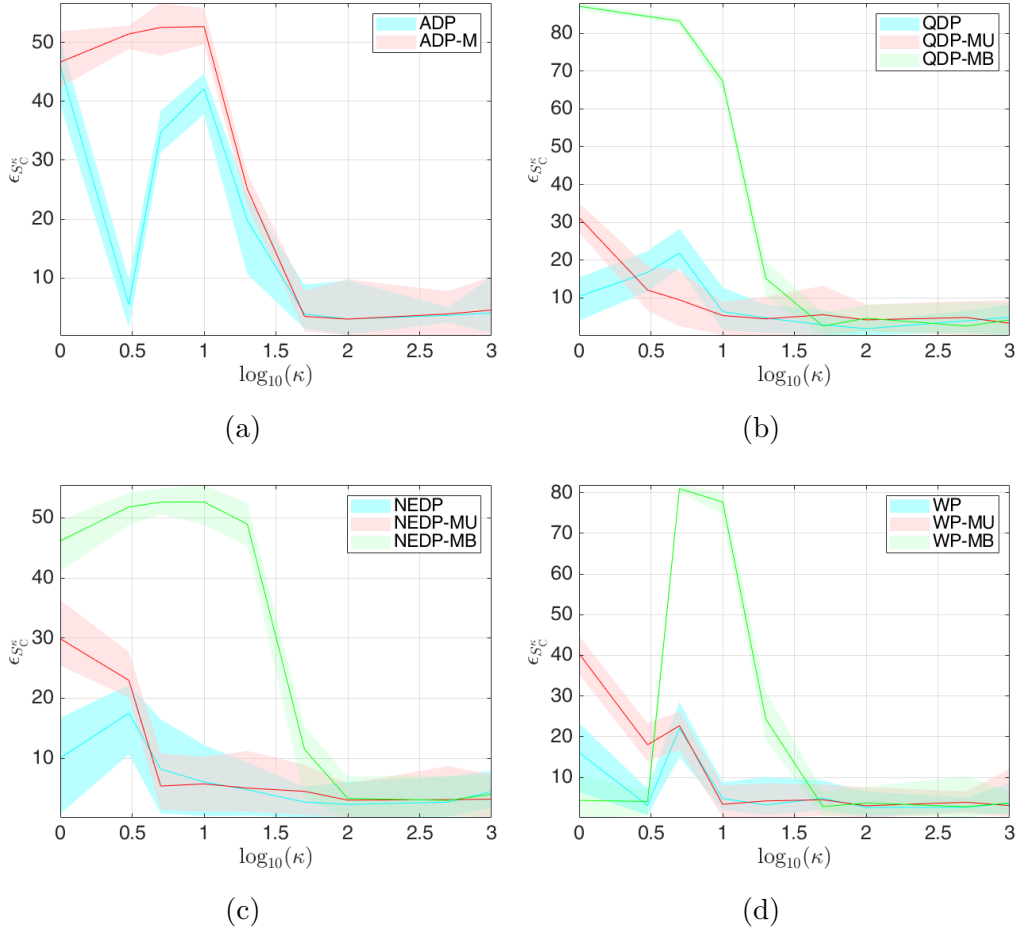


Figure 8.9: Test image **brain**. Expected values and confidence intervals for the SSIM values achieved in different counting regimes.

by multiplying $\bar{\mathbf{x}}_{\text{norm}}$ by as many photon-level factors $\kappa \in \mathbb{R}_{++}$, in particular:

$$\bar{\mathbf{x}}^\kappa = \kappa \bar{\mathbf{x}}_{\text{norm}}, \quad \kappa \in \{1, 3, 5, 10, 20, 50, 100, 500, 1000\}. \quad (8.29)$$

The photon-scaled images $\bar{\mathbf{x}}^\kappa$ are then corrupted by space-invariant Gaussian blur, with blur kernel generated by the Matlab routine `fspecial`, which is characterized by two parameters: the `band` parameter, representing the side length (in pixels) of the square support of the kernel, and `sigma`, that is the standard deviation (in pixels) of the isotropic bivariate Gaussian distribution defining the kernel in the continuous setting. In all our tests, we set `band` =

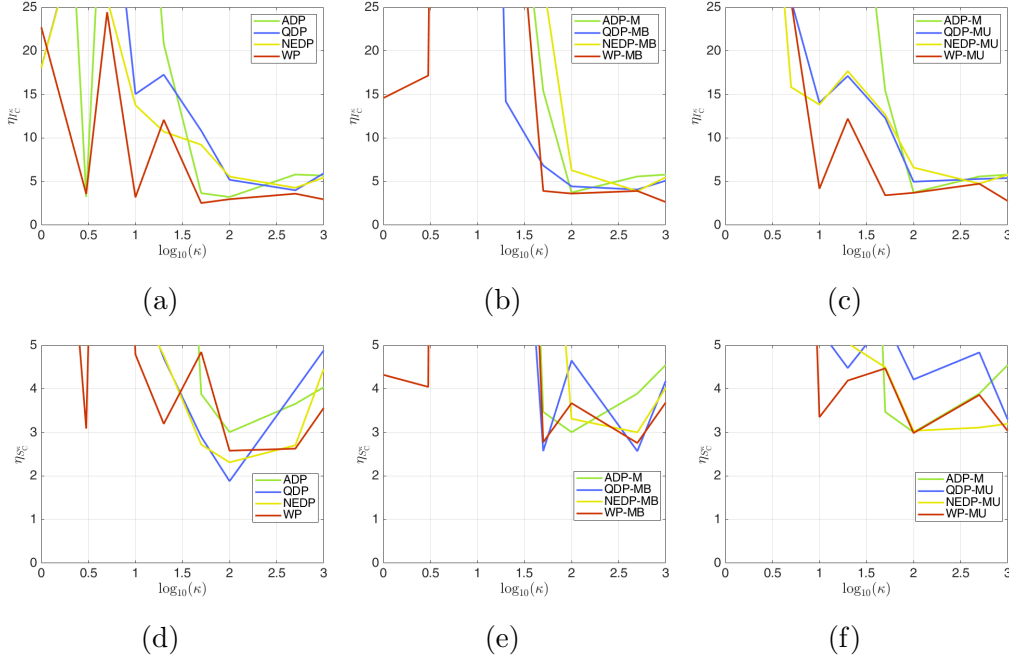


Figure 8.10: Test image **brain**. Zoom of the expected values $\eta_{I^{\kappa}}$ (top row), and $\eta_{S^{\kappa}}$ (bottom row) for the SNR and SSIM values achieved in different counting regimes.

5, $\sigma = 1$. Then, a constant background emission image \mathbf{b} is added to the blurred images, so as to get the nine noise-free degraded images $\bar{\boldsymbol{\lambda}}^{\kappa} = \mathbf{A}\bar{\boldsymbol{x}}^{(k)} + \mathbf{q}$. Finally, for each noise-free image $\bar{\boldsymbol{\lambda}}^{\kappa}$, ten different noisy observations

$$\mathbf{b}^{\kappa}(j), \quad j = 1, \dots, 10,$$

are generated by sampling as many independent realizations from an n -variate Poisson random process with mean $\bar{\boldsymbol{\lambda}}^{\kappa}$, using the Matlab routine `poissrnd`.

We remark that the factor κ in (8.29) represents the maximum number of photons that, on average, can hit any pixel of the image domain if no blur degradation ($\mathbf{A} = \mathbf{I}$) and a null emission background ($\mathbf{q} = \mathbf{0}$) are considered. In fact, in this case the noise-free image $\bar{\boldsymbol{\lambda}}^{\kappa}$ - which, we notice, contains the mean values of the Poisson noise distributions at all pixels - is given by $\bar{\boldsymbol{\lambda}}^{\kappa} = \mathbf{A}\bar{\boldsymbol{x}}^{\kappa} + \mathbf{q} = \bar{\boldsymbol{x}}^{\kappa}$, hence $\max\{\bar{\boldsymbol{\lambda}}^{\kappa}\} = \max\{\bar{\boldsymbol{x}}^{\kappa}\} = \kappa$. In general, for any given

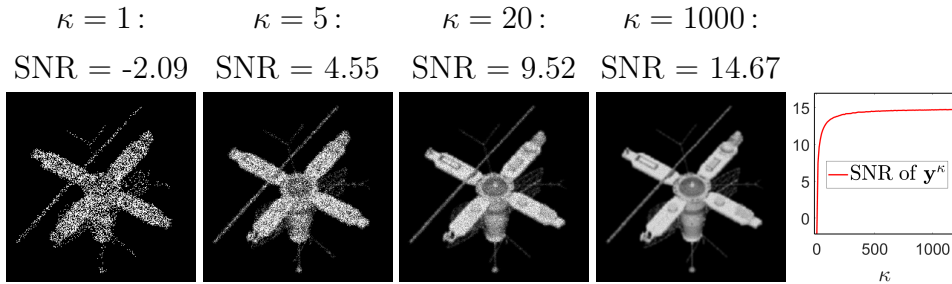


Figure 8.11: Test image `satellite` corrupted by blur and, from left to right, by decreasing levels of Poisson noise yielded by increasing values of the photon-level factor κ in (8.29). In the right-most graph, SNR value of the noisy observation \mathbf{b}^κ as a function of factor κ .

blur corruption and emission background, the factor κ is positively related to the photon-range of the experiment and, recalling that for a scalar Poisson random variable with parameter $\bar{\lambda}^\kappa = \kappa\bar{\lambda}$ the ratio between its mean (true signal) and its standard deviation (noise level) is equal to $\bar{\lambda}^\kappa / \sqrt{\bar{\lambda}^\kappa} = \sqrt{\kappa} \sqrt{\bar{\lambda}}$, also to the signal-to-noise ratio of the observed degraded image \mathbf{b}^κ to restore. To highlight clearly the effect of κ on the noise-level in the observation \mathbf{b}^κ and, hence, on the difficulty of the restoration process, in Figure 8.11 we show the test image `satellite` corrupted by Gaussian blur and by a realization of Poisson noise for four different values of κ as well as, on the right, the graph of the SNR value of the observation \mathbf{b}^κ as a function of the factor κ . This graph justifies the non-uniform grid of κ -values considered in (8.29) (the grid is finer for small κ -values where the SNR changes more rapidly) as well as the maximum value $k = 1000$ considered (the SNR curve stabilizes, hence taking $\kappa > 1000$ does not change significantly the results of the criteria comparison).

Test image `satellite`: parameter selection in the (TV-KL) model

We consider the restoration of the test image `satellite`. In this first example, we set $\mathbf{q} \equiv 2 \times 10^{-3}$ and, in light of the dominant piece-wise constant

features present in the image, we employ the TV regularization term in (TV)

We start analyzing the behavior of the expected and limiting values defined in (8.27), (8.28), respectively, within the four classes of ADP-, QDP-, NEDP- and WP-based criteria. In Figure 8.12 for each class we plot the sample means $\eta_{I_C^\kappa}$ corresponding to the different counting regimes κ expressed in \log_{10} -scale, and we show the confidence intervals determined by the limiting values $\bar{\epsilon}_{I_C^\kappa}$, $\underline{\epsilon}_{I_C^\kappa}$.

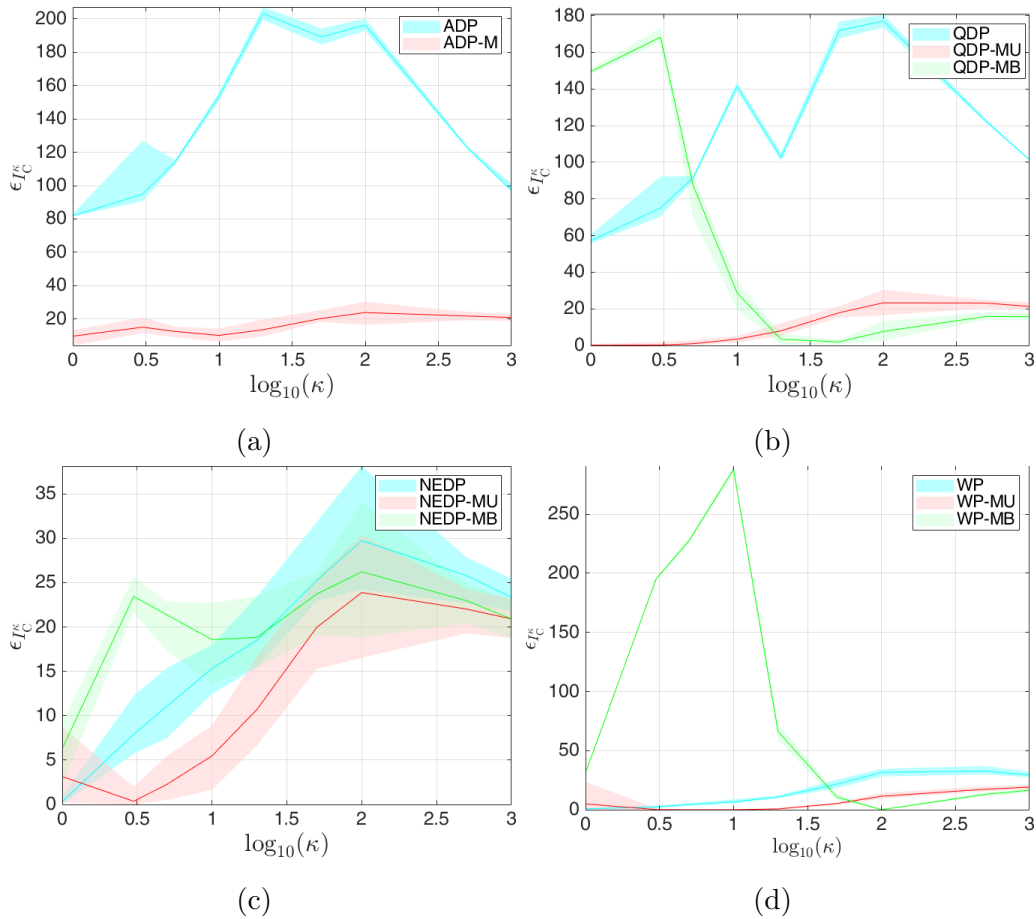


Figure 8.12: Test image `satellite`. Expected values and confidence intervals for the ISNR values achieved in different counting regimes.

For what concerns the ADP-based strategies, we recall that the MB and

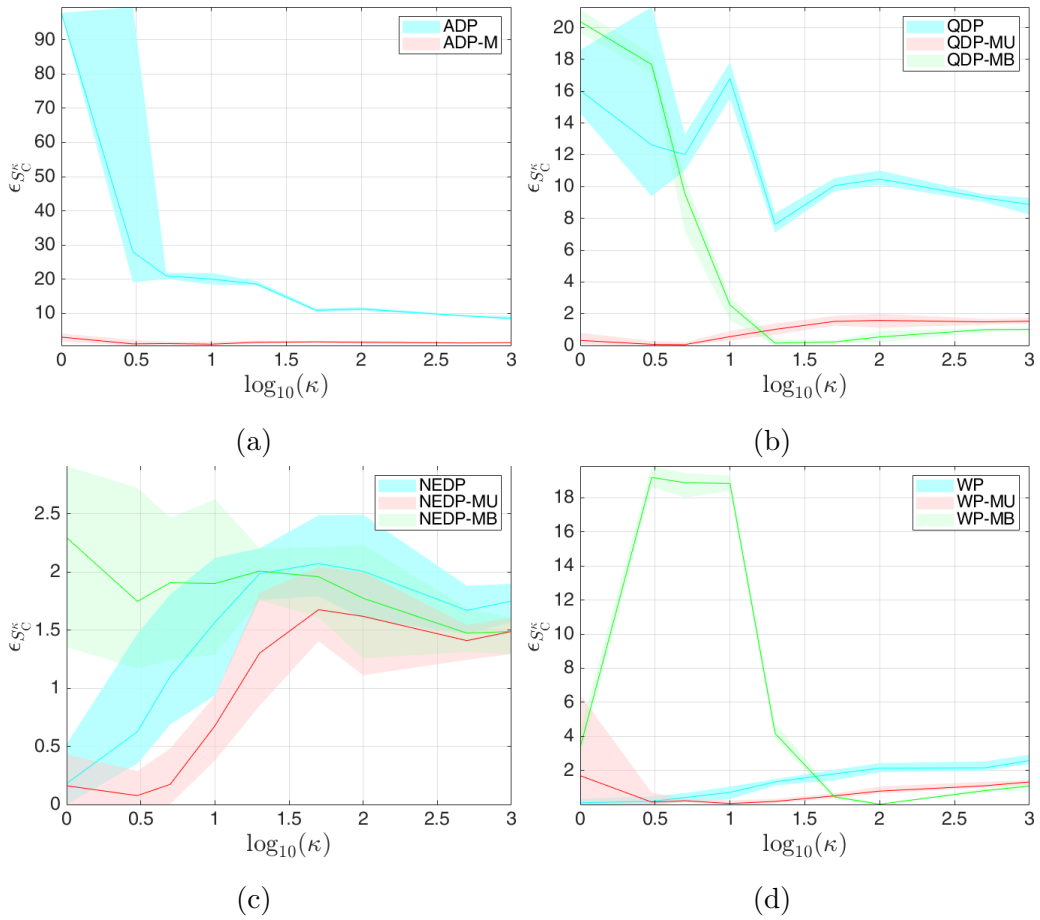


Figure 8.13: Test image `satellite`. Expected values and confidence intervals for the SSIM values achieved in different counting regimes.

MU versions of the principle coincide. Notice that the masked criterion achieves significantly better results as the red band stays below the 30% regardless of the counting regime, while the unmasked method stays above the 80%

In the case of QDP-based approaches, one can immediately observe that the percentage differences achieved by the unmasked principle are particularly large for every κ . In the lower counting regimes, i.e., $\kappa \leq 5$, the MB version returns very poor results, while its performance improves and stays below the 20% for $\kappa \geq 20$. On the other hand, we highlight that the MU

principle presents a very robust behavior along the whole range of counting factors, as the corresponding percentage differences are always below the 30% and approach 0 for the smaller κ s.

When analyzing the NEDP-based approaches, one can notice that the MB method returns the poorer results in the low counting regimes while, in expectation, it outperforms the unmasked version in the mid- and high-counting regimes. On the other hand, the MU principle achieves the larger INSR values for all the considered regimes.

Finally, for the WP-based principles we notice that the MB criterion performs poorly in the low- and mid- counting regimes, while the green band stays below the 30% for $\kappa \geq 50$. One can also observe that the unmasked and the masked unbiased principles present a robust behavior with respect to the considered κ -values, with the unmasked approaching 0 for $\kappa \leq 3$ and the masked unbiased outperforming the competitors for $\kappa > 3$.

Figure 8.13 shows, for each class of methods, the sample means $\eta_{S_C^\kappa}$ and the confidence intervals related to the computed $\bar{\epsilon}_{S_C^\kappa}$, $\underline{\epsilon}_{S_C^\kappa}$, i.e. the performances of the considered principles in terms of the SSIM. One can easily notice that the SSIM bands present the same behavior of the ISNR curves shown in Figure 8.12, so that similar conclusions on the performances of the unmasked, MB and MU criteria can be drawn.

To analyze the results from a different point of view, in Figures 8.14a, 8.14b, 8.14c we show the sample means $\eta_{I_C^\kappa}$ of the unmasked, masked biased and masked unbiased principles, respectively, in the range [0%, 25%], so as to visualize the best performances. In the unmasked category, NEDP and WP are the only principles staying below the 25% for $\kappa \geq 20$, with WP obtaining better results than the others for the low- and mid- counting regimes. Among the MB principles, QDP-MB and WP-MB stay in the interval of interest only in correspondence of the high-counting regimes, while ADP-M and NEDP-MB stay between 10% and 25% for each κ . Finally, in the MU class, all methods are in the visible range, with WP-MU being the best for $\kappa > 3$, followed by QDP-MU which reaches the highest ISNR for $\kappa \leq 3$.

Figures 8.14d, 8.14e, 8.14f show the sample means $\eta_{S_C^\kappa}$ of the unmasked, MB and MU principles, respectively, in the range up to [0%, 5%]. The three plots confirm the considerations done for the ISNR about the best method within each group.

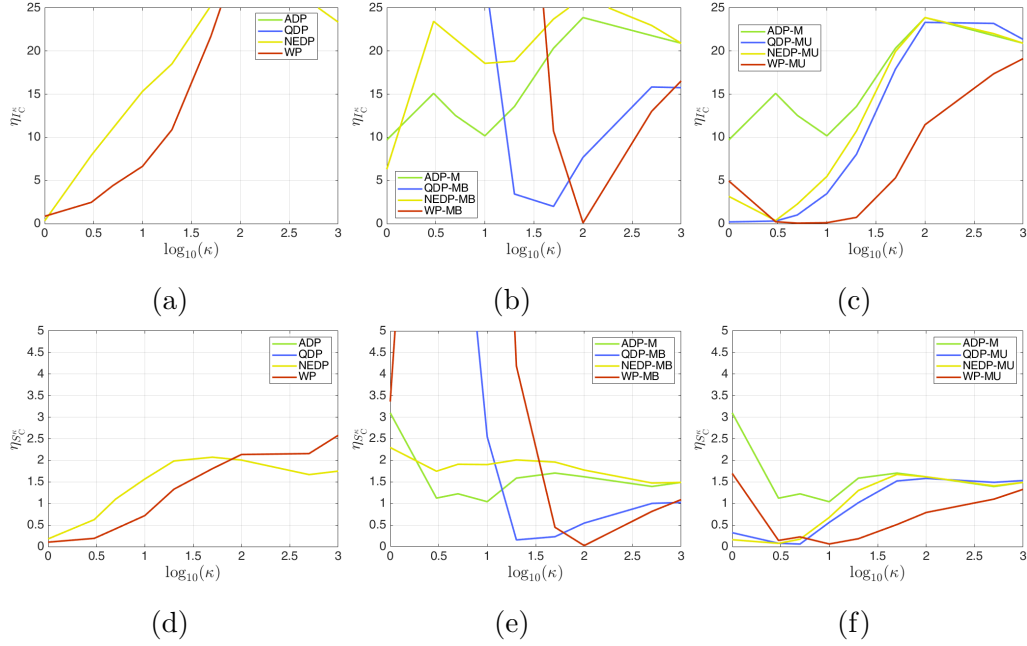


Figure 8.14: Test image **satellite**. Zoom of the expected values $\eta_{I_C^\kappa}$ (top row), and $\eta_{S_C^\kappa}$ (bottom row) for the ISNR and SSIM values achieved in different counting regimes.

Test image stem: parameter selection in the (TV²-KL) model

For the second example, we consider the restoration of the test image **stem**, with constant background emission $\mathbf{q} = 2 \times 10^{-3}$, this time using the TV² regularization term defined in (TV²) due to the target image resembling a piece-wise linear function more than a piece-wise constant one.

In Figure 8.15 we plot the sample means $\eta_{I_C^\kappa}$ and the confidence intervals corresponding to the different counting regimes κ for the four classes of ADP-, QDP-, NEDP-, and WP-based criteria. For the ADP-based approaches, one

can notice that the masked criterion reaches worse results than the unmasked one, which stays below the 40% for every counting regime. For what concerns the QDP-based strategies, we can immediately notice that, as for the previous image, the biased masked version returns poor results for lower counting regimes, but it improves for $\kappa \geq 50$. On the other hand, both the unmasked and the unbiased masked achieve good and similar results, as they return percentage differences that are always below 20% for all factors κ . In the case of the NEDP-based approaches one can notice a similar behavior to the QDP-based strategies, where the unmasked and unbiased masked achieve analogue results (except a little more variability across the different realization for the unmasked one) staying below the 20% for all κ and the biased masked strategy works poorly for $\kappa \leq 50$. Finally, for the WP-based principles, all of them return percentage differences less than 25%, with the biased masked working better for the mid- and high- count range, but worst for $\kappa \leq 5$. On the other hand, the unbiased masked reaches good results in the low- and mid- count range, with the exception of $\kappa = 1$ where the sample mean and the variability across the noise realization are higher than the one obtained with the unmasked strategy. The same observations can be done by analyzing the SSIM results plotted in Figure 8.16.

In Figure 8.17 we show the expected values $\eta_{I_{\mathcal{C}}^{\kappa}}$ (top row) and $\eta_{S_{\mathcal{C}}^{\kappa}}$ (bottom row), in the range [0%, 25%] and [0%, 5%] respectively, divided by the type of principle: unmasked, biased masked and unbiased masked. Looking at both the ISNR and SSIM graphs we can note that, in the unmasked category, the best result is achieved by the WP in all the range of κ . Among the biased masked strategies, the WP-MB seems the best as it achieves the highest value of ISNR for $\kappa = 10, 20$, but the behavior for $\kappa \leq 5$ is poorer when compared to the other plots (but is the best in its category). Finally, for the unbiased masked principles, the QDP-MU obtains the best result in terms of ISNR for the low-count regime (even among all the methods), while the WP-MU works well for the mid- and high- range.

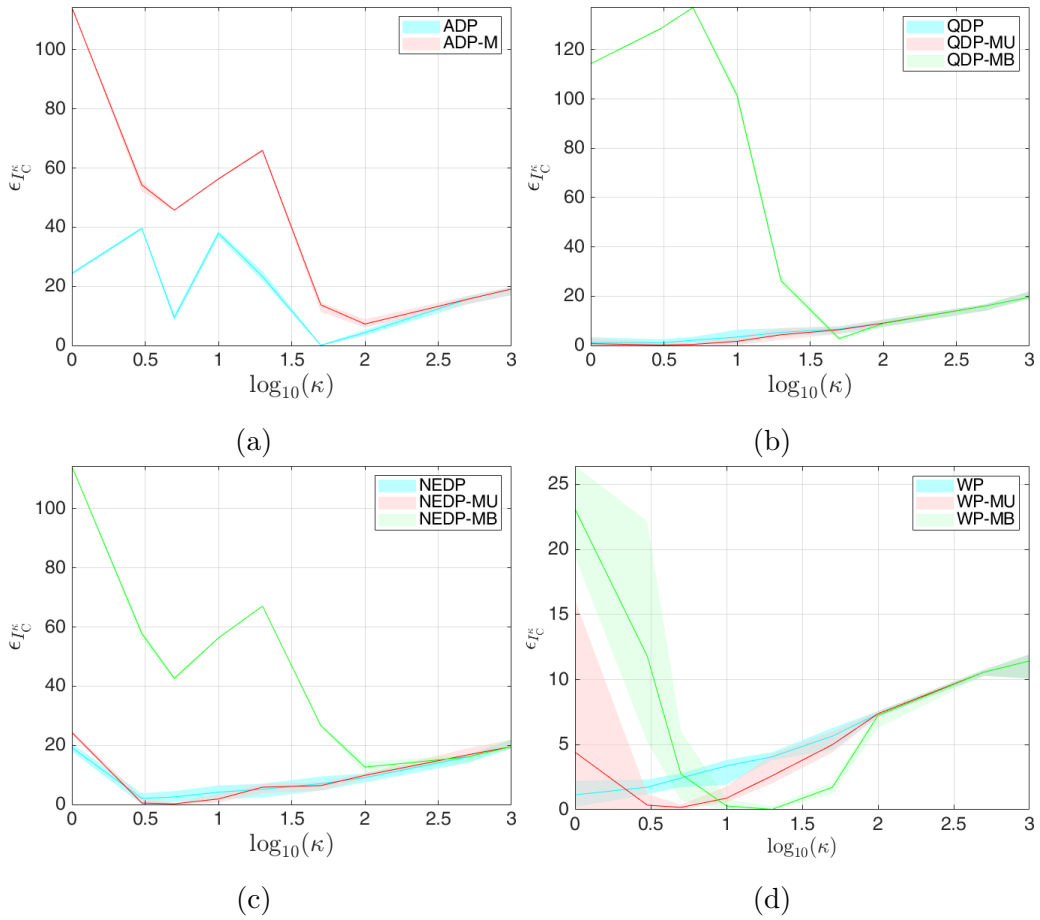


Figure 8.15: Test image `stem`. Expected values and confidence intervals for the ISNR values achieved in different counting regimes.

Test image cells: parameter selection in the (TGV²-KL model

In this third example, we consider the restoration of the test image `cells` by employing the TGV² regularization term to effectively deal with the composite nature of the specimen. For the TGV², we set $\alpha_0 = 0.8$, $\alpha_1 = 0.3$ so as to maximize the ISNR for the highest counting regime considered here, i.e. $\kappa = 1000$. Moreover, we set a constant background emission $\mathbf{q} = 10^{-1}$.

In Figure 8.18 we show the ISNR bands achieved by the ADP-, QDP-, NEDP- and WP-based principles. As for the test image `stem`, the ADP-M strategy performs poorly in the lowest counting regimes, while it outper-

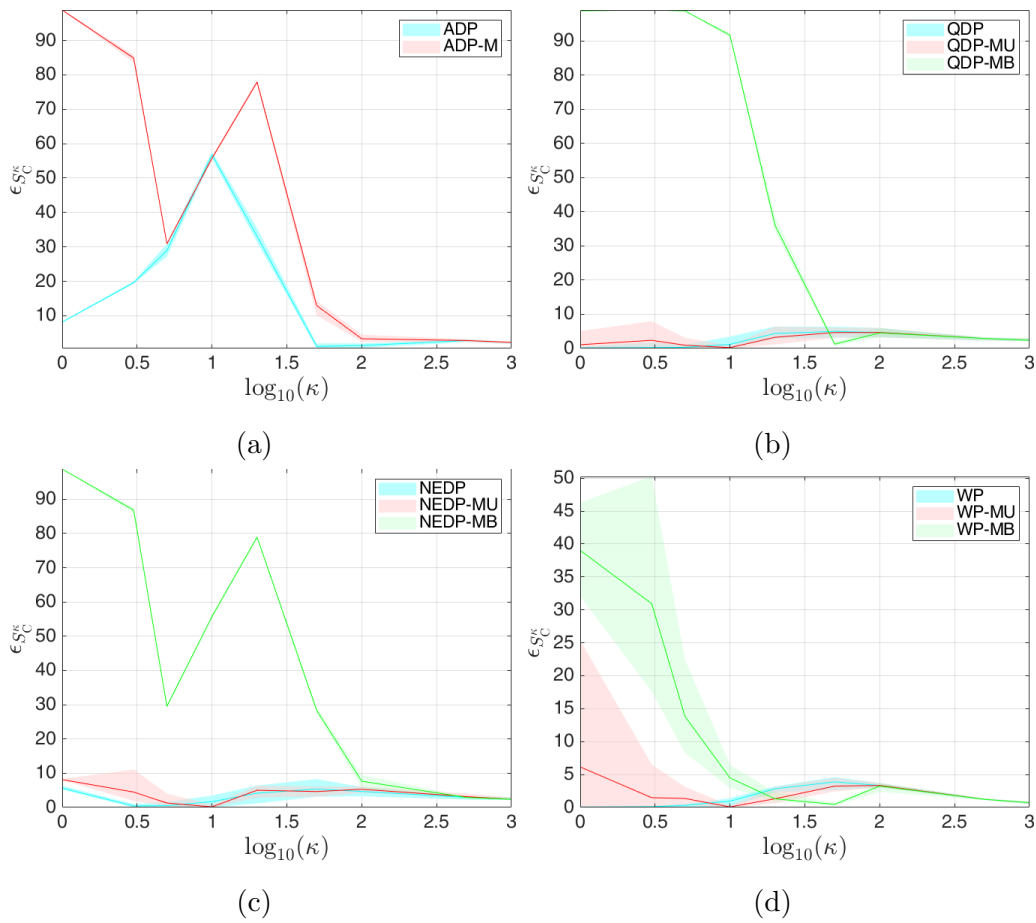


Figure 8.16: Test image `stem`. Expected values and confidence intervals for the SSIM values achieved in different counting regimes.

forms the unmasked version for $\kappa \geq 20$. On the other hand, the remaining three classes of methods present the same behavior: the MB versions of the principles achieve very low ISNR values in low- and mid-counting regimes, whereas the unmasked and MU principles present a very robust behavior with the latter achieving the best results.

Similar considerations can be drawn by looking at the SSIM bands reported in Figure 8.19.

Finally, in Figure 8.20 we show a close-up on the expected values $\eta_{I_C}^{\kappa}$, $\eta_{S_C}^{\kappa}$ in the range $[0\%, 25\%]$ dividing the principles into unmasked, MB and MU.

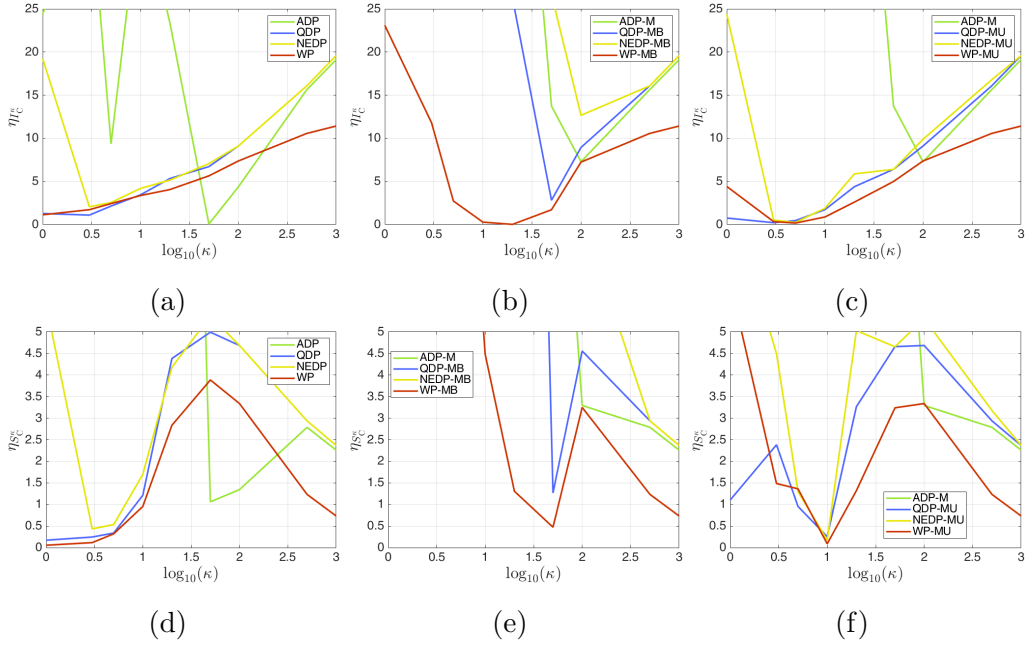


Figure 8.17: Test image *stem*. Zoom of the expected values η_{IC}^{κ} (top row), and η_{SC}^{κ} (bottom row) for the ISNR and SSIM values achieved in different counting regimes.

It is easy to conclude that the MU versions of the QDP, NEDP and WP return the best results both in terms of robustness and of quality measures achieved.

8.4.3 Discussion

The detailed analysis carried out so far allows to conclude that neglecting the zero-pixels in the acquired images, for the image restoration problem, as proposed in [31] can lead to particularly robust and successful parameter selection strategies provided that the proposed positive Poisson distribution is employed to model the modified data. Generally speaking, in terms of quality measures the QDP-MU achieves the best results for $\kappa \leq 3$, while the WP-MU returns higher quality restorations when $\kappa > 3$. Moreover, in accordance with the theoretical results given in Proposition 8.3.1, in the

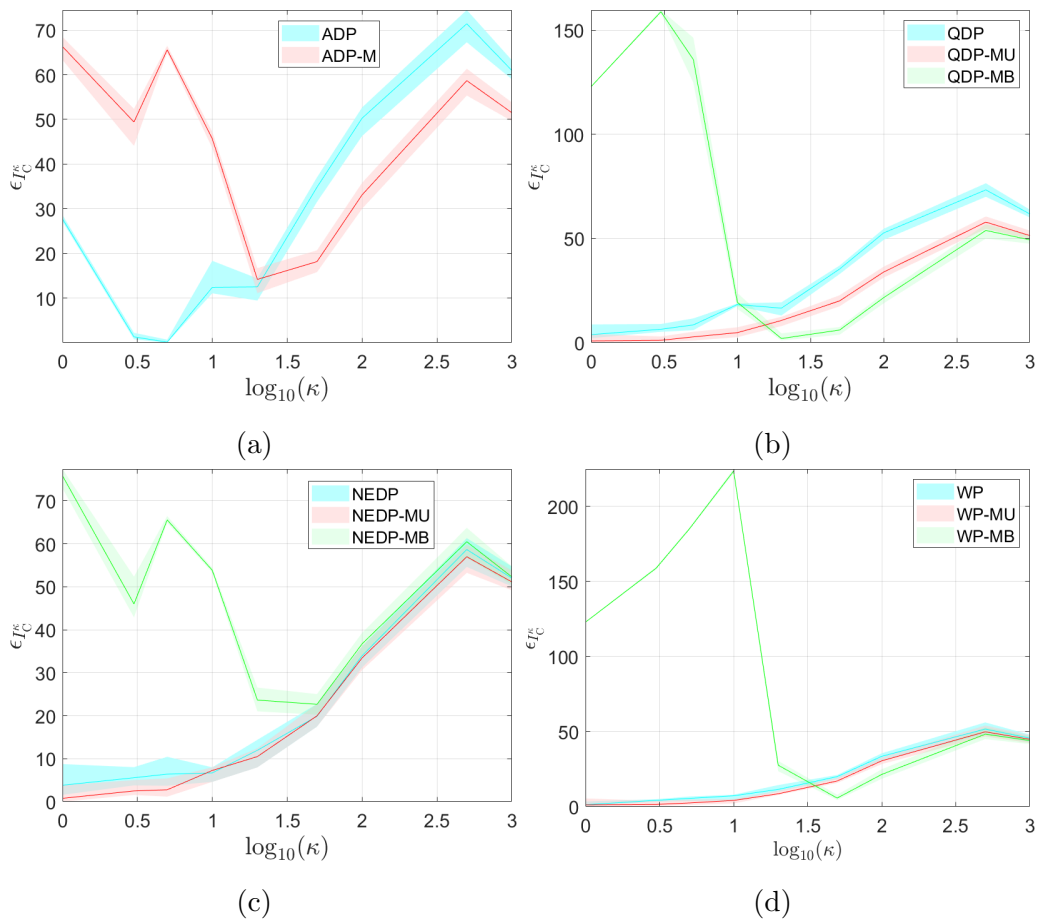


Figure 8.18: Test image `cells`. Expected values and confidence intervals for the ISNR values achieved in different counting regimes.

higher counting regimes the performed criteria show similar behaviors.

We highlight that the improvements yielded by employing the proposed MU principles with respect to their unmasked versions are particularly relevant in the first example of image restoration, that is for the test image `satellite`. To highlight a possible reason behind this phenomenon, in Table 8.1 we report the average percentages of zero-pixels in the acquired images for the counting regimes considered. Such values are clearly influenced by the gray-level statistics of the underlying test images as well as by the selected background emissions. It is immediate to observe that for the test image

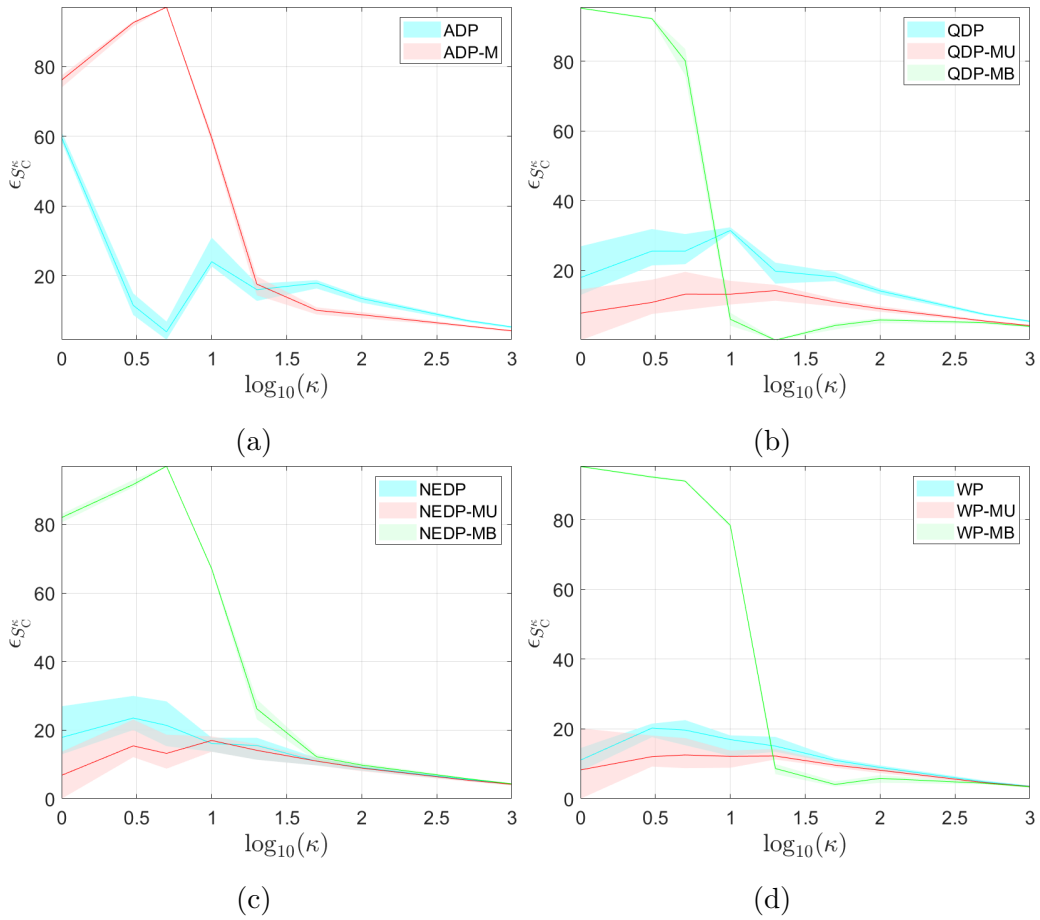


Figure 8.19: Test image `cells`. Expected values and confidence intervals for the SSIM values achieved in different counting regimes.

`satellite` the number of zero pixels is very large for all the κ -values. As a consequence, masking the data in this scenario is particularly effective.

This reflection is also linked to the fact that, for the CT reconstruction problem, the number of zero pixels in the data is smaller than for the image restoration of images with black background. This is because, in CT acquisitions, the background of the noiseless intensities $I_0 e^{-\mathbf{A}\bar{\mathbf{x}}}$ is equal to I_0 (as it indicates in which pixels the original X-ray is not attenuated) instead of zero (as for the image `satellite` in the image restoration problem); see the data `b` in Figures 6.6 and 6.8. Therefore, zero pixels in CT acquisitions are

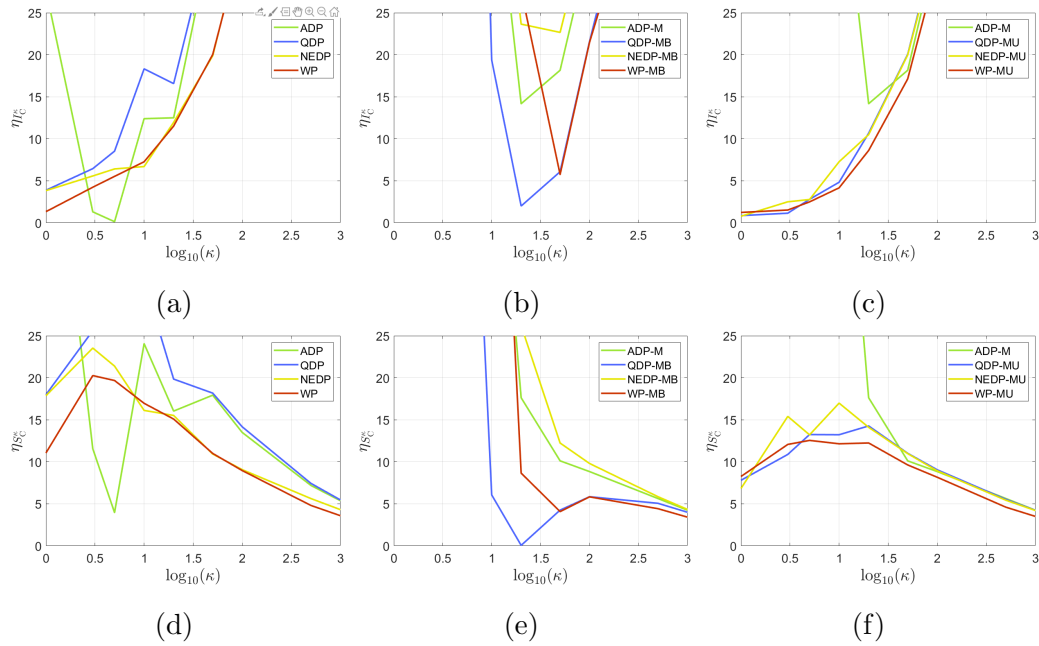


Figure 8.20: Test image cells. Zoom of the expected values $\eta_{I_C}^{\kappa}$ (top row), and $\eta_{S_C}^{\kappa}$ (bottom row) for the ISNR and SSIM values achieved in different counting regimes.

detected only for low values of I_0 and their presence depends on the Poisson noise degradation as well as the possibility that in some pixels all the photons are attenuated. For this reason, the improvements brought by the MU principles are not as visible as for the image restoration case and as a result the WP principle can be declared the best performing one for the CT reconstruction problem.

κ	1	3	5	10	20	50	100	500	1000
Shepp Logan	54%	23%	14%	5%	0.9%	0.01%	0%	0%	0%
brain	59%	31%	22%	12%	5%	0.7%	0.1%	0%	0%
satellite	90%	83%	80%	78%	76%	75%	74%	73 %	72%
stem	86%	66%	51%	28%	10%	1%	0.1%	0%	0%
cells	72%	49%	36%	22%	15%	11%	9%	6%	5%

Table 8.1: Average percentages of zero-pixels in the observed data for the different counting regimes considered in the tests.

Chapter 9

The Multi-parameter Whiteness Principle

Until now we have always considered forward models with only one source of noise (the Poisson noise given by the statistical nature of electromagnetic waves) and \mathcal{R} -KL models with one parameter to be determined. In the following we will introduce a more complex forward model that mimics better the CT acquisition process by considering the data as the sum of the realizations of two different noise processes. To solve the above, we will consider the variational model proposed in [48] and extend the Whiteness Principle to the case of selecting two parameters at the same time. Similar variational models for mixed noise have been proposed in [49, 50, 51, 52] for the image restoration problem, however they do not exploit the automatic selection strategies for the free parameters. In general, the solution of variational methods with two free parameters (e.g. TGV^2) is obtained by a bilevel optimization approach that is typically designed starting from a number of reference images, [56]. The discussion below and the related experiments are performed as a proof of concept for the multi-parameter Whiteness Principle, which will be addressed extensively in future works.

9.1 A more complex CT model

As discussed in 2.3, in clinical X-ray CT scanners the noise in the data comes from several causes, the most important of which is the statistical nature of electromagnetic waves modeled as a Poisson distribution in the model considered up to now. The second most important cause is the electronic noise, which is due to the conversion of the detected X-ray photons into an electrical signal and can be modeled as a Gaussian random variable with mean η and variance σ^2 . Since the mean η of background signals can be estimated using blank measurements prior to each scan, it is common to subtract it from the measured intensity and assume $\eta = 0$ in the model. In this way, the random field \mathbf{B} describing the CT acquisition can be defined as

$$\mathbf{B} \sim \mathcal{MPG}(\bar{\mathbf{A}}, \mathbf{0}_m, \sigma^2 \mathbf{I}_{m \times m}). \quad (9.1)$$

with $\bar{\mathbf{A}} = I_0 e^{-\mathbf{A}\bar{\mathbf{x}}}$ and $\sigma \in \mathbb{R}_{++}$. In this way, the data \mathbf{b} are a realization of the Mixed Poisson-Gaussian r.f. \mathbf{B} and can be written elementwise as

$$b_i = \nu_i + \tau_i \quad (9.2)$$

where ν_i is a realization of the Poisson r.v. with mean $\bar{\lambda}_i = g([\mathbf{A}\bar{\mathbf{x}}]_i) = I_0 e^{-[\mathbf{A}\bar{\mathbf{x}}]_i}$ ($\nu_i = \text{Poiss}(\bar{\lambda}_i)$) and τ_i is a realization of the Gaussian r.v. with mean 0 and standard deviation σ ($\tau_i = \text{Gauss}(0, \sigma^2)$), for $i = 1, \dots, m$.

In 2.3.1 we discussed different ways to approximate the mixed Poisson-Gaussian r.f. in (9.1); the Gaussian one replaces \mathbf{B} with the independent Gaussian r.f. $\mathcal{M} = M_i$:

$$\mathbf{B} \text{ approximated by } \mathcal{M} \sim \mathcal{G}(\bar{\mathbf{A}}, \text{diag}(\bar{\mathbf{A}} + \sigma^2 \mathbf{1}_m)).$$

Since the probability density function reads

$$\begin{aligned} p_{\mathbf{B}}(\bar{\mathbf{A}}, \mathbf{0}_m, \sigma^2 \mathbf{I}_{m \times m}) &\approx p_{\mathcal{M}}(\mathbf{B} \mid \bar{\mathbf{A}}, \text{diag}(\bar{\mathbf{A}} + \sigma^2 \mathbf{1}_m)) \\ &= \prod_{i=1}^m p_{M_i}(b_i \mid \bar{\lambda}_i, \sqrt{\bar{\lambda}_i + \sigma^2}) \\ \text{with } p_{M_i}(b_i \mid \bar{\lambda}_i, \sqrt{\bar{\lambda}_i + \sigma^2}) &= \frac{1}{\sqrt{2\pi(\bar{\lambda}_i + \sigma^2)}} e^{\frac{(b_i - \bar{\lambda}_i)^2}{2(\bar{\lambda}_i + \sigma^2)}} \end{aligned}$$

its negative log likelihood takes the following form:

$$\begin{aligned} -\log p(\mathbf{b} | \mathbf{x}) &= -\log p(\mathbf{b} | \boldsymbol{\lambda}, \sqrt{\lambda_i + \sigma^2}) = -\log \sum_{i=1}^m p(b_i | \lambda_i, \sqrt{\lambda_i + \sigma^2}) \\ &= \frac{1}{2} \sum_{i=1}^m \left(\frac{1}{\lambda_i + \sigma^2} (b_i - \lambda_i)^2 + \log(\lambda_i + \sigma^2) \right) \end{aligned}$$

where in the last equality the constant terms not depending on \mathbf{x} are omitted. Considering a generic regularizer $\mathcal{R}(\mathbf{x})$ the variational model to solve, to which we will refer with the term (\mathcal{R} -MixedNoise), is the following

$$\hat{\mathbf{x}}(\mu, \sigma) \in \arg \min_{\mathbf{x} \in \Omega} \left\{ \mu \mathcal{R}(\mathbf{x}) + \frac{1}{2} \left\| \frac{I_0 e^{-\mathbf{A}\mathbf{x}} - \mathbf{b}}{\sqrt{I_0 e^{-\mathbf{A}\mathbf{x}} + \sigma^2}} \right\|_2^2 + \frac{1}{2} \sum_{j=1}^m (\log(I_0 e^{-\mathbf{A}\mathbf{x}} + \sigma^2))_i \right\},$$

(\mathcal{R} -MixedNoise)

where the solution depends on two free parameters: the regularization parameter μ and the standard deviation of the electronic noise σ . In particular we write explicitly the TV-MixedNoise model:

$$\hat{\mathbf{x}}(\mu, \sigma) \in \arg \min_{\mathbf{x} \in \Omega} \left\{ \mu \text{TV}(\mathbf{x}) + \frac{1}{2} \left\| \frac{I_0 e^{-\mathbf{A}\mathbf{x}} - \mathbf{b}}{\sqrt{I_0 e^{-\mathbf{A}\mathbf{x}} + \sigma^2}} \right\|_2^2 + \frac{1}{2} \sum_{j=1}^m (\log(I_0 e^{-\mathbf{A}\mathbf{x}} + \sigma^2))_i \right\}.$$

(TV-MixedNoise)

9.2 The Multi-parameter Whiteness Principle

The WP expressed in (PWP) can be easily generalized to the case of multiple parameters for a general acquisition model. Let $\mathbf{p} = (p_1, p_2, \dots, p_r)$ be the vector of free parameters in a variational model. Then, the Multi-parameter Whiteness Principle (MWP) can be introduced as the following:

$$\text{Select } \mathbf{p} = \mathbf{p}^* \in \arg \min_{\mathbf{p}} \left\{ W(\mathbf{p}) := \mathcal{W}(\hat{\mathbf{Z}}(\mathbf{p})) \right\}, \quad (\text{MWP})$$

where

$$\mathcal{W}(\mathbf{Z}) := \|\mathbf{S}(\mathbf{Z})\|_2^2 = \sum_{(l,m) \in \mathbf{L}} (s_{l,m}(\mathbf{Z}))^2, \quad (9.3)$$

with the sample normalized autocorrelation matrix $\mathbf{S}(\mathbf{Z}) = (s_{l,m}(\mathbf{Z}))$ defined as

$$s_{l,m}(\mathbf{Z}) = \frac{1}{\|\mathbf{Z}\|_2^2} \sum_{(i,j) \in \mathcal{I}} z_{i,j} z_{i+l,j+m}$$

and with $\widehat{\mathbf{Z}}$ a suitable matrix-valued standardization function mapping from \mathbb{R}^n to $\mathbb{R}^{m_1 \times m_2}$ where $m_1 \times m_2$ is the dimension of the data.

9.2.1 The MWP for Mixed Poisson-Gaussian noise in CT reconstruction

In order to discuss the MWP for Mixed Poisson-Gaussian noise, it is useful to rewrite the vectorized data formation model (9.2) in its equivalent matrix form. Denoting by $\mathbf{B}, \bar{\mathbf{\Lambda}} \in \mathbb{R}^{m_1 \times m_2}$ and $\bar{\mathbf{X}} \in \mathbb{R}^{n_1 \times n_2}$ the matrix forms of vectors $\mathbf{b}, \bar{\boldsymbol{\lambda}} \in \mathbb{R}^m$ and $\bar{\mathbf{x}} \in \mathbb{R}^n$, respectively, it reads

$$\mathbf{B} = \mathbf{POISS}(\bar{\mathbf{\Lambda}}) + \mathbf{GAUSS}(\mathbf{0}_{m_1 \times m_2}, \sigma \mathbf{1}_{m_1 \times m_2}), \quad \bar{\mathbf{\Lambda}} = \mathbf{G}(\mathbf{A}(\bar{\mathbf{X}})), \quad (9.4)$$

where, with a little abuse of notation, $\mathbf{A} : \mathbb{R}^{n_1 \times n_2} \rightarrow \mathbb{R}^{m_1 \times m_2}$ indicates here the linear operator encoded by matrix $\mathbf{A} \in \mathbb{R}^{m \times n}$ in the vectorized model (9.2), and where $\mathbf{POISS}(\bar{\mathbf{\Lambda}}) = \{\text{Poiss}(\bar{\lambda}_{i,j})\}$, $\mathbf{G}(\mathbf{A}(\bar{\mathbf{X}})) = \left\{ g\left(\left(\mathbf{A}(\bar{\mathbf{X}})\right)_{i,j}\right) \right\}$ and $\mathbf{GAUSS}(\mathbf{0}_{m_1 \times m_2}, \sigma \mathbf{1}_{m_1 \times m_2}) = \{\text{Gauss}(0, \sigma)\}$ with $\sigma \in \mathbb{R}_{++}$, i.e. the matrix forms of vectors $\boldsymbol{\nu}$, $\mathbf{g}(\mathbf{A}\bar{\mathbf{x}})$ and $\boldsymbol{\tau}$ in (9.2).

Before applying the Multi-parameter Whiteness principle to the case of Mixed Poisson-Gaussian noise in CT reconstruction, and in particular to the two free parameters of the variational model (\mathcal{R} -MixedNoise), we propose again the definition of independent Mixed Poisson-Gaussian random field (presented in 2.3.3 in its vectorized form) and introduce the definition of standard Mixed Poisson-Gaussian random variable and independent random field which will be the basis for defining the $\widehat{\mathbf{Z}}$ standardization function in (MWP).

Definition 9.2.1 (independent Mixed Poisson-Gaussian random field). A random field $\mathcal{B} = \{B_{i,j}\}$ is said to be independent Mixed Poisson-Gaussian distributed with parameters $\mathbf{\Lambda} = \{\lambda_{i,j}\}$, $\mathbf{H} = \{\eta_{i,j}\}$ and $\mathbf{\Sigma} = \{\sigma_{i,j}\}$, denoted

by $\mathbf{B} \sim \mathcal{P}(\mathbf{\Lambda}, \mathbf{H}, \mathbf{\Sigma})$, if it satisfies:

$$\begin{aligned} B_{i,j} &\sim \mathcal{MPG}(\lambda_{i,j}, \eta_{i,j}, \sigma_{i,j}^2) \quad \forall (i, j) \in \mathbf{I}, \\ p_{\mathbf{B}}(\mathbf{B} \mid \mathbf{\Lambda}, \mathbf{H}, \mathbf{\Sigma}) &= \prod_{(i,j) \in \mathbf{I}} p_{B_{i,j}}(b_{i,j} \mid \lambda_{i,j}, \eta_{i,j}, \sigma_{i,j}^2). \end{aligned} \quad (9.5)$$

Definition 9.2.2 (standard Mixed Poisson-Gaussian random variable and independent random field). Let $B \sim \mathcal{MPG}(\lambda, \eta, \sigma^2)$. We call the discrete random variable Z defined by

$$Z = S_{\lambda, \eta, \sigma}(B) := \frac{B - \mathbb{E}[B]}{\sqrt{\text{Var}[B]}} = \frac{B - (\lambda + \eta)}{\sqrt{\lambda + \sigma^2}}, \quad (9.6)$$

as standard Mixed Poisson-Gaussian distributed with parameters λ , η and σ^2 , denoted by $Z \sim \widetilde{\mathcal{MPG}}(\lambda, \eta, \sigma^2)$. Let $\mathbf{B} \sim \mathcal{MPG}(\mathbf{\Lambda}, \boldsymbol{\eta}, \mathbf{\Sigma})$ an independent Mixed Poisson Gaussian r.f.; we call the random field defined by

$$\mathbf{Z} = \{Z_{i,j}\} \quad \text{with} \quad Z_{i,j} = S_{\lambda_{i,j}, \eta_{i,j}, \sigma_{i,j}}(B_{i,j}) \quad \forall (i, j) \in \mathbf{I}, \quad (9.7)$$

as independent standard Mixed Poisson-Gaussian distributed with parameters $\mathbf{\Lambda}$, $\boldsymbol{\eta}$ and $\mathbf{\Sigma}$, denoted by $\mathbf{Z} \sim \widetilde{\mathcal{MPG}}(\mathbf{\Lambda}, \boldsymbol{\eta}, \mathbf{\Sigma})$.

In light of Definition 9.2.1, the image formation model (9.4) can be written in probabilistic terms as follows:

$$\mathbf{B} \text{ realization of } \mathbf{B} \sim \mathcal{MPG}(\bar{\mathbf{\Lambda}}, \mathbf{0}_{m_1 \times m_2}, \sigma \mathbf{1}_{m_1 \times m_n}),$$

with matrix $\bar{\mathbf{\Lambda}}$ defined in (9.4). Then, based on Definition 9.2.2, after introducing the matrix

$$\mathbf{Z} = \{z_{i,j}\} \quad \text{with} \quad z_{i,j} = S_{\bar{\lambda}_{i,j}}(b_{i,j}) = \frac{b_{i,j} - \bar{\lambda}_{i,j}}{\sqrt{\bar{\lambda}_{i,j} + \sigma^2}}, \quad (9.8)$$

the probabilistic model (7.13) can be equivalently written in standardized form as

$$\mathbf{Z} \text{ realization of } \mathbf{Z} \sim \widetilde{\mathcal{MPG}}(\bar{\mathbf{\Lambda}}, \mathbf{0}_{m_1 \times m_2}, \sigma \mathbf{1}_{m_1 \times m_n}).$$

Denoting by $\widehat{\mathbf{X}}(\mu, \sigma) = \{\widehat{x}_{i,j}(\mu, \sigma)\}$ the matrix form of the solution of a \mathcal{R} -Mixed Poisson-Gaussian model - e.g., of the TV-MixedNoise model in (TV-MixedNoise) - we introduce the μ, σ -dependent matrices $\widehat{\mathbf{\Lambda}}(\mu, \sigma), \widehat{\mathbf{Z}}(\mu, \sigma) \in \mathbb{R}^{m_1 \times m_2}$ given by

$$\widehat{\mathbf{\Lambda}}(\mu, \sigma) = \{\widehat{\lambda}_{i,j}(\mu)\} = I_0 e^{-\mathbf{A}(\widehat{\mathbf{X}}(\mu))}, \quad (9.9)$$

$$\widehat{\mathbf{Z}}(\mu, \sigma) = \{\widehat{z}_{i,j}(\mu, \sigma)\} \quad (9.10)$$

$$\text{with } \widehat{z}_{i,j}(\mu, \sigma) = S_{\widehat{\lambda}_{i,j}(\mu, \sigma)}(b_{i,j}) = \frac{b_{i,j} - \widehat{\lambda}_{i,j}(\mu, \sigma)}{\sqrt{\widehat{\lambda}_{i,j}(\mu, \sigma) + \sigma^2}}. \quad (9.11)$$

The ideal goal of any criterion for choosing (μ, σ) in the class of \mathcal{R} -Mixednoise models is to select the values (μ^*, σ^*) yielding the closest solution image $\widehat{\mathbf{X}}(\mu^*, \sigma^*)$ to the target uncorrupted image $\overline{\mathbf{X}}$, according to some distance metric. The conjecture behind our proposal is that the closer the solution $\widehat{\mathbf{X}}(\mu, \sigma)$ is to the target $\overline{\mathbf{X}}$, the closer the matrix $\widehat{\mathbf{Z}}(\mu, \sigma)$ defined in (9.9)-(9.11) will be to \mathbf{Z} in (9.8), so the more $\widehat{\mathbf{Z}}(\mu)$ will resemble the realization of a white random field. Hence, the proposed criterion, that we refer to as the Multi-parameter Poisson Gaussian Whiteness Principle (MPGWP), consists in choosing the values of μ and σ leading to the less auto-correlated matrix $\widehat{\mathbf{Z}}(\mu, \sigma)$. Based on the scalar normalized auto-correlation measure introduced in (9.3), the MPGWP reads:

$$\text{Select } (\mu, \sigma) = (\mu^*, \sigma^*) \in \arg \min_{\mu, \sigma \in \mathbb{R}_{++}} \left\{ W(\mu, \sigma) := \mathcal{W}(\widehat{\mathbf{Z}}(\mu, \sigma)) \right\},$$

with matrix $\widehat{\mathbf{Z}}(\mu, \sigma)$ defined in (9.9)-(9.11) and function \mathcal{W} in (9.3).

(MPGWP)

9.3 Numerical Results

In this section, we show some preliminary results obtained on the performance of the proposed (MPGWP) for the selection of the regularization parameter μ and the standard deviation σ in the (TV-MixedNoise) model employed for the solution of CT imaging problems. For a quantitative evaluation, the accuracy of the reconstructed images $\widehat{\mathbf{x}}(\mu^*, \sigma^*)$ with respect to

the original image $\bar{\mathbf{x}}$ is measured by means of two scalar metrics: the SSIM and the SNR. The (TV-MixedNoise) model is solved by the ADMM approach outlined in Section 10.2 for a very fine grid of different μ and σ values and for each reconstructed image $\hat{\mathbf{x}}(\mu, \sigma)$ we compute the value of the whiteness function $W(\mu, \sigma)$ defined in (MPGWP). In particular, we calculate $W(\mu, \sigma)$ efficiently based on the Fourier-domain formula in (7.4). The (μ, σ) couple selected by the (MPGWP) is the one minimizing the function $W(\mu, \sigma)$ and will be denoted with $(\mu^{(W)}, \sigma^{(W)})$. Their associated reconstructed images will be indicated with $\hat{\mathbf{x}}(\mu^{(W)}, \sigma^{(W)})$. For each (μ, σ) -couple in the considered grid, we also compute the SNR and SSIM of the associated reconstructed image $\hat{\mathbf{x}}(\mu, \sigma)$. Moreover, to evaluate in absolute terms the performance of the three compared selection criteria, we also compute the values $(\mu^{(SNR)}, \sigma^{(SNR)})$ and $(\mu^{(SSIM)}, \sigma^{(SSIM)})$ which yield the reconstructed images exhibiting the highest SNR and the highest SSIM values, respectively. The two reconstructed images $\hat{\mathbf{x}}(\mu^{(SNR)}, \sigma^{(SNR)})$, $\hat{\mathbf{x}}(\mu^{(SSIM)}, \sigma^{(SSIM)})$ and the associated SNR and SSIM quality metrics are then regarded as the best theoretical results achievable by the compared selection strategies. In all the performed tests, the iterations of the ADMM approach used for the solution of the TV-KL model are stopped as soon as $\delta_{\mathbf{x}}^{(k)} < 10^{-6}$, where $\delta_{\mathbf{x}}^{(k)}$ is defined in (6.25), while the ADMM penalty parameter γ is set manually so as to fasten the convergence of the alternating scheme.

Data Generation For this experiment we consider the test images **shepp logan** (200×200 , pixel size = 0.4mm), with pixel values between 0 and 1. The acquisition process of the fan beam CT setup, i.e. the projection operator \mathbf{A} , is built using the ASTRA Toolbox [40] with the following parameters: 180 equally spaced angles of projections (from 0 to 2π), a detector with 200 pixels (detector pixel size = 1/5mm), distance between the source and the center of rotation = 300mm, distance between the center of rotation and the detector array = 200mm. Then, according to (9.2), we take the exponential of $-\mathbf{A}\bar{\mathbf{x}}$ and multiply it by a factor $I_0 \in \mathbb{N}_+$. We thus compute the noise-free

data $\bar{\lambda} = I_0 e^{-\mathbf{A}\bar{x}}$, while $\nu = \mathbf{Poiss}(\bar{\lambda})$ and $\tau = \mathbf{Gauss}(\mathbf{0}_m, \text{diag}(\sigma \mathbf{1}_m))$ are obtained by sampling from a m -variate independent Poisson random process with mean vector $\bar{\lambda}$ and a m -variate i.i.d Gaussian random process with mean 0 and standard deviation σ , respectively, with $m = 200 \cdot 180$. Finally, the observation \mathbf{b} are obtained by summing ν and τ . We performed the experiments by considering two cases in the mid-high count regimes:

- Case 1: $I_0 = 500$ and $\sigma = 10$,
- Case 2: $I_0 = 2500$ and $\sigma = 20$.

Results Figure 9.1 shows the reconstructed images according to the Multi-parameter Whiteness Principle, the best SNR and the best SSIM, together with the observed data for the case of $I_0 = 500$ and $\sigma = 10$. We can note that the image selected by the whiteness principle is very similar to the other two by presenting all the same inside structures and being also slightly less noisy. Moreover, the same Figure displays the SNR, SSIM and Whiteness function over the 2D grid of (μ, σ) values; the red dot corresponds to the selected $(\mu^{(W)}, \sigma^{(W)})$ couple (minimizing the Whiteness function), while the green diamonds indicated the maximum of the SNR and SSIM functions. By looking at the both the reconstructions and the plotted functions we can note that the Whiteness criteria selects (μ, σ) values that are very different from $(\mu^{(SNR)}, \sigma^{(SNR)})$ and $(\mu^{(SSIM)}, \sigma^{(SSIM)})$; however the red dot is close to the ridge of the SNR and SSIM curves, achieving values that are close to the maximum. Table 9.1 displays the selected μ and σ with the three criteria, together with their associated SNR and SSIM values.

For the second case ($I_0 = 2500$ and $\sigma = 20$), the reconstructed images and the SNR, SSIM and Whiteness functions are shown in Figure; while its numerical values are stored in the second part of table 9.1. By looking at the curves, one can note that the red dot (selected values according to the whiteness criteria) is close to both the maximum of the SNR and SSIM, with this proximity showing in the reconstructed images that look very similar.

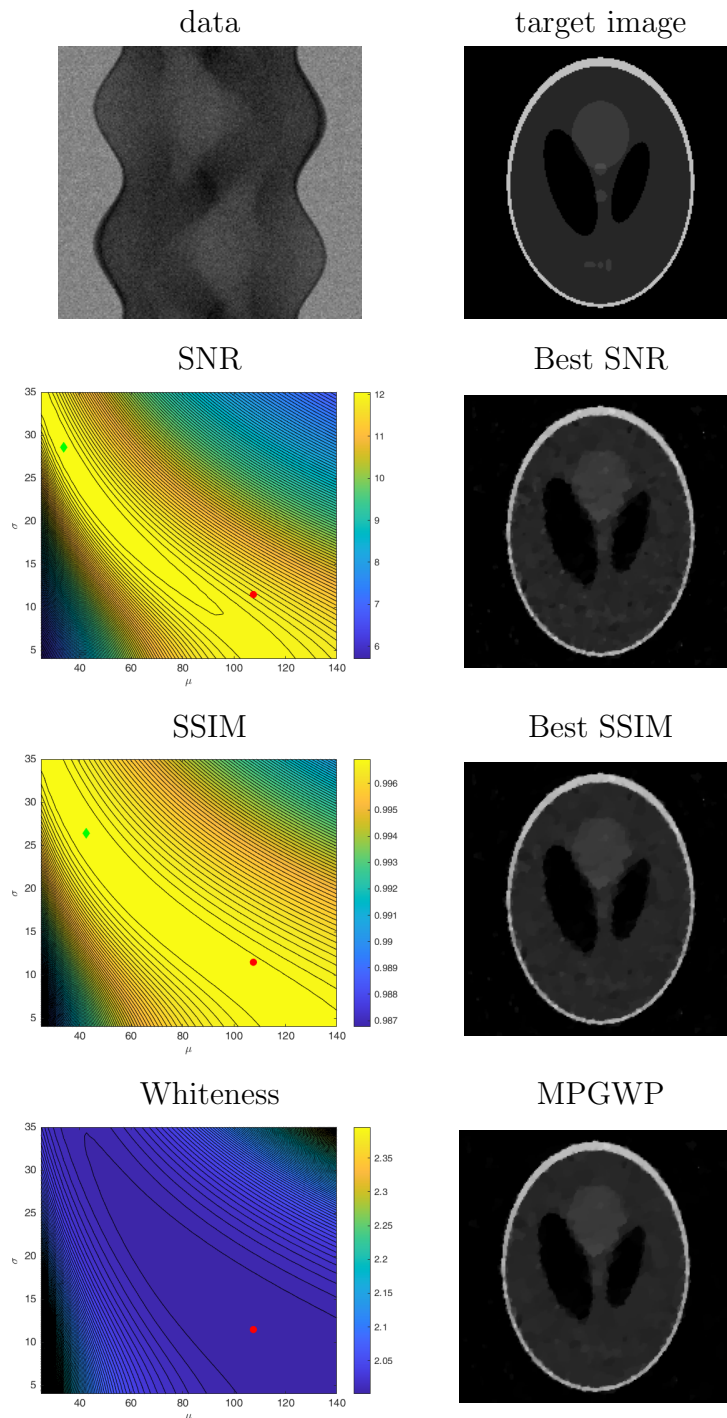


Figure 9.1: Case 1 ($I_0 = 500$, $\sigma = 10$). (Left column) Observed data, SNR, SSIM and Whiteness values values over the 2D grid. (Right column) Target image, reconstructed images with the TV-MixedNoise model referring to the parameters pair (μ, σ) chosen according to the best SNR, best SSIM and the Multi-parameter Whiteness Principle.

I_0	σ		TV-MixedNoise		
			Best SNR	Best SSIM	MPGWP
500	10	SNR	12.1172	12.0498	11.8297
		SSIM	0.9969	0.9970	0.9969
		σ^*	28.586	26.448	11.483
		μ^*	33.846	42.692	107.564
2500	20	SNR	17.0792	17.0174	16.5733
		SSIM	0.9991	0.9991	0.9990
		σ^*	88.462	81.538	83.846
		μ^*	37.692	49.487	61.282

Table 9.1: SNR, SSIM, μ^* and σ^* values of the reconstructed images with the TV-MixedNoise model referring to the parameters pair (μ, σ) chosen according to the best SNR, best SSIM and the Multi-parameter Whiteness Principle.

As for the first case, the $\hat{\mathbf{x}}(\mu^{(W)}, \sigma^{(W)})$ is less noisier than the two best SNR and SSIM while keeping all the significant structures.

9.3.1 Derivative free minimization of the Whiteness function

In the previous experiments we calculated the minimum of the Whiteness function by setting a fine grid of (μ, σ) values, computing the solution $\hat{\mathbf{x}}(\mu, \sigma)$ corresponding to each parameter couple and then by evaluating the Whiteness function on the solutions. This simple algorithmic scheme allowed us to validate the MWP for the mixed Poisson-Gaussian noise in CT reconstruction; however, as one can easily imagine, the optimization procedure turned out to be particularly costly. For this reason, here we propose to apply a zero order optimization scheme to minimize the Whiteness function; notice that this class of strategies is particularly useful in our case since it needs only function evaluations and no derivation of the considered function, [57]. In

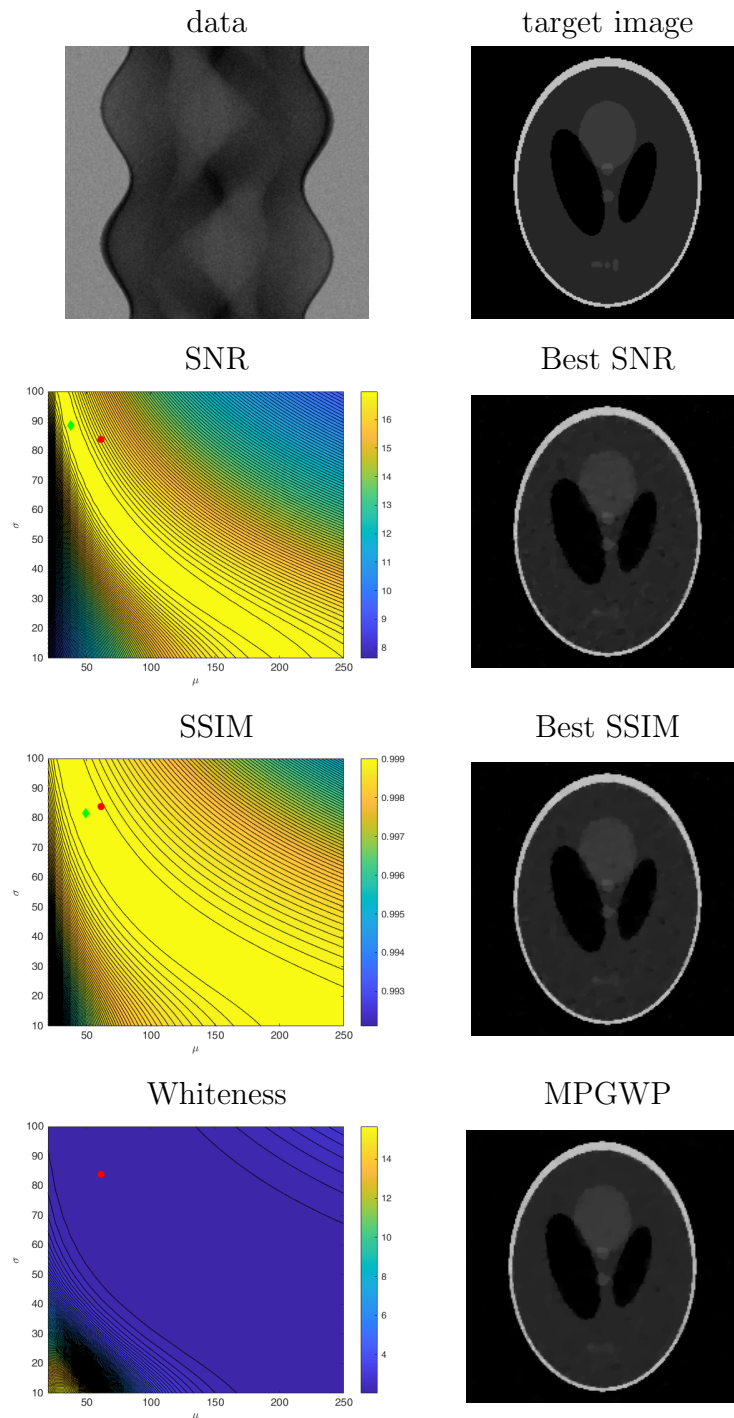


Figure 9.2: Case 1 ($I_0 = 2500$, $\sigma = 20$). (Left column) Observed data, SNR, SSIM and Whiteness values values over the 2D grid. (Right column) Target image, reconstructed images with the TV-MixedNoise model referring to the parameters pair (μ, σ) chosen according to the best SNR, best SSIM and the Multi-parameter Whiteness Principle.

particular, we applied the derivative free algorithm proposed in [58] that investigates the local behaviour of the objective function on the feasible set by sampling it along the coordinate directions. Whenever a suitable descent feasible coordinate direction is detected a new point is produced by performing a derivative free linesearch along this direction, so as to exploit the descent property of the search direction as much as possible. The information progressively obtained during the iterates of the algorithm can be used to build an approximation model of the objective function. The minimum of such a model is accepted if it produces an improvement of the objective function value. The algorithm is applied for the first application case ($I_0 = 500$ and $\sigma = 10$) with initial point $(\mu^{(0)}, \sigma^{(0)}) = (35, 18)$. Figure 9.3 shows the selected couples $(\mu^{(k)}, \sigma^{(k)})$ during the iterations over the contour lines of the Whiteness function, also the red dot represents the parameter couple selected by the *a posteriori* approach described before. As one can note, the pair of parameters obtained with the iterative algorithms converges to the *a posteriori* one in few iterations, reaching the values of $\hat{\mu}^{(MWP)} = 108.242$ and $\hat{\sigma}^{(MWP)} = 11.750$.

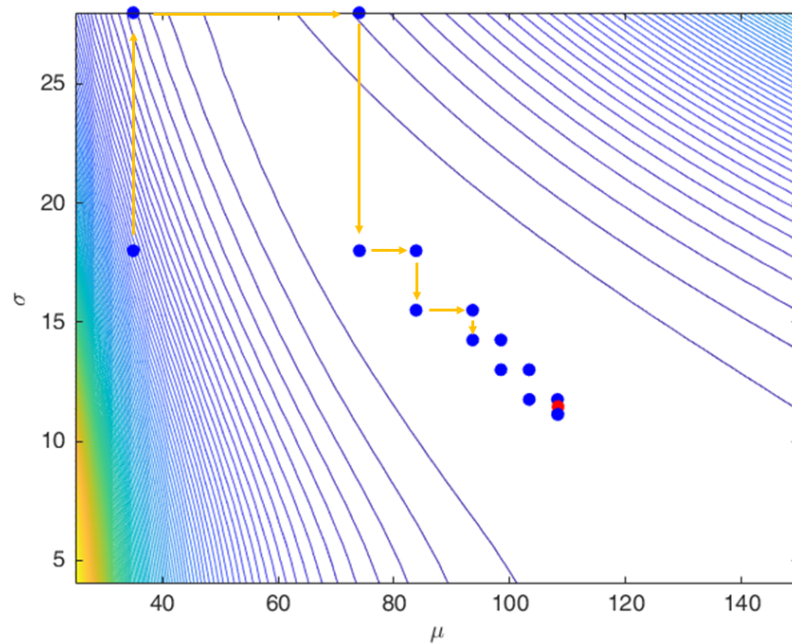


Figure 9.3: Derivative free minimization procedure [58] applied to the White-ness function for the Case 1 ($I_0 = 500$ and $\sigma = 10$).

Chapter 10

Numerical Solution of Variational Models by ADMM

In this chapter we will address the numerical solution of the variational models considered in the previous experiments. First we will focus on the \mathcal{R} -KL model (\mathcal{R} -KL) considered for the CT reconstruction and image restoration problem when the sole Poisson noise arises in the degradation process; more specifically, we will consider $\mathcal{R} = \text{TV}$, TV^2 and TVG^2 . We will then discuss the resolution for the model with mixed Poisson-Gaussian noise in (TV-MixedNoise). Notice that the single regularization parameter μ in the former case, and the two parameters μ , σ in the latter will be considered as fixed throughout the discussion.

10.1 Numerical solution for the \mathcal{R} -KL model

Before going into the details of solving the different \mathcal{R} -KL models, we briefly recall their expressions, for the case of $\mathcal{R} = \text{TV}$, TV^2 and TVG^2 . First, we recall the definitions of the (\mathcal{R} -KL) variational model and of the

(TV), (TV²) and (TGV²) regularizers, and by introducing the three matrices

$$\mathbf{D}_1 = \begin{pmatrix} \mathbf{D}_h \\ \mathbf{D}_v \end{pmatrix} \in \mathbb{R}^{2n \times n}, \quad \mathbf{D}_2 = \begin{pmatrix} \mathbf{D}_{hh} \\ \mathbf{D}_{vv} \\ \mathbf{D}_{hv} \\ \mathbf{D}_{vh} \end{pmatrix} \in \mathbb{R}^{4n \times n}, \quad \mathbf{D}_S = \begin{pmatrix} \mathbf{D}_h & \mathbf{0} \\ \mathbf{0} & \mathbf{D}_v \\ \frac{1}{2}\mathbf{D}_v & \frac{1}{2}\mathbf{D}_h \\ \frac{1}{2}\mathbf{D}_v & \frac{1}{2}\mathbf{D}_h \end{pmatrix} \in \mathbb{R}^{4n \times 2n},$$

with $\mathbf{D}_h, \mathbf{D}_v, \mathbf{D}_{hh}, \mathbf{D}_{vv}, \mathbf{D}_{hv}, \mathbf{D}_{vh} \in \mathbb{R}^{n \times n}$ finite difference matrices discretizing the first-order partial derivatives of image \mathbf{x} in the horizontal and vertical direction and the second-order partial derivatives of image \mathbf{x} in the horizontal, vertical, mixed horizontal-vertical and mixed vertical-horizontal directions (with $\mathbf{D}_{vh} = \mathbf{D}_{hv}$), respectively, the three models of interest can be equivalently written as

$$\widehat{\mathbf{x}}(\mu) \in \arg \min_{\mathbf{x} \in \mathbb{R}^n} \left\{ \iota_{\mathbb{R}_+^n}(\mathbf{x}) + \mu \text{KL}(\mathbf{g}(\mathbf{A}\mathbf{x}) + \mathbf{q}; \mathbf{b}) + \sum_{i \in \mathcal{J}} \|(\mathbf{D}_1 \mathbf{x})_i\|_2 \right\},$$

(TV-KL)

$$\widehat{\mathbf{x}}(\mu) \in \arg \min_{\mathbf{x} \in \mathbb{R}^n} \left\{ \iota_{\mathbb{R}_+^n}(\mathbf{x}) + \mu \text{KL}(\mathbf{g}(\mathbf{A}\mathbf{x}) + \mathbf{q}; \mathbf{b}) + \sum_{i \in \mathcal{J}} \|(\mathbf{D}_2 \mathbf{x})_i\|_2 \right\},$$

(TV²-KL)

$$\{\widehat{\mathbf{x}}(\mu), \widehat{\mathbf{w}}(\mu)\} \in \arg \min_{\substack{\mathbf{x} \in \mathbb{R}^n, \\ \mathbf{w} \in \mathbb{R}^{2n}}} \left\{ \iota_{\mathbb{R}_+^n}(\mathbf{x}) + \mu \text{KL}(\mathbf{g}(\mathbf{A}\mathbf{x}) + \mathbf{q}; \mathbf{b}) \right. \\ \left. + \alpha_0 \sum_{i \in \mathcal{J}} \|(\mathbf{D}_1 \mathbf{x})_i - \mathbf{w}_i\|_2 + \alpha_1 \sum_{i \in \mathcal{J}} \|(\mathbf{D}_S \mathbf{w})_i\|_2 \right\},$$

(TGV²-KL)

where $\iota_{\mathbb{R}_+^n}(\mathbf{x})$ denotes the indicator function of the non-negative orthant \mathbb{R}_+^n and where, with a little abuse of notation, we indicate by

$$\begin{aligned} (\mathbf{D}_1 \mathbf{x})_i &:= ((\mathbf{D}_h \mathbf{x})_i; (\mathbf{D}_v \mathbf{x})_i) \in \mathbb{R}^2 \\ (\mathbf{D}_2 \mathbf{x})_i &:= ((\mathbf{D}_{hh} \mathbf{x})_i; (\mathbf{D}_{vv} \mathbf{x})_i; (\mathbf{D}_{hv} \mathbf{x})_i; (\mathbf{D}_{vh} \mathbf{x})_i) \in \mathbb{R}^4 \end{aligned}$$

the discrete gradient and vectorized Hessian of image \mathbf{x} at pixel i , respectively. Moreover, we denote by

$$(\mathbf{D}_S \mathbf{w})_i := \left((\mathbf{D}_h \mathbf{w}_1)_i; (\mathbf{D}_v \mathbf{w}_2)_i; \frac{(\mathbf{D}_v \mathbf{w}_1)_i}{2} + \frac{(\mathbf{D}_h \mathbf{w}_2)_i}{2}; \frac{(\mathbf{D}_v \mathbf{w}_1)_i}{2} + \frac{(\mathbf{D}_h \mathbf{w}_2)_i}{2} \right) \in \mathbb{R}^4$$

the vectorized discrete symmetric Jacobian of vector field $\mathbf{w} = (\mathbf{w}_1; \mathbf{w}_2)$ at pixel i . Then, by introducing for the (TV-KL), (TV²-KL) and (TGV²-KL) models the auxiliary variable \mathbf{u} defined in the three cases, respectively, by

$$\mathbf{u} = \begin{pmatrix} \mathbf{u}_1 \\ \mathbf{u}_2 \\ \mathbf{u}_3 \end{pmatrix} = \begin{pmatrix} \mathbf{x} \\ \mathbf{A}\mathbf{x} \\ \mathbf{D}_1 \mathbf{x} \end{pmatrix}, \quad \mathbf{u} = \begin{pmatrix} \mathbf{u}_1 \\ \mathbf{u}_2 \\ \mathbf{u}_3 \end{pmatrix} = \begin{pmatrix} \mathbf{x} \\ \mathbf{A}\mathbf{x} \\ \mathbf{D}_2 \mathbf{x} \end{pmatrix},$$

$$\mathbf{u} = \begin{pmatrix} \mathbf{u}_1 \\ \mathbf{u}_2 \\ \mathbf{u}_3 \\ \mathbf{u}_4 \end{pmatrix} = \begin{pmatrix} \mathbf{x} \\ \mathbf{A}\mathbf{x} \\ \mathbf{D}_1 \mathbf{x} - \mathbf{w} \\ \mathbf{D}_S \mathbf{w} \end{pmatrix},$$

and setting $\mathbf{t} = \mathbf{x}$ for TV-KL and TV²-KL, $\mathbf{t} = (\mathbf{x}; \mathbf{w})$ for TGV²-KL, it is easy to verify that all the three models can be equivalently reformulated as the following standard two-blocks (additively) separable minimization problem with linear constraints:

$$\left\{ \widehat{\mathbf{t}}(\mu), \widehat{\mathbf{u}}(\mu) \right\} \in \arg \min_{\mathbf{t}, \mathbf{u}} \{ C_1(\mathbf{t}) + C_2(\mathbf{u}; \mu) \} \quad \text{subject to: } \mathbf{M}_1 \mathbf{t} + \mathbf{M}_2 \mathbf{u} = \mathbf{0}. \quad (10.1)$$

The explicit expressions of functions C_1 , C_2 and matrices \mathbf{M}_1 , \mathbf{M}_2 for the TV-KL model is

$$C_1(\mathbf{t}) = 0, \quad C_2(\mathbf{u}; \mu) = \iota_{\mathbb{R}_+}(\mathbf{u}_1) + \mu \text{KL}(\mathbf{g}(\mathbf{u}_2) + \mathbf{q}; \mathbf{b}) + \sum_{i \in \mathcal{J}} \|\mathbf{u}_{3,i}\|_2,$$

$$\mathbf{M}_1 = \begin{pmatrix} \mathbf{I} \\ \mathbf{A} \\ \mathbf{D}_1 \end{pmatrix} \in \mathbb{R}^{(m+3n) \times n}, \quad \mathbf{M}_2 = -\mathbf{I} \in \mathbb{R}^{(m+3n) \times (m+3n)},$$

while for the TV²-KL model we have

$$C_1(\mathbf{t}) = 0, \quad C_2(\mathbf{u}; \mu) = \iota_{\mathbb{R}_+}(\mathbf{u}_1) + \mu \text{KL}(\mathbf{g}(\mathbf{u}_2) + \mathbf{q}; \mathbf{b}) + \sum_{i \in \mathcal{J}} \|\mathbf{u}_{3,i}\|_2,$$

$$\mathbf{M}_1 = \begin{pmatrix} \mathbf{I} \\ \mathbf{A} \\ \mathbf{D}_2 \end{pmatrix} \in \mathbb{R}^{(m+5n) \times n}, \quad \mathbf{M}_2 = -\mathbf{I} \in \mathbb{R}^{(m+5n) \times (m+5n)}.$$

Finally, in the case of the TGV²-KL model they read

$$C_1(\mathbf{t}) = 0, \quad C_2(\mathbf{u}; \mu) = \iota_{\mathbb{R}_+}(\mathbf{u}_1) + \mu \text{KL}(\mathbf{g}(\mathbf{u}_2) + \mathbf{q}; \mathbf{b}) + \\ + \alpha_0 \sum_{i \in \mathcal{J}} \|\mathbf{u}_{3,i}\|_2 + \alpha_1 \sum_{i \in \mathcal{J}} \|\mathbf{u}_{4,i}\|_2,$$

$$\mathbf{M}_1 = \begin{pmatrix} \mathbf{I} & \mathbf{0} \\ \mathbf{A} & \mathbf{0} \\ \mathbf{D}_1 & -\mathbf{I} \\ \mathbf{0} & \mathbf{D}_S \end{pmatrix} \in \mathbb{R}^{(m+5n) \times 2n}, \quad \mathbf{M}_2 = -\mathbf{I} \in \mathbb{R}^{(m+5n) \times (m+5n)}.$$

The Lagrangian function \mathcal{L} and augmented Lagrangian function \mathcal{L}_γ associated with problem (10.1) read

$$\mathcal{L}(\mathbf{t}, \mathbf{u}, \boldsymbol{\rho}; \mu) = C_1(\mathbf{t}) + C_2(\mathbf{u}; \mu) + \boldsymbol{\rho}^\top (\mathbf{M}_1 \mathbf{t} + \mathbf{M}_2 \mathbf{u}), \quad (10.2)$$

$$\mathcal{L}_\gamma(\mathbf{t}, \mathbf{u}, \boldsymbol{\rho}; \mu) = \mathcal{L}(\mathbf{t}, \mathbf{u}, \boldsymbol{\rho}; \mu) + \frac{\gamma}{2} \|\mathbf{M}_1 \mathbf{t} + \mathbf{M}_2 \mathbf{u}\|_2^2, \quad (10.3)$$

where $\boldsymbol{\rho}$ is the vector of Lagrange multipliers associated to the system of linear constraints in (10.1) and $\gamma \in \mathbb{R}_{++}$ is a penalty parameter. Solving problem (10.1) amounts to seek the saddle point(s) $\{\hat{\mathbf{t}}(\mu), \hat{\mathbf{u}}(\mu), \hat{\boldsymbol{\rho}}(\mu)\}$ of the augmented Lagrangian \mathcal{L}_γ in (10.3) which, according to the standard two-blocks ADMM [53], can be computed as the limit point of the following

iterative procedure:

$$\begin{aligned} \mathbf{t}^{(k+1)} &= \arg \min_{\mathbf{t}} \mathcal{L}_\gamma(\mathbf{t}, \mathbf{u}^{(k)}, \boldsymbol{\rho}^{(k)}; \mu) \\ &= \arg \min_{\mathbf{t}} \left\{ C_1(\mathbf{t}) + \frac{\gamma}{2} \left\| \mathbf{M}_1 \mathbf{t} + \mathbf{M}_2 \mathbf{u}^{(k)} + \frac{1}{\gamma} \boldsymbol{\rho}^{(k)} \right\|_2^2 \right\}, \end{aligned} \quad (10.4)$$

$$\begin{aligned} \mathbf{u}^{(k+1)} &= \arg \min_{\mathbf{u}} \mathcal{L}_\gamma(\mathbf{t}^{(k+1)}, \mathbf{u}, \boldsymbol{\rho}^{(k)}; \mu) \\ &= \arg \min_{\mathbf{u}} \left\{ C_2(\mathbf{u}) + \frac{\gamma}{2} \left\| \mathbf{M}_2 \mathbf{u} + \mathbf{M}_1 \mathbf{t}^{(k+1)} + \frac{1}{\gamma} \boldsymbol{\rho}^{(k)} \right\|_2^2 \right\} \end{aligned} \quad (10.5)$$

$$\boldsymbol{\rho}^{(k+1)} = \boldsymbol{\rho}^{(k)} + \gamma (\mathbf{M}_1 \mathbf{t}^{(k+1)} + \mathbf{M}_2 \mathbf{u}^{(k+1)}) . \quad (10.6)$$

In the following subsections we detail how to solve the \mathbf{t} -subproblem in (10.4) and the \mathbf{u} -subproblem in (10.5) when tackling CT and image restoration imaging problems, together with the different choices of regularizer.

10.1.1 The \mathbf{t} -subproblem

Recalling the definition of the augmented Lagrangian function \mathcal{L} in (10.3), after dropping the constant terms the \mathbf{t} -update problem in (10.4) reads

$$\begin{aligned} \mathbf{t}^{(k+1)} &\in \arg \min_{\mathbf{t} \in \mathbb{R}^n} \left\{ \langle \boldsymbol{\rho}^{(k)}, \mathbf{M}_1 \mathbf{t} - \mathbf{u}^{(k)} \rangle + \frac{\gamma}{2} \|\mathbf{M}_1 \mathbf{t} - \mathbf{u}^{(k)}\|_2^2 \right\} \\ &= \arg \min_{\mathbf{t} \in \mathbb{R}^n} \left\{ Q^{(k)}(\mathbf{t}) := \frac{1}{2} \|\mathbf{M}_1 \mathbf{t} - \mathbf{v}^{(k)}\|_2^2 \right\}, \quad \mathbf{v}^{(k)} = \mathbf{u}^{(k)} - \frac{1}{\gamma} \boldsymbol{\rho}^{(k)} \end{aligned} \quad (10.7)$$

Since the cost function $Q^{(k)}$ in (10.7) is quadratic and convex, it admits global minimizers which are the solutions of the linear system of normal equations:

$$\mathbf{M}_1^T \mathbf{M}_1 \mathbf{t}^{(k+1)} = \mathbf{M}_1^T \mathbf{v}^{(k)} \iff \mathbf{t}^{(k+1)} = (\mathbf{M}_1^T \mathbf{M}_1)^{-1} \mathbf{M}_1^T \mathbf{v}^{(k)}. \quad (10.8)$$

that is, $\mathbf{t}^{(k+1)}$ is obtained by solving a linear system with coefficient matrix $\mathbf{M}_1^T \mathbf{M}_1$.

For the image restoration problem, i.e. $\mathbf{g}(\cdot) = \cdot$ and \mathbf{A} being the blur matrix, the matrix is symmetric and positive definite - hence, non-singular - in all the three choices of \mathcal{R} and, by assuming periodic boundary conditions for all the involved finite difference matrices, the linear system can be solved very

efficiently based on the 2D discrete Fourier transform, implemented by 2D fast Fourier transform (see, e.g., [41], [54], [55]). We note that $\mathbf{t}^{(k+1)} = \mathbf{x}^{(k+1)}$ for TV-KL and TV²-KL, $\mathbf{t}^{(k+1)} = (\mathbf{x}^{(k+1)}; \mathbf{w}^{(k+1)})$ for TGV²-KL.

When addressing the CT problem, the structure of matrix \mathbf{A} - which, we recall, in this case is a Radon matrix - does not allow for a Fourier diagonalization of matrix $\mathbf{M}_1^T \mathbf{M}_1$, thus yielding a significant computational burden related to the solution of linear system (10.8). A popular strategy for avoiding such difficulty is the linearized ADMM. It relies on computing $\mathbf{t}^{(k+1)}$ as the global minimizer of a surrogate function $\widehat{Q}^{(k)}$ of $Q^{(k)}$ in (10.7), namely

$$\mathbf{t}^{(k+1)} = \arg \min_{\mathbf{t} \in \mathbb{R}^n} \widehat{Q}^{(k)}(\mathbf{t}), \quad (10.9)$$

where $\widehat{Q}^{(k)}$ is a quadratic function of the following form

$$\begin{aligned} \widehat{Q}^{(k)}(\mathbf{x}) &= Q^{(k)}(\mathbf{t}^{(k)}) + \langle \nabla Q^{(k)}(\mathbf{t}^{(k)}), \mathbf{t} - \mathbf{t}^{(k)} \rangle \\ &\quad + \frac{\eta}{2} \|\mathbf{t} - \mathbf{t}^{(k)}\|_2^2, \quad \eta \geq \|\mathbf{M}_1\|_2^2. \end{aligned} \quad (10.10)$$

It can be easily proved that any function $\widehat{Q}^{(k)}$ in (10.10) is a *quadratic tangent majorant* of the original function $Q^{(k)}$ in (10.7) at point $\mathbf{t}^{(k)}$, that is it satisfies

$$\begin{aligned} \widehat{Q}^{(k)}(\mathbf{t}^{(k)}) &= Q^{(k)}(\mathbf{t}^{(k)}), \quad \nabla \widehat{Q}^{(k)}(\mathbf{t}^{(k)}) = \nabla Q^{(k)}(\mathbf{t}^{(k)}), \\ \widehat{Q}^{(k)}(\mathbf{t}) &\geq Q^{(k)}(\mathbf{t}) \quad \forall \mathbf{t} \in \mathbb{R}^n. \end{aligned}$$

It follows from (10.9)-(10.10) that the new iterate $\mathbf{t}^{(k+1)}$ computed by the linearized ADMM is given by

$$\mathbf{t}^{(k+1)} = \arg \min_{\mathbf{t} \in \mathbb{R}^n} \left\{ \langle \nabla Q^{(k)}(\mathbf{t}^{(k)}), \mathbf{t} \rangle + \frac{\eta}{2} \|\mathbf{t} - \mathbf{t}^{(k)}\|_2^2 \right\} \quad (10.11)$$

$$= \mathbf{t}^{(k)} - \frac{1}{\eta} \nabla Q^{(k)}(\mathbf{t}^{(k)}) \quad (10.12)$$

$$= \mathbf{t}^{(k)} - \frac{1}{\eta} \mathbf{M}_1^T (\mathbf{M}_1 \mathbf{t}^{(k)} - \mathbf{v}^{(k)}), \quad \eta \geq \|\mathbf{M}_1\|_2^2, \quad (10.13)$$

where in (10.11) we dropped the constant terms, in (10.12) we set $\mathbf{t}^{(k+1)}$ equal to the unique stationary point of the strongly convex cost function in (10.11) and, finally, in (10.13) we substituted the explicit expression of the gradient of the original cost function $Q^{(k)}$ defined in (10.7).

10.1.2 The \mathbf{u} -subproblem

For what regards the \mathbf{u} -update in (10.5), it is easy to verify that it takes the form

$$\mathbf{u}^{(k+1)} = \arg \min_{\mathbf{u}} \left\{ \sum_{j=1}^m U_j(\mathbf{u}_j) \right\} \iff \mathbf{u}_j^{(k+1)} = \arg \min_{\mathbf{u}_j} U_j(\mathbf{u}_j), \quad j = 1, \dots, m,$$

with $m = 3$ for TV-KL and TV²-KL models, $m = 4$ for TGV²-KL. This means that (10.5) is equivalent to 3 or 4 independent minimization subproblems each giving the updated value of one of the solution subvectors \mathbf{u}_j . Here we explain how to derive the formulation and solve the independent subproblems for the TV-KL model; the same procedure can be followed for other models, for which we will describe only the resolution of sub-problems.

TV-KL model

Recalling definition (10.3), the \mathbf{u} -subproblem in (10.5) reads

$$\begin{aligned} \mathbf{u}^{(k+1)} &\in \arg \min_{\mathbf{u} \in \mathbb{R}^{m+3n}} \left\{ C_2(\mathbf{u}) + \langle \boldsymbol{\rho}^{(k)}, \mathbf{M}_1 \mathbf{t}^{(k+1)} - \mathbf{u} \rangle + \frac{\gamma}{2} \|\mathbf{M}_1 \mathbf{t}^{(k+1)} - \mathbf{u}\|_2^2 \right\} \\ &= \arg \min_{\mathbf{u} \in \mathbb{R}^{m+3n}} \left\{ C_2(\mathbf{u}) + \frac{\gamma}{2} \|\mathbf{u} - \mathbf{s}^{(k)}\|_2^2 \right\}, \quad \mathbf{s}^{(k)} = \mathbf{M}_1 \mathbf{u}^{(k+1)} + \frac{1}{\gamma} \boldsymbol{\rho}^{(k)} \end{aligned} \quad (10.14)$$

Then, by recalling the definition of function C_2 for the TV-KL model and introducing the vectors $\boldsymbol{\rho}_1^{(k)} \in \mathbb{R}^{2n}$, $\boldsymbol{\rho}_2^{(k)} \in \mathbb{R}^m$ and $\boldsymbol{\rho}_3^{(k)} \in \mathbb{R}^n$ such that $\boldsymbol{\rho}^{(k)} = (\boldsymbol{\rho}_1^{(k)}; \boldsymbol{\rho}_2^{(k)}; \boldsymbol{\rho}_3^{(k)})$ and the vectors

$$\begin{aligned} \mathbf{s}_1^{(k)} &= \mathbf{u}_1^{(k+1)} + \frac{1}{\gamma} \boldsymbol{\rho}_1^{(k)} \in \mathbb{R}^n, & \mathbf{s}_2^{(k)} &= \mathbf{A} \mathbf{u}_2^{(k+1)} + \frac{1}{\gamma} \boldsymbol{\rho}_2^{(k)} \in \mathbb{R}^m, \\ \mathbf{s}_3^{(k)} &= \mathbf{D}_1 \mathbf{u}_3^{(k+1)} + \frac{1}{\gamma} \boldsymbol{\rho}_3^{(k)} \in \mathbb{R}^{2n} \end{aligned}$$

such that $\mathbf{s}^{(k)} = (\mathbf{s}_1^{(k)}; \mathbf{s}_2^{(k)}; \mathbf{s}_3^{(k)})$, problem (10.14) can be equivalently written as

$$\mathbf{u}^{(k+1)} \in \arg \min_{\mathbf{u} \in \mathbb{R}^{m+3n}} \{ U_1(\mathbf{u}_1) + U_2(\mathbf{u}_2) + U_3(\mathbf{u}_3) \}, \quad \text{with:}$$

$$\begin{aligned}
U_1(\mathbf{u}_1) &= \iota_{\mathbb{R}_+^n}(\mathbf{u}_1) + \frac{\gamma}{2} \|\mathbf{u}_1 - \mathbf{s}_1^{(k)}\|_2^2, \\
U_2(\mathbf{u}_2) &= \mu \text{KL}(\mathbf{g}(\mathbf{u}_2) + \mathbf{q}; \mathbf{b}) + \frac{\gamma}{2} \|\mathbf{u}_2 - \mathbf{s}_2^{(k)}\|_2^2, \\
U_3(\mathbf{u}_3) &= \sum_{i=1}^n \|\mathbf{u}_{3,i}\|_2 + \frac{\gamma}{2} \|\mathbf{u}_3 - \mathbf{s}_3^{(k)}\|_2^2.
\end{aligned} \tag{10.15}$$

Therefore, the updates of variables \mathbf{u}_1 , \mathbf{u}_2 and \mathbf{u}_3 can be addressed separately.

Update of \mathbf{u}_1 . It comes from (10.15) that the \mathbf{u}_1 -update problem reads

$$\mathbf{u}_1^{(k+1)} \in \arg \min_{\mathbf{u}_1 \in \mathbb{R}_+^n} \|\mathbf{u}_1 - \mathbf{s}_1^{(k)}\|_2^2,$$

that is $\mathbf{u}_1^{(k+1)}$ is given by the unique Euclidean projection of vector $\mathbf{s}_1^{(k)}$ onto the non-negative orthant \mathbb{R}_+^n , which admits the following component-wise closed-form expression:

$$u_{1,i}^{(k+1)} = \max \{s_{1,i}^{(k)}, 0\}, \quad i = 1, \dots, n. \tag{10.16}$$

Update of \mathbf{u}_2 . It follows from (10.15) that, after introducing the scalar $\tau = \mu/\gamma$, the updated vector $\mathbf{u}_2^{(k+1)}$ is given by

$$\begin{aligned}
\mathbf{u}_2^{(k+1)} &\in \arg \min_{\mathbf{u}_2 \in \mathbb{R}^m} \left\{ \tau \text{KL}(\mathbf{g}(\mathbf{u}_2) + \mathbf{q}; \mathbf{b}) + \frac{1}{2} \|\mathbf{u}_2 - \mathbf{s}_2^{(k)}\|_2^2 \right\} \\
&= \arg \min_{\mathbf{u}_2 \in \mathbb{R}^m} \left\{ \sum_{i=1}^m \left[\tau g(u_i) - \tau b_i \ln(g(u_i) + q_i) + \frac{1}{2} (u_i - s_i)^2 \right] \right\}, \tag{10.17}
\end{aligned}$$

where in (10.17) we substituted the explicit expression of the KL divergence term reported in (4.9), we dropped the constants and, for simplicity of notation, we set $u_i := u_{2,i} \in \mathbb{R}$ and $s_i = s_{2,i}^{(k)} \in \mathbb{R}$. Hence, similarly to the \mathbf{u}_1 update problem in (10.22), the m -dimensional minimization problem (10.17) is equivalent to the m following 1-dimensional problems

$$u_i^{(k+1)} = \arg \min_{u_i \in \mathbb{R}} \left\{ \tau g(u_i) - \tau b_i \ln(g(u_i) + q_i) + \frac{1}{2} (u_i - s_i)^2 \right\}, \tag{10.18}$$

$i = 1, \dots, m$.

In the IR scenario, i.e. when $g(u_i) = u_i$, the cost function in (10.18) is infinitely many times differentiable, strictly convex and coercive in its domain

$u_i \in (-q_i, +\infty)$. Hence, the solution $u_i^{(k+1)}$ of (10.18) exists, is unique and coincides with the unique stationary point of the cost function, given by

$$u_i^{(k+1)} = \frac{1}{2} \left[-(\tau + q_i - s_i) + \sqrt{(\tau + q_i - s_i)^2 + 4(s_i q_i + \tau(b_i - q_i))} \right].$$

For the CTIR problem, i.e. when $g(u_i) = I_0 e^{-u_i}$, problem (10.18) reads

$$u_i^{(k+1)} = \arg \min_{u_i \in \mathbb{R}} \left\{ \tau I_0 e^{-u_i} - \tau b_i \ln(I_0 e^{-u_i} + q_i) + \frac{1}{2}(u_i - s_i)^2 \right\}. \quad (10.19)$$

The cost function in (10.19) is infinitely many times differentiable and coercive in its domain $u_i \in \mathbb{R}$, hence it admits global minimizers. However, in the general case of a nonzero background, i.e. when $q_i \in \mathbb{R}_{++}$, problem (10.19) does not admit a closed-form solution and can only be addressed by employing iterative solvers.

On the other hand, when $q_i = 0$ the cost function is also strictly convex, hence $u_i^{(k+1)}$ in (10.19) is given by the unique solution of the first-order optimality condition

$$-\tau I_0 e^{-u_i} + \tau b_i + u_i - s_i = 0.$$

The above nonlinear equation can be manipulated so as to give

$$w_i e^{w_i} = \tau I_0 e^{\tau b_i - s_i}, \quad \text{with } w_i = u_i + \tau b_i - s_i. \quad (10.20)$$

Equations of the form in (10.20) admit solutions that can be expressed in closed-form in terms of the so-called Lambert W function [59]. In particular, when the right-hand side is non-negative - which is our case as $\tau I_0 e^{\tau b_i - s_i} \in \mathbb{R}_{++}$ - then the equation admits a unique solution given by

$$w_i = W(\tau I_0 e^{\tau b_i - s_i}).$$

It follows that problem (10.19) admits the unique solution

$$u_i^{(k+1)} = -(\tau b_i - s_i) + W(\tau I_0 e^{\tau b_i - s_i}). \quad (10.21)$$

Update of \mathbf{u}_3 . It comes from (10.15) that the update of \mathbf{u}_3 reads

$$\mathbf{u}_3^{(k+1)} = \arg \min_{\mathbf{u}_3 \in \mathbb{R}^{2n}} \left\{ \sum_{i=1}^n \left[\|\mathbf{u}_{3,i}\|_2 + \frac{\gamma}{2} \left(\mathbf{u}_{3,i} - \mathbf{s}_{3,i}^{(k)} \right)^2 \right] \right\}. \quad (10.22)$$

Hence, problem (10.22) is separable into n independent 2-dimensional problems

$$\mathbf{u}_{3,i}^{(k+1)} = \arg \min_{\mathbf{u}_{3,i} \in \mathbb{R}^{2n}} \left\{ \|\mathbf{u}_{3,i}\|_2 + \frac{\gamma}{2} \left(\mathbf{u}_{3,i} - \mathbf{s}_{3,i}^{(k)} \right)^2 \right\}, \quad i = 1, \dots, n, \quad (10.23)$$

which represent the proximal map of the Euclidean norm function $\|\cdot\|_2$ in \mathbb{R}^2 calculated at points $\mathbf{s}_{3,i}^{(k)}$, $i = 1, \dots, n$. Such a proximal map admits a well-known explicit expression which leads to the following closed-form solution of problem (10.23):

$$\mathbf{u}_{3,i}^{(k+1)} = \max \left\{ \left\| \mathbf{s}_{3,i}^{(k)} \right\|_2 - \frac{1}{\gamma}, 0 \right\} \frac{\mathbf{s}_{3,i}^{(k)}}{\left\| \mathbf{s}_{3,i}^{(k)} \right\|_2}, \quad i = 1, \dots, n.$$

where $0 \cdot \mathbf{0} / 0 = \mathbf{0}$ is assumed.

TV²-KL and TGV²-KL models

Following the above path, we introduce a partition of the vector of Lagrange multipliers $\boldsymbol{\rho}^{(k)}$ into m subvectors $\boldsymbol{\rho}_j^{(k)}$ having the same size of the corresponding solution subvectors \mathbf{u}_j . Hence, for TV²-KL we define $\boldsymbol{\rho}^{(k)} = (\boldsymbol{\rho}_1^{(k)}; \boldsymbol{\rho}_2^{(k)}; \boldsymbol{\rho}_3^{(k)})$, whereas for TGV²-KL we set $\boldsymbol{\rho}^{(k)} = (\boldsymbol{\rho}_1^{(k)}; \boldsymbol{\rho}_2^{(k)}; \boldsymbol{\rho}_3^{(k)}; \boldsymbol{\rho}_4^{(k)})$. By defining

$$\mathbf{s}_1^{(k)} = \mathbf{x}^{(k+1)} + \frac{1}{\gamma} \boldsymbol{\rho}_1^{(k)} \in \mathbb{R}^n, \quad \mathbf{s}_2^{(k)} = \mathbf{A}\mathbf{x}^{(k+1)} + \frac{1}{\gamma} \boldsymbol{\rho}_2^{(k)} \in \mathbb{R}^m,$$

$$\mathbf{s}_3^{(k)} = \begin{cases} \mathbf{D}_2 \mathbf{x}^{(k+1)} + \frac{1}{\gamma} \boldsymbol{\rho}_3^{(k)} \in \mathbb{R}^{4n} & \text{for TV}^2\text{-KL model,} \\ \mathbf{D}_1 \mathbf{x}^{(k+1)} + \frac{1}{\gamma} \boldsymbol{\rho}_3^{(k)} - \mathbf{w}^{(k+1)} \in \mathbb{R}^{2n} & \text{for TGV}^2\text{-KL model,} \end{cases}$$

the three subproblems for variables \mathbf{u}_1 , \mathbf{u}_2 and \mathbf{u}_3 admit the same pixel-wise close-form solutions as the TV-KL model.

Finally, for the TGV²-KL model, the fourth subproblem for variable $\mathbf{u}_4 \in \mathbb{R}^{4n}$ can also be solved in pixel-wise closed-form based on the ℓ_2 -norm proximal map; in formula,

$$\mathbf{u}_{4,i}^{(k+1)} = \max \left\{ 1 - \frac{1}{\gamma \left\| \mathbf{s}_{4,i}^{(k)} \right\|_2}, 0 \right\} \mathbf{s}_{4,i}^{(k)}, \quad \mathbf{s}_4^{(k)} = \mathbf{D}_S \mathbf{w}^{(k+1)} + \frac{1}{\gamma} \boldsymbol{\rho}^{(k)},$$

for $i = 1, \dots, n$, with $\mathbf{u}_{4,i}^{(k+1)}, \mathbf{s}_{4,i}^{(k)} \in \mathbb{R}^4$.

10.2 Numerical solution for the mixed noise model

We now discuss the solution of the general model (TV-MixedNoise) arising in presence of mixed Poisson-Gaussian noise:

$$\widehat{\mathbf{x}}(\mu) \in \arg \min_{\mathbf{x} \in \mathbb{R}^n} \left\{ \iota_{\mathbb{R}_+^n}(\mathbf{x}) + \mu \sum_{i \in \mathcal{J}} \|(\mathbf{D}_1 \mathbf{x})_i\|_2 + \frac{1}{2} \left\| \frac{I_0 e^{-\mathbf{A}\mathbf{x}} - \mathbf{b}}{\sqrt{I_0 e^{-\mathbf{A}\mathbf{x}} + \sigma^2}} \right\|_2^2 + \frac{1}{2} \sum_{j=1}^m (\log(I_0 e^{-\mathbf{A}\mathbf{x}} + \sigma^2))_i \right\}.$$

Considering the auxiliary variable \mathbf{u} defined as

$$\mathbf{u} = \begin{pmatrix} \mathbf{u}_1 \\ \mathbf{u}_2 \\ \mathbf{u}_3 \end{pmatrix} = \begin{pmatrix} \mathbf{x} \\ \mathbf{A}\mathbf{x} \\ \mathbf{D}_1 \mathbf{x} \end{pmatrix},$$

the above model can be reformulated as a standard two-blocks separable minimization problem with linear constraints:

$$\{\widehat{\mathbf{x}}(\mu), \widehat{\mathbf{u}}(\mu)\} \in \arg \min_{\mathbf{x}, \mathbf{u}} \{C_1(\mathbf{x}) + C_2(\mathbf{u}; \mu)\} \quad \text{subject to: } \mathbf{M}_1 \mathbf{x} + \mathbf{M}_2 \mathbf{u} = \mathbf{0}. \quad (10.24)$$

with functions

$$C_1(\mathbf{x}) = 0 \quad (10.25)$$

$$C_2(\mathbf{u}; \mu, \sigma) = \iota_{\mathbb{R}_+^n}(\mathbf{u}_1) + \mu \sum_{i \in \mathcal{J}} \|\mathbf{u}_{3,i}\|_2 + \frac{1}{2} \left\| \frac{I_0 e^{-\mathbf{u}_2} - \mathbf{b}}{\sqrt{I_0 e^{-\mathbf{u}_2} + \sigma^2}} \right\|_2^2 + \frac{1}{2} \sum_{j=1}^m (\log(I_0 e^{-\mathbf{u}_2} + \sigma^2))_i \quad (10.26)$$

and matrices

$$\mathbf{M}_1 = \begin{pmatrix} \mathbf{I} \\ \mathbf{A} \\ \mathbf{D}_1 \end{pmatrix} \in \mathbb{R}^{(m+3n) \times n}, \quad \mathbf{M}_2 = -\mathbf{I} \in \mathbb{R}^{(m+3n) \times (m+3n)}.$$

Notice that, according to the above definitions, the Lagrangian function \mathcal{L} and augmented Lagrangian function \mathcal{L}_γ associated with problem (10.24) take the same form of the ones introduced in (10.3) with \mathbf{x} replacing \mathbf{t} . It follows that the problem can be solved by the ADMM procedure as the limit point of the iterative procedure

$$\mathbf{x}^{(k+1)} = \arg \min_{\mathbf{x}} \left\{ C_1(\mathbf{x}) + \frac{\gamma}{2} \left\| \mathbf{M}_1 \mathbf{x} + \mathbf{M}_2 \mathbf{u}^{(k)} + \frac{1}{\gamma} \boldsymbol{\rho}^{(k)} \right\|_2^2 \right\} \quad (10.27)$$

$$\mathbf{u}^{(k+1)} = \arg \min_{\mathbf{u}} \left\{ C_2(\mathbf{u}) + \frac{\gamma}{2} \left\| \mathbf{M}_2 \mathbf{u} + \mathbf{M}_1 \mathbf{x}^{(k+1)} + \frac{1}{\gamma} \boldsymbol{\rho}^{(k)} \right\|_2^2 \right\} \quad (10.28)$$

$$\boldsymbol{\rho}^{(k+1)} = \boldsymbol{\rho}^{(k)} + \gamma (\mathbf{M}_1 \mathbf{x}^{(k+1)} + \mathbf{M}_2 \mathbf{u}^{(k+1)}) . \quad (10.29)$$

where $\boldsymbol{\rho}^{(k)}$ is the vector of Lagrange multipliers $\boldsymbol{\rho}^{(k)} = (\boldsymbol{\rho}_1^{(k)}; \boldsymbol{\rho}_2^{(k)}; \boldsymbol{\rho}_3^{(k)})$ with $\boldsymbol{\rho}_2^{(k)} \in \mathbb{R}^{2n}$, $\boldsymbol{\rho}_3^{(k)} \in \mathbb{R}^m$ and $\boldsymbol{\rho}_1^{(k)} \in \mathbb{R}^n$.

The \mathbf{x} - subproblem

Recalling the definition of the augmented Lagrangian function \mathcal{L}_γ in (10.3) and the definition of $C_1(\mathbf{x}), C_2(\mathbf{u})$ in (10.25)(10.26), the \mathbf{x} -update problem in (10.27) reads:

$$\begin{aligned} \mathbf{x}^{(k+1)} &\in \arg \min_{\mathbf{x} \in \mathbb{R}^n} \left\{ \langle \boldsymbol{\rho}^{(k)}, \mathbf{M}_1 \mathbf{x} - \mathbf{u}^{(k)} \rangle + \frac{\gamma}{2} \|\mathbf{M}_1 \mathbf{x} - \mathbf{u}^{(k)}\|_2^2 \right\} \\ &= \arg \min_{\mathbf{x} \in \mathbb{R}^n} \left\{ Q^{(k)}(\mathbf{x}) := \frac{1}{2} \|\mathbf{M}_1 \mathbf{x} - \mathbf{v}^{(k)}\|_2^2 \right\}, \end{aligned} \quad (10.30)$$

where $\mathbf{v}^{(k)} = \mathbf{x}^{(k)} - \frac{1}{\gamma} \boldsymbol{\rho}^{(k)}$. In analogy with the discussion done for the solution of the \mathbf{t} subproblem in 10.1.1 in the case of the matrix A being the Radon transform, the new iterate $\mathbf{x}^{(k+1)}$ can be computed by the linearized ADMM given by

$$\mathbf{x}^{(k+1)} = \mathbf{x}^{(k)} - \frac{1}{\eta} \mathbf{M}_1^\top (\mathbf{M}_1 \mathbf{x}^{(k)} - \mathbf{v}^{(k)}), \quad \eta \geq \|\mathbf{M}_1\|_2^2$$

The \mathbf{u} - subproblem

As in 10.1.2, the \mathbf{u} subproblem can be split into 3 independent minimization subsubproblems each updating a subvector \mathbf{u}_i of \mathbf{u} . By introducing

$$\begin{aligned} \mathbf{s}_1^{(k)} &= \mathbf{u}_1^{(k+1)} + \frac{1}{\gamma} \boldsymbol{\rho}_1^{(k)} \in \mathbb{R}^n, & \mathbf{s}_2^{(k)} &= \mathbf{A} \mathbf{u}_2^{(k+1)} + \frac{1}{\gamma} \boldsymbol{\rho}_2^{(k)} \in \mathbb{R}^m, \\ \mathbf{s}_3^{(k)} &= \mathbf{D}_1 \mathbf{u}_3^{(k+1)} + \frac{1}{\gamma} \boldsymbol{\rho}_3^{(k)} \in \mathbb{R}^{2n}, \end{aligned}$$

the three subsubproblems read

$$\begin{aligned} \mathbf{u}_1^{(k+1)} &\in \arg \min_{\mathbf{u}_1} \left\{ \iota_{\mathbb{R}_+^n}(\mathbf{u}_1) + \frac{\gamma}{2} \|\mathbf{u}_1 - \mathbf{s}_1^{(k)}\|_2^2 \right\}, \\ \mathbf{u}_2^{(k+1)} &\in \arg \min_{\mathbf{u}_2} \left\{ \frac{1}{2} \left\| \frac{I_0 e^{-\mathbf{u}_2} - \mathbf{b}}{\sqrt{I_0 e^{-\mathbf{u}_2} + \sigma^2}} \right\|_2^2 + \frac{1}{2} \sum_{j=1}^m (\log(I_0 e^{-\mathbf{u}_2} + \sigma^2))_{i+} + \frac{\gamma}{2} \|\mathbf{u}_2 - \mathbf{s}_2^{(k)}\|_2^2 \right\}, \\ \mathbf{u}_3^{(k+1)} &\in \arg \min_{\mathbf{u}_3} \left\{ \sum_{i=1}^n \|\mathbf{u}_{3,i}\|_2 + \frac{\gamma}{2} \|\mathbf{u}_3 - \mathbf{s}_3^{(k)}\|_2^2 \right\}. \end{aligned}$$

The update of \mathbf{u}_1 (in the same way as (10.16)) is obtained by projecting the vector $\mathbf{s}_1^{(k)}$ onto the non-negative orthant \mathbb{R}_+^n and can be written component-wise as

$$u_{1,i}^{(k+1)} = \max \left\{ s_{1,i}^{(k)}, 0 \right\}, \quad i = 1, \dots, n.$$

Since the function to minimize for the \mathbf{u}_2 subproblem is smooth, differentiable, nonconvex and separable, one needs a first order optimality condition on the function to be minimized so that one ends up to solve a non-linear one-dimensional equation. Such problem can be addressed by multiple methods such as, e.g., the Newton's algorithm. Finally, the update of \mathbf{u}_3 is performed by solving n independent 2-dimensional problems which amounts to compute the proximal operator of the Euclidean norm function in s_3 ; such problem admits a closed-form solution expressed as

$$\mathbf{u}_{3,i}^{(k+1)} = \max \left\{ \left\| \mathbf{s}_{3,i}^{(k)} \right\|_2 - \frac{1}{\gamma}, 0 \right\} \frac{\mathbf{s}_{3,i}^{(k)}}{\left\| \mathbf{s}_{3,i}^{(k)} \right\|_2}, \quad i = 1, \dots, n.$$

Part III

Spectral CT

Chapter 11

Material Decomposition in Spectral Tomography

In Chapter 3 we introduced the generation of X-rays, together with the detection process and the Lambert-Beer Law of attenuation. In particular, we remark that when CT scans involve an X-rays spectrum (as in Figure 3.2) that includes multiple energies and whose continuous formulation is expressed in (3.6) and recalled below:

$$I(s) = \int_{E_{min}}^{E_{max}} I_0(E) e^{-\int_0^s \bar{x}(\ell, E) d\ell} dE.$$

where s denotes the length of the linear path followed by the X-ray. Spectral Computed Tomography is an increasingly used technique which allows to analyze how different materials attenuate X-rays based on the considered energy. In fact, while in conventional CT the detector pixels sum all the incoming photons from all the energy spectrum, spectral CT features a photon-counting detector that records the energy of individual photons. This means that, for each projection angle and detector pixel the data is no longer a single scalar, as for standard CT, but it is an energy-dependent quantity, Figure 11.1. Most of the time, in spectral tomography one considers a “very low” energy dependence that means that the energy channels are few, ranging from the 2 of dual energy CT to 5, and refer to wide spectrum bands.

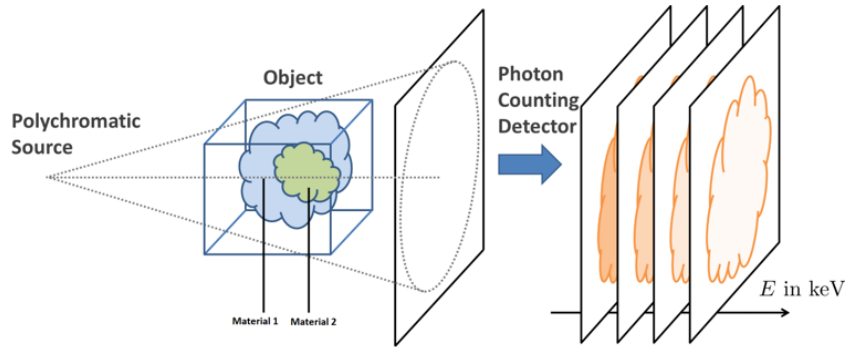


Figure 11.1: Scheme of Spectral Tomography

On the other hand, the special case of spectral CT which addresses the case of many energy channels (e.g. more than 5) and a fine energy resolution (ca 1 KeV), is referred as Hyperspectral Computed Tomography. Figure 11.2 shows the differences between the different types of CT by means of the data energy levels: for standard CT the detected polychromatic beam is integrated over the whole spectrum, while for the Dual Energy the multilayer detector divides the data in two parts. Finally, for spectral and hyperspectral CT, the photon counting detectors count the number of incoming photons and separate them into different photon bins based on their energy level, with wide and fine energy grid respectively.

In the following sections we will explain how to manage the energy dependent data and what information we can derive from them.

11.1 The attenuation coefficients and the energies

In Figure 11.3 we show some of the energy dependent sinograms (after the log transformation) of a real and a synthetic hyperspectral Fan Beam CT dataset. By looking at the images we can note that sinogram data changes with the energy variation in two ways: noise and highlighted features. We recall - see Section 2.3 - that the noise level depends on the number of pho-

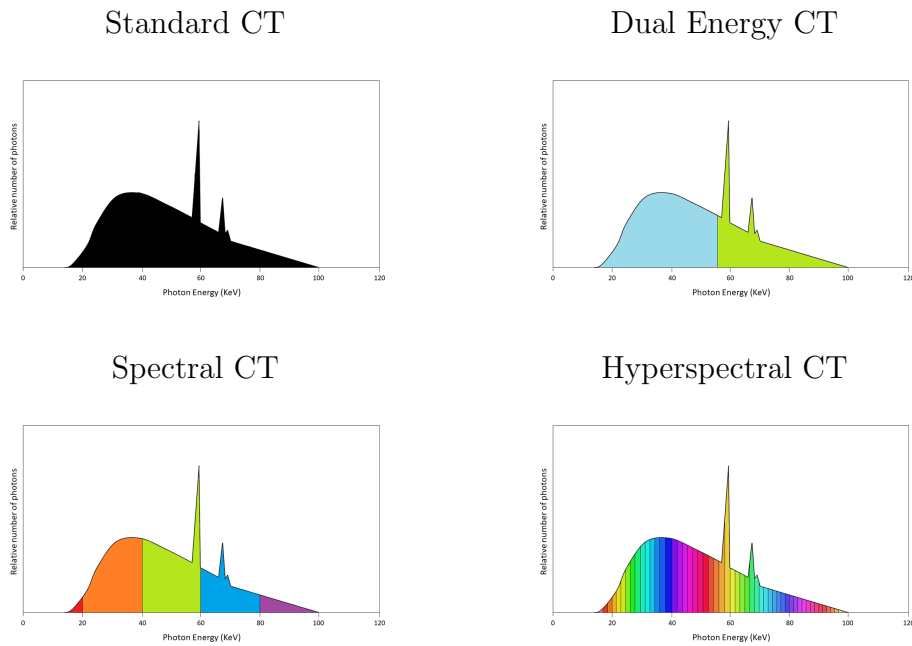


Figure 11.2: Top Left: in Standard CT the detected polychromatic beam is integrated over the whole spectrum. Top Right: in dual energy CT (top right), data is acquired dividing the spectra in two using a multilayer detector. Bottom Left: in spectral CT the detectors count the number of incoming attenuated photons individually and separate them into different photon bins based on their energy levels (wide spectrum bands). Bottom Right: In Hyperspectral CT, photon counting detectors separate the incoming photons into a fine grid of energy channels.

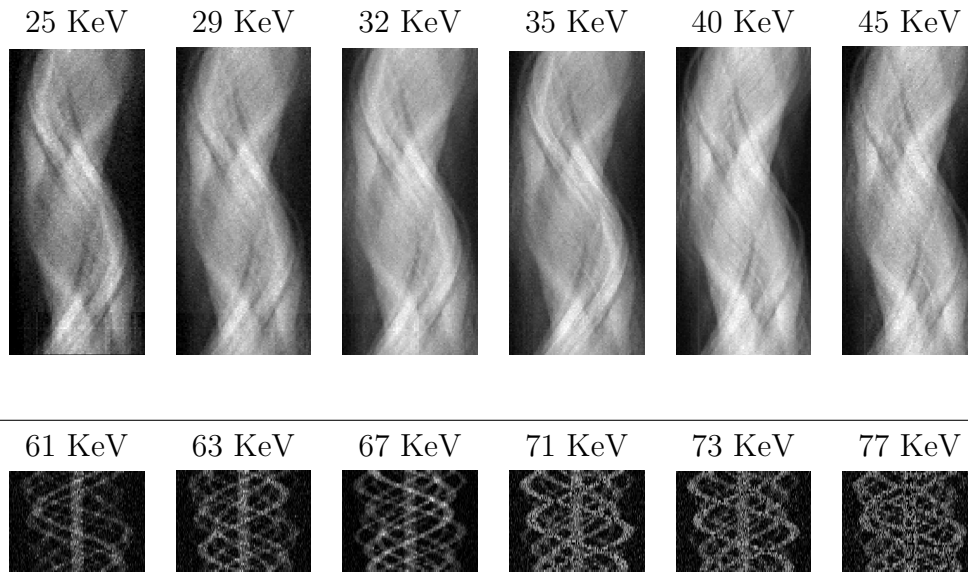


Figure 11.3: Energy dependent sinogram data of a real (top panels) and a synthetic (bottom panels) Hyperspectral Fan Beam CT dataset, with energy levels increasing from left to right.

tons that reach the detector, and, as shown in Figure 11.2, such number is different in every energy bin; hence the resulted data can be affected by different noise levels across the energies. Moreover, given that in spectral CT the photons are classified by the detector based on their energy levels and summed together within each energy band, the energy dependent data are noisier compared to the one acquired by a standard CT (or by a spectral CT with wider bands) with the same initial intensity. The other feature that distinguishes the data across the energies, and that it makes their analysis particularly interesting, is the energy dependence of the attenuation coefficients of the materials. In fact, different materials not only have distinct attenuation coefficients, but they also depend on the energy level of the incoming photons, Figure 11.4. This is reflected on the sinograms, whose shape changes with the energy and the attenuation curve of the materials.

In particular, by looking at Figure 11.4 we can note that the mass attenuation curves have different behaviors: some of them are smooth, while other

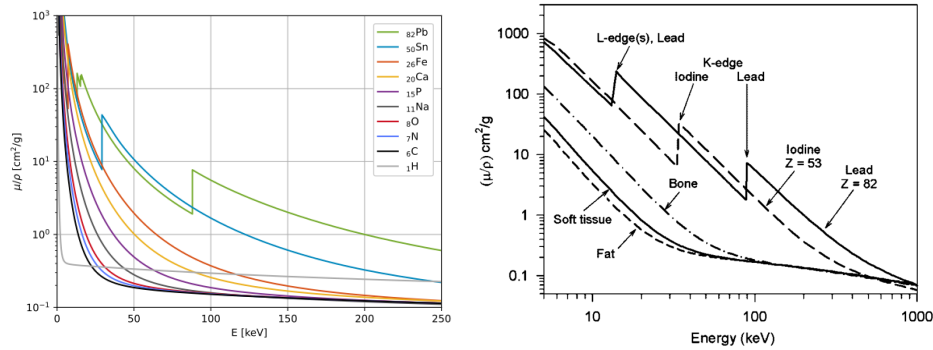


Figure 11.4: Mass attenuation curves for different materials, [64, 63].

present one or more edges, referred to as K-edges, [64]. The K-edge is a sudden increase in X-ray absorption occurring when the energy of the X-rays is just above the binding energy (namely the smallest amount of energy required to remove a particle from a system of particles) of the innermost electron shell of the atoms interacting with the photons.

In this way, the hyperspectral CT technique allows to distinguish materials that have similar attenuation coefficient for an energy range, but different in another, or to highlight the presence of a specific material by looking around its K-edge. Therefore, by exploiting the energy dependence of the data and the attenuation coefficients, spectral CT is often used not only to simply reconstruct the attenuation coefficients, but also to decompose the object into its constitutive materials, [61, 62].

11.2 Spectral Tomography and its model

After describing the main aspects of spectral CT, here we define its forward model by introducing the concept of concentration maps, which will be the target of the material decomposition problem, [60].

With the term concentration map for a material M_m we refer to vectorized image $\bar{\mathbf{x}}_m \in [0, 1]^n$ whose pixel values denote the percentage of material M_m inside the pixels of the object and where n indicates the number of pixels of the object. For an object composed by N_{mat} materials $M_1, M_2, \dots, M_{N_{mat}}$,

the values of $\bar{x}_{m,j}$ indicate the percentage of material M_m in the pixel j of the object. Since we suppose that more materials can be present in each pixel of the object, as the case of a chemical mixture, the following constraint can be considered:

$$\sum_{m=1}^{N_{mat}} \bar{x}_{m,j} \leq 1 \quad \forall j = 0, \dots, n.$$

Depending on the specific application, different constraints can be applied on the concentration maps; this is the case of [65] where the authors impose that a pixel can be composed by only one material and employ this assumption into the decomposition process.

After defining the concentration maps, the attenuation coefficient of the target can be calculated considering the materials present at each pixels, their percentage of presence, and the specific attenuation curves (which is energy dependent). With this in mind, the attenuation coefficient \bar{h}_{ej} of the object at the pixel j and for the energy index e can be written as

$$\bar{h}_{ej} = \sum_{m=1}^{N_{mat}} \mu_{em} \bar{x}_{mj}, \quad e \in \{1, \dots, N_e\}, \quad j \in \{1, \dots, n\}$$

where N_e is the number of energy channels and μ_{em} denotes the mass-attenuation coefficient of the material m at the energy index e . Recalling that the attenuation profiles $\{\mu_{em}\}$ are known, the final aim of material decomposition is to find the concentration maps for all the materials, i.e., $\{\bar{x}_{mj}\}$.

Based on the Beer's Law (3.4), the X-ray intensity collected by the detector after the attenuation process is described by:

$$I_{ie}^{\theta_l} = I_{0e} \exp \left(- \sum_{j=1}^n a_{ij}^{\theta_l} \bar{h}_{ej} \right) = I_{0e} \exp \left(- \sum_{j=1}^n a_{ij}^{\theta_l} \left(\sum_{m=1}^{N_{mat}} \mu_{em} \bar{x}_{mj} \right) \right), \quad (11.1)$$

where, similar to the standard CT model in 2.5, $I_{ie}^{\theta_l}$ denotes the expected photon count at the detector pixel i for the energy level e at projection angle θ_l , I_{0e} is the incoming source intensity, i.e. the number of photons for the energy index e that are expected to be detected at pixel i of the

detector if there was no attenuating object, and $a_{ij}^{\theta_l}$ represents the projection coefficient for the detector pixel i and the object pixel j at projection angle θ_l . Considering s projection angles in which acquisitions must be made, the corresponding matrix formulation is

$$\mathbf{I} = \mathbf{I}_0 e^{-\mathbf{A}\bar{\mathbf{H}}^T} = \mathbf{I}_0 e^{-\mathbf{A}(\mathbf{M}\bar{\mathbf{X}})^T} = \mathbf{I}_0 e^{-\mathbf{A}\bar{\mathbf{X}}^T\mathbf{M}^T}$$

where $\mathbf{I} = (\mathbf{I}^{\theta_1}; \dots; \mathbf{I}^{\theta_s}) \in \mathbb{R}_+^{s \times d \times N_e}$ with $\mathbf{I}^{\theta_l} = (I_{ie}^{\theta_l}) \in \mathbb{R}_+^{d \times N_e}$, $\mathbf{I}_0 = (I_{0ie}) \in \mathbb{R}_+^{N_e}$, $\mathbf{M} = (\mu_{em}) \in \mathbb{R}_+^{s \times N_{mat}}$, $\bar{\mathbf{H}} = (\bar{h}_{em}) \in \mathbb{R}_+^{N_e \times n}$, $\bar{\mathbf{X}} = (\bar{x}_{mj}) \in \mathbb{R}_+^{N_{mat} \times n}$, $\mathbf{A} = (\mathbf{A}^{\theta_1}; \dots; \mathbf{A}^{\theta_s}) \in \mathbb{R}_+^{s \times d \times n}$ with $\mathbf{A}^{\theta_l} = (a_{ij}^{\theta_l}) \in \mathbb{R}_+^{d \times n}$, d is the number of the detector pixels and the product between \mathbf{I}_0 and $e^{-\mathbf{A}\bar{\mathbf{H}}^T}$ is considered point-wise.

As explained in 2.3, the collected data is affected by noise, whose behaviour can be described by an independent Poisson random field in the following way:

$$\mathcal{B} = \{B_{ie}^{\theta_l}\} \sim \mathcal{P}(\bar{\Lambda}), \quad \bar{\Lambda} = \mathbf{I}$$

with $i = 1, \dots, d$, $e = 1, \dots, N_e$ and $l = 1, \dots, s$. In this case, the measured data $\mathbf{B} = (\mathbf{B}^{\theta_1}, \dots, \mathbf{B}^{\theta_s}) \in \mathbb{R}_+^{s \times d \times N_e}$ is a realization of the random field \mathcal{B} , with $\mathbf{B}^{\theta_l} = (b_{ie}^{\theta_l}) \in \mathbb{N}^{d \times N_e}$ and $b_{ie}^{\theta_l} \in \mathbb{N}$ a realization of the random variable $B_{ie}^{\theta_l} \sim \mathcal{P}(\bar{\lambda}_{ie}^{\theta_l})$, $\bar{\lambda}_{ie}^{\theta_l} = I_{ie}^{\theta_l}$.

11.3 Reconstruction and Material Decomposition Methods

The energy dependent data can be exploited both to reconstruct the energy dependent attenuation coefficients of the object, namely $\bar{\mathbf{H}} = (\bar{h}_{e,m})$, as well as to decompose the object into its constitutive materials, i.e. obtaining the concentration maps $\bar{\mathbf{x}}_1, \dots, \bar{\mathbf{x}}_{N_{mat}}$. While the first task can be addressed considering each individual energy independently and then unifying the reconstructions, the latter problem has to be tackled by processing the energy dependent data all together. In fact, the behavior of materials in presence of

the variation of energy is the feature that allows us to identify, quantify and differentiate them inside the reconstructed object.

As mentioned before, the reconstruction methods aim to recover the energy dependent attenuation coefficients $\bar{\mathbf{H}} = (\bar{h}_{em})$, that is solving the following inverse problem:

$$\text{find } \mathbf{H} \in \mathbb{R}_+^{N_e \times n} \text{ such that } \mathbf{B} \text{ is a realization} \\ \text{of } \mathcal{P} \text{ applied to } \mathbf{\Lambda} = \mathbf{I} = \mathbf{I}_0 e^{-\mathbf{A}\mathbf{H}^T}.$$

This problem can be seen as the extension of the standard CT inverse problem ((4.2) with $g(\cdot) = I_0 e^{-\mathbf{A}\cdot}$) to the energy dependent case. The simplest strategies consider individually each energy and apply a CT reconstruction algorithm to solve the N_e inverse problems, while, the more advanced ones employ a variational approach that reconstruct directly the all energy dependent attenuation coefficients. Those variational methods aim to solve the following problem:

$$\hat{\mathbf{H}}(\mu) \in \arg \min_{\mathbf{H} \in \mathbb{R}_+^{N_e \times n}} \{ \mathcal{J}(\mathbf{H}, \mu) := \mathcal{R}(\mathbf{H}) + \mu \mathcal{F}(\mathbf{H}; \mathbf{I}_0, \mathbf{A}, \mathbf{B}) \}.$$

However, most of the time the regularizer $\mathcal{R}(\mathbf{H})$ is chosen to enhance the spacial features of the object (such as TV on the spatial dimentions) without considering the energy dimension. In recent year some studies incorporated the energy dimension into the regularizer, by proposing a spatio-spectral TV and a combination of a Total Variation with a Total Generalized Variation (TGV) along the spatial and spectral dimensions respectively, [75, 73].

The material decomposition methods, aimed at reconstructing the material-specific images, namely the concentration maps $\mathbf{x}_1, \dots, \mathbf{x}_{N_{mat}}$, from the energy dependent data can be divided into two main categories: two-stage and one-stage methods.

11.3.1 Two-stage

In the two-stage methods the task of decomposing the materials and reconstructing the related images are separated and can be applied one before

the other or vice versa. The image-based methods first reconstruct the energy images and then perform material decomposition from reconstructed images, e.g the works in [68, 69]. Their functioning can be formalized as follows:

- find $\mathbf{H} \in \mathbb{R}_+^{N_e \times n}$ such that \mathbf{B} is a realization of the r.f. $\mathcal{B} \sim \mathcal{P}(\mathbf{\Lambda})$ with $\mathbf{\Lambda} = \mathbf{I} = \mathbf{I}_0 e^{-\mathbf{A}\mathbf{H}^T}$
- perform the material decomposition, i.e. find the concentration maps $\mathbf{X} \in \mathbb{R}^{N_{mat} \times n}$, by solving the linear system $\mathbf{M}\mathbf{X} = \mathbf{H}$.

The main advantage of these methods is that standard reconstruction strategies (such as FBP or SIRT applied on the sinograms $\mathbf{Y} = -\log\left(\frac{\mathbf{B}}{I_0}\right)$) can be employed energy-wise in the first step to obtain the energy dependent attenuation coefficients \mathbf{H} . However, as discussed before, the noise in the data of spectral CT is higher compared to standard CT; as a results such algorithms amplify the noise in data and cause artifact in the reconstruction that will be reflected in the subsequent material decomposition step. These downsides can be avoided by considering advanced methods (such as variational methods) to solve the first step, nonetheless the computational cost increases considerably and it is more convenient to use other strategies, e.g. the one stage approaches.

On the other hand, projection-based methods first decompose the multi-energy projections to each material, then perform image reconstruction independently. [66, 67]. In other words, they solve the two following problems:

- get the material decomposition of the data by finding $\mathbf{Z} \in \mathbb{R}^{s \times d \times N_{mat}}$ such that \mathbf{B} is a realization of the r.f. $\mathcal{B} \sim \mathcal{P}(\mathbf{\Lambda})$ with $\mathbf{\Lambda} = \mathbf{I} = \mathbf{I}_0 e^{-\mathbf{Z}\mathbf{M}^T}$
- perform the reconstruction by finding \mathbf{X} such that $\mathbf{Z} = \mathbf{A}\mathbf{X}^T$.

However, even the projection-base methods are susceptible to noise, due to instability of the decomposition step.

Before going ahead with the discussion, here we define the \mathcal{R} -L₂ variational model that can be employed to solve the material decomposition step of the

image-base methods:

$$\widehat{\mathbf{X}}(\mu) \in \arg \min_{\mathbf{X} \in \Omega} \{\mathcal{J}(\mathbf{X}, \mu) := \mathcal{R}(\mathbf{X}) + \mu \mathcal{L}_2(\mathbf{X}; \mathbf{M}, \mathbf{H})\} \quad (\mathcal{R}\text{-L}_2)$$

where \mathbf{H} is the output of the first step, namely the energy images, $\mathcal{R}(\mathbf{X})$ is the regularization term applied on the concentration maps and

$$\mathcal{L}_2(\mathbf{X}; \mathbf{M}, \mathbf{H}) := \|\mathbf{H} - \mathbf{M}\mathbf{X}\|_2^2. \quad (11.2)$$

For the regularizer, one can relate to the discussion ahead for the one-stage methods, since the regularizer will be applied on the concentration maps.

11.3.2 One-stage

The one-stage methods formulate the material decomposition and the reconstruction tasks as a single problem and solve it jointly, [72, 70, 71]. In this case, the reconstruction/decomposition can be obtained with a variational method by solving an optimization problem in the form

$$\widehat{\mathbf{X}}(\mu) \in \arg \min_{\mathbf{X} \in \Omega} \{\mathcal{J}(\mathbf{X}, \mu) := \mathcal{R}(\mathbf{X}) + \mu \mathcal{F}(\mathbf{X}; \mathbf{I}_0, \mathbf{M}, \mathbf{A}, \mathbf{B})\} \quad (11.3)$$

where the regularization term $\mathcal{R}(\mathbf{X})$ imposes properties on the concentration maps and the fidelity term $\mathcal{F}(\mathbf{X}; \mathbf{I}_0, \mathbf{M}, \mathbf{A}, \mathbf{B})$ contains information on the noise distribution and the complete forward model, hence, it depends on the decomposition matrix \mathbf{M} and on the CT projection matrix \mathbf{A} , thus allowing for a unification of the two stages. Moreover, we require that all elements in \mathbf{X} are bounded in $[0, 1]$: $\mathbf{X} \in \Omega := [0, 1]^{N_{mat} \times n}$. In principle one could also enforce that within each pixel these should sum to 1 but we do not explore such scenario in this thesis.

As discussed in previous chapters, under the action of Poisson noise, the data-fidelity term becomes the generalized Kullback-Leibler (KL) divergence, defined in (4.9), between $\boldsymbol{\Lambda} = \mathbf{I}_0 e^{-\mathbf{A}\mathbf{X}^T\mathbf{M}^T}$ and \mathbf{B} . More precisely, the noise should be modelled as mixed Poisson-Gaussian, but the algorithmic descriptions given in Chapter 10 both for the mixed noise, as well as for Poisson one, would be too expensive in this context.

Nonetheless, to mitigate the computational cost, in this last chapter we will consider a quadratic approximation for Poisson data according to which the KL term can be turned into a weighted least square, see (WL₂), [1].

Quadratic approximation for Poisson data Explicitly writing the KL between $\Lambda = \mathbf{I}_0 e^{-\mathbf{A}(\mathbf{M}\mathbf{X})^T}$ and \mathbf{B} , and considering only the terms depending on \mathbf{X} , we have that

$$\begin{aligned} \text{KL}(\Lambda, \mathbf{B}) &= \sum_{\substack{i=1,\dots,d \\ e=1,\dots,N_e \\ l=1,\dots,s}} \left(\left(\mathbf{I}_0 e^{-\mathbf{A}(\mathbf{M}\mathbf{X})^T} \right)_{ie}^{\theta_l} - b_{ie}^{\theta_l} \log \left(\mathbf{I}_0 e^{-\mathbf{A}(\mathbf{M}\mathbf{X})^T} \right)_{ie}^l \right) \quad (11.4) \\ &= \sum_{\substack{i=1,\dots,d \\ e=1,\dots,N_e \\ l=1,\dots,s}} \left(\left(\mathbf{I}_0 e^{-\mathbf{A}(\mathbf{M}\mathbf{X})^T} \right)_{ie}^{\theta_l} - \underbrace{b_{ie}^{\theta_l} \log \mathbf{I}_0}_{\text{constant}} + b_{ie}^{\theta_l} (\mathbf{A}(\mathbf{M}\mathbf{X})^T)_{ie}^{\theta_l} \right) \\ &\propto \sum_{\substack{i=1,\dots,d \\ e=1,\dots,N_e \\ l=1,\dots,s}} \left(\left(e^{-\mathbf{A}(\mathbf{M}\mathbf{X})^T} \right)_{ie}^{\theta_l} + \frac{b_{ie}^{\theta_l}}{\mathbf{I}_0}_{ie} (\mathbf{A}(\mathbf{M}\mathbf{X})^T)_{ie}^{\theta_l} \right) \end{aligned}$$

notice that, since we are interested in minimizing KL, the constant term in the second equality can be neglected. Recalling that the noisy sinograms are defined as $\mathbf{Y} = (y_{ie}^{\theta_l}) \in \mathbb{R}^{s \times d \times N_e}$ with $y_{ie}^{\theta_l} = -\log \left(\frac{b_{ie}^{\theta_l}}{\mathbf{I}_0}_{ie} \right)$, by replacing $\frac{b_{ie}^{\theta_l}}{\mathbf{I}_0}_{ie}$ with $e^{-y_{ie}^{\theta_l}}$ in (11.4) the KL function reads

$$\begin{aligned} \text{KL}(\mathbf{I}_0 e^{-\mathbf{A}(\mathbf{M}\mathbf{X})^T}, \mathbf{B}) &= \sum_{\substack{i=1,\dots,d \\ e=1,\dots,N_e \\ l=1,\dots,s}} D_{ie}^l \left((\mathbf{A}(\mathbf{M}\mathbf{X})^T)_{ie}^{\theta_l} \right) \\ &\quad \text{with } D_{ie}^l(\tau) = e^{-\tau} + e^{-y_{ie}^{\theta_l}} \cdot \tau. \end{aligned}$$

Using a second-order Taylor expansion of D_{ie}^l at $y_{ie}^{\theta_l}$ and ignoring terms independent of \mathbf{X} we arrive at a quadratic approximation of $D_{ie}^l(\tau)$ and the corresponding WL₂ likelihood:

$$\mathcal{F}(\mathbf{X}; \mathbf{I}_0, \mathbf{A}, \mathbf{M}, \mathbf{B}) = \text{WL}_2(\mathbf{X}; \mathbf{I}_0, \mathbf{A}, \mathbf{M}, \mathbf{B}) := \|\mathbf{Y} - \mathbf{A}(\mathbf{M}\mathbf{X})^T\|_{\mathbf{W}}^2 \quad (11.5)$$

where $\mathbf{W} = e^{\mathbf{Y}} = \frac{\mathbf{B}}{\mathbf{I}_0}$ and $\|\Phi\|_W^2 = \sum_{i,e,l} w_{ie}^{\theta_l} (\zeta_{ie}^{\phi_l})^2$. In our numerical experiments, we compare the reconstruction results by using WL_2 with the ones achieved by employing the most common L_2 data-fidelity term, i.e.,

$$\mathcal{F}(\mathbf{X}; \mathbf{I}_0, \mathbf{A}, \mathbf{M}, \mathbf{B}) = L_2(\mathbf{X}; \mathbf{I}_0, \mathbf{A}, \mathbf{M}, \mathbf{B}) := \|\mathbf{Y} - \mathbf{A}(\mathbf{M}\mathbf{X})^T\|_2^2. \quad (11.6)$$

The choice of the regularization term, $\mathcal{R}(\mathbf{X})$, depends on the prior information on \mathbf{X} . Several regularization techniques have been applied to hyperspectral CT. For example, regularization by denoising [79], total variation (TV) [72, 80, 70], Non Local Total Variation (NLTV) [71], and the point-wise separation regularizer for dual energy CT [65]. We will introduce different regularization to different materials depending on their properties and consider the sum of them, each with a specific regularization parameter. In particular, we will consider L_1 regularization for materials that are present with spikes and total variation (TV) regularization for the piece-wise constant materials. The TV and L_1 regularization term on the material m , i.e, $\mathbf{x}_m = (x_{m1}, \dots, x_{mn})^T \in \mathbb{R}^n$, are defined respectively as

$$\text{TV}_m(\mathbf{X}) = \text{TV}(\mathbf{x}_m) = \sum_{j=1}^n \|(D\mathbf{x}_m)_j\|_2, \quad (11.7)$$

$$L_{1m}(\mathbf{X}) = L_1(\mathbf{x}_m) = \|\mathbf{x}_m\|_1.$$

11.4 Numerical results

In this work, we focus on material decomposition for distinguishing materials that have high atomic number with similar attenuation coefficients and K-edges in the considered energy range. Further, we consider the case with a small number of projections in order to keep the scan time reasonable. Photon counting detectors, especially with high energy resolution, are slow and have limits on flux they can handle. Therefore, a small number of projections ensure that the scan time is acceptable. Here we perform some preliminary comparative studies with simulated data to establish which method is more

promising so as to set the stage for further study. Specifically, we aim to address three questions.

- (1) Is it worthwhile employing the more involved one-stage method or is the simpler two-stage method sufficient?
- (2) How to model the noise, i.e. which data-fidelity term to employ?
- (3) Which regularizer to use for sparse materials: TV or L_1 ?

Each experiment tries to address one of the questions.

11.4.1 Experimental setup

In this section we explain the setup for the material decomposition experiments for hyperspectral CT that will be carried out. With the focus on materials with high atomic number and similar attenuation coefficients, we consider an object $\bar{\mathbf{X}}$ with five different materials: Ytterbium (Yb), Lutetium (Lu), Tantalum (Ta), Osmium (Os) and water (H_2O). In particular, we choose the first four materials due to their attenuation profiles, which are all approximately in the same range and characterized by a jump (K-edge) 2, 4, and 6 keV apart from each other, see Figure 11.5 (*Left*). We allow to more than one material to be present at each pixel of the object. For this reason, we constructed phantoms in which some materials are present both alone and mixed with others. Furthermore, we assume that all materials are surrounded by water. Figure 11.6 shows two phantoms, formed by different concentration maps of the materials Yb, Lu, Ta, Os and H_2O respectively. Note that in phantom 2 the third material is present in very small quantities. The phantoms in Figure 11.6 as well as all reconstructions in the following sections are shown in the range $[0, 1]$. Also, we will refer to Yb, Lu, Ta, Os and H_2O as material 1,2,3,4 and 5 respectively.

We focus here on an X-ray energy range surrounding the K-edges i.e. from 60 keV to 80 keV. In reality, during the CT acquisition, all the energies in the considered spectrum contribute to the process; but the spectral CT

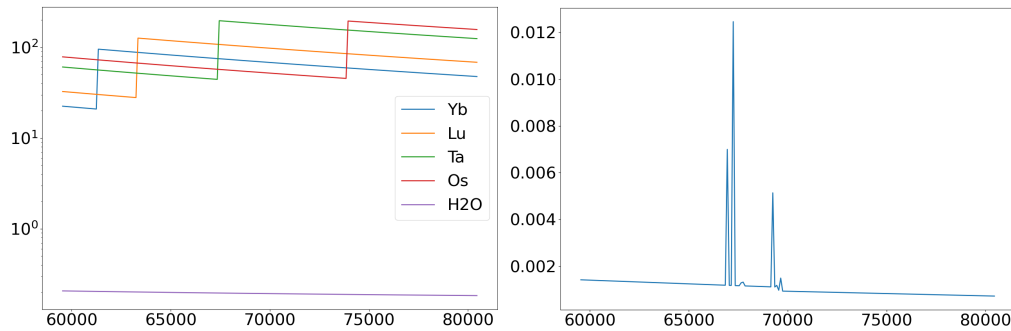


Figure 11.5: *Left*. Attenuation profiles of the five materials obtained by multiplying the mass attenuation coefficients with the density of each material. *Right*. Normalized source spectrum. The spectrum is shown only in the considered energies, but it is normalized over all the energy range (from 1 to 121 KeV). The x -axes represent the energy level in eV.

detector is only able to distinguish photons with a limited energy resolution, for example 1 keV. In order to mimic this process, and especially to avoid the inverse crime, we simulate data on a finer grid of energies, followed by binning (summing) data into 1 keV energy bins. Specifically, we considered a fine energy grid between 59550 and 80450 eV with a width of 0.1 keV. Figure 11.5 (*Right*) shows the normalized source spectrum for the fine grid of considered energies. After applying the Beer's Law and the noise (as in (11.1)) the photons are binned into 21 energy bins centered around 60, 61, \dots , 79 and 80 KeV.

The data was generated considering a phantom with $t = 256^2$ pixels (pixel size $4.6875^2 \mu\text{m}^2$) and a fan-beam setup with 45 projections in the range $[0, 2\pi]$, 256 detector pixels (pixel size $7.8125 \mu\text{m}$), a distance of 0.5 cm between the source and the detector and 0.3 cm between the source and the center of rotation. The experiments are carried out with few projections (only 45) and a short exposure time, thus leading to noisy data with reduced information content. From the data shown in Figure 11.7, one can easily note how the different materials and K-edges, together with the noise levels based on the spectrum, lead to differently looking sinograms over the energy bins.

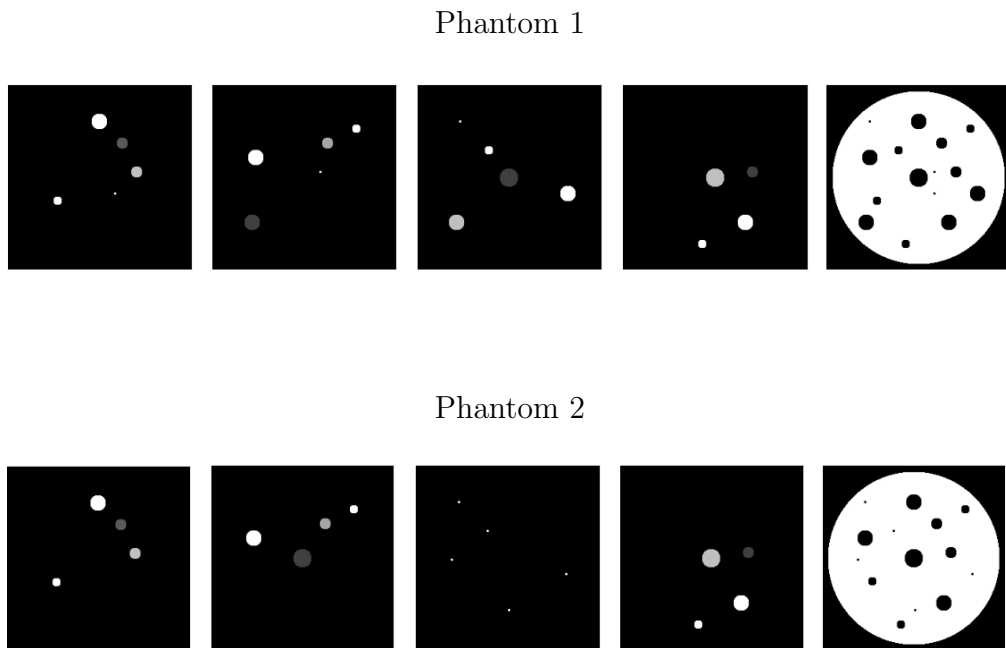


Figure 11.6: From left to right, concentration maps of materials Yb, Lu, Ta, Os and H_2O for phantom 1 (top) and phantom 2 (bottom).

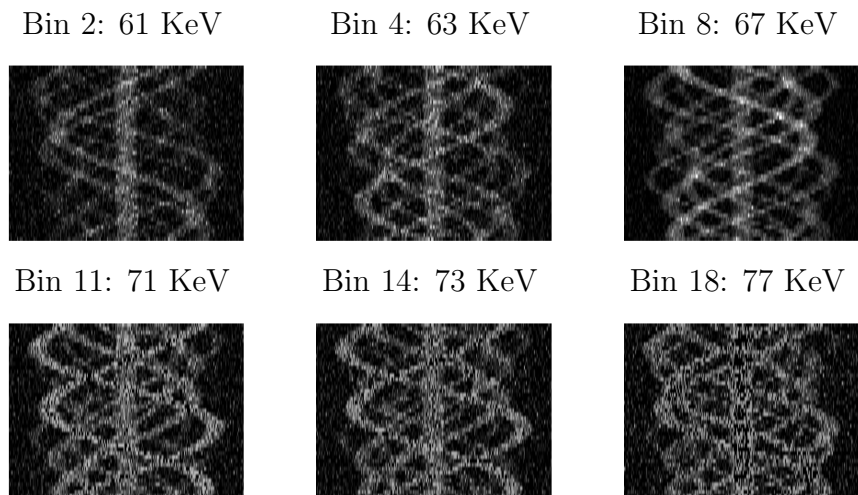


Figure 11.7: Sinogram data for some energy bins. Each row of the sinogram corresponds to a projection.

Reconstruction quality is addressed qualitatively by visual inspection and quantitatively by PSNR (in dB) on each material [76]. All the experiments are performed using the Core Imaging Library (CIL) [74, 75], an open-source Python framework for tomographic imaging that allows us to generate the data and reconstruct it using both standard techniques such as filtered back-projection (FBP) and advanced ones that incorporate some regularizations. To solve the minimization problem in (11.3) we use the primal dual hybrid gradient (PDHG) [82] algorithm which is available in CIL. In addition, the SpekPy toolkit [77] is used to calculate and manipulate the X-ray tube spectra, while the XrayDB library [78] provides the attenuation profiles of the materials in Figure 11.5.

11.4.2 One-stage vs two-stage method

	PSNR (in dB)				
Material	1	2	3	4	5
Two-Stage	21.79	26.26	17.48	16.27	2.50
One-Stage	22.33	26.78	22.70	20.10	2.11

Table 11.1: PSNR values of the reconstructions (on each material) with two-stage method (FBP in the first step and $L_2 + TV$ in the second) and the one-stage method (directly $L_2 + TV$).

In section 11.3 we outlined the differences between two-stage and one-stage methods. In this test we use phantom 1 given in Figure 11.5 to compare in experimental terms the performance of these two types of the methods. For the two-stage method, we apply FBP on each energy data first and then solve the material decomposition problem (\mathcal{R} - L_2) by using the L_2 data-fidelity term (11.2) together with the TV regularization on each material (11.7). For the one-stage method, we obtain the reconstruction by solving the minimization problem (11.3) with fidelity L_2 (11.6) and the sum of TV (11.7) regularizer

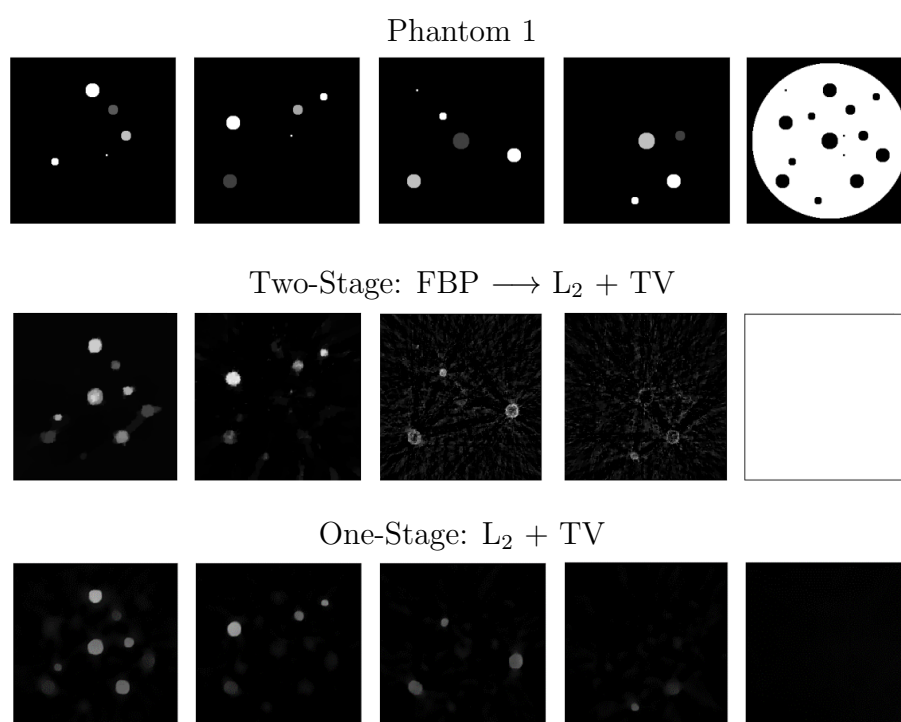


Figure 11.8: Reconstruction with two-stage method (using FBP in the first step and $L_2 + TV$ in the second) and the one-stage method.

applied on each material. In Figure 11.8 we show the reconstruction results from both methods, while Table 11.1 lists the PSNR results. One can see that the second step of the two-stage method is not able to compensate the lack of information present in the energy images obtained with FBP, as we can notice by looking at the circles that are assigned to material 1 instead of material 4.

11.4.3 L_2 vs WL_2

In this experiment we compare the results obtained with the one-stage methods by using L_2 defined in (11.6) and WL_2 given in (11.5) as data-fidelity terms. L_2 is the most commonly used data-fidelity term, and it potentially assumes that the noise model is additive Gaussian. WL_2 is an approximation of the data-fidelity term coming from Poisson noise model. In Figure 11.9 we show the phantom and the reconstructions from both L_2 and WL_2 together with the TV regularization on each material, while Table 11.2 contains the PSNR values of the decomposed materials in all the cases. The test is done for two levels of noise and the different data are obtained by halving the incoming source spectrum \mathbf{I}_0 . The regularization parameters are chosen manually to give the highest PSNR. It is obvious that WL_2 gives better reconstructions than L_2 . In particular, for the lower noise case, the reconstruction from WL_2 is almost the same as the ground truth and its PSNR values are more than 4 dB higher than from L_2 (except for material 5). For the higher noise case, L_2 cannot recognize material 3 and 4 and considers that most of the circles are made by material 1. But WL_2 , whose PSNR values are significantly higher, detects correctly most of them except that it has a bit difficulty to distinguish material 1 and 4. This might happen because the two materials have similar attenuation coefficients for energies between 62 and 74 KeV. Furthermore, as we can see in Figure 11.5, this energy interval corresponds to higher values of the energy spectrum which makes the data obtained from this energy range more powerful than the others. Regarding material 5, with its small attenuation profile if compared to the other materials, neither method is able

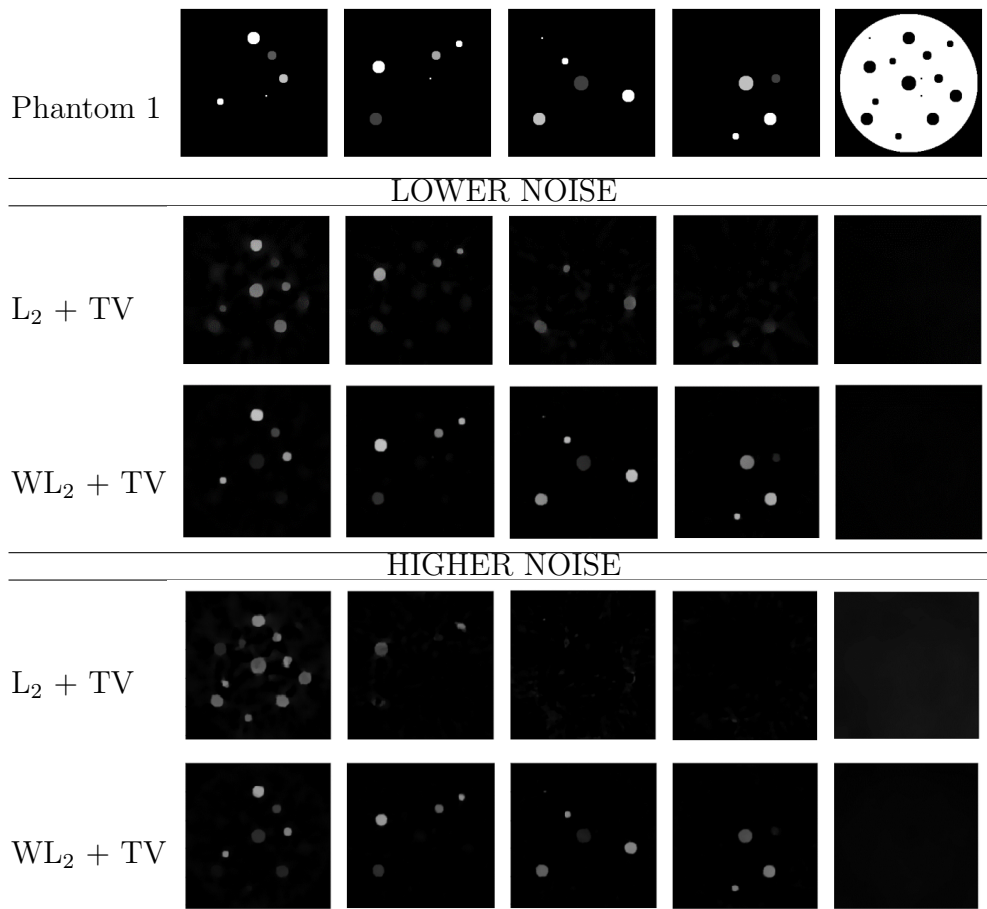


Figure 11.9: Reconstruction from one-stage methods with L_2 and WL_2 data-fidelity term and TV regularization for two different noise levels.

to recognize it, thus expressing the need of further developments.

11.4.4 Regularization

In previous experiments, TV is used for all materials, since we suppose that the materials are distributed in a piece-wise constant way across the object. In reality, the materials may be located in different manners. For example, in Phantom 2 the third material is present as spikes. In this experiment, we consider a regularizer on each material depending on its properties: TV on material 1,2,4 and 5 and L_1 on material 3, and we compare its results

		PSNR (in dB)				
Material		1	2	3	4	5
LOWER	$L_2 + TV$	22.33	26.78	22.70	20.10	2.11
NOISE	$WL_2 + TV$	28.99	30.03	29.40	27.22	2.32
HIGHER	$L_2 + TV$	21.2039	22.7809	19.6872	19.2476	3.5111
NOISE	$WL_2 + TV$	25.9380	27.0200	24.9557	23.7285	2.6190

Table 11.2: PSNR values of the reconstructions obtained with the TV regularization on each material and two data-fidelity terms: WL_2 and L_2 . The table reports the results for two noise levels.

		PSNR (in dB)				
Material		1	2	3	4	5
	$WL_2 + TV$	26.32	27.20	34.85	23.90	2.56
	$WL_2 + TV + L_1$	26.40	26.48	29.68	23.87	2.23

Table 11.3: PSNR values of the reconstructions for Phantom 2 with WL_2 and different regularizers on the materials: TV on each material ($WL_2 + TV$) and TV on material 1, 2, 4 and 5 and L1 on material 3 ($WL_2 + TV + L_1$).

with the one using TV on all materials. Both the TV and L_1 parameters are set manually to give the highest PSNR; the one chosen for L_1 is three orders of magnitude smaller than for TV. Figure 11.10 shows the visual results, while Table 11.3 list the PSNR value for each material. We can see that the reconstructions are similar for material 1,2,4 and 5, while, for material 3, the images present some differences. This is also reflected by PSNR that are similar with the exception of the third material. To better highlight these differences, in Figure 11.11 one can observe the line plots of one crucial row and one column of material 3 for the WL_2+TV and WL_2+TV+L_1 reconstructions together with the groundtruth. The results obtained with WL_2+TV

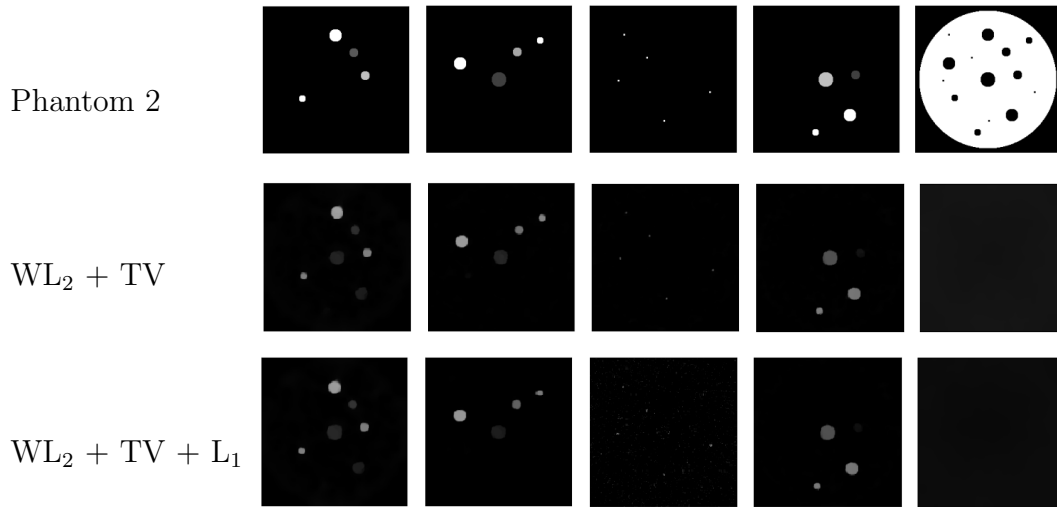


Figure 11.10: Reconstruction with one-stage methods with Weighted L_2 fidelity term and different regularizers on the materials: in the first case TV on each material and in the second case TV on material 1,2, and 5 and L_1 on material 3.

does not contain noise, but the values on the small dots are equal or less than 0.5 while they should be around 1. On the other hand, WL_2+TV+L_1 reconstruct the dots with the right values so they are more visible compared to the TV case, but some small spikes appear in the images, making it noisier. These results perfectly reflect the behavior of the two regularizers: TV leads to smoother images with shorter jumps and higher values of PSNR, while the L_1 feature of sparsifying the object lowers the PSNR results but identifies correctly the values of the small dots.

11.4.5 Test on Real Data

In this last experiment we apply the one-stage WL_2 -TV method on a real dataset. This dataset was presented in [81] and regards a mouse hindlimb whose blood vessels were perfused by a Barium solution and its soft tissue stained by a Iodine solution. Since the soft tissue is stained by the Iodine solution which has higher attenuation coefficient and by reconstructing the

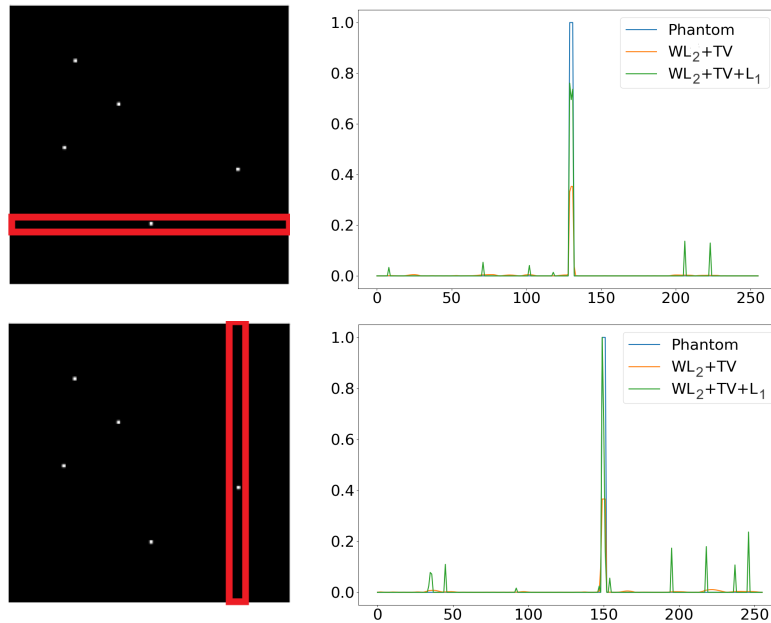


Figure 11.11: Line plots of some crucial rows and columns of the reconstructions using WL_2+TV+L_1 and WL_2+TV .

Iodine concentration map we automatically know the position of the soft tissue, in this experiment we consider only three materials: Iodine, Barium and Calcium (the bones).

The data are acquired using a cone-beam source, with sample rotation stage and detector oriented in a parallel configuration along the same imaging plane, 180 angles between 0 and 2π and 80×80 detector resolution (pixels). The key difference is that here the authors replaced the standard energy-integrating detector with an energy-sensitive, hyperspectral imaging detector capable of distinguishing the photon energies from 0 to 120 KeV. Figure 11.12 shows the 3D volume explaining the position of the three materials and a virtual cross-section obtain with an higher resolution acquisition. In addition, Figure 11.13 display the attenuation curves of the materials, while its energy dependent data can be seen in Figure 11.3.

In order to be able to process the data, we consider only the energies between 25 and 45 KeV, which are informative for the Iodine and Barium

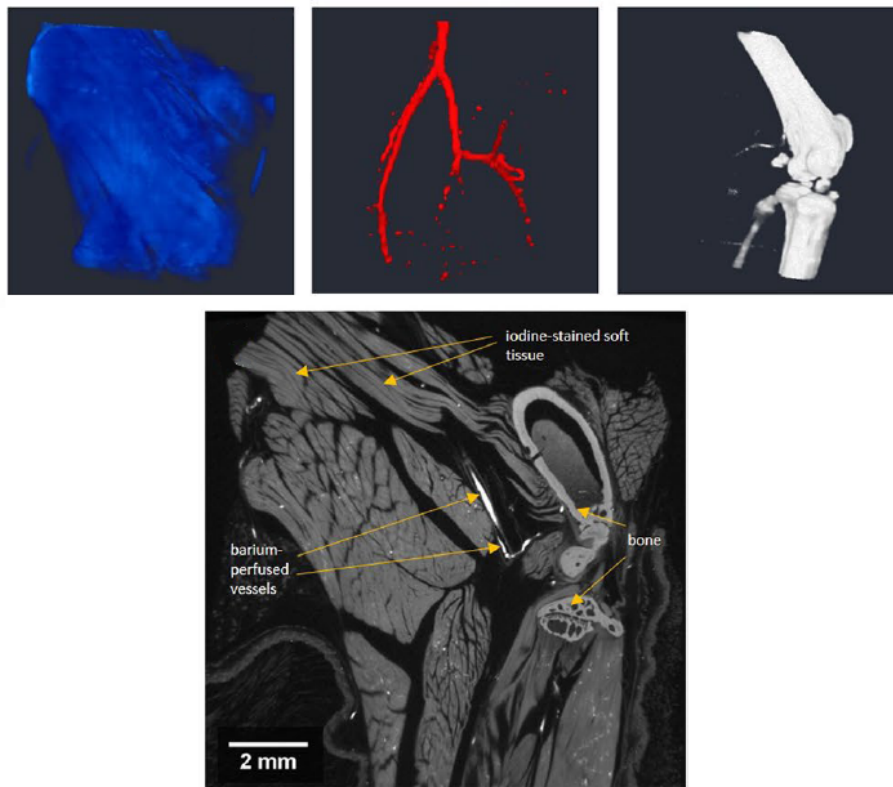


Figure 11.12: Top: 3D volume explaining the position of iodine-, barium- and calcium-containing regions (left, middle, right respectively). Bottom: virtual cross-section from a high spatial resolution scan of the mouse hindlimb, showing the equivalent image slice of the target.

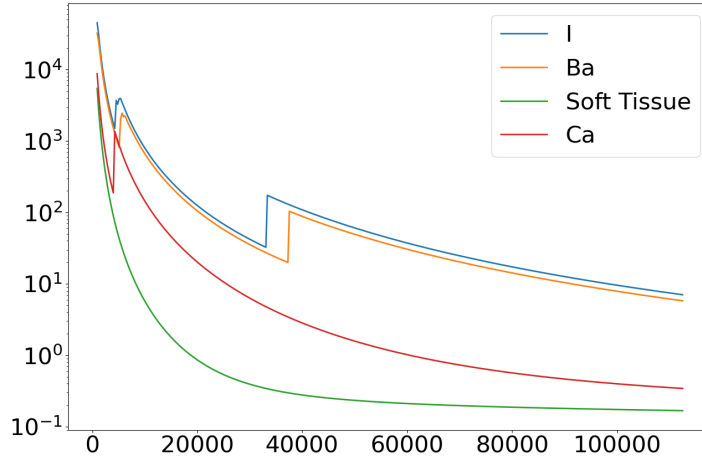


Figure 11.13: Attenuation curves of Iodine (I), Barium (Ba), Soft tissue and Calcium (Ca).

both presenting a K-edge in the selected range. Moreover, we restrict the data even in the spatial dimension by considering the central horizontal slice of each projection. With this set up, it is important to note that the blood vessels shown in Figure 11.12 (top center) will be visible as small dots (and no longer as lines), representing the horizontal section of each vessel.

Finally, by solving the one-stage WL_2 -TV method and optimizing the regularization parameter we obtain the material decomposition in Figure 11.14. From the reconstructed concentration maps we can note that all the three materials are recognized and located inside the object. However, traces of the tissue are present in the Calcium maps as well as in the Barium one.

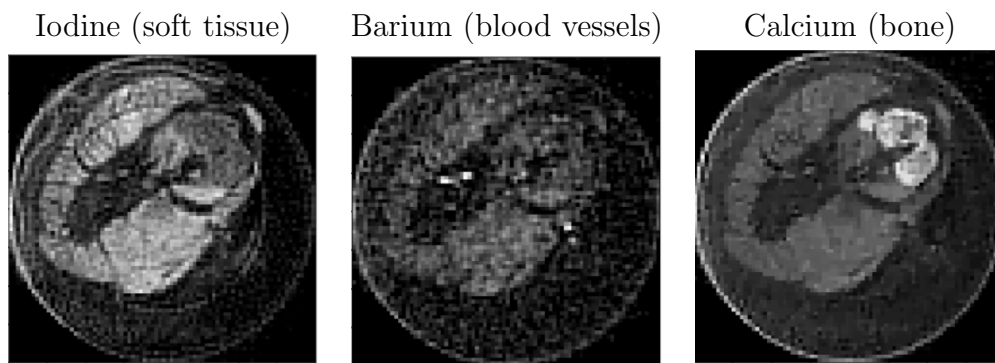


Figure 11.14: Material decomposition results of the real mouse hindlimb phantom obtain with the one-stage method WL_2 -TV.

Conclusions

In this work we focused on low dose CT acquisition scenarios where the standard reconstruction techniques can not be employed because of their poor results due to the high level of Poisson noise in the data. In this cases, variational methods have proven to drastically improve the quality of the reconstruction. However, their performance crucially depend on the values of the free parameters in the model, which are often chosen empirically. Despite the existence of many parameter selection strategies proposed for the case of a single parameter under additive Gaussian noise, few of them can be extended to the case of Poisson noise that characterizes the X-ray CT procedures.

In Chapter 6 we proposed an automatic selection strategy for the regularization parameter of variational image reconstruction models under Poisson noise corruption based on a nearly-exact version of the approximate discrepancy principle originally proposed in [25]. Our approach relies on Monte-carlo simulations, which have been designed with the purpose of providing meaningful insights on the limitations of the original approximate strategy, especially in the low-count Poisson regime. The proposed version of the discrepancy principle has then been derived by means of a weighted least-square fitting and embedded along the iterations of an efficient ADMM-based optimization scheme. Our approach has been extensively tested on different images (both for CT reconstruction and image restoration) and for different photon-count values, ranging from very low to high values. When compared to the original approximate selection criterion, the proposed strategy has

been shown to drastically improve the quality of the output restorations in low-count regimes and in mid-count/high-count regimes on images characterized by few large pixel values.

In Chapter 7 we introduced a novel parameter selection strategy that relies on the extension of the whiteness principle designed for additive white noise to a suitably standardized version of the Poisson-corrupted observation. The derived Poisson whiteness principle has been extensively tested on image restoration and CT reconstruction problems. The Poisson whiteness principle has been compared experimentally with both the popular approximate discrepancy principle [25] and our nearly exact version of it illustrated in Chapter 6. The newly introduced approach has been shown to outperform the competitors especially in the low-counting regime.

In Chapter 8 we discussed the idea of masking the observed data, as originally proposed in [31] to effectively deal with low-count regimes. Nonetheless, we proved that discarding the zero pixels in the data without modifying its distribution accordingly introduces a bias in the resulting principles. Hence, after defining the novel positive Poisson distribution, we proposed the masked unbiased versions of the original criteria. The unmasked, masked biased and masked unbiased strategies have been extensively tested on different images, with different regularization terms and for a wide range of counting regimes. The new class of masked unbiased principles have been proven to outperform, on average, the corresponding unmasked and masked biased counterparts for the image restoration case, while the whiteness principle can be elected the best performing one for CT reconstructions.

Motivated by the performance of the whiteness principle for Poisson noise, in Chapter 9 we extended it principle to the case of multi-parameter selection and tested it, as a proof of concept, for CT data corrupted by both Poisson and Gaussian noise for which a variational model including two free parameters has been adopted. The few experiments show more than encouraging results, both for the quality of the reconstructions and the possibility of solving the problem in a relative shorter time.

Finally, in Chapter 11 we introduced the problem of material decomposition for hyperspectral CT and conducted a preliminary study for the material decomposition of materials with high atomic number with K-edges close to each other in the considered energy range, as well as a test on real data. From the comparison between the two-stage and one-stage methods, we choose the latter and performed more tests to analyse the different data-fidelity and regularization terms. The weighted least squares data fidelity increases considerably the quality of the reconstruction, while the choice of the regularizer depends on the property of the single material. These preliminary findings are promising, as they leads towards the possibility of performing accelerated energy-resolved imaging with better separation of materials. They set the stage for our continued research, as our future work includes further development of dedicated regularizers to separate materials reliably especially for small features, including an investigation of why materials 1 and 4 blend and how to resolve the issue.

The methods developed in this thesis are clearly related to the choice of working in a model-based, variational framework. It would be interesting to study their combination with machine learning-based strategies in order to develop hybrid techniques. In fact, despite their excellent results, deep learning approaches strongly depend on the quality and quantity of the training data and are still characterized by a lack of rigorous mathematical theory that, on the other hand, supports model-based approaches such as variational methods, [85]. This is particularly important for Computed Tomography, where the target reconstructions, used for the training data set, are not available and can only be approximately computed by reconstructing high dose acquisitions, [84, 86], or synthetically generated. Therefore, hybrid strategies that combine model-based and data-driven approaches showed to be the best techniques; they bring the best of both worlds and compensate for each other's disadvantages, [83]. Moreover, the literature on estimating the free model parameters based on learning approaches when noise is of Poisson type is lean. Anyway, selecting the parameters based on the statistics of the corrupting

noise - as we did in this thesis - appears to us more solid than learning them from some training sets which implicitly corresponds to assume some specific prior for the target image. With this idea, we are interested and curious to pair our results with learning strategies and to explore different ways of doing it.

Bibliography

- [1] Hansen, P. C., Jørgensen, J. S., Lionheart, B.: *Computed Tomography: Algorithms, Insight, and Just Enough Theory*. SIAM (2021)
- [2] Buzug, T. M.: *Computed Tomography From Photon Statistics to Modern Cone-Beam CT*. Springer (2008)
- [3] Hounsfield, G.N.: *Computerized transverse axial scanning (tomography): Part 1. Description of system*. Br J Radiol.; 46(552) : 1016-22, (1973).
- [4] Kak, A.C., Slaney, M.: *Principles of computerized tomographic imaging*. Society for Industrial and Applied Mathematic, (2001).
- [5] Preston, C.: *Random fields*. Springer, vol. 534,(2006).
- [6] Kaczmarz, S.: *Angenäherte Auflösung von Systemen linearer Gleichungen*, Bulletin International de l'Académie Polonaise des Sciences et des Lettres. Classe des Sciences Mathématiques et Naturelles. Série A, Sciences Mathématiques, vol. 35, pp. 355-357, (1937)
- [7] Stiller, W.: *Basics of iterative reconstruction methods in computed tomography: a vendor-independent review*. Eur J Radiol.;109:147-54, (2018).
- [8] Willemink, M.J., de John, P.A., et al: *Iterative reconstruction techniques for computed tomography Part 1: Technical principles*. Eur J Radiol.;23:1623-31, (2013).

-
- [9] Geyer, L.L., Schoepf J., et al.: *State of the art: iterative CT reconstruction techniques*. Radiology.;276(2):339-57, (2015).
- [10] Bertero, M., Boccacci P. and Ruggiero V.: *Inverse Imaging with Poisson Data: From cells to galaxies* IOP Publishing Ltd, (2018).
- [11] Elfving, T., Hansen P.C. and Nikazad T.: *Semi-convergence properties of Kaczmarz's method*, Inverse Problems, vol 30, n 5, 055007, (2014).
- [12] Cesareo, R.: *X-ray physics: Interaction with matter, production, detection*. Riv. Nuovo Cim. 23, 1-231 (2000).
- [13] Duan, X., Wang, J., Leng, S., Schmidt, B., Allmendinger, T., Grant, K., Flohr, T., and McCollough, C.H.: *Electronic Noise in CT Detectors: Impact on Image Noise and Artifacts*, American Journal of Roentgenology, vol. 201, iss. 4, pag. W626 - W632, (2013).
- [14] Calvetti, D., Somersalo, E.: *An Introduction to Bayesian Scientific Computing. Ten Lectures on Subjective Computing* Springer, (2007).
- [15] Bayes, T.: *An essay towards solving a Problem in the Doctrine of Chances. By the late Rev. Mr. Bayes, F.R.S. Communicated by Mr. Price in a Letter to John Canton A.M.F.R.S.* Phil. Trans. 53, 370-418 (1763).
- [16] Lanza, A., Morigi, S., Pragliola, M. and Sgallari, F. *Space-variant TV regularization for image restoration*, in VipIMAGE 2017, J. M. R. Tavares and R. Natal Jorge, eds., Cham, Springer, (2018).
- [17] Geman, S.; Geman, D. *Stochastic relaxation, Gibbs distributions, and the Bayesian restoration of images*. IEEE Trans. Pattern Anal. Mach. Intell., 6, 721-741, (1984).
- [18] Rudin, L.I.; Osher, S.; Fatemi, E.: *Nonlinear total variation based noise removal algorithms*. Physica D, 60, 259-268, (1992).

- [19] Lysaker, M., Lundervold, A. and Tai, X.-C.: *Noise removal using fourth-order partial differential equation with applications to medical magnetic resonance images in space and time*. IEEE Trans. Image Process., 12 1579-90, (2003).
- [20] Hintermüller M., Papafitsoros K., Rautenberg C.N., *Analytical aspects of spatially adapted total variation regularisation*, Journal of Mathematical Analysis and Applications, vol. 454, iss. 2, pag. 891-935, ISSN 0022-247X, (2017).
- [21] Kunisch, K.; Bredies, K. and Pock, T.: *Total generalized variation* J. Imaging Sci., 3 492-526, (2010).
- [22] Craven, P.; and Wahba, G.: *Smoothing noisy data with spline functions*. Numer. Math., 31 377-403, (1978).
- [23] Gu, C.: *Cross-validating non-Gaussian data* J. Comput. Graph. Stat., 1 169-79, (1992).
- [24] Wahba, G. and Xiang, D.: *A generalized approximate cross validation for smoothing splines with non-Gaussian data*. Stat. Sin., 6 675-92, (1996)
- [25] Bertero, M., Boccacci, P., Talenti, G., Zanella, R. and Zanni, L.: *A discrepancy principle for poisson data*. Inverse Problems, 26 105004, (2010).
- [26] Zanella, R., Boccacci, P., Zanni, L. and Bertero, M. *Efficient gradient projection methods for edgepreserving removal of Poisson noise*. Inverse Problems, 25 045010, (2009).
- [27] Zanella, R., Boccacci, P., Zanni, L. and Bertero, M.: *Corrigendum: efficient gradient projection methods for edge-preserving removal of Poisson noise* Inverse Problems, 29 119501, (2013).

-
- [28] Sixou, B., Hohweiller, T. and Ducros, N.: *Morozov principle for Kullback-Leibler residual term and Poisson noise* Inverse Problems Imaging, 12 607-34, (2018).
- [29] Teuber, T., Steidl, G. and Chan, R. H.: *Minimization and parameter estimation for seminorm regularization models with l -divergence constraints* Inverse Problems, 29 035007, (2013).
- [30] Zanni, L., Benfenati, A., Bertero, M. and Ruggiero, V.: *Numerical methods for parameter estimation in Poisson data inversion* J. Math. Imaging Vis., 52 397-413, (2015).
- [31] Carlavan, M. and Blanc-Feraud, L.: *Sparse Poisson noisy image deblurring* IEEE Trans. Image Process., 21 1834-46, (2012).
- [32] Bardsley, J.M. and Goldes J.: *Regularization parameter selection methods for ill-posed Poisson maximum likelihood estimation.* Inverse Problems, 25(9):095005, (2009).
- [33] Bonettini, S., Prato, M.: *Accelerated gradient methods for the x-ray imaging of solar flares.* Inverse Problems 30, 055004, (2014).
- [34] Benvenuto, F.: *A study on regularization for discrete inverse problems with model-dependent noise.* SIAM Journal on Numerical Analysis 55, 2187-2203, (2017).
- [35] Guastavino, S., Benvenuto, F.: *A mathematical model for image saturation with an application to the restoration of solar images via adaptive sparse deconvolution.* Inverse Problems 37, 0150104, (2021).
- [36] Wang, Z., Bovik, A.C., Sheikh, H.R., Simoncelli, E. P.: *Image quality assessment: from error visibility to structural similarity.* IEEE Transactions on Image Processing 13, 600-612, (2004).
- [37] Johnson, N.L., Kemp, A.W., Kotz, S.: *Univariate Discrete Distributions.* New York: Wiley, (2005).

- [38] Grinvald A. and Steinberg I. Z.: *On the analysis of fluorescence decay kinetics by the method of least-squares* Analytical Biochemistry, 59(2):583-598, (1974).
- [39] Bevilacqua, F., Lanza, A., Pragliola, M., Sgallari F.: *Nearly exact discrepancy principle for low-count Poisson image restoration*, Journal of Imaging 8 (1) 1-35, (2022).
- [40] van Aarle, W., Palenstijn, W.J., Cant, J., Janssens, E., Bleichrodt, F., Dabravolski, A., Beenhouwer, J.D., Batenburg, K.J., Sijbers, J.: *Fast and flexible X-ray tomography using the ASTRA toolbox*, Optics Express 24(22) 25129-25147, (2016).
- [41] Bevilacqua, F., Lanza, A., Pragliola, M., and Sgallari, F.: *Whiteness-based parameter selection for Poisson data in variational image processing*. Applied Mathematical Modelling, vol. 117, pag. 197-218, ISSN 0307-904X, (2023).
- [42] Hansen, P., Kilmer, M., Kjeldsen, R.: *Exploiting residual information in the parameter choice for discrete ill-posed problems*, BIT Numerical Mathematics 46, 41-59, (2006).
- [43] Almeida, M., Figueiredo, M.: *Parameter estimation for blind and non-blind deblurring using residual whiteness measures*, IEEE Transactions on Image Processing 22, 2751-2763, (2013).
- [44] Lanza, A., Pragliola, M., Sgallari, F.: *Residual whiteness principle for parameter-free image restoration*, Electronic Transactions on Numerical Analysis 53, 329-351, (2020).
- [45] Pragliola, M., Calatroni, L., Lanza, A., Sgallari, F.: *Residual whiteness principle for automatic parameter selection in l_2 - l_2 image super-resolution problems*. A. Elmoataz, J. Fadili, Y. Qu àeau, J. Rabin, L. Simon (Eds.), Scale Space and Variational Methods in Computer Vision, Springer International Publishing, Cham, pp. 476-488, (2021).

- [46] Pragliola, M., Calatroni, L., Lanza, A., Sgallari, F.: *ADMM-based residual whiteness principle for automatic parameter selection in single image super-resolution problems*, Journal of Mathematical Imaging and Vision, 1-35, (2022).
- [47] Lanza, A., Pragliola, M., Sgallari, F.: *Automatic fidelity and regularization terms selection in variational image restoration*, BIT Numerical Mathematics 62 (3), 931-964, (2022).
- [48] Ding, Q., Long, Y., Zhang, X. and Fessler J. A. *Modeling Mixed Poisson-Gaussian Noise in Statistical Image Reconstruction for X-Ray CT*. The 4th International Conference on Image Formation in X-Ray Computed Tomography, (2016).
- [49] Calatroni, L., De Los Reyes, J.C. , Schönlieb C.B. *Infimal convolution of data discrepancies for mixed noise removal*. Society for Industrial and Applied Mathematics, Vol. 10, No. 3, pp. 1196-123, (2017).
- [50] Jezierska, A., Chouzenoux, E., Pesquet, J.-C. and Talbot, H.: *A primal-dual proximal splitting approach for restoring data corrupted with Poisson-Gaussian noise*. IEEE International Conference on Acoustics, Speech and Signal Processing, Kyoto, (2012).
- [51] Jezierska, A., Chouzenoux, E., Pesquet, J.-C. and Talbot, H.: *A Convex Approach for Image Restoration with Exact Poisson-Gaussian Likelihood*. SIAM Journal on Imaging Science, 62(1):17-30, (2015).
- [52] Lanza, A., Morigi, S., Sgallari, F. and Wen, Y.-W.: *Image restoration with poisson-gaussian mixed noise*. Computer Methods in Biomechanics and Biomedical Engineering: Imaging and Visualization, 2:12-24, (2014).
- [53] Boyd, S., Parikh, N., Chu, E., Peleato, B. and Eckstein, J.: *Distributed optimization and statistical learning via the alternating direction method*

- of multipliers*. Foundations and Trends in Machine Learning, 3(1):1-122, (2011).
- [54] Lefkimmiatis, S. and Unser, M.: *Poisson image reconstruction with hessian Schatten-norm regularization*. IEEE Transactions on Image Processing, 22(11):4314-4327, (2013).
- [55] di Serafino, D., Landi, G. and Viola, M.: *Directional TGV-based image restoration under Poisson noise*. Journal of Imaging, 7(6):99, (2021).
- [56] Hintermüller M., Papafitsoros K., Rautenberg C.N. and Sun H. *Dualization and Automatic Distributed Parameter Selection of Total Generalized Variation via Bilevel Optimization* Numerical Functional Analysis and Optimization, 43:8, 887-932, (2022).
- [57] Larson, J., Menickelly, M. and Wild, S. *Derivative-free optimization methods*. Acta Numerica, 28, 287-404, (2019).
- [58] Lucidi, S., Sciandrone, M. *A Derivative-Free Algorithm for Bound Constrained Optimization*. Computational Optimization and Applications 21, 119-142, (2002).
- [59] Corless, R.M., Gonnet, G.H., Hare, D.E., Jeffrey, D.J., Knuth, D.E.: *On the Lambert W function*. Advances in Computational Mathematics, 5, 329-359, (1996).
- [60] Bevilacqua, F., Dong, Y., Jørgensen, J.S.: *Regularized Material Decomposition for K-edge Separation in Hyperspectral Computed Tomography*. Scale Space and Variational Methods in Computer Vision. SSVM 2023. Lecture Notes in Computer Science, vol 14009. Springer, Cham. (2023).
- [61] Lu, G., Fei, B.: *Medical hyperspectral imaging: a review* J Biomed Opt., Jan;19(1):10901, (2014).
- [62] Yoon, J.: *Hyperspectral Imaging for Clinical Applications*. BioChip J 16, 1-12, (2022).

- [63] Seibert, J. and Boone, J.: *X-Ray Imaging Physics for Nuclear Medicine Technologists. Part 2: X-Ray Interactions and Image Formation*. Journal of nuclear medicine technology. 33. 3-18, (2005).
- [64] Hubbell, J.H. and Seltzer, S.M.: *X-Ray Mass Attenuation Coefficients. NIST Standard Reference Database 126*
- [65] Gondzio, J., Lassas, M., Latva-Äijö, S.-M., Siltanen, S., Zanetti, F. *Material-separating regularizer for multi-energy xray tomography*. Inverse Problems 38 025013, (2022).
- [66] Alvarez, R.E., Macovski, A.: *Energy-selective reconstructions in X-ray computerized tomography*. Phys. Med. Biol. 21 733-44, (1976).
- [67] Schlomka, J.P., Roessl, E., Dorscheid, R., Dill, S., Martens, G., Istel, T., Bäumer, C., Herrmann, C., Steadman, R., Zeitler, G., Livne, A., Proksa, R.: *Experimental feasibility of multi-energy photon-counting K-edge imaging in pre-clinical computed tomography*. Phys. Med. Biol. 53 4031 (2008).
- [68] Feng, J., Yu, H., Wang, S., Liu, F.: *Image-Domain Based Material Decomposition by Multi-Constraint Optimization for Spectral CT*. in IEEE Access, vol. 8, pp. 155450-155458, (2020).
- [69] Tao, S., Rajendran, K., McCollough, C.H., Leng, S.: *Material decomposition with prior knowledge aware iterative denoising (MD-PKAID)*. Phys. Med. Biol. 63 195003, (2018).
- [70] Schmidt, T.G., Barber, R.F., Sidky, E.Y.: *A Spectral CT Method to Directly Estimate Basis Material Maps From Experimental Photon-Counting Data*. IEEE Trans Med Imaging, 36(9):1808-1819, (2017).
- [71] Liu, J., Ding, H., Molloy, S., Zhang, X., Gao, H.: *TICMR: Total Image Constrained Material Reconstruction via Nonlocal Total Variation Regularization for Spectral CT*. IEEE Transactions on Medical Imaging, vol. 35, no. 12, pp. 2578-2586, (2016).

- [72] Mory, C., Sixou, B., Si-Mohamed, S., Boussel, L., Rit, S.: *Comparison of five one-step reconstruction algorithms for spectral CT*. Phys. Med. Biol. 63 235001, (2018).
- [73] Warr R, Ametova E, Cernik RJ, Fardell, G., Handschuh, S., Jørgensen, J.S., Papoutsellis, E., Pasca, E., Withers, P.J.: *Enhanced hyperspectral tomography for bioimaging by spatio-spectral reconstruction*. Sci Rep. 2021 Oct 21;11(1):20818, (2021).
- [74] Jørgensen, J.S., Ametova, E., Burca, G., Fardell, G., Papoutsellis, E., Pasca, E., Thielemans, K., Turner, M., Warr, R., Lionheart, W.R.B., Withers, P.J.: *Core Imaging Library Part I: a versatile python framework for tomographic imaging*. Phil. Trans. R. Soc. A 20200192, (2021).
- [75] Papoutsellis, E., Ametova, E., Delplancke, C., Fardell, G., Jørgensen, J.S., Pasca, E., Turner, M., Warr, R., Lionheart, W.R.B., Withers, P.J.: *Core Imaging Library - Part II: multichannel reconstruction for dynamic and spectral*. Phil. Trans. R. Soc. A 20200193, (2021).
- [76] Horé, A., Ziou, D.: *Image Quality Metrics: PSNR vs. SSIM*. In: 2010 20th International Conference on Pattern Recognition, pp. 2366-2369, Istanbul, Turkey, (2010).
- [77] Poludniowski, G., Omar, A., Bujila, R., Andreo, P.: *Technical Note: SpekPy v2.0-a software toolkit for modeling x-ray tube spectra*. Med. Phys. 48 (7), 3630-3637, (2021).
- [78] *X-ray Reference Data in SQLite library* xraypy.github.io/XrayDB/
- [79] Perelli, A., Andersen, M.S.: *Regularization by denoising sub-sampled Newton method for spectral CT multi-material decomposition*. Phil. Trans. R. Soc. A.379: 20200191, (2021).
- [80] Hu, Y., Andersen, M.S., Nagy, J.G.: *Spectral Computed Tomography with Linearization and Preconditioning*. SIAM Journal on Scientific Computing, vol. 41 iss. 5, (2019).

-
- [81] Warr, R., Handschuh, S., Gl øsmann, M., Cernik, R.J., Withers, P.J.: *Quantifying multiple stain distributions in bioimaging by hyperspectral X-ray tomography*. Sci Rep 12, 21945, (2022).
- [82] Chambolle, A., Pock, T.: *A First-Order Primal-Dual Algorithm for Convex Problems with Applications to Imaging*. Journal of Mathematical Imaging and Vision, 40, pp 120-145, (2011).
- [83] Bubba T. A., Kutyniok G., Lassas M., März M., Samek W., Siltanen S., Srinivasan V.: *Learning The Invisible: A Hybrid Deep Learning-Shearlet Framework for Limited Angle Computed Tomography*. Inverse Problems 35 064002, (2019).
- [84] Betcke M.M., Schönlieb C.: *Mathematics of biomedical imaging today - a perspective*. Prog. Biomed. Eng. 5 043002, (2023).
- [85] Arridge, S., Maass, P., Öktem, O., and Schönlieb, C.. *Solving inverse problems using data-driven models* Acta Numerica, pp. 1-174, (2019).
- [86] Koetzier, L.R., Mastrodicasa, D., Szczykutowicz, T.P., van der Werf, N.R., Wang, A.S., Sandfort, V., van der Molen, A.J., Fleischmann, D., Willeminck M.J.: *Deep Learning Image Reconstruction for CT: Technical Principles and Clinical Prospects* Radiology, 306:3, (2023).